Mechanochemical Reduction of Lithium-Ion Battery Black Mass for Selective Lithium Extraction

Zur Erlangung des akademischen Grades eines

DOKTORS DER NATURWISSENSCHAFTEN
(Dr. rer. nat.)

von der KIT-Fakultät für Chemie und Biowissenschaften

des Karlsruher Instituts für Technologie (KIT)

genehmigte

DISSERTATION

von

M.Sc. Raphael Sieweck

1. Referent: Prof. Dr. Helmut Ehrenberg
2. Referentin: Prof. Dr. Daria Mikhailova
Tag der mündlichen Prüfung: 20.07.2026



Dieses Werk ist lizenziert unter einer Creative Commons Namensnennung 4.0 International Lizenz (CC BY 4.0): https://creativecommons.org/licenses/by/4.0/deed.de

Selbständigkeitserklärung

Hiermit versichere ich, dass ich die vorliegende Arbeit selbstständig verfasst habe, dassich keine anderen als die angegebenen Quellen und Hilfsmittel benutzt habe, dass ichdie wörtlich oder inhaltlich übernommenen Stellen als solche gekennzeichnet habeund dass ich die Satzung des KIT zur Sicherung guter wissenschaftlicher Praxis in derjeweils gültigen Fassung beachtet habe.

Karlsruhe, den 10.06.2026

Raphael Sieweck

Contents

1 Introduction **1**
1.1 The lithium-ion battery . . . 2
1.2 Critical raw materials . . . 6
1.3 Recycling . . . 8
1.3.1 Pretreatment . . . 9
1.3.2 Pyrometallurgy . . . 10
1.3.3 Hydrometallurgy . . . 11
1.3.4 Direct recycling . . . 12
1.4 Battery recycling in Europe . . . 12
1.5 Mechanochemistry . . . 13
1.5.1 Basics . . . 13
1.5.2 The energy transfer by impacts . . . 15
1.5.3 Physico-chemical transformations induced by ball-milling . . . 17
1.5.4 Collision model based energetic considerations . . . 18
1.5.5 Mechanochemistry in battery recycling . . . 21
1.5.6 Mechanically-induced self-propagating reaction (MSR) . . . 24

2 Motivation **27**

3 Analytical Techniques **29**
3.1 X-ray techniques . . . 29
3.1.1 Generation of X-rays . . . 29
3.1.2 X-ray diffraction . . . 29
3.1.3 X-ray absorption spectroscopy (XAS) . . . 31
3.2 Scanning electron microscopy with energy dispersive X-ray spectroscopy . . . 33
3.3 Inductively coupled plasma optical emission spectroscopy . . . 34
3.4 Ion-selective electrode . . . 35

4 Materials and Methods **37**
4.1 Materials . . . 37
4.2 Characterization . . . 37
4.2.1 X-ray diffraction (XRD) . . . 37
4.2.2 X-ray absorption near edge structure (XANES) . . . 37
4.2.3 Thermogravimetric analysis (TGA) . . . 38
4.2.4 Static Light Scattering . . . 38
4.2.5 Scanning electron microscopy and energy dispersive x-ray spectroscopy (SEM & EDX) . . . 39
4.2.6 Inductively coupled plasma optical emission spectroscopy (ICP-OES) . . . 39

4.2.7 Ion-selective electrodes . . . 39
4.2.8 UV-Vis Spectrometer . . . 39
4.3 Methods . . . 40
4.3.1 High-energy ball-milling . . . 40
4.3.2 Aqueous lithium extraction . . . 41
4.3.3 Cobalt leaching . . . 43

5 Results and Discussion **44**
5.1 Overview . . . 44
5.2 Experiments on pristine CAMs . . . 46
5.2.1 The Mechanism behind the mechanochemical reduction of LCO with Al . . . 46
5.2.2 Other reducing agents . . . 55
5.2.3 The effect of process parameters . . . 60
5.2.4 Influence of Graphite . . . 69
5.2.5 Mechanochemical processing of CAMs with Sulfur . . . 71
5.3 Black Mass . . . 79
5.3.1 Analysis of the Black Mass . . . 80
5.3.2 Reactive Milling of the black mass . . . 84
5.3.3 The effect of milling parameters on black mass . . . 90
5.3.4 The influence of volatiles and organics . . . 92
5.3.5 Selective Lithium extraction from milled black mass . . . 95
5.4 Further optimization and process implementation . . . 100
5.5 Safety Considerations . . . 102

6 Summary **104**

7 Conclusions **105**

8 Outlook **106**

References **107**

SI: Supporting Information **123**
1 Supporting Tables . . . 123
2 Supporting Figures . . . 132
S1 XRD-Pattern . . . 132
S2 Milling plots . . . 137
S3 X-ray Spectroscopy . . . 139
S4 Supporting Pictures . . . 147

List of Figures

1.1 Schematic representation of a) a lithium-ion battery cell and b) a cylindrical cell set-up. 2
1.2 Crystal structures of common cathode active materials. 3
1.3 Typical mass fractions of components in a NMC based lithium-ion battery cell, adapted from Tembo et al.[32] 5
1.4 Graphical overview of lithium-ion batteries and materials. a) Demand for LIBs in EVs and stationary energy storage 6
1.5 Timeline for recycling quotas according to the battery regulation.[10] 12
1.6 Main stress types occurring in ball-milling experiments. 14
1.7 Schematic representation of a) a shaker ball-mill (SPEX), b) a planetary ball-mill, and c) an attritor mill. 15
1.8 Illustration of a Herzian collision and of force chains in a coarse powder under compression. 16
1.9 Schematic representation of balls trajectory in a planetary ball-mill 20
3.1 Illustration of X-ray reflection on crystal lattice planes (adapted from[157]). 30
3.2 XANES spectra of NMC-111 at the Co-K_α edge. 32
4.1 Setup of the planetary ball-milling vial with sensors for internal temperature and pressure in the lid.[175] 40
5.1 Evolution of XRD pattern during BM-Al processing in the SPEX mill. 45
5.2 Temperature and pressure profiles during the mechanochemical transformation of LCO and Al. 47
5.3 Microscopy images with EDX mapping of LCO milled with Al for different times. . . 49
5.4 SEM and EDX images of cross sections of Sample II (a, b) and Sample III (c, d) . . 50
5.5 Evolution of the particle size distribution during the mechanochemical treatment of LCO with Al. 51
5.6 Evolution of XRD patterns during the mechanochemical reduction of LCO with Al . 52
5.7 XRD pattern of an isolated metallic piece 53
5.8 Ignition times of the MSR reaction of $LiCoO_2$ with different reducing agents. 56
5.9 XRD pattern of powder after the mechanochemical reactions of LCO with different reducing agents. 57
5.10 Lithium extraction yields of LCO milled with various reductants. 58
5.11 XRD patterns of the dried soluble fraction obtained from leaching the milled mixture of LCO with the respective reducing agent. 59
5.12 Influence of the rotation speed and the ball size on the mechanochemical reduction of LCO with Al and Mg 61
5.13 Comparison of the specific milling dose D_{ig} and the specific activation dose D^*_{ig} for the ball sizes a) 3 mm, b) 6.35 mm, and c) 12.7 mm in the mechanochemical reaction between LCO and Al, and d) for LCO-Mg using the 6.35 mm balls. 63

5.14 Impact of the 1/BSR and ball size on a) the ignition time and b) the specific energy dose of the mechanochemical reaction between LCO and Al 66
5.15 Photographs of metallic pieces, obtained after the MSR between LCO and Al at BSR = 8. 67
5.16 Influence of the total filling of the milling vial. 68
5.17 XRD pattern of the mechanochemical reduction of LCO with Al and in the presence of 0 - 60 wt% of graphite after a) 10 min and b) 60 min of milling 70
5.18 Mechanochemical reaction progress in equimolar LCO-S mixture. Evolution of a) XRD pattern, b) XANES spectra at the Co K-edge and c) phase fractions quantified by LCF.[198] 72
5.19 a) Evolution of atomic Co fraction as LCO during the mechanochemical reaction between LCO and S at different η quantified by LCF analysis. b) Final phase fractions derived from LCF analysis after the reaction of LCO with S.[198] 74
5.20 Li and Co extraction yields obtained from aqueous leaching of LCO milled with S at η in the range of 1 to 3, together with the pH of the respective leachates.[198] 75
5.21 Dependency of Cobalt dissolution on addition of H_2O_2[198] 77
5.22 Evolution of XRD pattern during the mechanochemical processing of the LCO-graphite-S system.[198] 78
5.23 XRD pattern of the received black mas.[176] 80
5.24 a) Photograph and b-f) SEM images of the received black mas.[176] 81
5.25 SEM images of the black mass at two locations with EDX based elemental overlay.[176] 82
5.26 a) Thermo gravimetric analysis (solid line) and its derivative (dashed line) of the black mass in oxygen atmosphere. b) Phase composition of the black mass.[176] 83
5.27 Evolution of XRD pattern during the mechanochemical processing of black mass with Al. 85
5.28 Evolution of XANES spectra during the milling process of BM with Al at the Mn- (a), Co- (b) and Ni-K_α edge (c) alongside with the spectra of respective reference metallic foils. Panels d – f) show the evolution of phase fractions in the milled powder obtained by linear combination fitting.[176] 86
5.29 Evolution of XRD patterns during milling of the received BM with Mg.[176] 88
5.30 Evolution of XANES spectra during the milling process of BM with Mg at the a) Mn-, b) Co-, and c) Ni-K_α edge, alongside with the spectra of respective reference metallic foils. Panels d) – f) show the evolution of phase fractions in the milled powder obtained by linear combination fitting.[176] 89
5.31 Influence of the total ball mass and the BSR on the milling time for of the mechanochemical reduction of BM with Mg using a) 6.35 mm and b) 12.7 mm balls. c) Total energy consumption of the planetary ball-mill scaled to the powder mass.[176] 91
5.32 Comparison between 12.7 mm and 6.35 mm balls in the mechanochemical reduction of black mass using 20.2 wt% Mg powder, 123 g balls, and a BSR of 10. 92
5.33 TGA (solid lines) and dTG (dotted lines) of the black mass in argon atmosphere.[176] 93

5.34 Evolution of mean oxidation state provided by XANES analysis during the mechanochemical processing of different treated BM with Al (black) and Mg (red) as the reducing agent. Enlarged data points represent the dis-appearance of NMC reflections in the XRD.[176] 94
5.35 Flow sheet of the aqueous lithium extraction from milled black mass.[176] 96
5.36 Evolution of XRD during the aqueous lithium extraction of dried BM milled with Al a)-c) and Mg d). Separation was per-formed by direct filtration a) and d), after *Carbonatization* b) and after *Katoite* process c). Panel e shows the Li extraction yield. The error bars indicate the spread of two independent extraction experiments. Panel f) shows the relative concentrations of Al and F-ions in the recovered Li salt solution.[176] 97
5.37 Evolution of XRD pattern during the purification process of the Li salt solution. The pattern were collected using Cu-$K_{\alpha 1}$ radiation. 101
S1.1 XRD pattern of the insoluble residue obtained after aqueous leaching of LCO milled with Si, P, and S. 132
S1.2 Evolution of XRD pattern during the milling of LCO with Al at 350 rpm with 3.0 mm balls. 132
S1.3 XRD pattern of pristine graphite. 132
S1.4 Evolution of XRD pattern during the mechanochemical processing of LCO with different amounts of elemental Sulfur, and a comparison of the final XRD pattern.[198] 133
S1.5 Evolution of XRD pattern during the selective Li-extraction of a milled S:LCO mixture in various molar ratios η.[198] 134
S1.6 XRD pattern of black mass milled with Al for 120 min. As reference materials, NMC, NiO and CoO are presented with the COD ID 4002443, 1010095 and 1533087, respectively. 135
S1.7 Evolution of XRD pattern during the milling of commercial NMC powder mixed with graphite and Al.[175] 135
S1.8 Evolution of XRD patterns during the reaction of BM_{dried} with a) Al, b) Mg and of BM_{washed} with c) Al and d) Mg.[176] 136
S1.9 XRD pattern of the insoluble fraction, obtained from the carbonatization process. As reference materials, $LiMn_2O_4$, Co_3O_4 and NiO are presented with the COD ID 1513962, 5910031 and 1010095, respectively. 136
S2.1 Measured t_{ig} during mechanochemical reaction of LCO with Al (a-c) and LCO with Mg (d). The lines represent the best fit of the formula $t_{ig}=A \cdot \nu^b$ 137
S2.2 Measured t_{ig} during mechanochemical reaction of LCO with Al (a-c) and LCO with Mg (d). The lines represent the best fit of the formula $t_{ig}=A \cdot \nu^b$ 137
S2.3 Temperature and pressure profile during the milling of LCO with Al using 65 g of 3 mm balls and 2.17 g of powder at 350 rpm. 138
S2.4 Temperature and pressure profiles recorded during the milling of LCO with Al and 0 - 60 wt% graphite.[175] 138

S2.5 Pressure and temperature profiles, recorded during the milling of received black mass with a) Al and b) Mg. The zig-zag profiles show alternating cycles of 5 min milling and 5 min resting. The strong drops in T and p show the sampling points, where the milling vial was opened. When referred to the milling time, the resting time is not included. Therefore the spike in the pressure curve in panel b is after 206 min (41 x 5 min + 1 min) of milling.[176] 138

S3.1 Evolution of EDX-spectra during the mechanochemical reduction of LCO with Al. . . 139

S3.2 XANES spectra of Reference materials at the Co K_α-edge. 139

S3.3 Evolution of XANES Spectra and atomic fractions determined by LCF during the mechanochemical reaction between LCO and S at molecular ratios η of a,b) 1.5, c,d) 2.0, e,f) 2.5 and g,h) 3.0.[198] 140

S3.4 XANES spectra of on the K_α-edges of a) Mn, b) Co, and c) Ni of the BM and the LCF showing the presence of NMC-111.[176] 141

S3.5 Linear combination fitting of XANES Co-K_α edge obtained from initial black mass milled with Al.[176] 141

S3.6 Linear combination fitting of XANES Mn-K_α edge obtained from initial black mass milled with Al.[176] 142

S3.7 Linear combination fitting of XANES Ni-K_α edge obtained from initial black mass milled with Al.[176] 142

S3.8 Linear combination fitting of XANES Mn-K edge obtained from black mass milled with Mg.[176] 143

S3.9 Linear combination fitting of XANES Co-K edge obtained from black mass milled with Mg.[176] 143

S3.10 Linear combination fitting of XANES Ni-K edge obtained from black mass milled with Mg.[176] 144

S3.11 Evolution of XANES spectra during the milling process of BM_{dried} with Al at the Mn- (a), Co- (b) and Ni-K_α edge (c), alongside with the spectra of respective reference metallic foils. Panels d – f show the evolution of phase fractions in the milled powder obtained by linear combination fitting.[176] 144

S3.12 Evolution of XANES spectra during the milling process of BM_{dried} with Mg at the Mn- (a), Co- (b) and Ni-K_α edge (c), alongside with the spectra of respective reference metallic foils. Panels d – f show the evolution of phase fractions in the milled powder obtained by linear combination fitting.[176] 145

S3.13 Evolution of XANES spectra during the milling process of BM_{washed} with Al at the Mn- (a), Co- (b) and Ni-K_α edge (c), alongside with the spectra of respective reference metallic foils. Panels d – f show the evolution of phase fractions in the milled powder obtained by linear combination fitting.[176] 145

S3.14Evolution of XANES spectra during the milling process of BM_{washed} with Mg at the Mn- (a), Co- (b) and Ni-K_α edge (c), alongside with the spectra of respective reference metallic foils. Panels d – f show the evolution of phase fractions in the milled powder obtained by linear combination fitting.[176] 146
S4.1 Light microscopy images of Sample III from the mechanochemical reaction between LCO and Al immediately after the pressure rise. 147
S4.2 Relative concentrations of transition metals in the recovered lithium salt solution from different extraction processes.[176] 147

List of Tables

5.1 Samples collected from the mechanochemical reaction of LCO and Al at 650 rpm with 65 g balls (6.35 mm), 2.17 g of powder, LCO/Al =1.0 and a BSR of 30. 48
5.2 Summery of calculated parameters, obtained by variation of the rotation speed in the mechanochemical reduction of LCO 63
S1 Elemental composition, determined by ICP-OES, of Products obtained after mechanochemical reaction between LCO and Al at 650 rpm using 65 g balls (6.35 mm), 2.17 g of powder, LCO/Al =1.0 and a BSR of 30. A large metallic piece was obtained milling was stopped after 3.2 min, directly after the spike in pressure was observed. A homogeneous powder was analyzed after 60 min of total milling.[175] 123
S2 Experimental and calculated data presented in Fig. 5.12. Milling of LCO with Al at different ν_R using small balls.[175] 123
S3 Experimental and calculated data presented in Fig. 5.12. Milling of LCO with Al at different ν_R using large balls. 124
S4 Experimental and calculated data presented in Fig. 5.12. Milling of LCO with Al at different ν_R using medium balls.[175] 124
S5 Experimental and calculated data presented in Fig. 5.12. Milling of LCO with Mg at different ν_R using medium balls.[175] 125
S6 Experimental and calculated data presented in Fig. 5.14: Milling of LCO with Al at different $1/BSR$ using small balls.[175] 125
S7 Experimental and calculated data presented in Fig. 5.14: Milling of LCO with Al at different $1/BSR$ using medium balls.[175] 126
S8 Experimental and calculated data presented in Fig. 5.14: Milling of LCO with Al at different $1/BSR$ using large balls.[175] 127
S9 Experimental and calculated data presented in Fig. 5.16. Milling of LCO with Al at different ν_R using 32 medium balls. 127
S10 Experimental and calculated data presented in Fig. 5.16. Milling of LCO with Al at different ν_R using 128 medium balls. 128

S11 Kinematic calculations based on Burgios model. Data obtained from a study by Vauloup et. al.[182] . . . 128
S12 Normal potentials of redox pairs in aqueous solutions (pH=1 and 14) according to Ref. [132] . . . 128
S13 Ion concentrations determined by ICP-OES in filtrates obtained from mechanochemical reaction between sulfur and LCO at different molar ratios η.[198] . . . 129
S14 Elemental analysis of the Black Mass done by ICP-OES measurements of three independent samples. . . . 129
S15 Standard enthalpy of formation of selected compounds. . . . 129
S16 Elemental analysis in mg/L of the combined filtrated obtained from different leaching routes of dried black mass. . . . 130
S17 Elemental analysis in wt% of the insoluble residue obtained from different leaching routes of dried black mass.[176] . . . 130
S18 Elemental analysis in wt% of the recovered and purified Li_2CO_3 salt obtained from different leaching routes of dried black mass. . . . 131

Abbreviations and Symbols

Abbreviations

BM	Black mass
CAM	Cathode active material
COD	Crystallographic open database
EDX	Energy dispersive X-ray spectroscopy
EoL	End-of-life
Eq.	Equation
EU	European Union
ISE	Ion-selective electrode
KIT	Karlsruhe Institute of Technology
LCF	Linear combination fit
LIB	Lithium-ion battery
MSR	Mechanically-induced self-propagating reaction
SEM	Scanning electron microscopy
SLS	Static light scattering
TISAB	Total ionic strength adjustment buffer
TM	Transition metal
XANES	X-ray absorption near-edge structure
XRD	X-ray diffraction

Chemicals

Chemicals	**Formula**	**Name**
EDTA	$C_{10}H_{16}N_2O_8$	ethylenediaminetetraacetic acid
LACHH	$Li_2Al_4(CO_3)(OH)_{12} \cdot 3\,H_2O$	Lithium aluminum carbonate hydroxy hydrate
LCO	$LiCoO_2$	Lithium cobalt oxide
LFP	$LiFePO_4$	Lithium iron phosphate
LMO	$LiMn_2O_4$	Lithium manganese oxide
NMC-xyz	$LiNi_xCo_yMn_zO_2$	Lithium nickel cobalt manganese oxide
NMP	C_5H_9NO	N-methyl pyrrolidone
PVDF	$[-CH_2-CF_2-]_n$	polyvinylidene difluoride

Symbols

BSR	Ball-to-sample mass ratio
c_i	Concentration of i
D	Specific milling dose
D^*	specific activation dose
d_b	ball diameter
ΔH	Enthalpy
ΔE_b^*	maximum kinetic energy transferred from a ball to the sample by an impact
E_0	Energy threshold
ε_0	normal potential
η	Molecular ratio
f_b	collision frequency
M(x)	Molar weight of x
m_p	powder mass
N_b	Number of balls
N_{tot}	Total number of impacts
ν_R	rotation speed
θ	diffraction angle
T	Temperature
t_{ig}	milling time till ignition
χ_i	weight fraction of i
Y_i	Extraction yield of i

Danksagung

Im Laufe meiner Promotion wurde ich von vielen Personen tatkräftig unterstützt, denen ich an dieser Stelle meinen aufrichtigen Dank aussprechen möchte.

Mein besonderer Dank gilt Prof. Dr. Helmut Ehrenberg für die Aufnahme als Doktorand am IAM-ESS sowie für die Übernahme des Erstgutachtens. Ebenso danke ich Prof. Dr. Daria Mikhailova herzlich für die Übernahme des Zweitgutachtens. Dr. Michael Knapp danke ich besonders für die kontinuierliche Betreuung während der gesamten Promotionszeit, die zahlreichen hilfreichen Diskussionen sowie das Korrekturlesen meiner Manuskripte.

Ein großer Dank gilt ebenfalls Dr. Arseniy Bokov für die vielen wertvollen fachlichen Diskussionen und Denkanstöße, für das sehr sorgfältige Korrekturlesen von Manuskripten sowie für die Wartung der XRD-Geräte. Dr. Oleksandr Dolotko danke ich für die fundierte thematische Einarbeitung und seine engagierte Betreuung, die er sogar noch über seine Anstellung hinaus weiterführte.

Ich danke Udo Geckle für die Durchführung der SEM-Messungen sowie Dr. Ramon Zimmermann für die XAS-Messungen. Liuda Mereacre danke ich herzlich für die Organisation des Labors, die Unterstützung in zahlreichen praktischen Fragen sowie für die Aufnahme einiger SEM-Bilder. Dr. Thomas Bergfeldt danke ich für die Durchführung der Elementanalysen, und Almut Kriese für die administrative Unterstützung. Dr. Isabelle Südmeyer danke ich für die Unterstützung beim Management des RHINOCEROS-Projekts. Mein Dank gilt außerdem Luis Sanchez Neudeck für seinen zuverlässigen IT-Support sowie Heinz Göbel für seine Unterstützung bei Reperatur von Geräten und dem Versenden von Proben.

Bedanken möchte ich mich auch bei meinen Bachelor- und Masterstudenten Niklas Gehrke, Pirmin Koch und Alexander Pöplow sowie bei den studentischen Hilfskräften Devika Satheesh Lal und Triantafillia Malliaridou für die gute und produktive Zusammenarbeit, die wesentlich zum Fortschritt meiner Arbeit beigetragen hat. Ebenso möchte ich mich bei allen Kolleginnen und Kollegen am IAM-ESS bedanken, die durch fachliche und persönliche Gespräche und Kaffeepausen zu einer angenehmen und bereichernden Zeit beigetragen haben.

Darüber hinaus danke ich allen Partnern im RHINOCEROS-Projekt für die interessanten Projekttreffen und die wertvollen Einblicke in unterschiedliche Bereiche des Batterierecyclings. Mein besonderer Dank gilt dem Projekt selbst, das die finanzielle Grundlage meiner Promotion bildete (Grant Agreement Nr. 101069685).

Ein ganz besonderer Dank gilt meiner Frau Ruth Sieweck, die mich jederzeit mit großer Geduld, Verständnis und Unterstützung begleitet hat.

Zusammenfassung

In dieser Arbeit wurde ein mechanochemischer Ansatz zum Recycling von Lithium-Ionen-Akkumulatoren untersucht, mit dem Ziel, Lithium durch wässriges Auslaugen in hohen Ausbeuten und hoher Reinheit aus einer Schwarzmasse zu extrahieren. Dieser Ansatz basiert auf einer mechanisch induzierten Reduktion des Kathodenmaterials mit einem Reduktionsmittel wie Aluminium. Dabei sollen sich wasserlösliche Lithiumsalze bilden, die von den anderen unlöslichen Bestandteilen mittels Filtration abgetrennt werden können.

Im Fokus der Arbeit steht es, ein tieferes Verständnis des mechanochemischen Prozesses zu entwickeln, den Prozess zu optimieren und ihn letztlich auf eine industriell hergestellte Schwarzmasse anzuwenden. Somit soll die Anwendbarkeit unter realitätsnahen Bedingungen getestet werden. Da der zugrunde liegende Mechanismus noch nicht bekannt war, wurden zunächst Experimente an einem Modellsystem aus Lithium-Cobalt(III)-Oxid (LCO) und Aluminiumpulver durchgeführt. Das Vermahlen der beiden Komponenten in einer Hochenergie-Kugelmühle führte nach einer kurzen Aktivierungsphase zu einer abrupten, stark exothermen Reaktion und der Bildung von metallischem Cobalt und $LiAlO_2$. Solch eine abrupte Reaktion ist in der Literatur als mechanisch induzierte selbst-ausbreitende Reaktion (MSR) bekannt.

Ein für diesen Mechanismus charakteristischer Sprung des Innendrucks signalisiert die Initiierung der selbst-ausbreitenden Reaktion und wurde fortlaufend als Indikator verwendet, um den Einfluss verschiedener Parameter auf die Mahldauer zu untersuchen. Neben Aluminium konnte eine MSR auch mit Magnesium, Silizium und Phosphor festgestellt werden, während eine Reaktion mit Schwefel nicht abrupt, sondern deutlich langsamer und gleichmäßiger verlief. Insgesamt zeichnen sich Aluminium, Magnesium und Schwefel aus unterschiedlichen Gründen als gute Reaktionspartner aus.

Die Reaktion mit Schwefel unterscheidet sich grundlegend von den anderen und wird daher in einem separaten Abschnitt behandelt. LCO wird dabei in Abhängigkeit von der Schwefelmenge in ein Gemisch aus Cobaltsulfid, Cobaltdisulfid, Cobaltoxid und Lithiumsulfat überführt. Lithium kann daraufhin in Ausbeuten zwischen 84 und 91 % selektiv durch wässriges Auslaugen extrahiert werden. Der Unlösliche Rückstand kann danach durch Zugabe von Wasserstoffperoxid in Lösung gebracht werden, ohne zusätzliche Säure zu verwenden.

Da dieses Projekt auf die Lithiumextraktion aus Schwarzmasse abzielt, die neben dem Kathodenmaterial typischerweise auch große Mengen an Graphit enthält, wurde auch dessen Einfluss getestet. Allerdings zeigte die mechanisch getriebene Reaktion von LCO mit Schwefel in der Gegenwart von Graphit kaum Umsetzung. Eine Kombination aus mechanischer Aktivierung und thermischer Reaktion bei etwa 350 °C scheint eine effiziente Lösung für dieses Problem zu sein, doch das wird in der Thesis nicht weiter behandelt.

In der mechanochemischen Umsetzung von LCO mit Aluminium konnte eine Unterdrückung der MSR ab einem Graphitanteil von 20 wt% beobachtet werden. Stattdessen erfolgte eine kontinuierliche Reduktion des LCO. Durch die Unterdrückung der MSR und damit das Ausbleiben einer abrupten Temperatur- und Druckerhöhung lässt sich die Reaktion besser kontrollieren und der Prozess sicherer betreiben.

Um Aussagen über den Prozess unter realistischeren Bedingungen treffen zu können, wurde die mechanochemische Reduktion auf eine industriell hergestellte NMC-basierte Schwarzmasse angewandt. Nach ausgiebiger Charakterisierung wurde die Schwarzmasse mit Aluminium und mit Magnesium gemahlen und der Reaktionsverlauf mittels Röntgendiffraktometrie und Röntgenabsorptionsspektroskopie verfolgt. Dabei konnte festgestellt werden, dass die MSR unter der Verwendung von Aluminium unterdrückt wird, während sie bei Verwendung von Magnesium als Reduktionsmittel beobachtet wurde. Außerdem führten flüchtige Bestandteile der Schwarzmasse zu einer deutlichen Verlangsamung der Reaktionskinetik. Nach der Optimierung der Mahlbedingungen und insbesondere durch eine vorgeschaltete Vakuumtrocknung konnte die Mahldauer von 3 h auf 1 h in der Aluminium geführten Reaktion und von 4 h auf 2.5 h in der Magnesium geführten Reaktion gesenkt werden.

Zuletzt wurde Lithium durch verschiedene wässrige Extraktionsprozesse aus der mechanochemisch verarbeiteten Schwarzmasse wiedergewonnen und die Ausbeute und Reinheit der erhaltenen Lithiumsalze untersucht. In der mit Aluminium gemahlenen Schwarzmasse zeigten sich dabei insbesondere Aluminiumsalze und Fluoride als Herausforderung, um eine hohe Ausbeute und Reinheit zu erreichen. Die höchste Lithiumausbeute von 99 % konnte durch die Zugabe von Kalziumhydroxid erreicht werden, das bei 90 °C mit $LiAlO_2$ zu Katoit reagiert, LiOH in Lösung abgibt und gleichzeitig Fluoridionen bindet Das so wiedergewonnene Lithiumcarbonat zeigte eine Reinheit von 98 %.

Auch die mit Magnesium reduzierte Schwarzmasse wurde wässrig ausgelaugt. Bei Raumtemperatur konnten durch einfaches Auswaschen 82 % des Lithiums extrahiert werden, ohne dass andere Kationen nennenswert in Lösung gingen. Allerdings erforderte die hohe Fluorkonzentration einen zusätzlichen Aufreinigungsprozess, der pH Anpassungen und die Fällung von CaF_2 beinhaltet. Somit konnte Lithiumcarbonat aus einer industriell hergestellten Schwarzmasse mit einer Reinheit von 99.9 % wiedergewonnen werden.

1 Introduction

The storage of electrical energy plays a central role in the ongoing transition from fossil fuels to renewable energy[1] For this purpose, various technologies are employed that can be grouped into mechanical, thermal, chemical, and electrochemical storage systems. Lithium-ion batteries (LIBs) belong to the latter category, as they store and release electric energy through reversible redox reactions, utilizing lithium ions as charge carriers. After the first research in the 1950s, Sony commercialized the first LIB in 1991.[2,3] Numerous innovations in the following years led to the development of cells with outstanding combinations of energy density, power density, efficiency, and lifetime, establishing LIBs as the dominant power source in small consumer electronics. Further developments extended the field of their application to power tools, electric vehicles (EV), and stationary energy storage systems.[4]

A LIB is a complex multi-component system that is designed for its specific application. Some of its components, such as the anode and cathode active materials, are produced from raw materials, including lithium, cobalt, or nickel salts that are listed as critical by the European Union (EU),[5] highlighting their strategic importance for our daily life and for a resilient supply chain. During their lifetime, LIBs undergo many reversible charging and discharging cycles. However, either due to various aging processes or external factors, they degrade and eventually do not fulfill their requirements for the application, reaching the end-of-life, and becoming hazardous battery waste.[6]

The drastically rising volume of battery waste makes a proper management and in particular recycling essential for environmental, economic, and political reasons. After the collection of batteries, conventional recycling routes typically begin with a pretreatment, that provides the feedstock for subsequent pyro- or hydrometallurgical processes. However, as these technologies focus only on selected valuable compounds and often rely on corrosive reagents, and may suffer from high energy consumption, hazardous emissions, secondary waste generation, or low recovery rates. Consequently, the scientific community and also the industry pushed in the recent years the development of innovative recycling methods including direct recycling, bio-hydrometallurgy, or mechanochemistry.[7–9]

Furthermore, the EU targets a transition towards a climate-neutral economy by 2050, where batteries play a central role. To promote a safe and sustainable battery landscape, the EU agreed on the Battery Regulation.[10] In the Horizon Europe framework and the follow-up program Horizon 2020, the EU is funding a variety of projects dedicated to battery materials development, cell production, and circular economy.[11]

1.1 The lithium-ion battery

In order to understand the challenges in LIB recycling, it is essential to know how batteries are constructed and what components they contain. LIBs are complex devices with many components.[7] Generally, a LIB cell is set up as presented in Fig. 1.1a. It consists of two electrode materials that are coated on current collectors. These are connected by a cable to an electrical load, enabling electron flow. The two electrodes are immersed in an electrolyte solution, allowing ion transport, but a porous separator prevents direct contact, ensuring electrical isolation. During discharging, electrons flow from the negative anode to the positive cathode. At the same time, lithium ions migrate from the anode through the electrolyte and separator to the cathode to compensate for the charge. The resulting open-circuit voltage is determined by the difference in the chemical potential of the cathode and the anode.

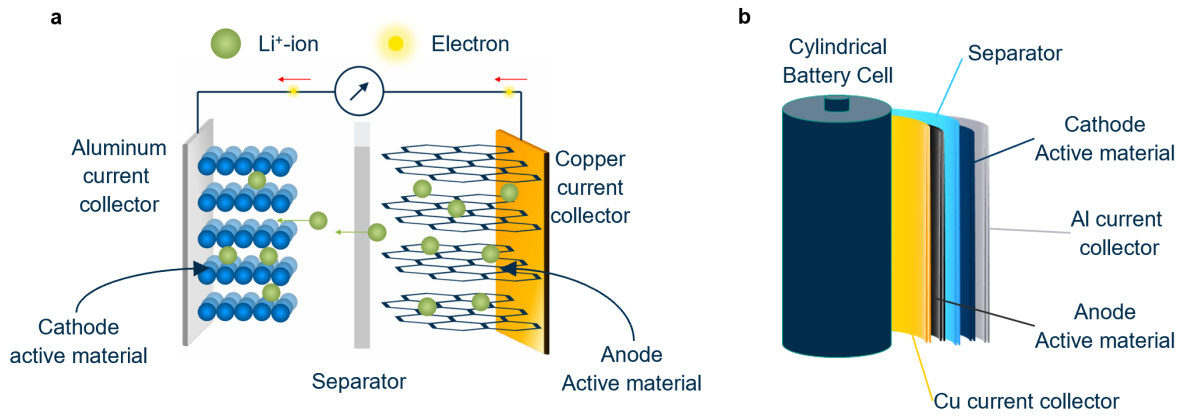


Figure 1.1: Schematic representation of a) a lithium-ion battery cell and b) a cylindrical cell set-up.

Cathode, separator and anode are arranged in layers that can be rolled together and placed in a steel can to produce a cylindrical cell as shown in Fig. 1.1b. Alternatively, the layers can be stacked or folded and placed in a steel casing to produce a prismatic cell geometry, or the layers can be placed in a plastic coated aluminum bag to produce a more flexible pouch cell. Often a single cell is not sufficient to power a device, and therefore multiple cells are connected in series or parallel to form a battery module, which fulfills the applications requirements. For large applications, multiple modules can be connected in a battery pack. Beside the cells, the battery pack contains peripheral devices such as the battery management system, the cooling system, cables, and sensors.[12]

The cathode typically consists of an aluminum foil as current collector coated with the cathode active material (CAM). The CAM is mixed with carbon to increase the electric conductivity, and with a binder, which provides flexibility, keeps the particles together, and adheres them to the aluminum current collector. In most commercial batteries, a fluorinated hydrocarbon such as polyvinylidene difluoride (PVDF) is used.

The CAM itself defines many key parameters for the cell performance and has a high material diversity, which can be grouped in three categories: The layered oxides, the poly-anionic materials, and spinel-type materials.

The CAMs based on layered oxides are in the focus of this study. As presented in Fig. 1.2a, this material class is composed of alternating planes of Li^+ and transition metal (TM) ions, which are octahedrally coordinated to oxygen, and the compounds have the general chemical formula $LiTMO_2$. The layered structure allows for fast two-dimensional Li diffusion via neighboring tetrahedral voids. The most common materials are lithium cobalt oxide ($LiCoO_2$, LCO), which is mostly used in small consumer electronics, and lithium nickel manganese cobalt oxide ($LiNi_xMn_yCo_zO_2$, NMC), which is often used in EVs.[13,14] The layered-oxide materials inherit fast charge and discharge characteristics and a high volumetric energy density, but suffer from high costs due to the consumption of critical raw materials, in particular cobalt.[15–17]

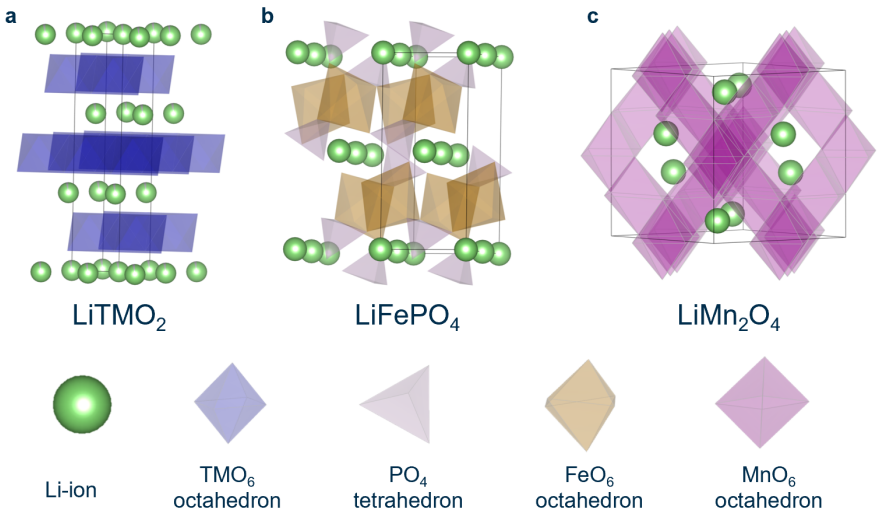


Figure 1.2: Crystal structures of common cathode active materials. The green spheres represent the Li-ions. Blue, brown, and magenta shapes represent octahedrons with a transition metal, iron or manganese ion in the center and oxygen on the edges. The gray tetrahedrons represent phosphate ions.

The most prominent representative of poly-anionic materials is lithium iron phosphate ($LiFePO_4$, LFP), which crystallizes in the olivin-type structure (Pnma No. 62) as shown in Fig. 1.2b. Fe^{2+} and Li^+ are located in the octahedral voids of the hexagonal closed packed lattice of oxygen. Phosphorus is located in the tetrahedral positions with covalent bonds to the oxygen and distorts the structure. The Li coordination octahedra are connected by edges, which allows for a one-dimensional Li diffusion along the b-axis.[18]

LFP stands out for its high chemical and cyling stability resulting in safe operation and long lifetime, making it preferred for home storage systems.[19] Moreover, the material does not contain critical transition metals, resulting in lower costs. However, LFP suffers from a relatively low energy density

and challenging large scale production.[18] Nevertheless, due to the incorporation of manganese into the structure and advanced battery pack designs, LFP (or LFMP) is increasingly used in EVs, particularly in the Asian market.[19,20]

The spinel-type materials are often based on manganese like $LiMn_2O_4$. As illustrated in Fig. 1.2c the compound crystallizes in a cubic spinel structure, where the TM ions occupy half of the octahedral sites and the Li-ions 1/8 of the tetrahedral sites. The edge shared TM-octahedra offer a three dimensional diffusion network for the Li-ions, enabling a high rate capability.[14] As manganese based materials, they are typically cost-effective and have a low toxicity. However, they inherit low capacity and relatively fast degradation.[21] With their high voltage and rate capability, spinel-type materials are often used in high power applications.[22]

The anode consists of a copper foil as the current collector that is coated with the anode active material, mixed with conductive carbon and a binder. The binder is typically PVDF, but also fluoride-free and water soluble alternatives, such as carboxymethylcellulose, styrene-butadiene rubber, or acrylates, become frequently used.[23] Similar to the cathode, the anode must reversibly store and release Li-ions. Graphite based materials are the most common anodes and have a market share of over 90 %.[24]. It consists of stacked layers of hexagonally arranged carbon atoms. In between these layers, Li can reversibly intercalate. Graphite shows high two-dimensional electric and ionic conductivity parallel to the planes, low working potential, long cycle life, and low costs.[25]

However, the capacity of graphite is limited by the maximum Li content of LiC_6. Metallic Li or an alloy of Li, for instance, with silicon or tin, show much higher capacities but suffer from low cycle stability and safety. Therefore, their application is very limited yet. The current trend is leading to composite materials of graphite and silicon or tin to increase energy densities while maintaining long cycle stability and safety.[24,26]

The electrolyte for a LIB typically consists of a polar aprotic solvent mixture, a conductive Li-salt, and additives. The solvent is in contact with all other cell components, so its chemical and electrochemical stability is crucial. Moreover, the solvent should show high solubility of Li-salt, low viscosity, liquid state within the operating conditions, and low toxicity is desirable. State of the art solvents are a mixture of cyclic and linear organic carbonates, typically ethylene carbonate (EC), propylene carbonate (PC), dimethyl carbonate (DMC), diethyl carbonate (DEC) and ethyl methyl carbonate (EMC).[27] The conductive salt should completely dissociate in the polar aprotic solvent to obtain highly mobile Li-ions and dissolved anions. Therefore, complex anions with a low charge density are used. The most prominent conductive salt is lithium hexafluorophosphate ($LiPF_6$). Additives can improve specific properties of the battery. For instance vinylene carbonate (VC) is used to improve the formation and to tune the composition of the solid electrolyte interphase.[28] In addition to the described liquid electrolyte, solid electrolytes have attracted interest in recent years because they could allow the safe application of a Li-metal anode in solid-state batteries.[29]

The separator serves as an electrically insulating barrier between the electrodes to prevent internal short circuit. Despite low electrical conductivity, the material has to be porous and wettable with the electrolyte to allow high ionic conductivity. By preventing direct contact, the separator fulfills an important safety task. Therefore, chemical and mechanical stability is important to limit thermal shrinkage or puncture. In commercial batteries, the separators are mostly polyolefines such as polyethylene or polypropylene.[30,31]

Overall, a wide variety of different materials are used in a single cell. As an example, the composition of a typical NMC based cell is presented in Fig.1.3. Moreover, multiple cell geometries are used, and the rapid developments in each component of the battery further increase the variety of LIBs.

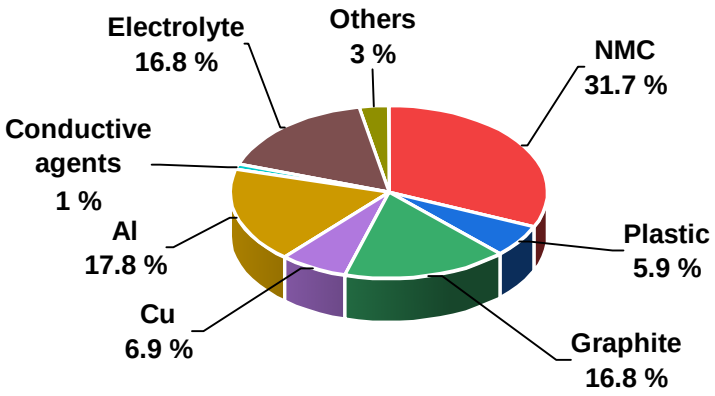


Figure 1.3: Typical mass fractions of components in a NMC based lithium-ion battery cell, adapted from Tembo et al.[32]

The production of LIBs is a highly complex process.[33] First the electrode pastes are produced by mixing the respective active material with the binder and additives in a suitable solvent such as N-methyl pyrrolidone (NMP). The obtained thoroughly mixed slurry is then coated on aluminum foil for the cathode or copper foil for the anode. The coating has to be defect-free to achieve the desired cell performance. Afterwards, the coating is dried on the foil and then compressed by calendering to increase volumetric energy density end electrical conductivity.[33]

Subsequently, the coated foils are cut to the right size and notched for the electric connection. Depending on the process, the anode, separator, and cathode are now rolled together or stacked in alternating layers to form a jelly roll. After the electric connections are formed by welding, the jelly roll is placed in a housing, which is typically made of aluminum or stainless steel. The housing protects the electrodes from external mechanical force and moisture and prevents evaporation of the electrode. Remaining solvent residues and moisture are removed in a vacuum drying step before the cell is filled with the electrolyte. All cell components must be fully soaked before cell formation can start.[33–35]

During the formation stage, the cell is charged for the first time, leading to the creation of the solid electrolyte interphase. As the electrolyte is partly consumed hereby, it may need to be refilled. Then,

the cell is closed and various current and voltage profiles are applied, which is called aging, and finally, the cell performance is tested.[33–35]

Errors can occur in any stage of production, including incorrect stoichiometry of the synthesized materials, formation of unwanted phases, contamination, agglomeration in the slurry, wrinkling of the foil during coating and calendaring, and inhomogeneities. Therefore, a constant quality control is necessary. Errors usually cannot be corrected, which results in the production of large amounts of production waste, especially during the ramp up of large production lines.[36]

1.2 Critical raw materials

The previous chapter demonstrated that LIBs are complex systems composed of many diverse materials. Many of the raw materials required for battery production are classified as critical due to their high economic importance combined with a possible supply risk.[5] The international energy agency collects, evaluates and publishes data on energy technologies, including batteries. Over the past decade, the demand for LIBs experienced immense growth, which was driven in particular by EV production (Fig. 1.4a).[37]

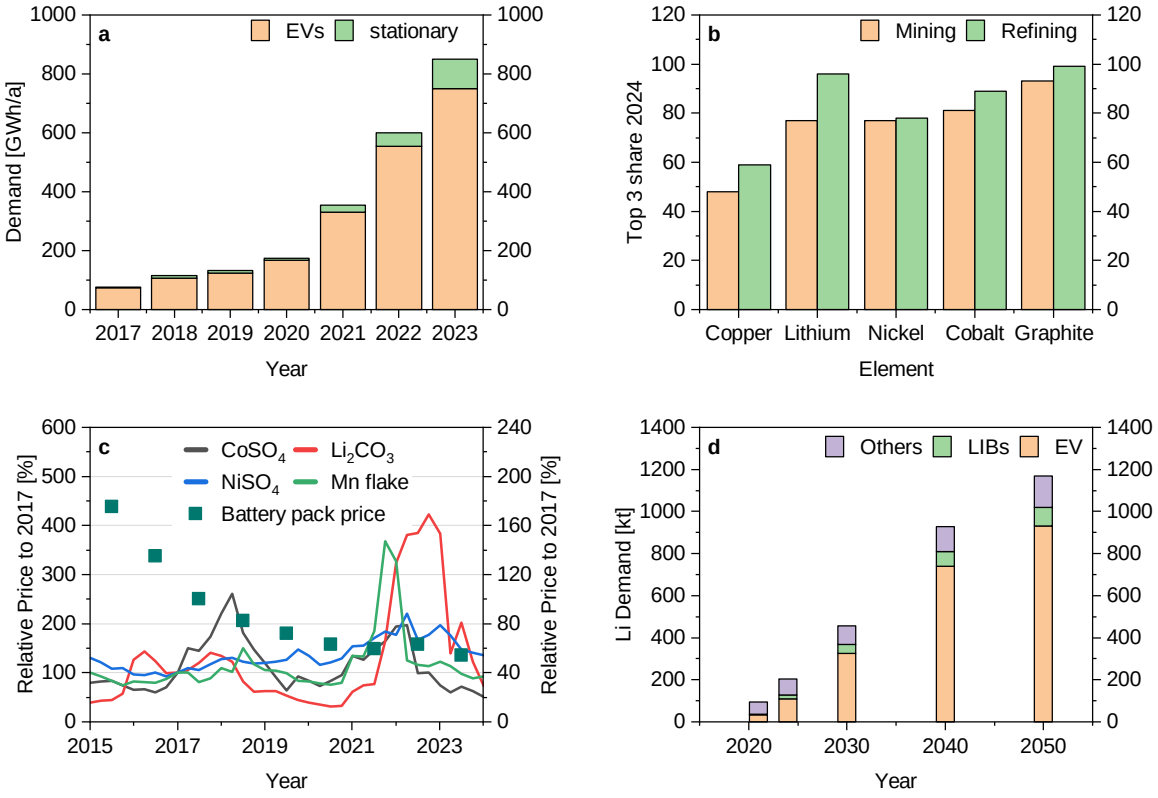


Figure 1.4: Graphical overview of lithium-ion batteries and materials: a) Demand for LIBs in EVs and stationary energy storage,[37] b) Mining and refining share for battery raw materials of top 3 suppliers in 2024,[20] c) Price development of battery raw materials (left) and battery packs (right) relative to 2017,[38] d) Expected annual Li demand (elemental) by application.[20]

When the LIB production worldwide ramped up, so did their raw materials production. However, the growth in mining and refining activities was located in only a few countries, leading to a strong geopolitical dependence of the battery material supply chain. The concentration in material supply is illustrated in Fig. 1.4b, which shows the market share for mining and refining in 2024 for selected battery materials in the three leading countries.[20]

For instance, the majority of nickel mining and refining occurs in Indonesia, cobalt mining in the Democratic Republic of the Congo, and China holds large shares of mining and refining for all materials (31 - 96 %).[20] Such a concentration amplifies the supply risk and contributes to price volatility, as many mines are located in politically unstable countries or key suppliers might introduce export restrictions.

Raw material production outpaced demand in recent years, resulting in a slight oversupply, leading to a decrease in prices.[39] While lower prices are beneficial for the battery manufacturer and the consumer, they induce pressure on the material supplier, counteracting diversification of the supply chain.

In Fig. 1.4c the recent price development of some battery materials normalized to their 2017 levels is illustrated.[38] Lithium experienced the strongest price volatility among battery-grade raw materials. Li occupies a unique role because it is essential for all LIBs, regardless of the cathode or anode chemistry. While the other battery raw materials have significant application outside the battery sector such as steal production, the demand for lithium has become primary based on LIB production. More than 60 % of the mined Li is currently used in batteries and its share is still growing (Fig. 1.4d). Consequently, lithium and LIB prices are tightly coupled.

Lithium resources are found in either hard rocks, such as spodumene and lepidolite, or dissolved in brines. Most of lithium is mined in Chile, Australia and China, while the refinement of battery grade Li-salts is concentrated in China and Chile.[20]

The processing of hard rocks typically includes the comminution and concentration of lithium bearing phases with a subsequent calcination to induce chemical reactions. The resulting material is then leached with an acidic or alkaline solution to extract lithium salts. Impurity ions are removed by precipitation or solvent extraction, and lithium carbonate is precipitated with Na_2CO_3.[40,41]

Lithium containing brines, for instance in Chile, are processed by concentration driven by evaporation, removal of impurities, and precipitation of Li_2CO_3. The high temperatures and low humidity in South-American counties facilitate rapid natural evaporation and therefore lowering operating costs.[42,43]

However, mining activities can have a high socioeconomic and environmental impact.[44–46] Recently, direct lithium extraction technologies emerged as more sustainable alternatives. These processes allow for the selective extraction of Li from geothermal brine and from brine produced by oil and gas production.[47–49]

1.3 Recycling

Lithium-ion batteries have become increasingly important to our daily life, but their production consumes significant amounts of critical raw materials, such as lithium, manganese, cobalt, nickel, copper, and graphite. Their extraction is often associated with an high environmental impact and the worldwide supply of material is dominated by only a few countries[20]

Driven by the rising demand for LIBs, the volume of battery waste is increasing. This waste contains many valuable compounds and elements in relatively high concentrations, but at the same time, the waste components can be toxic or flammable. Consequently, battery waste represents an attractive feedstock for valuable materials and simultaneously a risk to the environment and human health.[50]

The lithium-ion battery waste can be grouped in three categories: (i) Production scrap from the manufacturing process, which is typically well sorted and often contains only a few components. (ii) Spent batteries from small electronic devices. This waste stream is the most diverse and is not well standardized. (iii) EoL batteries from EVs and large storage applications, which are typically in good condition, relatively well standardized, and can be sorted to produce a defined feedstock. A battery typically reaches its end of life, when it retains only 80 % of its initial capacity.[51]

The recycling of Lithium-ion battery waste faces several inherent challenges, which are summarized here.[9]

- Batteries are often designed for the application and not for recycling. For instance, the extensive use of adhesives complicates physical separation techniques.
- Diverse waste stream: Various cell chemistries that might even be mixed, yield in complex mixtures.
- Rapidly developing technologies require flexible and robust solutions.
- The high variety of cell formats complicates automated processes.
- New generation battery materials are often made of low value materials, which limits economic viability and increases the competition with the primary raw material suppliers.

Industrial recycling begins with collection and sorting to allow for more specified downstream processing resulting in higher purity and better recovery yield. The batteries are then processed by multiple pretreatment steps, including discharging, shredding, and classification to split the materials according to their physical properties into multiple waste streams to enable more specified subsequent recycling methods.[52] One of these fractions contains primarily the electrode active materials and is called black mass (BM), which is fed to pyro- or hydrometallurgical plants for raw materials recovery. Direct recycling as a third option aims to recover the material value and not the elemental value.[8] The processes are described below for large application battery packs. However, not every step has to be included in a process, and also the sequence of steps may vary between individual processes.[50,51] An

overview of process combinations that companies are currently using on an industrial or pilot scale can be found in a review published by Pinegar and Smith.[53]

1.3.1 Pretreatment

Discharging

In the collected EoL battery packs, some energy might still be stored, which increases the risk of fires and even explosions during storage or treatments. For safe downstream handling, the batteries are deeply discharged in a controlled way to voltages below 2 V.[51] Discharging can be divided into three methods: electrical, electrochemical, and thermal discharge.

As long as the battery is still intact, it can be discharged electrically by connecting an electrical load or by releasing the energy into the power grid. This process needs information on the battery, such as capacities and voltage ranges, skilled personnel, as well as higher investment costs. To ensure a deep discharge, the depleted battery is short-circuited at the end.[51]

In the electrochemical discharge route, the battery is placed in a water bath with dissolved salts, such as NaCl or $FeSO_4$. Under suitable conditions, the salty water acts as a heat sink and discharges the battery due to its conductivity. However, electrolysis may result in gas evolution and corrosion in casings and electrical connectors, that leads to leakage of transition metal ions and electrolyte and formation of HF, which could inhibit complete discharge or limit subsequent recycling efficiency[54].

In the thermal discharge process, either very low or high temperatures are employed. Cooling the battery below -175 °C with liquid nitrogen results in crystallization of the electrolyte and therefore inhibits its ion conductivity. The low temperature temporarily reduces the reactivity for further processing. At high temperatures in an oxygen free atmosphere, the electrolyte solvent can be removed in the range of 100 - 300 °C, and when exceeding 400 °C pyrolysis of organic compounds such as PVDF binder starts. Without an electrolyte and binder, the electric contact is interrupted and the cells are deactivated. While the thermal decomposition of the binder can improve subsequent liberation of the active materials from the current collector, it requires extensive off gas treatment to capture organics and HF.[51]

Dismantling:

After discharge, the battery pack can be opened to isolate the modules while removing the outer casing, cables, cooling system, battery management system, and other peripheral components. Note that discharging can also be performed after dismantling on the module level. Further disassembly to the cell level and below increases complexity and risks. Automated dismantling systems are the focus of many ongoing research projects, but different cell, module, and pack designs, as well as adhesives or rusted bolts remain challenging. However, the further and cleaner the disassembly, the less contamination can be expected in subsequent steps and may open the path to direct recycling methods of spent batteries.[51,55]

Mechanical Processing

The mechanical processing typically includes shredding, milling, and granulation and can be performed on complete packs, modules, or cells after discharging. It aims for the production of small particles that can be separated according to their physical properties. A particular focus of this step lies on the liberation of active materials from their current collectors, which is essential to produce a high quality black mass in the subsequent classification step. Residual stored energy causes risks for ignition and produced gas and dust are harmful. Therefore, processes are typically carried out under an inert atmosphere, or less common under cryogenic conditions or in water.[56]

Classification

After mechanical processing, the materials are sorted into different waste streams according to their physical properties. Magnetic and eddy-current separation is employed to separate ferrous metals, non-ferrous metals, and non-metals. In electrostatic separation, the waste stream is charged and separated by their response to an external electric field, allowing for instance the removal of plastics. Sieving is used for particle size classification, where active materials are typically recovered in the fine fraction ($<$250 µm), while current collectors (Cu, Al), casing (Fe, Al), plastics and cables show larger particle sizes. The fine fraction with the active materials is called black mass and serves as a feedstock for the subsequent chemical recycling methods. Furthermore, froth flotation is emerging in LIB recycling processes. This technique utilizes differences in hydrophobicity of material surfaces to separate, for instance, non-polar graphite from polar transition metal oxides.[51,56]

1.3.2 Pyrometallurgy

Pyrometallurgy is a relatively old technique, with a knowledge base developed largely from steel reprocessing. In the early days of battery recycling, when the volumes of spent batteries were small, they were fed in small fractions to existing smelters for transition metal recycling. Nowadays, there are smelters dedicated to LIB recycling, which can process black mass but also complete cells or modules.[57]

In general, this technique is based on thermally induced reduction processes performed at very high temperatures (1000 - 1700 °C) to produce molten alloys of valuable materials such as Co, Ni and Cu. Carbonaceous materials including graphite, hard carbon, electrolyte, and plastics are combusted to generate heat and act as carbothermal reducing agents. If Al is still present, it also serves as a reducing agent and heats the reactor by its exothermic oxidation.[58] Flux agents such as CaO or SiO_2 are added to the furnace to promote slag formation and improve the isolation of the molten TMs. The produced slag consists of an oxidic mixture of Ca, Si, Mn, Al, and Li and can trap further impurities. The isolated transition metal alloy has to be further purified by hydrometallurgy methods to reach high purities.[57]

The pyrometallurgycal route offers a mature and very robust technology that can process various cell chemistries at once, requires minimal pretreatment, and achieves a high recovery yield for Co, Ni, and Cu. However, there are also some drawbacks: Other elements such as Li or Mn are often not recovered, as their extraction from the slag is often economically unattractive. The high temperature and combustion of carbonaceous materials result in high greenhouse gas emissions and toxic flue gasses.[59,60]

1.3.3 Hydrometallurgy

Hydrometallurgy relies on the dissolution of battery waste material with subsequent separation and precipitation of salts in a multistage process. Battery waste material (BM or production scrap) is typically dissolved in strong mineral acids such as H_2SO_4, HNO_3 and HCl, often assisted by reducing agents such as H_2O_2 or $NaHSO_3$. Filtration then separates leachate from insoluble compounds such as graphite.[8]

After dissolution, the ions in the leachate have to be isolated by selective precipitation, solvent extraction, and electrowinning. Solvent extraction utilizes two immiscible phases such as water and kerosene, with metal ions showing a concentration preference for one phase (the polar aqueous phase). An extractant is added, which is typically an organic molecule with a polar coordination site and long aliphatic chains. The extractant coordinates with the ions with their polar parts, often as chelates. The nonpolar side chains reduce the polarity around the ion. Therefore, the equilibrium concentration distribution changes to a preference of the nonpolar phase. When the extractant shows a high preference for a specific ion, selective extraction is possible[8].

Selective precipitation is performed most often by pH adjustments. An alkaline solution is carefully added to the acidic leachate. The solubility of various metals exhibits different pH dependencies, and in principle, they can be precipitated one after another as hydroxides. However, co-precipitation often prevents high selectivity and therefore other precipitants such as $Na_2C_2O_4$ are sometimes added.

Electrowinning utilizes electrical energy to drive the reduction of dissolved metal ions and their deposition on the cathode as metal. The metals can be recovered according to their standard redox potential by controlling the voltage.[61]

Because of co-extraction, co-precipitation, and co-plating, none of the methods typically achieves high purities and yields in a single step. Therefore, multiple steps are performed in sequence in an often complex flow sheet. Hydrometallurgy allows for the recovery of most metals in high purity and good yields. The energy consumption is relatively low, and less toxic gasses are formed than in the pyrometallurgical route. However, the process to achieve high quality products is very complex. During operation, concentrated acids and a lot of water are necessary and consequently large volumes of aqueous salty waste water are produced that may be contaminated with toxic transition metals.[59] Lithium can in principle be recovered in the and of the hydrometallurgical process at high pH, but

during the many steps, it can be partially lost in other material streams or the introduced process agents make its purification difficult.[62]

1.3.4 Direct recycling

In direct recycling processes, the active material is isolated, regenerated, and reused. Because impurities are difficult to remove afterwards without decomposing the active materials, a very precise disassembly and delamination are needed to recover high quality materials. This makes a good level of knowledge of the feed material and its degradation essential to decide on the proper treatment. Typical degradation in NMC includes Li-loss and Ni-ions located at the Li-sites, forming a stable rock-salt phase. This phase inherits lower Li conductivity and capacity. Regeneration is possible by processes such as relithiation or by calcination in oxygen atmosphere. High temperatures increase ion diffusion and drive the Ni ion back into the TM plane.[6,63]

Potentially, this recycling route consumes the least chemicals, allows the recovery of most compounds, and preserves the highest value. However, impurities typically cannot be removed and, therefore, the process cannot be combined efficiently with state of the art pretreatment processes. In contrast, for well sorted production scrap direct recycling is an attractive route.[64]

1.4 Battery recycling in Europe

The EU has recognized batteries as an important technology. Based on this importance and the risk of supply disruptions, many battery related materials have been listed as critical.[5] Furthermore, the European battery regulation that was agreed on in 2023 defines a circular economy framework for the battery market. According to the regulation, battery producers are responsible for end-of-life treatment. This includes the financing and organizing of battery collection and recycling operations, as well as providing information about the battery.[65] Moreover, the regulations establish mandatory element specific recycling targets (Fig. 1.5), and set a minimum share of recycled materials in newly manufactured batteries that will increase stepwise within the next decade.[10]

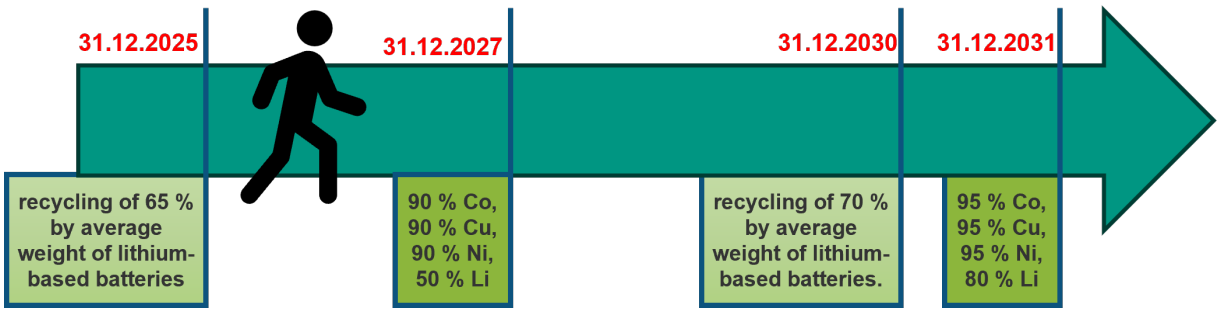


Figure 1.5: Timeline for recycling quotas according to the battery regulation.[10]

This legislative is accompanied by large investments in national, European and industrial research programs. In this context, the EU founded numerous projects within Horizon 2020 and Horizon Europe, with regard to battery manufacturing, recycling, and raw material production. (RHINOCEROS, LICORNE, and others)[66]

The recycling industry in Europe has adapted and developed to meet the regulations, creating opportunities for start-ups with innovative processes such as Viridis, Tozero, or Cylib. Thereby, a general trend away from pyrometallurgy toward hydrometallurgy is observed. Overall, an expanded recycling company network emerged in Europe, resulting in a slight overcapacity with respect to battery return quantities.[67] However, many companies focus on black mass production, which is largely exported outside the EU for economic reasons. This removes the battery materials from the European market. Therefore, more cost-effective recycling technologies are needed to establish a European circular economy for LIBs.[68]

This thesis is produced as part of the EU-founded RHINOCEROS project. This project aims for the development, improvement, and demonstration of an economically and environmentally viable recycling route for EV and stationary batteries in an industrially relevant environment.[66] Within the project, the entire recycling chain is addressed, from collection and dismantling through various pretreatment processes and chemical recycling routes to the final resynthesis of battery materials.[69] As part of the project, this work aims for the development and application of an mechanochemical approach to recover high purity lithium salts from an industrially produced black mass.

1.5 Mechanochemistry

1.5.1 Basics

Mechanochemistry studies how the application of mechanical energy triggers physicochemical changes and transformations.[70] Mechanical energy can act on matter in any state through forces such as compression, shear, and torque, covering a very broad scientific field. To transfer mechanical energy to the material, various tools are used, including numerous types of mills, mortars, extruder, ultrasonic treatments or even atomic force microscopes, enabling a wide range of applications[71–75] from organic synthesis,[76] to solid-state synthesis,[77] mining,[41] waste treatments,[78,79] catalysis[80] and production of pharmaceutics.[81]

Mechanochemistry is often considered as a green and sustainable processing approach because it can significantly reduce or even eliminate solvent use, prevent waste generation, and lower overall energy consumption. Furthermore, it has a high potential to use less hazardous materials, induce catalytic reactions, and it is often a simple process.[75,82]

In the present work, high-energy ball-milling is used for mechanochemical experiments, and therefore the principles of mechanochemistry that are discussed here are focused on this tool. Ball-mills typically

consist of a moving milling chamber that is loaded with the milling balls and the feed material. The motion of the milling chamber imparts acceleration to the balls, resulting in mill specific trajectories. These trajectories depend on parameters such as the motion of the milling chamber, the geometry of the milling chamber, the relative size of the milling balls, and the properties of the substrates.

As illustrated in Fig. 1.6, balls can be pressed against the chamber wall without a relative movement (compression), balls can roll or slide along the wall (shear), and a ball can detach from the wall on one side of the milling chamber, fly toward the other side of the chamber, and collide with the wall there (impact). Furthermore, similar interactions can occur between two balls. If powdered material is trapped between a ball and the wall or between two balls, it experiences mechanical stress, which may induce physicochemical transformations.[78]

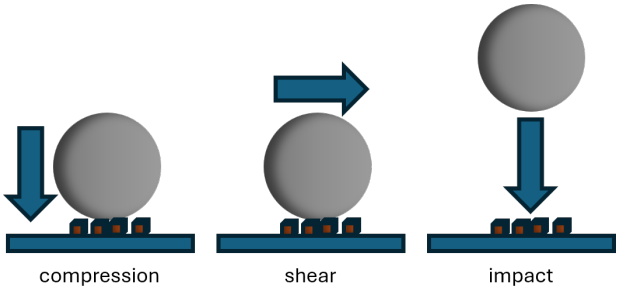


Figure 1.6: Main stress types occurring in ball-milling experiments.

Typical industrial ball-mills are tumbler or drum mills, which consist of a hollow cylinder that is partially filled with balls and feed material. The cylinder (drum) rotates around its axes, which causes the balls to grind the feed. Furthermore, the balls can be lifted along the wall and subsequently drop down to the feed due to gravity, causing impact. The velocity at impact depends on the diameter of the drum, as it defines the length a ball is affected by gravitational acceleration. However, these mills are usually used for comminution, as their impact energy is considered relatively low.[78]

High-energy ball-mills utilize additional movements to overcome the barrier of gravitational acceleration and can achieve high energies while having a compact size. For instance, a shaker mill, often referred to as a SPEX mill, moves the entire milling vial back and forth with high frequency. Typically a second lateral movement is introduced, resulting in a vial movement that describes an eight (Fig. 1.7a). In the SPEX mill the vial typically moves with an amplitude of 5 cm at a high frequency, resulting in ball velocities of around 4.2 m/s with 140 impacts per second.[83] The energy is transferred predominantly by head on collisions with small frictional contributions.[84,85] These mills have to oscillate the milling vial very fast and are therefore limited in size.

In planetary ball-mills, such as the *Pulverisette 7* from Fritsch used in this study, the milling vials are located outside the center of a rotating disk. Additionally, the vials themselves rotate around their own axis in a counter direction to the disk. Due to the rotation in counter direction, alternating centrifugal forces in the same direction and in opposite direction act on the balls. This causes the

balls to slide along the inner wall, resulting in local friction until they detach and collide with the wall on the opposite side causing an impact (Fig. 1.7b).[86] Planetary mills can be filled up to a third of their volume and allow larger and heavier milling vials than a shaker mill. Therefore, more material can be processed. Due to high centrifugal forces and complicated movement, planetary ball-mills are constructed for laboratory and pilot scales with milling vials up to 1 L.[86]

For larger applications, rotary or attritor mills can be used. Such a mill consists of a horizontal milling jar. Instead of a moving vial, a fast rotating impeller is placed inside the milling chamber. The impeller blades hit the balls, causing impacts and acceleration of the balls (Fig. 1.7c).[87]

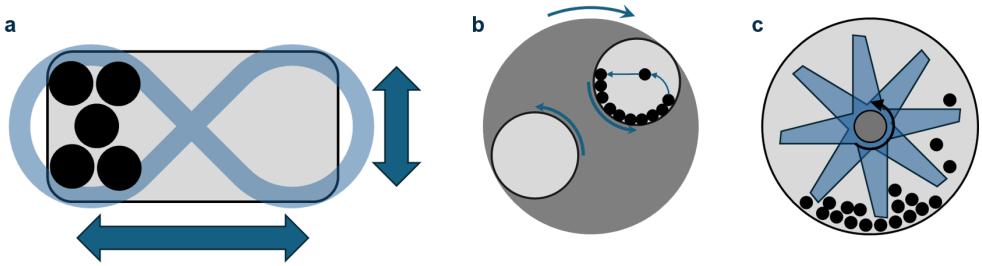


Figure 1.7: Schematic representation of a) a shaker ball-mill (SPEX), b) a planetary ball-mill, and c) an attritor mill.

1.5.2 The energy transfer by impacts

In a ball-mill, the kinetic energy is transferred from the milling media to the powder through physical interaction. The most energetic interactions are impacts, which are expected to play a dominant role in driving physicochemical changes.[78,88] Without a feed material, such impacts can be described by the Herzian theory for the elastic, non-adhesive collision of two spheres. In such a collision, the spheres with radius r_b are subjected to the force F_0 (Fig. 1.8a). Their centers of mass approach each other closer than $2r_b$, up to their closest distance at δ_0, resulting in an elastic deformation. In the collision zone, a circular contact area forms between the two spheres, which reaches a maximal size with a radius a_0 at δ_0. The radius depends on the materials young module, the Poisson ratio, the ball masses and their impact velocities. After the closest approach at δ_0, the spheres move away from each other and regain their original shape.[89]

The strongest impacts in a ball-mill typically occur between a ball and a wall and not between two spheres. However, the principle of the Herzian impact remain the same, and the equations provided in the literature can be used to estimate the contact area and duration of an impact.[90] For instance, in this work stainless steel balls with $r_b = 3.175$ mm and $m_b = 1.01$ g are used. In the experiments, impact velocities (v_{imp}) between 2 m/s and 11 m/s are estimated. Therefore, the radius of the contact area can range from 0.15 mm to 0.3 mm, and the duration of such a collision is between 15 and 21 µs. The described Herzian model holds true for elastic impacts without powder. If powder is present during the milling process, it is subjected to mechanical load and the impact becomes inelastic.

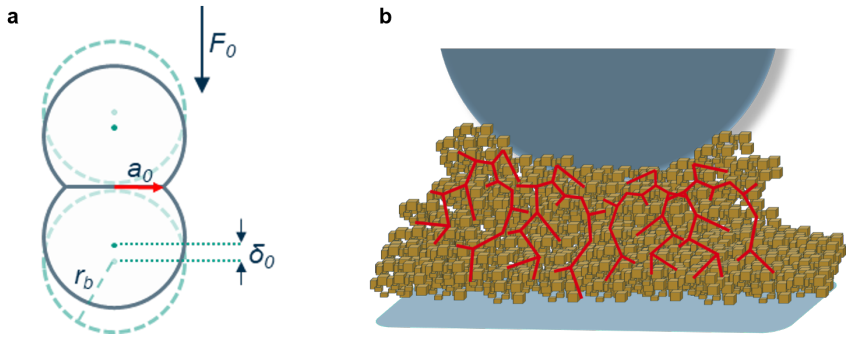


Figure 1.8: Illustration of a) a Herzian collision and b) of force chains in a coarse powder under compression (adopted from Carta[89]).

Usually, it can be assumed that the powder consists of coarse particles much smaller than the ball size. Upon mechanical load, the force is distributed through the powder via interparticle contacts under the formation of force chains (Fig. 1.8b).[91] This implies that the force is not evenly distributed, but is mostly concentrated in some small sub-volumes. Within these regions, the powder is subjected to intense compression and shear stress. The resulting mechanical load, concentrated in randomly distributed microscopic sub-volumes, supplies sufficient energy to activate mechanochemical transformations. Consequently, chemical and physical changes are expected to occur locally within these highly stressed micro-domains.[92,93]

The effects of an impact on the material strongly depend on the impact energy and the properties of the material. Theories published in the second half of the 20th century suggest that the impacts give rise to high local deformation, a strong increase in temperatures, and even the formation of a plasma on the surface.[94] These conditions lead to the excitation of very short living states, which can relax through various pathways, including fracturing, dislocations, photon emission, and recombination of plasma products.[77,95]

Other theories focus more on the increase in the potential energy of the feed material. Dislocations and fragmentation during ball-milling produce particles with high surface energy, which cannot be stabilized in the duration of an impact and are prone to chemical reaction.[77,95]

The atoms of organic molecules are connected via covalent bonds. Shear and compression during ball-milling can alter the lengths or angles of the bonds, which result in changes in the potential energy landscape of the compounds. Therefore, the activation energy of the reaction pathways changes, which allows otherwise inaccessible reactions.[75,96]

Although there are different models and theories to describe the effect of mechanical force on powdery compounds in a ball-mill, they have some points in common.

- The mechanical load is highest in some small sub-volumes, located at the surface of grain boundaries, and leads to dislocations of atoms.

- The temperature will rise in the sub-volumes and heat dissipates afterwards in the entire volume
- The duration of a single event is short, but some effects can accumulate with multiple impacts.
- The Gibbs energy of the milled material increases.

1.5.3 Physico-chemical transformations induced by ball-milling

In the previous section, the energy transfer from the milling media to the powder by repeated mechanical stressing events through collisions and grinding is explained. In the following, the response of the feed material to mechanical stress is presented. The effect on the material can be divided into mechanical activation, mechanical alloying, and mechanochemical reaction.

Mechanical activation is typically the first stage of all ball-milling processes and increases the reactivity of the powder. The constant movement of balls inside the milling chamber and the repetitive compaction and crushing of powder leads to effective mass transport and thorough mixing of the feed material. Particles can break apart as a result of mechanical load, leading to reduction in particle size and surface area generation. At the same time, the compaction of the powder leads to agglomeration, contradicting the reduction of the particle size. The smaller the particles, the more pronounced is the tendency for agglomeration. Eventually, particle size reduction and agglomeration reach an equilibrium and the mean particle size remains at a constant value typically in the micron to sub-micron range.[85]

Dislocation activities during further milling induce internal strain in the material. Due to the consecutive impacts, the strain increases and excess enthalpy can accumulate, which ultimately increases the Gibbs free energy of the material.[97] Hereby, the type of bonds in the material seems to be important. Massalimov et al. suggested in a study that excess enthalpy can only be stored in materials with covalent contributions in their bonds, while in purely ionic materials like NaCl no enthalpy is accumulated.[98] Furthermore, dislocations lead to an overall decrease in long range periodicity of the crystal lattice, which enables the formation of amorphous or thermodynamically less stable phases.[97]

Mechanical alloying involves the intense mixing of two or more compounds, typically metals, to form phases such as intermetallics, solid solutions, or nanocomposites. The process is somewhat similar to the mechanical activation, but not the goal. Instead of enhancing the materials reactivity, the mechanical, chemical or physical properties are improved by phenomena such as cold welding and work hardening. Hereby, the ductility of the initial compounds is important. For example, two ductile materials form large lamellar structures, while a brittle material becomes dispersed or dissolved in the ductile one.[85,88]

Mechanochemical reactions are highly diverse.In general, a chemical reaction takes place when groups of atoms move from one metastable arrangement (the reactants) to another (the products) on a

multidimensional potential energy surface, crossing an energy barrier in the process.[75] In principle, there are multiple pathways for a reaction to proceed, and the one with the lowest energy barrier is the preferred one. When the reactants are subjected to mechanical force or stress, the shape of the potential energy surface can be altered, for instance, by elongation, compression, or bending of a chemical bond. As a consequence, the activation barriers can change and other products or selectivity preferences can be obtained.[75,96]

In addition to the deformation of bonds or molecules, a high-energy collision can produce locally restricted unique reaction conditions for a short time. In the collision zone, part of the impact energy is transformed to heat by frictional processes, fracturing brittle materials[99] or formation of shear bands in ductile materials.[100] In the fraction of a millisecond during an impact, heat cannot dissipate and consequently temperatures of several hundred degrees and high pressures can be expected. Only a short distance from the collision zone, almost ambient conditions are present at the same time. However, the analysis of the conditions between colliding milling bodies with powder trapped in between is hard because of the short time, the strong gradients, the small volume, that is covered by the milling media and the dynamic motion of a ball-mill.[101–104]

Furthermore, diffusion plays an important role in mechanochemical reactions. In typical solid-state reactions, the product formation proceeds at the grain boundaries of reactants, but the inherently low diffusion constants of solid materials prevent further reaction in the bulk. Therefore, high temperatures are required to overcome the diffusion barriers.[105] The intense mixing, particle deformation, and compaction during milling constantly bring fresh surfaces of reactants in close contact, causing shorter diffusion lengths. Additionally, the distortion of the crystal lattice and the formation of defects can increase the ion mobility.[72]

The combination of rapid heating and cooling, high temperatures and pressures, and changes in the potential energy surface can provide very unique reaction conditions, restricted in small volumes between colliding milling bodies. The rapid changes in the conditions allow for the formation of metastable phases that are stabilized by kinetic barriers, typical for solids. This can allow the formation of product phases that are not accessible by traditional solvothermal or high-temperature solid-state reaction routes.[59]

1.5.4 Collision model based energetic considerations

In the ball-milling experiments, kinetic energy is transferred from the balls to the powdered material primary by impacts, driving the physico-chemical transformations. The estimation of the kinetic energies involved as well as the number of impacts is useful for a better understanding of a mechanochemical reaction. For instance, it allows for the comparison between similar reactions, between various milling parameters for the same reaction, or the transferability of a reaction between different ball-mills. The exact calculation of the kinetic energy and the number of impacts can be highly complex and often

requires simulations. However, collision-based models allow the estimation of involved energies by solving kinematic equations that depend on a few readily measured parameters.

Burgio et al. first introduced such a set of equations to model impact velocities, frequencies and connected parameters[106] and Kessler adopted them specifically for the *Pulverisette 7*.[107] The kinetic energy of a ball before the impact (E_b) can be described after Eq. 1.1 with m_b and v_b being the mass and the velocity of the ball.

$$E_b = \frac{1}{2} m_b v_b^2 \tag{1.1}$$

After the impact, the velocity of the ball changes to v_s and so does the kinetic energy (E_s).

$$E_s = \frac{1}{2} m_b v_s^2 \tag{1.2}$$

Therefore, the energy released in a collision is their difference (ΔE_b). Furthermore, the constant K_a was introduced to regard the elasticity of the impact. K_a is 1 for a fully inelastic collision (high energy transfer) and 0 for an elastic collision (no energy transferred). For most mechanochemical experiments, the ball is covered with powdered material, resulting in almost completely inelastic collision, and a value of 1 can be assumed. After the inelastic collision, v_s is not 0, as the ball is immediately accelerated by the wall. With that in mind, ΔE_b can be estimated after Eq. 1.4. ω_J and ω_P represent the angular velocities of the milling jar and of the central plate, while R_J and R_P stand for their radius Fig. 1.9).

$$\Delta E_b = K_a (E_b - E_s) \tag{1.3}$$

$$\Delta E_b = -m_b \left(\frac{\omega_J^3 (R_J - r_b)}{\omega_P} + \omega_P + \omega_J R_P \right) (R_J - r_b) \tag{1.4}$$

In addition, the factor φ_b should be introduced, which corrects ΔE_b by taking ball-to-ball interactions into account and can be calculated according to Eq. 1.5-1.7. It depends on the number N_b and size r_b of the milling balls in relation to the inner dimensions of the milling vial (radius R_J, height H_J), on the number of balls N_{bv} to completely fill the milling vial and the number of balls N_{bs} to cover $\frac{1}{3}$ of the inner walls surface.

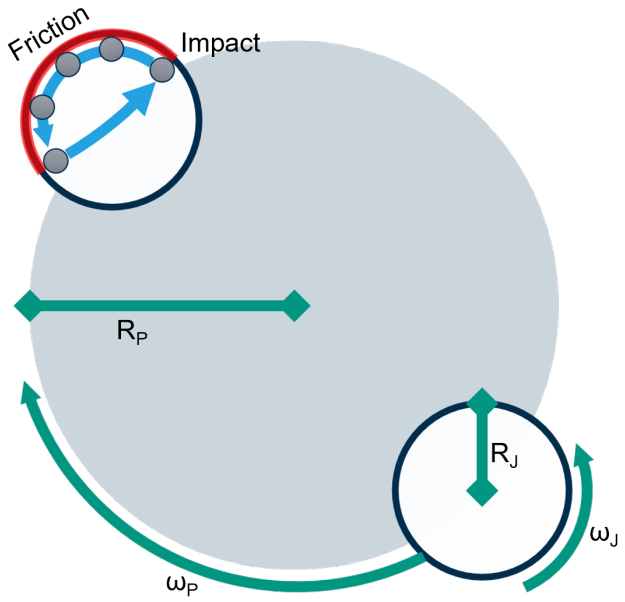


Figure 1.9: Schematic representation of balls trajectory in a planetary ball-mill

$$\varphi_b = 1 - \left(\frac{N_b}{N_{bv}}\right)^{\varepsilon} \tag{1.5}$$

$$N_{bs} = \frac{\pi(R_J - r_b)H_J}{r_b^2} \tag{1.6}$$

$$\varepsilon = \frac{\log_{10}(0.05)}{\log_{10}\left(\frac{N_{bs}}{N_{bv}}\right)} \tag{1.7}$$

When specified for the *Pulverisette 7*, the angular velocities are fixed to $\omega_J = -2\omega_P$, which in turn depend on the rotation speed ν_R after $\omega_P = 2\pi\nu_R/60$. The corrected energy that is released in a collision ΔE_b^* can be expressed with Eq. 1.8 and will further be called the impact energy for simplicity.

$$\Delta E_b^* = 8m_b \left(\frac{\pi\nu_R}{60}\right)^2 (4(R_J - r_b)^2 + R_P(R_J - r_b))\varphi_b \tag{1.8}$$

Beside the impact energy of a single ball, the collision frequency f_b is important (Eq. 1.9), as it allows for the calculation of the number of total collisions N_{tot} (Eq. 1.10). The product of ΔE_b^* and N_{tot} provides the specific milling dose D per gram of feed material m_p (Eq. 1.11), which provides a measure of the energy transferred during the milling process.[107,108] In many cases, mechanochemical

reactions are hindered by an activation barrier or an impact energy threshold E_0. The activation energy can be included according to Eq. 1.12 to calculate the specific activation dose or the scaled milling dose D^*, which can provide more accurate results.[109]

$$f_b = \frac{K\nu_R}{20} \tag{1.9}$$

$$N_{tot} = N_b f_b t \tag{1.10}$$

$$D = \frac{N_{tot}\Delta E_b^*}{m_p} \tag{1.11}$$

$$D^* = \frac{(E - E_0)N_{tot}}{m_p} \tag{1.12}$$

It is worth noting, that this kinematic model is based solely on collisions and neglects friction, which can have a significant contribution to the mechanical energy.[107] Additionally, friction can alter the motion of the milling balls to more, or less efficient trajectories. Moreover, the model assumes ideal trajectories and therefore, it provides an estimate for the upper bound on the impact energy. In practice, the impact energies can vary in the order of magnitudes at given milling conditions,[110,111] and only a fraction of the kinetic energy is transferred to the powder, while a significant part dissipates as heat. A more detailed description of the limitations is provided by Peterson.[112]

Despite these simplifications, the collision model relies on easily assessable parameters (m_b, r_b, ν_R, R_P and R_J) and allows for a qualitative estimation of the energies involved, which often align with experimental results.[106,113,114] More accurate predictions can be obtained with discrete element simulations, but these can be computationally intensive, especially when complex chemical phenomena are included.[83,86,111,115,116]

1.5.5 Mechanochemistry in battery recycling

Mechanochemical processing has recently attracted interest in the recycling of LIBs as it offers advantages such as a simple operation under ambient conditions, shorter reaction times, less chemical consumption, and improved selectivity.[117] A mechanical treatment is already often employed in industrial LIB recycling processes, but usually with the focus on delamination and particle size reduction. Therefore, it can be argued that a more intense mechanical treatment with the goal to induce physico-chemical changes could be easily integrated in the recycling process flow.

Milling of cathode active materials such as LFP, NMC, or LCO leads to particle size, a higher surface, and increased porosity. This activation improves leaching kinetics in subsequent hydrothermal

processes.[117] Seo et al. milled NMC from spent batteries without any additive and achieved an Li-extraction yield of around 19 %, while the transition metals remained in the insoluble fraction. However, the recovered Li_2CO_3 contained 3 wt% fluoride ions, which drastically lowered the performance and increased degradation of the resynthesized NMC material. The authors suggest that fluoride is released from the decomposition of PVDF during ball-milling.[118]

Others utilized co-grinding agents to facilitate the complete dissolution of CAMs. For instance LCO was dry milled with ethylenediaminetetraacetic acid (EDTA),[119] wet milled with a mixture of H_2O_2 and alginic acid[120] or with H_2O_2 and EDTA,[121] wet milled with citric acid[122] and in combination with biomass waste grape skins.[123] The common point of all these studies is that the layered structure of LCO is destroyed during milling. A reducing agent (H_2O_2, citric acid) is added during milling to transform insoluble Co(III) to soluble Co(II), and a chelating agent (EDTA, alginic acid, organics in bio waste) is used to enhance the solubility of transition metal ions, while keeping the pH in the subsequent leaching process at a moderate level.

The milling of other layered oxide materials such as NMC under similar milling conditions leads to comparable results to LCO. In contrast, when LFP cathode material is processed, the formation of insoluble $FePO_4$ is observed while Li can be selectively leached.[124,125] Some authors tested the co-milling of LCO and LFP, by taking advantage of their intrinsic redox potentials.[126] The joint processing of both CAMs results in the oxidation of LFP to $FePO_4$ and the reduction of LCO to CoO and thereby forming Li_2O. Up to 53 % of Li were selectively extracted in an aqueous leaching step. The residual Li alongside with 88.6 % of Co was subsequently extracted under mild acidic conditions, while 98.9 % of Fe remains insoluble. This process also works with NMC instead of LCO.[127]

Another interesting mechanochemical approach is the processing of LCO from spent LIBs with dry ice in a planetary ball-mill.[128] The collisions lead to the collapse of the layered structure and the accumulation of surface oxygen atoms. The oxygen on the surface adsorbs or reacts with CO_2 to form Li_2CO_3 and Co_3O_4. Subsequent aqueous leaching with vacuum filtration allows the selective extraction of 95 wt% Li_2CO_3 in high purity. Finally, Co_3O_4 was thermally reduced with carbon to CoO and metallic Co.

It is also possible to use the materials that are already present in LIBs as reactants in milling experiments. Rao et al. published the reactive milling of LCO with Cu-foil, both isolated from spent LIBs. The mechanical treatment leads to the formation of soluble Li_2O and insoluble CoO and CuO, allowing the selective recovery of lithium salts. The oxidized Cu(II) can be reduced to metallic Cu using ascorbic acid, while CoO dissolves under these acidic conditions.[129]

Dolotko et al. reported the mechanochemical reduction of LCO in a high-energy shaker mill, using reactive metals including Li, Al, and Ca.[130] Later, the range of cathode materials was expanded to NMC, LMO, and LFP, while narrowing down the reducing agent to Al.[131] It is noteworthy that Al is used in LIBs as the current collector of the cathode. Therefore, such an approach could provide the option to skip the delamination of the cathode. Furthermore, Al is abundant, has a low redox

potential ($\varepsilon_0(Al/Al^{3+})$ = -1.676 in acidic and -2.31 in an alkaline environment)[132] and can provide three electrons to the redox reaction, making it an attractive reducing agent. During milling, the CAM becomes reduced to the metallic state by Al, forming soluble Li salts and insoluble Al_2O_3. Eq. 1.13 shows the overall reaction for the LCO case.

$$LiCoO_2 + Al \longrightarrow Li_2O + Al_2O_3 + Co \tag{1.13}$$

In a subsequent acid-free aqueous leaching step, Li can be selectively extracted. The formed metallic cobalt is attracted by a magnetic field, which could enable magnetic separation from the Al-salts.[130] However, during the mechanochemical reduction the formation of $LiAlO_2$ was evidenced by XRD, which limits the yield and selectivity of Li-extraction. Moreover, the milled powder in an aqueous suspension results in strong alkaline conditions and forms a lithium aluminum hydroxide (Eq. 1.14-1.15). Due to the high pH, CO_2 dissolves in the suspension and upon evaporation facilitates the formation of lithium aluminum carbonate hydroxy hydrate (LACHH) according to Eq. 1.16.[131]

$$LiAlO_2 + H_2O \longrightarrow Li_xAlO_x(OH)_z \tag{1.14}$$

$$\{Li_2O + Al_2O_3\} + H_2O \longrightarrow \{LiOH + Li_xAlO_x(OH)_z + Al_2O_3\} \tag{1.15}$$

$$Li_xAlO_x(H_2O)_z + CO_2 + H_2O \longrightarrow Li_2Al_4(CO_3)(OH)_{12} \cdot 3\,H_2O \tag{1.16}$$

The formed lithium aluminum hydroxide shows a low solubility under the leaching conditions. In consequence, the reported Li-extraction rate is only 30 - 40 % and the recovered salts are contaminated with Al, making further purification necessary.

An improved leaching process was introduced to address this problem. In the carbonatization step, LACHH formation is facilitated and in a subsequent thermal treatment at 350 °C, LACHH is decomposed, as shown in Eq. 1.17. The subsequent leaching and evaporation steps allow for the recovery of up to 76 % Li as Li_2CO_3 with good purity.

The mechanochemical treatment for the selective lithium extraction showed good results for LCO, NMC and LMO, whereas the treatment of LFP leads to unfavorable side reactions.[131] The reason is that Al reduces not only the Fe^{2+} but also the phosphate to produce phosphides such as AlP, FeP and Fe_2P. This leads to an enhanced Al consumption and upon contact with humidity or water, AlP violently reacts to form toxic phosphane gas, which may even ignite.[133]

$$Li_2Al_4(CO_3)(OH)_{12} \cdot 3\,H_2O \longrightarrow Li_2CO_3 + 2\,Al_2O_3 + 9\,H_2O\uparrow \tag{1.17}$$

The insoluble residue of the leaching step contains Al_2O_3 and the transition metals as a composite. Alternative to a magnetic separation, the dissolution of the composite was reported. Compared with

pristine cathode materials, the mechanochemically reduced delithiated metallic composites inherit lower oxidation states of TMs and smaller particle sizes. This leads to higher leaching kinetics, which allows for lower acid consumption, shorter reaction times, and no need for additional reducing agents. Compared to traditional recycling routes, a more cost-effective and environmentally friendly recycling process could be expected, which can handle several cathode materials at once.[134]

1.5.6 Mechanically-induced self-propagating reaction (MSR)

The mechanochemical reduction of LCO with Al, as reported by Dolotko et al., should be highly exothermic, similar to the thermite reaction, where Fe_2O_3 is reduced with Al. In the thermite reaction, the starting materials form a metastable mixture with a high activation barrier. The reaction is hindered by the dense alumina layer on the Al particles and the slow diffusion constants in solid materials at room temperature. However, when the activation energy is provided by locally high temperatures, reaction heat is released, which can ignite the surrounding powder, and a reaction front propagates through the material. Such a reaction does not need any external energy or substances such as oxygen for propagation and is therefore called a self-sustaining reaction. Resulting high temperatures may even lead to the melting of all feed materials.[135–137]

Such highly exothermic reactions have been studied in ball-milling experiments and were found to proceed via a mechanically-induced self-propagating reaction pathway.[138] This pathway consists of three stages: activation, reaction, and refinement or cooling.[136]

In the activation stage, the powdery mixture experiences multiple collisions leading to particle size reduction, surface generation, intense mixing, strain accumulation, fracturing, cold welding, and an overall slight temperature increase. Eventually, agglomerates form with lamellar structures of mixed starting materials.[137,139] At this stage, no or almost no product is formed.[101] When a critical activation level is reached, the activation stage ends after the milling time t_{ig} and the reaction stage begins. A single impact under the right conditions can overcome the activation barrier and induce a reaction in the small volume fraction that is compressed in the collision. The heat released from the reaction can then provide the activation energy to thermally induce the reaction in the surrounding powder. A fast reaction front propagates through the entire reaction volume, resulting in a rapid, almost instantaneous, heat release and potentially in melting of reaction components.[140] The heat dissipates through the milling media and the reaction cools down. However, often not all starting materials are consumed immediately after the combustion. In the subsequent refinement stage, further milling drives the reaction to completion and results in a uniform product mixture.[141,142]

MSRs are observed in many systems including metal-chalcogen reactions (Zn + S), some metal-metal alloying (Ni + Al), metal-carbon (Ti + C), and thermite like displacement reactions (Fe_2O_3 + Al). As a rule of thumb, an MSR could be achieved when the ratio of reaction heat and heat capacity $-\Delta H^0_{f,RT}/C_{p,RT}$ is higher than 2000 K.[136]

The activation stage is critical for the process as it defines the conditions for the ignition and, therefore, this stage has been the focus of many studies. Chakurov et al. highlighted the importance of agglomeration during the activation stage. He suggested that a critical minimum powder volume must be compressed in the collision zone, as the amount of powder in which the reaction is mechanically induced is related to the released heat that ignites the surrounding material.[143]

Schaffer et al. analyzed milled powders of a metal oxide and a reducing agent by differential thermal analysis.[144] They reported that a reaction in the powder is initiated at a specific ignition temperature T_{ig} that first decreases with milling time, reaches a minimum, and then increases again. The increase in T_{ig} is related to the formation of the product phase and a decrease in the fraction of the activated starting material. In addition, it was observed that under certain milling conditions, no ignition occurred in the powder mixture. That formed the basis of the hypothesis that repeated collisions result in activation which lowers T_{ig} and induces local hot spots (impact heat and local reaction heat) with T_{max}. When T_{ig} becomes lower than T_{max} the MSR is initiated, but if the minimum of T_{ig} remains above T_{max} a gradual non-combustive reaction will be observed.

The formation of TiC from elemental titanium and graphite is one of the best studied MSR systems.[101,139,145–149] While XRD analysis did not show product formation before ignition, off-stoichiometric, amorphous and/or nano-crystalline TiC detection was reported by Raman spectroscopy, XPS, and TEM. A thin layer (≈2.8 nm) of nano-TiC was found by Oghenevweta et al. in the vicinity between amorphous carbon and nano-crystalline Ti. Upon ignition, rapid grain growth occurs in old and new TiC crystals.[101,139]

Nonetheless, the systematic influence of inert additives on the MSR was studied only in a few studies. Typically, a longer activation stage was observed with an increasing fraction of additives until the ignition is completely suppressed. The suppression of the MSR has been explained by (i) a reduced contact area between the reactants, which limits the reaction rate, (ii) a change in the tendency for agglomeration and covering of milling tools, and (iii) a diluting effect including a lower $-\Delta H^0/C_p$-ratio. Furthermore, inert additives can lower the maximum temperature in the combustion front and lead to smaller particle sizes in the product.[136,143]

The activation stage and the ignition in an MSR is a complicated interplay of material properties and milling conditions that is not yet fully understood.[141] Even when comparing relatively similar reactions such as the reduction of Fe_3O_4 with Al or with Mg, notable differences may occur, which are hard to explain. For instance, an increasing fraction of Al in the stoichiometric mixture lowers t_{ig} while for Mg it is the opposite.[150,151]

However, the rapid increase in temperature at the ignition point allows for the precise determination of t_{ig} and the length of the activation stage, which can be used for investigating the milling conditions that affect MSR and the energy input. Carta and Delogu showed that the measured t_{ig} vary below 10 % in a gaussian distribution, verifying its precision and the high sensitivity to milling parameters.[152] It has also been reported that the reaction rate is approximately proportional to the impact energy.[148]

When the reciprocal number of collisions is plotted against the impact energy, a linear trend typically emerges with a non-zero intercept on the x-axis. This is connected to a minimal impact energy that is required to trigger micro-structural changes necessary to meet the combustive conditions. The energy can therefore be considered as some sort of activation energy. Moreover, it has been demonstrated that the activation milling dose for the ignition D_{ig}^{*} is not affected by the impact energy.[108,109,146,153]

2 Motivation

The ongoing electrification of the transport sector and the expansion of stationary electric energy storage systems globally drive the rising production of lithium-ion batteries. Consequently, the demand for critical raw materials such as copper, cobalt, nickel, and especially lithium experiences a significant growth. At the same time, the volume of battery production scrap and end-of-life batteries increases significantly. Recycling of these waste streams offers immense potential to reduce the demand for primary resources, to minimize environmental damage caused by mining activities, and to strengthen the resilience of critical raw materials.

Conventional recycling processes are based on a pretreatment to produce a black mass, which is subsequently fed to pyro- or hydrometallurgical plants. These processes are typically focused on the recovery of valuable transition metals, such as cobalt, nickel, and copper. In contrast, lithium is often recovered inefficiently or is lost in other waste streams, requiring extra efforts to reach purity benchmarks for battery production. Moreover, battery grade lithium compounds exhibit an enormous price volatility, making it difficult to plan for economic viability. The recovery of lithium is therefore a particular challenge in battery recycling.

The implementation of the European Union battery regulation even further increased the importance of efficient lithium-ion battery recycling processes. The policy introduced element specific recycling quotas, which increases for lithium stepwise up to 80 % at the end of 2031. This underlines the demand for innovative and efficient recycling routes to meet the demands for recovery rates and product purity. In this context, a mechanochemical approach has attracted much interest in recent years. This approach is based on a high-energy ball-milling step, where mechanical force induces a solid-state reaction between cathode active materials and aluminum from the battery's current collector. The reduction of the cathode materials enables the selective lithium extraction in a subsequent acid-free aqueous leaching process and the simple separation of transition metals. Compared to other recycling processes, this approach has been reported to be advantageous as it is robust, cost effective, and energy efficient.

Overall, the mechanochemical approach seems to be an interesting research topic that could contribute to the development of more sustainable and efficient battery recycling processes and a circular economy.

Nevertheless, despite its high potential, there are still some gaps in the understanding of the reaction mechanism as well as in the influence of key parameters on the reaction. In particular, it remains unclear which factors define the reaction kinetics, the extraction yield, or the purity. Furthermore, the process has so far been applied only to fresh cathode active material or to batteries that have been manually disassembled, with components carefully separated. Its applicability to a real waste stream, the black mass, has not been investigated yet.

This motivates to systematically investigate the mechanochemical reaction between layered-oxide based cathode materials and aluminum, to identify important process parameters and optimize the conditions when necessary. The second focus is on the development and adaptation of subsequent lithium extraction routes to improve recovery rates and purity of the final lithium products. This work was performed as part of the EU project RHINOCEROS, which addresses the entire lithium-ion battery recycling value chain, from collection through the production of black mass, chemical recycling, and the resynthesis of components. Within the project, the applicability of this process to industrially produced black mass will be tested to recover high-purity lithium salts and to consider its potential integration into a sustainable recycling landscape.

3 Analytical Techniques

During this doctoral project, multiple analytical methods were used to analyze solid and liquid samples along the recycling processes. The theoretical basis behind the most important techniques is described below, to provide sufficient context for the discussion of the results.

3.1 X-ray techniques

3.1.1 Generation of X-rays

X-rays are electromagnetic waves with a short wavelength between 10 nm and 10 pm.[154] The interaction of this radiation with matter can lead to phenomena such as absorption and scattering, which allows its application in analytical tools including diffraction and spectroscopy. For analytical tools, X-rays with a defined wavelength are necessary. There are two options for their generation: X-ray tubes and synchrotron generation.

In general, an X-ray tube consists of a tungsten filament cathode and a metal anode, which are enclosed in a vacuum-sealed glass tube. At high voltages of around 60 kV, electrons are released from the cathode, accelerated, and collide with the metal anode. By interaction with the anode, electrons lose kinetic energy, which results in the emission of bremsstrahlung. If the energy of the electron is sufficient, it can interact with the electrons bound to the metal of the anode, leading to their excitation and ejection. The produced vacancies can be filled with outer-shell electrons, thereby emitting characteristic radiation. The spectrum of the radiation is a superposition of the bremsstrahlung and the characteristic radiation and therefore depends on the type of metal used as the anode and the applied current. Typically, the most intense characteristic peak, for instance the $K_{\alpha 1}$, is selected for X-ray applications. The other wavelength can be removed by using metallic filters or monochromators.[155,156]

In synchrotron facilities, X-rays are generated by accelerating electrons with magnetic fields along a circular, ultra-high vacuum tube. Due to changes in the direction of the electron momentum, bremsstrahlung is emitted. The synchrotron facilities have several advantages, including high intensities and a continuous energy spectrum, where the required wavelength can be selected. However, synchrotrons are expensive, large scale facilities, with limited beam time availability.[155,156]

3.1.2 X-ray diffraction

X-ray diffraction makes use of the elastic scattering of X-rays on the electron densities of atoms. In crystalline materials, atoms are arranged in a well-ordered periodic lattice. When an incident X-ray beam interacts with this lattice, it is scattered in specific directions, leading to constructive and

destructive interference patterns known as Bragg diffraction. Analysis of these interference patterns provides detailed information about the crystal structure, including lattice parameters and atomic arrangement.

The Bragg diffraction of an X-ray beam on the lattice planes is illustrated in Fig. 3.1. The incoming beam of coherent X-rays is scattered on the electron density of the atoms in the crystal lattice, and a fraction of the beam is reflected at the lattice planes with the angle of incidence equaling the angle of reflection. The high energetic X-rays are not completely reflected, and the major fraction penetrates the sample, leading to further beam reflections at parallel planes separated by d_{hkl}. The reflected beams have a phase shift of $\overline{ABC} = 2\overline{AB}$. For constructive interference, the phase shift of the reflected beams must be a multiple of the wavelength λ. This leads to the condition for constructive interference on a crystal lattice known as the Bragg equation in Eq. 3.1.[157]

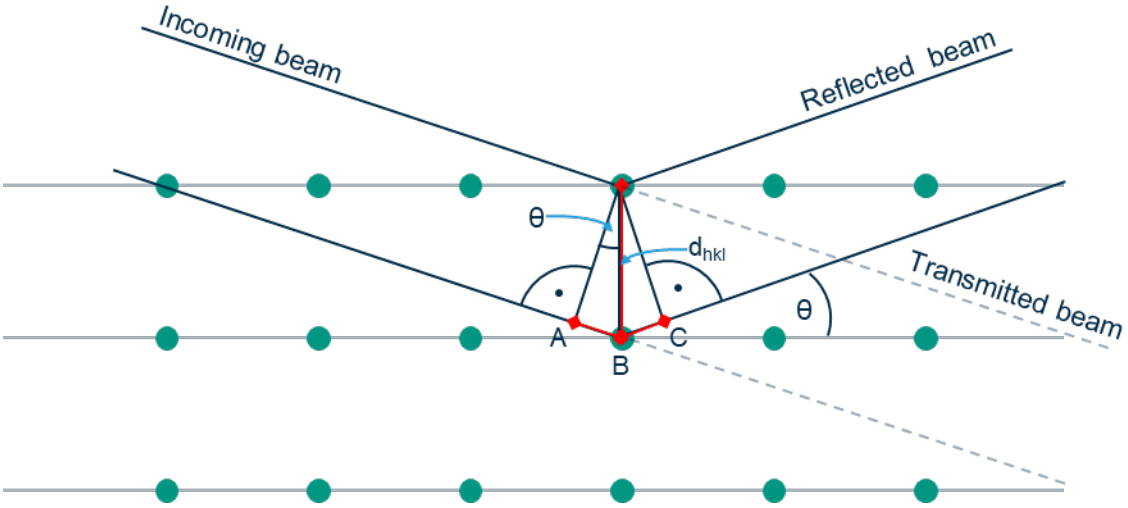


Figure 3.1: Illustration of X-ray reflection on crystal lattice planes (adapted from[157]).

$$sin\ \theta = \frac{n\lambda}{2d_{hkl}} \tag{3.1}$$

In the case of single crystals, the beam is reflected in a defined direction for each lattice plane that meets the condition for constructive interference. In the case of polycrystalline materials, multiple crystals are oriented randomly and, therefore, the reflections appear as cones.In a typical powder diffraction experiment, a detector collects the intensities of reflections as a cross section through the cones in one plane, either in transmittance or in reflective mode. The intensities are plotted against 2θ to produce a diffractogram.

The position of a reflection in a diffractogram (typically in values of 2θ) depends primarily on λ and the distance between lattice planes (d_{hkl}), and thus on the lattice parameters. However, visibility of specific reflections is defined by the symmetry of the crystal. The intensity, width and the shape of

reflections are affected by multiple factors and can provide detailed information about the measured sample or the machine.

A recorded XRD pattern of an unknown solid can be compared with existing patterns from data bases to perform phase analysis by matching peak positions and intensities. As the intensities are proportional to the number of atoms, the phase fractions of a mixture of crystalline samples can be determined.

Imperfections in the crystal lattice, such as vacancies, impurities, or strain, result in a reduced periodicity of the crystal lattice. In consequence, the reflections are getting broader, and an asymmetry may indicate anisotropic contributions. When the particle size is very small, the number of planes that scatter the X-rays is reduced, and, in consequence, the peaks observe a Lorentzian broadening. Preferred orientations can also be observed in a diffractogram. Crystals with anisotropic dimensions like needles or platelets, show a reduced number of planes in one dimension, resulting in the broadening of the respective reflections. In some cases, it is possible that the crystallites are not randomly oriented but show a preferred orientation. Depending on the geometry of the diffractometer, this can result in a reduced or increased intensity for specific reflections.[158]

The selection of the wavelength can be a crucial factor. In most diffractometers, the Cu-$K_{\alpha 1}$ emission of 1.540562 Å is used primarily due to its good properties for X-ray generation, including good heat conductivity and high intensity of the characteristic emission. However, the energy related to λ is slightly higher than the absorption edge of Co, and therefore significant X-ray absorption is observed, when the sample contains Co, Fe, or Mn. This lowers the penetration of the sample and therefore the intensity. Furthermore, absorbed X-ray energy can be released as X-ray fluorescence, which results in a high background intensity and a lower signal to noise ratio.[157]

This problem can be addressed by using a different X-ray source, for instance with Mo radiation (Mo-$K_{\alpha 1}$ = 0.70930 Å), which shifts the absorption edge to higher atomic numbers (Yttrium). However, the increased intensity comes with a cost. According to the Bragg equation (Eq. 3.1, the reflections are shifted to lower values of 2θ, and compressed closer together, which can reduce the resolution of the diffractogram.

3.1.3 X-ray absorption spectroscopy (XAS)

X-ray absorption spectroscopy is based on the inelastic interaction of X-rays with matter and allows the element specific investigation of the local atomic environment and the electronic structure. X-rays can be absorbed by atoms, which results in the excitation of core a electron in an unoccupied state or the continuum. The electron's initial state can be, for instance, 1s for a K_1 absorption, a 2s or a 2p state for a L_1 and L_2 absorption, respectively. Thereby, only excitations with a change in the orbital angular momentum $\Delta l = \pm 1$ are allowed.[156] In consequence, the main absorption of an s-electron is a s-p-transition to the lowest unoccupied p-orbital or the ejection of the electron in the continuum

to produce a photoelectron. After excitation, relaxation can proceed by emission of a photon called X-ray fluorescence or by the emission of an Auger electron. The intensities of both are proportional to the intensity of absorbed X-rays and therefore can be used as measurement parameters instead of the transmitted intensity I_t. The energy required for the absorption depends primarily on the atomic number and therefore XAS is a highly element specific method.[159]

In an XAS measurement, the photon energy of a monochromatic X-ray beam is slowly increased and the beam intensity before (I_0) and after the sample (I_t) is measured. The absorption coefficient $\mu(E)$ can be obtained from Lambert Beer's law (Eq. 3.2) with d as the sample thickness, to produce a spectra as in Fig. 3.2.[156]

$$I_t = I_0 \cdot \exp(-\mu(E)d) \tag{3.2}$$

When the photon energy exceeds the binding energy of a core level electron, absorption may occur, and the election is excited to an unoccupied state or ejected to produce a photoelectron. The excitation results in a step like increase in $\mu(E)$, called the absorption edge.[160] The region around the absorption edge is used for X-ray absorption near edge structure spectroscopy (XANES). It consists of the absorption edge and the intense oscillation at slightly higher energies. Depending on the material, a very intense absorption peak emerges at the absorption edge, which is often referred to as the white line. Furthermore, pre-edge peaks can emerge, which can be assigned to formally forbidden transitions (for instance, an s-d transition with $\Delta l = \pm 2$) and therefore they typically show low intensities.[160]

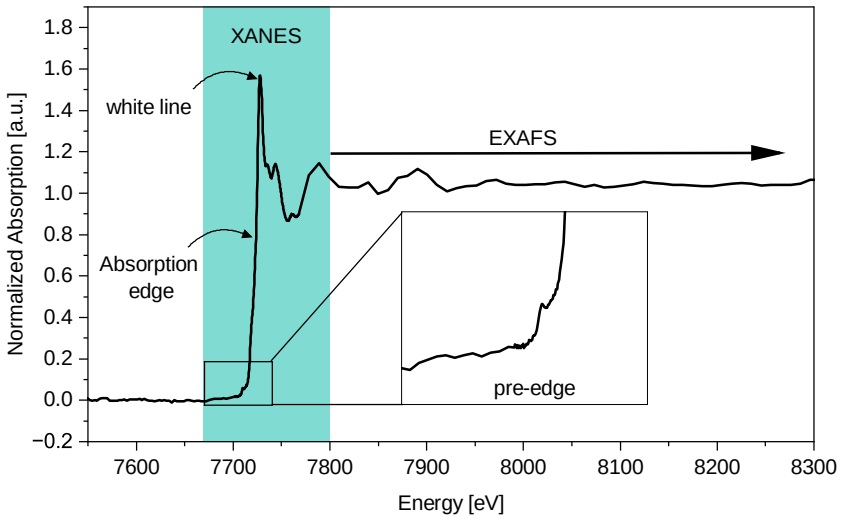


Figure 3.2: XANES spectra of NMC-111 at the Co-K_α edge.

The XANES region provides information about the electronic structure and the symmetry of the metal site. The shape and intensity of the edge and the peaks depend on the orientation and nature of the ligands around the metal. An asymmetry in the local structure, such as broken inversion, enables formally forbidden transitions and gives rise to the pre-edge peak.[156] The position of the absorption

edge is related to the electron density on the metal, and can therefore be used to determine its oxidation state. For instance, the absorption edge of Fe_2O_3 is shifted to higher photon energies compared to FeO, because the core electrons are stronger bound due to the higher overall positive charge at the metal site. Therefore, the determination of oxidation states is only relative between compounds and requires reference materials with similar symmetry and ligands. Moreover, a comparison of oxidation states is hardly possible between compounds that strongly differ in symmetry and ligands. XANES can also be used to identify a compound or to calculate phase fractions, since the spectrum of a mixed sample is a superposition of the spectra of pure compounds.[156]

At higher energies, the spectra show an oscillation of μ, which is related to scattering processes of the ejected photoelectron with backscattered waves from the surrounding atoms, resulting in constructive and destructive interference. This region is used for the extended X-ray absorption fine structure (EXAFS), which provides information on interatomic distances.[156,159]

3.2 Scanning electron microscopy with energy dispersive X-ray spectroscopy

Scanning electron microscopy is a technique in which the surface of a sample is scanned in vacuum using a focused electron beam. Compared to optical microscopy, SEM offers a much higher resolution (down to 1-2 nm) and a significantly higher magnification (up to 200 000x). This improvement arises from the much higher deBroglie wavelength of electrons, compared to visible light.[161]

In SEM, electrons are emitted from an electron gun and accelerated by high acceleration voltages of up to 30 kV towards the sample. A system of electromagnetic lenses focus the electron beam to a small spot, and electromagnetic coils deflect the beam in the x-y plane to scan the sample surface. Upon contact with the sample, the electrons penetrate into the material at a depth of a few microns, which depends on the composition of the material and the acceleration voltage. In the material, the electrons undergo various scattering processes, which results in the emission of backscattered electrons (BSE), secondary electrons (SE), and X-rays. The intensities can be recorded by different detectors to provide complementary information about the sample.[161]

The backscattered electrons originate from multiple successive scattering events of the incident beam. Each time, the electrons' direction of the travel is changed until it eventually may return to the samples surface and exit the sample. The yield of backscattered electrons increases with the atomic number. Consequently, regions containing elements with a high atomic number appear brighter than regions composed of lighter elements. BSE imaging therefore provides compositional information. In addition to compositional effects, the orientation of the surface relative to the incident beam significantly influences the BSE intensity. Tilted or inclined surfaces tend to emit more backscattered electrons and thus appear brighter. This angular dependence introduces a degree of topographic contrast.[162]

Secondary electrons are produced by inelastic scattering of the incident electron beam in the sample under the ejection of weakly bound valence bond electrons. These electrons typically have a low kinetic energy between 1 and 50 eV. As they travel through the sample, further inelastic scattering processes lead to rapid energy loss. When the electron reaches the sample surface with enough energy, it can be ejected into the vacuum and be detected. Due to their low energy, secondary electrons have a very short mean free path, typically less than 5 nm. Only the SE that are produced at the samples surface can be ejected into vacuum and be detected. At surface features such as edges, tips, or surface areas parallel to the electron beam, more SE escape the sample, and the point appears brighter. This strong sensitivity to surface geometry gives SEM images their characteristic three-dimensional appearance and enables detailed topographic and morphological characterization.[163]

The samples may become charged by the incident electron beam, which can cause deflection of incoming electrons and lead to image distortions or artificially bright spots. To prevent sample charging, the sample must be sufficiently conductive to allow charge dissipation. If necessary, conductivity can be improved by applying a thin conductive coating.

The X-rays during SEM analysis are produced similarly to processes in an X-ray tube. The electrons in the focused beam undergo inelastic scattering with the core-level electrons of the atoms in the sample. The core electron can be ejected, which creates a vacancy, for instance, in the K-shell. An electron from a higher-lying shell may perform a transition to fill this vacancy, releasing excess energy in the form of an x-ray photon. The photon energy corresponds to the difference between the electronic energy levels and is element specific (e.g., K_α- or K_β-lines).[164]

The detection and analysis of these X-rays is the basis for energy dispersive X-ray spectroscopy (EDX). Each element in the analyzed volume emits a set of characteristic X-ray lines, which can be used to determine the elemental composition of the sample. In principle, the intensity of these lines is related to the atomic fraction in the volume when factors such as the atomic-number-dependent ionization cross sections, X-ray absorption, and fluorescence effects are considered. Light elements are difficult to detect as their emission is already absorbed in the sample or the detector window and may not reach the detector.

Matrix effects, peak overlaps, and uneven or rough surfaces can further influence the detected X-ray intensities and therefore limit the reliability of a quantitative or semi quantitative analysis. Nevertheless, the recorded intensities can be effectively used to identify spatial distributions of elements on or near the surface, and to produce elemental maps.[165,166]

3.3 Inductively coupled plasma optical emission spectroscopy

Inductively coupled plasma optical emission spectroscopy (ICP-OES) is an analytical technique used to quantify elemental concentrations in liquid samples. The method is based on the excitation of valence and near-valence electrons of atoms and ions within a hot plasma.

In ICP-OES, a liquid sample is nebulized into an aerosole, which is transported away with an argon carrier gas and spayed into an argon plasma with temperatures of around 8000 - 10000 °C. The plasma is generated with a plasma torch, and the energy required to sustain it is provided by a radio-frequency generator. At these high temperatures, the aerosol dries rapidly and the compounds atomize and partially ionize. Eventually, electrons in the atoms and ions are excited to higher-lying energy levels by collisions with energetic electrons in the plasma.[167] When excited species relax to their ground state, photons are emitted, whose energy correspond to the difference between the electronic states. Photons are separated according to their wavelengths, for instance, with a monochromator, and intensities are recorded to produce an emission spectrum.[168]

The set of emission lines is characteristic for each element and the intensity of a given line is proportional to the number of emitting atoms or ions in the plasma. This allows the simultaneous detection of a wide range of elements down to the µg/L region, and with proper calibration, concentrations can be quantified over a wide range.

However, not all elements can be detected, or detected reliably. For instance, halogens exhibit high excitation energies, and consequently, only a small fraction of atoms are excited in the plasma. Additionally, their strongest emission lines have short wavelengths, which may result in the absorption of the photons by the sample, atmosphere, or optical components before entering the detector.[169]

3.4 Ion-selective electrode

An ion-selective electrode (ISE) is an analytical instrument for quantifying the concentration of a specific ion in solution. This method is based on the electrochemical potential difference at an ion-selective membrane, which is measured relative to a reference electrode.

An ISE consists of a body, which is sealed at the bottom with an ion-selective membrane, exhibiting high ion conductivity for a specific ion. The electrode body is filled with a reference solution in which the actual electrical contact is immersed. When the electrode is placed into the sample solution, an electrochemical potential emerges as a result of the different activity of the target ion at both sides of the membrane. This potential can be described by the Nernst equation (Eq. 3.3). Here, E is the measured electrode potential, E_0 is the respective standard potential, R is the ideal gas constant, T the temperature, z is the charge of the electron, F is the Faraday constant, and a_i is the activity of the target ion.[170,171]

$$E = E_0 + \frac{RT}{zF} ln(a_i) \tag{3.3}$$

The activity of ions is related to their concentration with the activity coefficient according to $a_i = f_i c_i$. In dilute systems $f_i \approx 1$ and the activity is approximately the concentration. Under these conditions, the measured potential depends linearly on the logarithm of the target ions concentration. By

calibration with standard solutions, the concentration of the target ion in an unknown sample can be determined.[171]

An ISE allows for a simple, fast, and inexpensive analysis with minimal sample preparation. However, there are some limitations that need to be considered. At very low or very high concentrations, the potential shows no linear dependence according to the Nernst equation. In addition, the selectivity of the membrane for other ions is low but not zero. Therefore, high concentrations of other ions can interfere with the measurement. For instance, high Na^+ or H^+ concentrations in the lithium selective electrode result in an overestimation of the Li concentration.

Furthermore, the ion activity depends on the total ionic strength of the solution. Variations in the ionic strength can therefore influence the electrode response, which often makes the addition of a total ionic strength adjustment buffer (TISAB) necessary. Some ions tend to form complexes in solution, which are no longer selective for the membrane. This effect is particularly relevant for fluoride detection, where the formation of HF or Al-F complexes reduces the activity of free F^- and prevents an accurate analysis. For a reliable ISE measurement, the addition of suitable complexing agents and additives to buffer pH and ionic strength is therefore often required.[172]

4 Materials and Methods

4.1 Materials

Several chemical reagents were used throughout this study. These include the commercial cathode active materials $LiCoO_2$ (LCO) and $LiNi_{1/3}Mn_{1/3}Co_{1/3}O_2$ (NMC-111), which were purchased from Thermo Fisher Scientific and BASF, respectively. Reactive Mg metal powders (<75 µm, 99.8 %) were obtained from Carl Roth, while aluminum (-325 mesh, 99.5 %) and silicon (-100 mesh, 99.9 %) were purchased from Alfa Aeser. The elemental powders of red phosphorus (97 %) and sulfur (99.9 %) were purchased from Sigma-Aldrich. All of these chemicals were stored in an argon-filled glovebox to prevent oxidation and moisture uptake. The graphite used in the experiments was battery-grade graphite obtained from Imerys Graphite & Carbon.

Additional chemicals, including calcium hydroxide (95 %), sodium carbonate (98 %), polyethylene oxide (PEO, MW = $5\,x\,10^{\,6}$ g/mol), as well as hydrochloric acid and sulfuric acid, were purchased from Thermo Fisher Scientific or VWR.

The black mass provided by SK TES was produced from spent EV batteries by mechanical processing, including inert shredding.

4.2 Characterization

4.2.1 X-ray diffraction (XRD)

X-ray diffraction patterns were collected from powders on a STOE Stadi P powder diffractometer with monochromatic Mo$-K_{\alpha 1}$ radiation (λ = 0.709300 Å) in transmission geometry. The XRD measurements were performed at room temperature in the range of $2\,\theta$ = 5 to 35° with 0.015° angular resolution. The samples were prepared by placing the powder on an adhesive Kapton foil. An empty Kapton film was measured, and its intensity was subtracted from the experimental patterns as a background correction. A phase identification was performed using Match3! software connected to the crystallographic open database (COD).

Some diffraction patterns were collected from the powders using monochromatic Cu$-K_{\alpha 1}$ radiation (λ = 1.54056 Å). These measurements were performed at room temperature in the range of $2\,\theta$ = 10 to 70° with 0.015° steps.

4.2.2 X-ray absorption near edge structure (XANES)

X-ray absorption spectroscopy, or more precisely, X-ray absorption near edge structure, was used to monitor the oxidation state of the initial black mass and milled products during the mechanochemical

reduction process. The spectra were recorded on an easyXAFS 300+ spectrometer (easyXAFS LLC) in transmission mode at 40 kV, 30 mA (1.2 kW). The machine was equipped with a Si crystal monochromator and had a 8x3 mm slit size.

For sample preparation, 60 mg of the powdered material was mixed with 100 mg of polyethylene oxide inside an argon-filled glovebox to prevent oxidation. The mixture was homogenized by grinding in an agate mortar for 20 min and subsequently pressed into a pellet using a 13 mm pressing die at 7 tons. The pellet was sealed in a Kapton foil to protect it from the atmosphere.

XANES spectra were acquired in the element specific ranges for K_α-edge absorption of Mn (6485 – 6994 eV), Co (7559 – 8089 eV), and Ni (8187 – 8902 eV). Data processing and evaluation was performed using the Larch software package,[173] including energy calibration against the corresponding metallic foil, normalization of absorption spectra, and linear combination fitting (LCF). The LCF is based on the superposition of absorption spectra from reference materials with defined oxidation states. The reference samples were prepared and measured identically to the original sample. As reference materials commercial NMC-111, the metallic foils of Co, Ni and Mn, as well as the oxides MnO, Mn_2O_3, MnO_2, CoO, Co_3O_4, and NiO were used. For experiments utilizing sulfur, the range of reference materials was extended to CoS, CoS_2, and $CoSO_4 \cdot 7\,H_2O$.

4.2.3 Thermogravimetric analysis (TGA)

Thermogravimetric analysis (TGA) was carried out using a Netzsch Jupiter 449 C to estimate the mass fractions of volatiles, binder, and carbon in the black mass. Approximately 20 mg of the powdery sample was placed in a corundum crucible and heated from 30 °C to 1400 °C at a heating rate of 10 K/min. Argon gas was used as the protective gas and the purge gas, and a constant flow rate of 40 mL/min was kept during all measurements. For measurements under oxidizing conditions, an additional oxygen gas flow of 10 mL/min was introduced. After the experiment, a blank measurement was subtracted„ and the derivative was calculated to obtain the differential signal (dTG).

4.2.4 Static Light Scattering

The particle size distributions were measured by laser scattering with an LA-950 analyzer (HORIBA GmbH). For each measurement, approximately 150 mg of powder was suspended in 5 mL of isopropanol and dispersed by ultrasonication for 1 min using a SONOPULS HD 2200.2 (Bandelin GmbH). The resulting suspension was introduced dropwise into the instrument measuring chamber until a transmittance of approximately 85 % was obtained.

4.2.5 Scanning electron microscopy and energy dispersive x-ray spectroscopy (SEM & EDX)

Scanning electron microscope images of various samples were collected under vacuum with a Zeiss Merlin microscope (ZEISS SMT Ag) operating at acceleration voltages between 3 and 5 kV. Energy-dispersive X-ray spectroscopy (EDX) measurements were performed at 15 or 20 keV, using the integrated XFlash detector (Bruker). The collected EDX data were processed in Python 3 with the HyperSpy package[174] to generate elemental maps and SEM-EDX overlays.

4.2.6 Inductively coupled plasma optical emission spectroscopy (ICP-OES)

The elemental analysis of the cations was performed using ICP-OES on an iCAP 7600 DUO (Thermo Fisher Scientific). Solid samples were dissolved with acid in a graphite oven and analyzed as triplicates. The liquid samples were measured directly as triplicates.

4.2.7 Ion-selective electrodes

The fluoride content of the solutions was analyzed using a freshly calibrated fluoride selective electrode (Ionplus Sure-Flow Combination ISE, Thermo Fisher). Liquid samples were transferred into a volumetric flask of suitable size. Based on the volumetric flask, 10 vol% of TISAB III concentrate was added, and the remaining volume was filled with DI water. The TISAB solution contains a mixture of an acetate buffer, cyclohexylene dinitrilotetraacetic acid, and sodium chloride to ensure a constant pH, ionic strength, and to reduce interference with dissolved Al^{3+} or Fe^{3+}. The solution was filled in a plastic beaker, and the potential was measured with the ISE at room temperature and under constant stirring.

The routine determination of the Li^{+} concentration of the solutions was carried out with a freshly calibrated DX207-Li ion selective electrode (Mettler Toledo). The liquid sample was filled together with DI water into a volumetric flask. The sample of known volume was transferred to a beaker, and the voltage was measured at room temperature under constant stirring.

4.2.8 UV-Vis Spectrometer

UV-Vis spectra were recorded on a Cary 5000 Series UV-Vis-NIR Spectrometer (Agilent). A 10 g/L Co^{2+} stock solution was prepared from $CoSO_4$ and acidified with H_2SO_4 to pH 1 for calibration. From this stock, a series of calibration standards containing 3.0, 2.5, 2.0, 1.5, 1.0, 0.75, and 0.677 g/L Co^{2+} was prepared. Spectra were acquired with a 0.1 s integration time, and the absorbance at 512 nm was recorded.

4.3 Methods

4.3.1 High-energy ball-milling

During the study, the shaker mill 8000D from SPEX SamplePrep (now Cole Palmer) and the *Pulverisette 7* planetary ball-mill from Fritsch were used. The planetary ball-mill was selected as the preferred one due to its greater flexibility and its capability to monitor internal parameters such as temperature and pressure. Unless otherwise stated, all experiments and results presented in this work refer to this mill.

An 80 mL stainless steel vial, equipped with an internal sensor for pressure and temperature in the lid (EasyGTM-setup, Fritsch), was loaded with stainless steel balls (Fig. 4.1). The balls are characterized by their number N_b, diameter d_b, and mass m_b. Balls in three different diameters were used: 3.0 mm (109 mg), 6.35 mm (1.01 g) and 12.7 mm (8.20 g). In most cases the vial was transferred into the argon filled glovebox and loaded with the reaction mixture, which consists of a cathode active material (LCO, NMC-111, or BM), a reducing agent such as Mg, Al, Si, P, or S, and optionally with an additive such as graphite.

The vial was sealed inside the glove box with an O-ring and 6 screws and then transferred to the mill. The milling program can be described by the rotation speed ν_R, the duration of a milling cycle, the resting time between the cycles, and the number of cycles. In this work, the milling time is an important measurement parameter, which can be defined as the product of cycle duration and cycle number, but does not include the resting time.

After certain time intervals, milling was interrupted, the vial was transferred to the glovebox, and a sample was collected. Depending on the mass of the collected sample, the respective number of balls was removed to preserve the initial ball-to-sample mass ratio. When the milling was completed, the powder was separated from the balls by sieving. The collected samples and final products were stored in the glovebox until subsequent measurements or further treatments are performed.

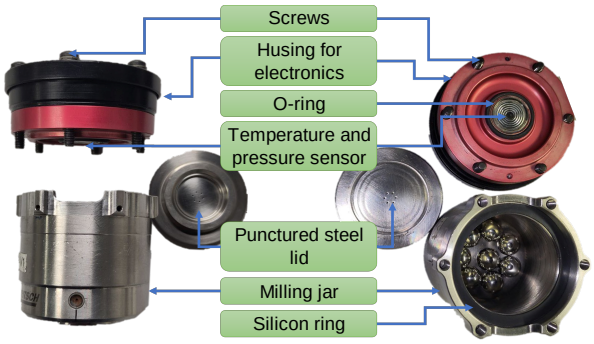


Figure 4.1: Setup of the planetary ball-milling vial with sensors for internal temperature and pressure in the lid.[175]

For some specific experiments, the SPEX shaker mill was also used. This ball-mill provides a higher ratio of head on collisions and less friction than the planetary ball-mill, and it was used in previous studies that form the starting point of this work. Experiments were carried out by loading the vial in the argon filled glovebox with four 6.35 mm and two 12.7 mm balls alongside the required amount of reaction mixture required to obtain the right ball-to-sample mass ratio. The sealed milling vial was transferred to the machine and milled for a certain time in cycles of up to 90 min with 20 min of rest in between.

4.3.2 Aqueous lithium extraction

The exact process for lithium extraction was developed and improved during the period of this doctoral project, and therefore the general approach for aqueous leaching is described first and then four final processes.

Generally, the as-milled powder was weighted in the glovebox, transferred to an air atmosphere, and carefully added to deionized water (DI) under continuous stirring to obtain a suspension with a defined solid-to-liquid ratio (s/l). Weighting in an inert atmosphere is necessary to prevent oxygen or water uptake, which would interfere with yield calculations. After being stirred for a certain time, the suspension was filtered off by suction. Typically, the solid was re-suspended two times in DI water and filtered again. The filtrates were either analyzed separately or combined. The Analysis may include the determination of pH and ion concentrations, especially of Li. In addition, the water was evaporated and the solid obtained was dried in an oven at 80 °C and analyzed by XRD and other methods.

The lithium extraction yield Y_{Li} was calculated according to Eq. 4.1 as the fraction of recovered Li (n_{rec}) and the initial amount of Li in the powder before leaching (n_{init}). The recovered Li content was determined by measuring the Li concentration of the solutions obtained using ISE or ICP-OES (Eq. 4.2).

$$Y_{Li} = \frac{n_{rec}(Li)}{n_{init}(Li)} \tag{4.1}$$

$$n_{rec}(Li) = c_{sol}(Li) \cdot V_{sol} \tag{4.2}$$

The initial amount of Li $n_{init}(Li)$ was calculated with Eq. 4.3 based on the chemical formula of the respective CAM or with Eq. 4.4, which is based on the Li mass fraction in the black mass $\chi_{Li}(BM)$. The parameter χ_{RA} is the mass fraction of the reducing agent, m_p is the mass of the powder used for leaching and χ_V the weight loss if a pretreatment was performed before milling, such as drying.

$$n_{init}(Li) = \frac{m_p(1-\chi_{RA})}{M(CAM)} \tag{4.3}$$

$$n_{init}(Li) = \frac{m_p \cdot \chi_{Li}(BM) \cdot (1-\chi_{RA}) \cdot (1-\chi_V)}{M(Li)} \tag{4.4}$$

The purity of the recovered Li_2CO_3 was determined from ICP-OES according to Eq. 4.5 with i = Al, F, Fe, Co, Ni, Mn, Ca, and Mg.

$$Purity(Li_2CO_3) = \frac{m_{Li_2CO_3}}{m_{Li_2CO_3} + \sum_i m_i} \tag{4.5}$$

Four aqueous leaching processes were finally performed on the dried and milled black mass, which are described below. The direct aqueous leaching was applied to the BM-Al system as the first route and to the BM-Mg system as the fourth route.

Direct aqueous leaching

In the first and the fourth route, 2 g of the as-milled powder were added to 80 mL of DI water. After stirring for 10 min, the suspension was filtered and the solid was washed twice by re-suspending it for 10 min in 80 mL of DI water, followed by filtration. After each extraction cycle, the filtrate was brought to a total volume of 100 mL, and the lithium concentration was measured with a Li-ion-selective electrode. The combined filtrates and the final solid residue were analyzed using ICP-OES. Both the solid residue and the filtrate were dried at 80 °C and subsequently analyzed by XRD.

***Carbonatization* process**

The second route introduces a carbonatization step, as described by Dolotko et al., to decompose $LiAlO_2$.[131] Two grams of the as-milled powder were mixed with 50 mL of DI water and heated to 90 °C for 1 h. The suspension was then dried at 80 °C, and the resulting powder was heated in air at 350 °C for 3 h. After thermal treatment, the same extraction steps described in the direct lithium extraction route were applied.

***Katoite* process**

In the third route, 2 g of the as-milled powder was added at 90 °C to a pre-heated suspension containing 1.4 g of $Ca(OH)_2$ in 80 mL of DI water. The mixture was stirred at 90 °C for 1 h. The hot suspension was filtered, and the solid was washed twice by re-suspending it for 10 min in 80 mL of DI water, followed by filtration. After each extraction cycle, the filtrate was adjusted to a total volume of 100 mL, and the Li concentration was measured with a Li-ion-selective electrode. The combined filtrates and the solid residue were characterized by ICP-OES. An additional purification step was performed by stirring the Li-containing solution for 1 h and then filtering again. Both the solid residue and the filtrate were dried at 80 °C for XRD analysis.

Purification after direct Li extraction from the Mg-system

The combined filtrates of the direct Li extraction of the BM-Mg system were acidified with HCl to pH = 5. Then, about 180 mg of $CaCl_2$ were dissolved in 10 mL of DI water and added to the Li-bearing solution under vigorous stirring, resulting in colorless precipitation (identified as CaF_2). Subsequently, the suspension was concentrated to 40 mL, and the solid was separated by filtration. A saturated solution of Na_2CO_3 (1 mL) was added to the filtrate, and the precipitate formed (identified as $CaCO_3$) was removed by filtration. Afterwards, the solution was concentrated to 2 mL, and the colorless precipitate formed (identified as Li_2CO_3) was isolated by centrifugation. For recrystallization, the isolated solid was suspended in 14 mL of DI-water, pressed through a syringe filter, and heated in an oil bath of 110 °C. After the liquid phase was approximately reduced to 2 mL, it was decanted, and a white precipitate was collected and dried to yield 160 mg of Li_2CO_3. Its purity was determined by ICP-OES.

4.3.3 Cobalt leaching

The insoluble residue obtained after aqueous lithium extraction was subsequently treated to convert the insoluble cobalt disulfide phase into a soluble cobalt compound. DI-water and hydrogen peroxide were employed as leaching agents. The H_2O_2 dosage was adjusted relative to the stoichiometric requirement calculated from Eq. 5.10, which indicates that seven moles of H_2O_2 are needed for each mole of CoS_2.

To calculate the required amount of H_2O_2 per gram of powder, it was assumed that the powder consisted solely of pure CoS_2, without any impurities. Leaching tests were carried out at room temperature by adding 100 mg of powder to 10 mL of a pre-prepared H_2O_2 solution containing 0 to 8 times the stoichiometric amount of H_2O_2 required according to Eq. 5.10. After sirring for 20 min, the slurry was filtered through a syringe filter, and the filtrate volume was adjusted to 20 ml with DI-water in a volumetric flask. The Co^{2+} concentration in the solution was then quantified by UV-Vis spectroscopy.

5 Results and Discussion

5.1 Overview

Chapter 5 is divided into two main sections that contain results from already published and submitted articles. The investigation of the LCO-Al model system in Section 5.2 is based on the publication "*Mechanistic Investigation of the Mechanochemical Reduction of $LiCoO_2$ with Al in the Context of Lithium-Ion Battery Recycling*"[175]. Most of the results in Section 5.3 on the mechanochemical reduction of industrial black mass with subsequent lithium extraction are submitted as a manuscript for publication under the title *"Improved Mechanochemical Reduction of Industrial NMC-based Black Mass with Subsequent Selective Lithium Extraction"*[176].

As it is discussed in Section 1.5.5 of the present thesis, the mechanochemical reduction of common CAMs with reactive metals such as aluminum and calcium has been reported to be a promising and robust approach to an efficient and environmentally friendly recycling process of LIBs, that enables selective lithium extraction without any acid consumption.[130,131,133]

Based on these findings, the present work investigates the transferability of this mechanochemical approach from idealized, pristine CAMs to a real-world scenario with industrially produced black mass (BM). As a first proof of concept, the reported process was applied without modification to the industrial BM. About 2 g of the starting materials (BM + 21 wt% Al) were milled in a SPEX mill with a BSR of 10. While for NMC a complete reduction has been reported in less than 3 h,[131] the utilization of BM led to a surprisingly long reaction time of 20 h.

Fig. 5.1 shows the evolution of the XRD pattern during the described mechanochemical processing of BM. The figure demonstrates (i) the slow and continuous decrease of the NMC 003 reflection at $2\theta = 18.6°$ and (ii) the disappearance of the graphite 002 reflection at $2\theta = 26.4°$. The 003 reflection of NMC exhibits a high intensity, while expected intermediates or products show no or no intense reflection around this position. Therefore, the reflection is suitable for monitoring the progress of the reactions. It should be noted that these patterns were measured using Cu-$K_{\alpha 1}$ radiation, while most other patterns in this work were collected using Mo-$K_{\alpha 1}$ radiation, resulting in smaller 2θ values.

In addition to the long milling times, the milled products showed enhanced sensitivity towards air, which could even lead to a self-ignition. Furthermore, the recovered Li salt after aqueous leaching showed intense reflections of LiF in the XRD and a dark gray appearance, indicating further contamination.

It can, therefore, be concluded that the mechanochemical approach can in principle be applied to a black mass, as the CAM becomes reduced and Li can be extracted. However, the process cannot be directly transferred, but has to be improved to decrease the reaction time, and therefore the energy input, and to increase the lithium extraction yield and the purity of the recovered product.

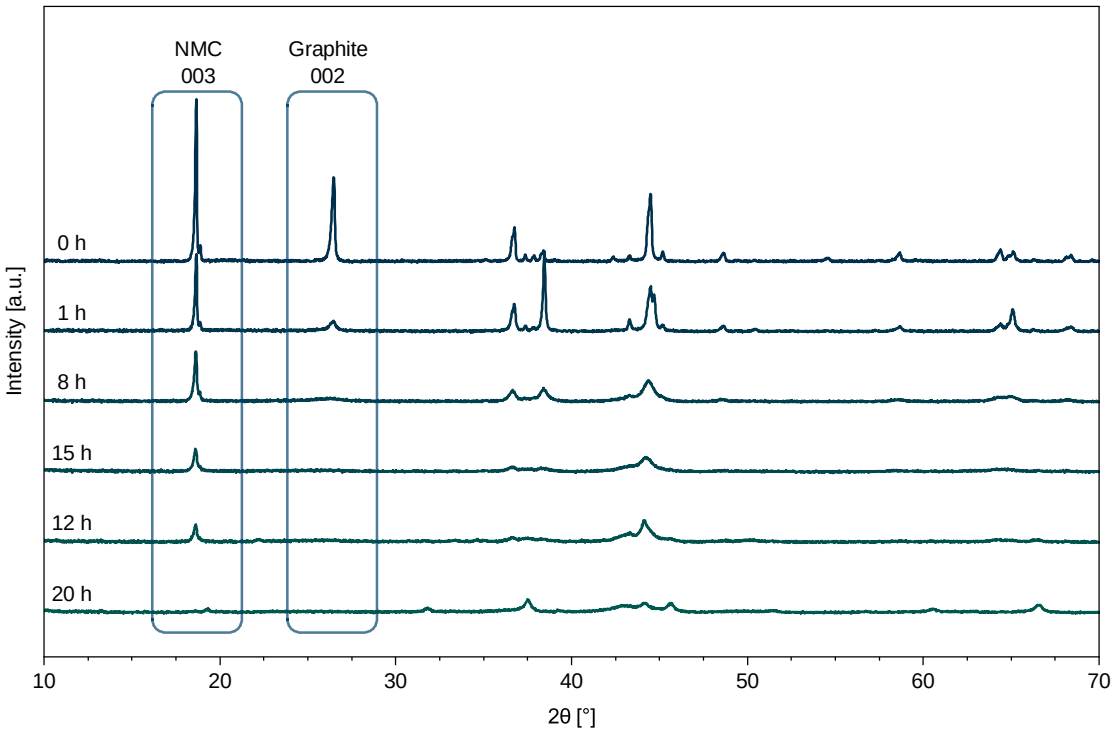


Figure 5.1: Evolution of XRD pattern during milling of BM with 21 wt% Al in a SPEX mill using a BSR of 10:1, with two 12.7 mm and four 6.35 mm stainless steel balls. Patten were collected using Cu-$K_{\alpha 1}$ radiation.

This poses several scientific questions, which are addressed in this thesis. (i) What happens inside the mill and what is the mechanism? (ii) What influence have the process parameters with respect to the milling time, efficiency, and product formation? (iii) What influence do other compounds contained in the BM have on the milling process? (iv) How can the lithium recovery yield and the purity of the final lithium products be increased?

To answer these questions, the mechanochemical transformation of LCO is rationalized within the model material system. The evolution of the internal pressure and temperature, the powder morphology and particle sizes as well as the evolution of crystalline phases were investigated to gain a deeper understanding of the reduction process of LCO with aluminum, induced by ball-milling. The reduction process is then extended to other reducing agents to validate the product formation and the effects on the mechanism. Further, the influence of the process parameters, such as ball size, rotation speed, BSR, and filling degree are tested under the consideration of impact energies, the milling dose, and energy efficiency. Additionally, the effect of graphite on the mechanochemical reduction of LCO with Al is investigated in preparation to the process application on the industrial BM. Beside the mechanochemical reduction of LCO with reactive metals, the reaction with elemental sulfur proved to be a promising alternative processing route.

The following results and discussions are mostly focused on the case of a real black mass. It starts with a thorough analysis of its composition followed by its mechanochemical processing to reduce

the CAMs contained therein. Several process parameters and further pretreatments of the BM were evaluated regarding efficiency and scalability. Finally, aqueous leaching of the milled powders was performed to selectively extract lithium salts. Existing leaching procedures were tested and compared with those in the literature, and new routes were developed to improve the Li extraction yield and the purity of the recovered salts.

5.2 Experiments on pristine CAMs

5.2.1 The Mechanism behind the mechanochemical reduction of LCO with Al

The results of this section have been published in *RSC Mechanochemistry*.[175] In previous studies, Dolotko et al. reported that various layered-oxide CAMs showed comparable behavior when milled with reducing agents such as Al, Li, and Ca.[130,131] The CAMs are reduced to metallic composites and soluble lithium salts form. However, these studies did not elucidate the underlying reaction mechanism, and a deeper understanding of the milling process is essential for targeted improvements and safe application. Therefore, a model system is first investigated with the experiments designed on the basis of the following considerations:

The reaction can be simplified as a layered-oxide material, with transition metal ions in high oxidation states and thus a high standard electrode potential, that is brought into physical contact with an element that possesses a much lower standard electrode potential. Although the thermodynamic driving force is typically high for such reactions, the kinetic barrier prevents such a reaction under ambient conditions. Therefore, mechanical action is needed to overcome these barriers.

LCO is selected as a reasonable representative for layered-oxide CAMs, because it consists of only a single transition metal (TM). This simplifies the system and allows for a reliable analysis. Moreover, LCO has been extensively studied, which allows comparison with literature, and is still widely used in small consumer electronics, highlighting its relevance.

Aluminum powder is selected as the reducing agent, because the cathode current collector in LIBs consists of this metal. Inherently, it has low electrochemical potential, making it a strong reducing agent, and Al is an abundant material. The most stable oxidation states of Al are 0 and +III, therefore, metallic Al can be assumed to provide 3 electrons upon reaction and to be oxidized to Al^{3+} without intermediates. The particle size of the starting materials can influence the kinetics in a mechanochemical reaction. Therefore, powder was used in these experiments to exclude the contribution based on the size reduction of Al foil. The overall reaction between LCO and Al is expressed in Eq. 5.2.

Instead of the SPEX shaker mill, which was used in studies by Dolotko et al.[130,131] and Geiß, Dolotko, Indris, et al.[133], a planetary mill was used to process pristine LCO powder together with metallic Al powder. This mill provides greater experimental flexibility and the option to monitor internal pressure

and temperature through a sensor in the lid of the milling vial (Fig. 4.1). Pressure and temperature data were recorded in-situ in intervals of 1-2 s, providing good time-resolution data.

In this section, the process is analyzed by recording the temperature and pressure curves, as well as characterizing samples collected during the process at defined points. The milling experiments were performed at 650 rpm, using 65 g of stainless steel balls (d=6.35 mm) and 2.17 g of powder mixture (BSR=30). The resulting profiles are displayed in Fig. 5.2.

After milling for 1 h without interruption, the reaction and the mill were allowed to cool down to room temperature and a second cycle of 1 h under identical conditions was performed. As a later discussion reveals, the reaction is completed within the first cycle, and therefore, the recorded temperature and pressure curves of the second cycle can serve as baselines. This allows for the separation of pure mechanical contributions from reaction effects on internal temperature and pressure. The respective profiles are plotted in Fig. 5.2 as dashed lines.

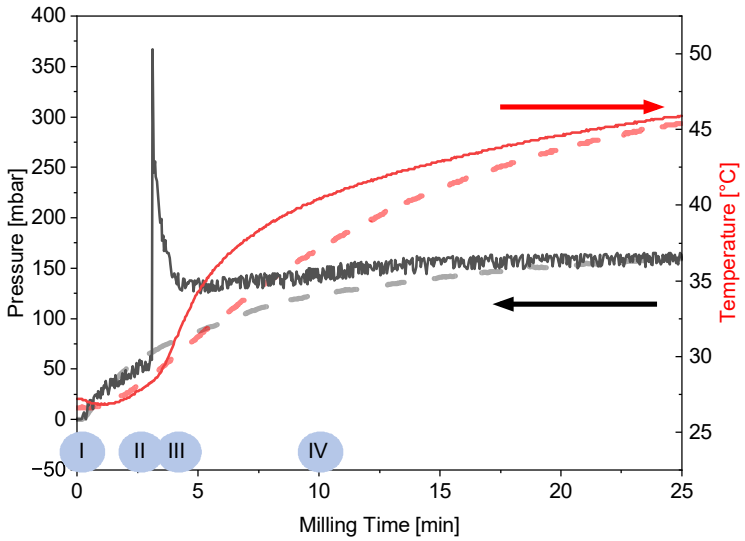


Figure 5.2: Temperature (red) and pressure (black) profiles during the mechanochemical transformation of LCO and Al at 650 rpm with 60 balls (6.35 mm), 2.0 g of powder, LCO/Al = 1.0 and a BSR of 30. Solid lines are experimental values and the dashed lines are recorded from the reference experiment.[175]

A pronounced spike appears after 3.2 min of milling in the pressure curve, even though gas evolution is not expected. Moreover, if there would be any gas evolution, the pressure would not decline that fast, given that the milling vial is tightly sealed. In contrast, the pressure in the baseline experiment slowly increases and eventually reaches the same level as in the initial milling cycle. The spike in pressure can therefore be directly linked to a chemical reaction. A comparison of the temperature curves supports this interpretation. The baseline temperature rises gradually as a result of friction and impacts heating, whereas the initial LCO-Al mixture exhibits a steeper temperature rise immediately after the spike in pressure, indicating the onset of an exothermic reaction.

As the pressure spike is more distinct than the rise in temperature, it is therefore used as a reaction marker. Accordingly, specific time points are selected to collect samples of the reaction and analyze them using optical microscopy, SEM-EDX, XRD, DTA, and static light scattering. The samples were collected according to Table 5.1, and their subsequent analysis is discussed in the following paragraphs to gain deeper insights into the reaction process.

Table 5.1: Samples collected from the mechanochemical reaction of LCO and Al at 650 rpm with 65 g balls (6.35 mm), 2.17 g of powder, LCO/Al =1.0 and a BSR of 30.

Sample	Total time [min]	Description
I	0	Before milling
II	2.7	Shortly before pressure spike
III	3.2	Directly after pressure spike
IV	10	After 10 min of milling
V	60	After 60 min of milling

During sampling, remarkable changes were observed, even in the physical appearance of the samples. Fig. 5.3 shows microscopy images of the powder after successive milling times. The higher magnification of the SEM, equipped with an EDX detector, allows simultaneous observation of morphological changes and elemental distributions.

Before milling, the gray mixture of starting materials in Sample I consists of well-separated particles ranging between 3 and 15 µm with only a limited contact area. The mixed Co-O phase appears to be distinctly different from the Al particles. (Fig. 5.3a-e).

Shortly before the pressure spike, a sample was collected after 2.7 minutes of milling (Sample II). The SEM images of the fine black powder show a significant reduction in the size of individual crystallites, whereas agglomerates of varying sizes are visible. EDX-based elemental mapping indicates intense mixing of all three elements within the agglomerates (Fig. 5.3f-j).

Milling was stopped as soon as the pressure spike was registered, and an inhomogeneous mixture of coarse gray particles and large metallic fragments up to the centimeter scale was observed (Sample III). More optical microscopy images of this sample are provided in Fig. S4.1. The SEM imaging (Fig. 5.3l) distinguishes smooth-surfaced particles with sharp edges from smooth spheres and porous agglomerates. A strong segregation of spherical cobalt phases from the aluminum phase is demonstrated by the elemental maps. (Fig. 5.3m–o).

After continued milling, a fine black powder was obtained again as Sample IV after a total milling time of 10 minutes. In the SEM image, it appears as a collection of amorphous agglomerates in which Co, Al, and O are evenly distributed with some local enrichment in Co (Fig. 5.3p-t). The final sample, taken after 1 h of milling, closely resembles Sample IV, except that the agglomerates appear smaller and the elements are distributed more homogeneously (Fig. 5.3u-y). However, the EDX spectrum showed increasing intensities of iron and chromium peaks as the milling time increased.

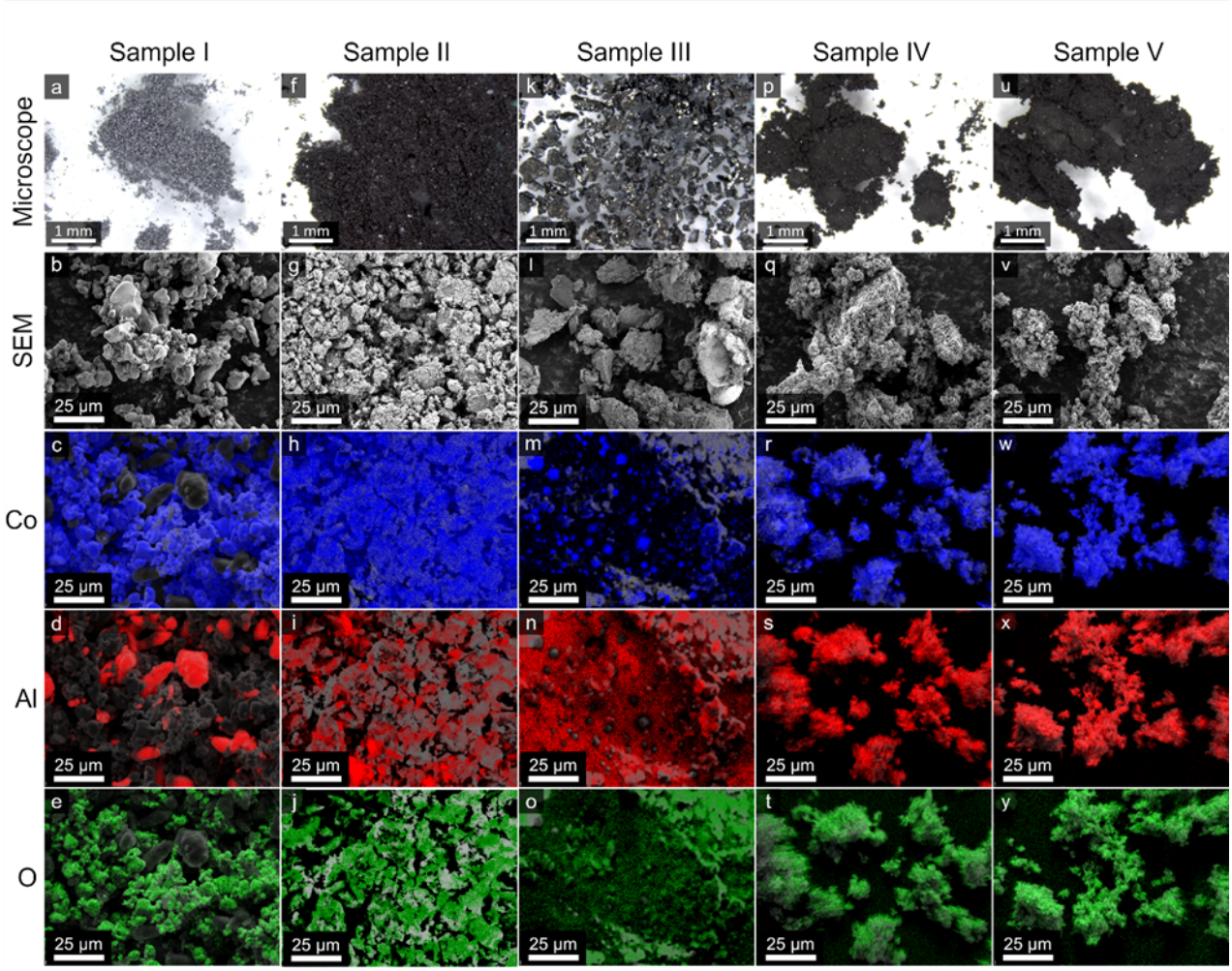


Figure 5.3: Microscopy images and respective EDX images for Co (blue), Al (red) and O (green) of the Samples I-V collected during the mechanochemical reaction between LCO and Al at 650 rpm with 60 balls (6.35 mm), 2.0 g of powder, LCO/Al =1.0 and a BSR of 30 using repeating cycles of 5 min milling and 5 min resting.[175]

These elements are the main components of the milling media, and the rising intensities indicate abrasion (Fig. S3.1).

As described, the micrographs in Fig. 5.3 show pronounced changes in morphology and elemental distribution between Sample II and III, which align with the spike in pressure. To get a clearer picture of the elemental distribution in the agglomerates, both samples were sieved and the fractions <500 µm were embedded in resin, cut and polished to provide a clean cross-section.

The resulting SEM image (Fig. 5.4a) shows a coarse matrix with micron-sized capsules that fractured during polishing, exposing a nanoscale needle-like structure. According to the elemental map in panel b, these capsules are rich in oxygen, which may indicate local oxidation when exposed to air. Furthermore, the Co and O signals continue to overlap, whereas the Al signals appear to be spatially

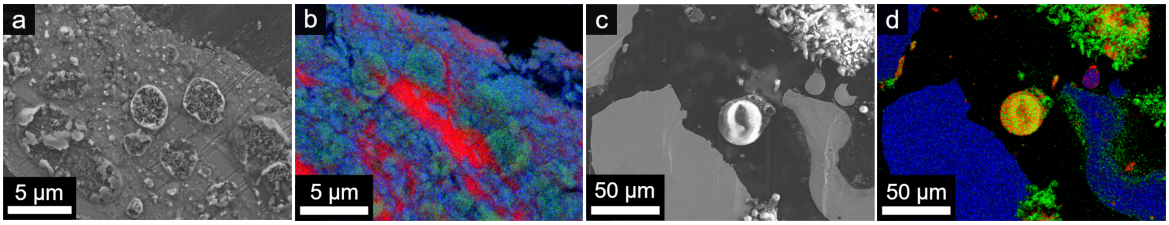


Figure 5.4: SEM and EDX images of cross sections of Sample II (a, b) and Sample III (c, d). Co, Al and O are presented in blue, red and green color respectively.[175]

separated. Despite this separation, the Co-O and the Al phases are mixed on the nanoscale, forming lamellar structures.

The sub-figures 5.4c and d representing the resin of Sample III show considerably larger particles than in Sample II. These particles can be grouped into three categories. A Co-rich phase, which has only weak Al and O contributions, exhibits smooth surfaces with clearly visible grain boundaries, and small spherical voids suggest former inclusions. The second type is an Al-O mixed phase with almost no Co signal. The third phase category are agglomerates that are mixed with all three elements and closely resemble the particles in Sample II.

In Figs. 5.4c and d, some particles show a rough surface with crystalline needles, which were most likely formed by the reaction with humid air. The spherical particles could indicate partial melting during the reaction, suggesting very high local temperatures. The tiny spherical particles are probably the origin of the spherical holes observed in the cobalt phase.

In the microscopy images (Fig. 5.3), strong changes in particle size are observed during the milling process. To quantify this evolution, static light scattering (SLS) was employed with corresponding results displayed in Fig. 5.5. When comparing Sample I (0 min) and Sample II (2.7 min), the particle size distribution is shifted to larger sizes and broadens remarkably, indicating that the primary particles agglomerate. In Sample III, the reaction mixture consists of a coarse powder and large metallic fragments. Prior to SLS analysis, the mixture was sieved and only the fraction $<$500 µm was measured. The graph shows a broad multimodal distribution with the largest volume fraction centered around 400 µm.

This substantial increase in particle size aligns with the observations made through optical microscopy, as depicted in Fig. 5.3k and Fig. S4.1. Nonetheless, the observation of smaller particle sizes in the SEM (Fig. 5.3i) is attributable to artifacts introduced during the sample preparation process. The large particles did not adhere well to the adhesive carbon sample holder and were removed before the SEM measurement. When milling was continued up to 10 min, intense particle size reduction and a broad size distribution can be observed in Sample IV. Further milling then leads to agglomeration of the smallest particles resulting in a narrower and more homogeneous distribution in Sample V (60 min).

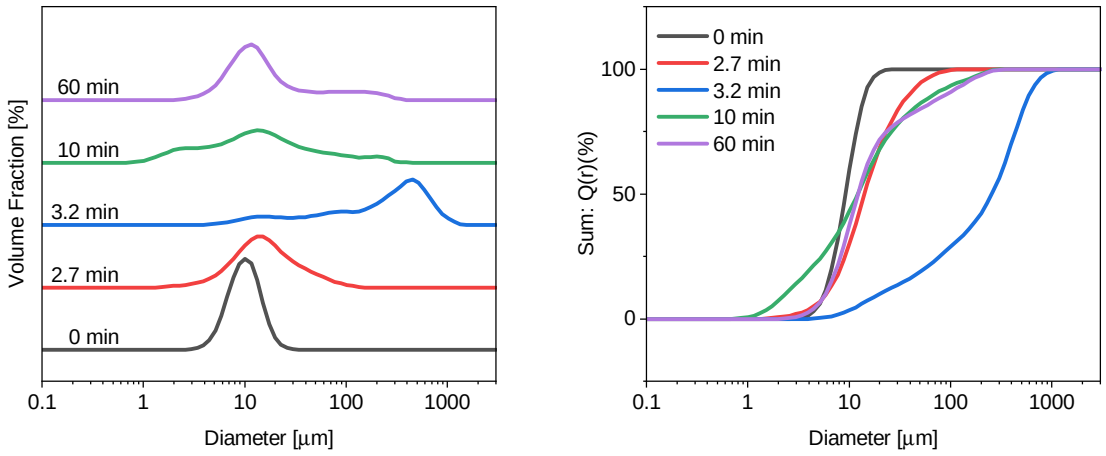


Figure 5.5: Evolution of the particle size distribution during the mechanochemical treatment of LCO with Al at 650 rpm with 60 balls (6.35 mm), 2.0 g of powder, LCO/Al = 1.0 and a BSR of 30.[175]

The evolution of phase composition in all five samples was analyzed by XRD. In the unmilled mixture (Sample I), two distinct crystallographic phases are present, namely LCO and metallic Al (Fig. 5.6, 0 min). After 2.7 min of milling (Sample II), the diffraction pattern does not show new reflections, indicating that little or no chemical reaction has taken place. However, the peaks become much broader reflecting a reduction in crystallite size and an increase in internal strain (Fig. 5.6, 2.7 min).

After 30 s of further milling, i. e. immediately after the spike in pressure, the XRD pattern of Sample III displays remarkable changes. (Fig. 5.6, 3.2 min). New sharp reflections emerge that correspond to tetragonal γ-$LiAlO_2$ in the space group $P4_12_12$ (No. 92, COD:1008166). Elemental cobalt is detected in two polymorphs: a cubic closed-packed structure corresponding to the space group Fm-3m (No. 225, 9008466) and a hexagonal structure described by the space group $P6_3/mmc$ (No. 194, COD:9008492). The cubic cobalt phase is its high temperature modification, which is usually thermodynamically stable above 450 °C. The fact, that this phase is nevertheless present at room temperature can be explained by either the presence of nanocrystalline domains[177] or by a stabilization due to impurity doping[178] and mechanical strain.[179,180] Weak reflections from the starting materials, LCO and Al, are still detectable and several new peaks can be attributed to a cubic Li containing CoO phase ($Li_xCo_{1-x}O$, with $0<x<0.2$)[181] in the space group Fm-3m (No. 225, COD:1541446).

The XRD pattern corresponding to Sample IV (10 min of milling) is dominated by reflections from both polymorphs of Co (Fig. 5.6, 10 min). The previously sharp and intense peaks of γ-$LiAlO_2$ have now become weak and broad, making them difficult to identify and suggesting a reduced crystallinity. The mechanical decomposition of γ-$LiAlO_2$ to amorphous Li_2O and Al_2O_3 should also be considered.[131]

As milling proceeds, the reflections broaden further, and by the time Sample V is measured, only four peaks remain observable (Fig. 5.6, 60 min). The appearance of broad or missing reflections suggests

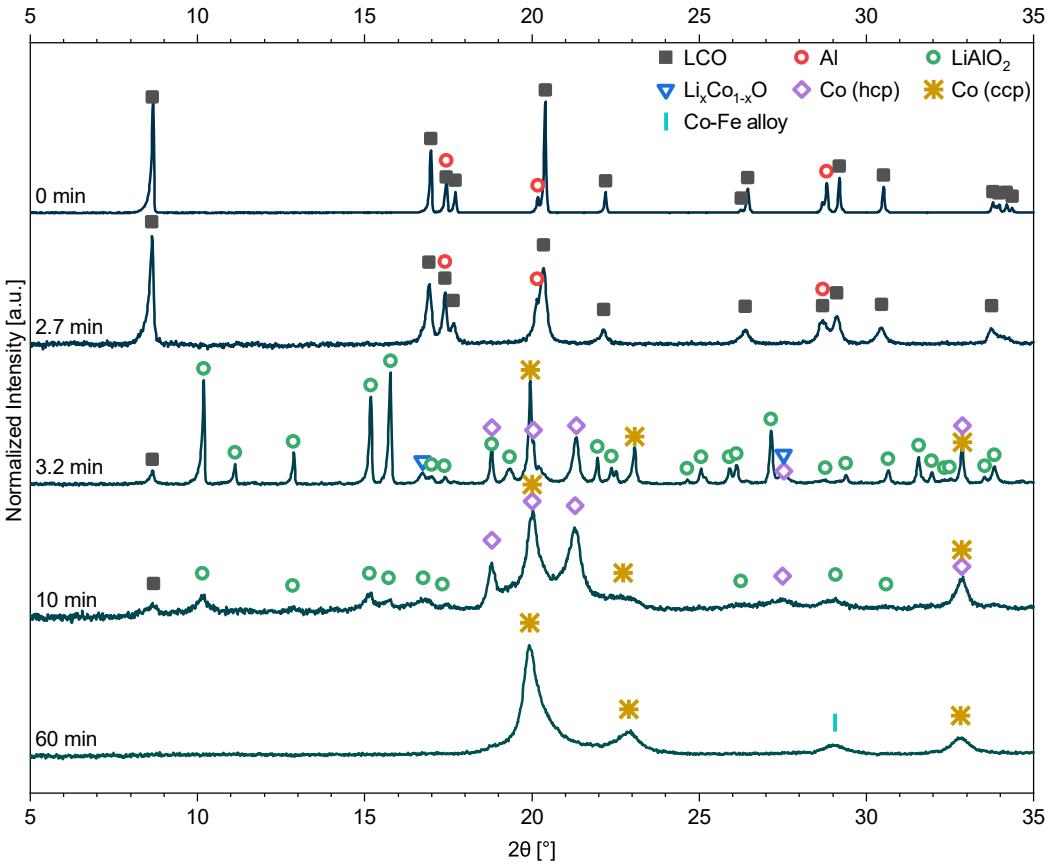


Figure 5.6: Evolution of XRD patterns for the Samples I-V, collected during the mechanochemical reaction between LCO and Al at 650 rpm with 60 balls (6.35 mm), 2.0 g of powder, LCO/Al =1.0 and a BSR of 30 using repeating cycles of 5 min milling and 5 min resting.[175]

that the phases are highly strained and exhibit nanocrystalline domains. Three of these reflections can be assigned to the cubic cobalt phase. The single peak at $2\theta \approx 29.3°$ does not mach well any known phase in the crystallographic open database, that consists of a combination of Li, Co, Al and/or O. A group around Vauloup et al. also studied this reaction and assigned the peak to a cubic Co-Fe alloy in the space group $Im\bar{3}m$ (No. 229, COD:1524167), which would generate reflections near 20.3° and 28.9° of 2θ. The first of these peaks overlaps with the intense Co reflection, resulting in an asymmetry on the high-angle side, while the second one is shifted to lower angles, potentially caused by a different stoichiometric composition. The presence of iron has been already confirmed by EDX (Fig. S3.1) and determined by ICP-OES for 2.7 wt% (Table S1), verifying the possible formation of the Co-Fe alloy.

The larger metallic fragments obtained from Sample III after sieving were cleaned of adherent particles by sonication in water. The XRD pattern of an individual fragment is displayed in Fig. 5.7 and shows cobalt primarily in the hcp structure (No. 194) together with a minor amount of its cubic polymorph (No. 225), while no additional phases are detected. ICP-OES analysis (Table S1) validates

that the fragment contains 97 wt% ± 1.9 wt% Co and only 0.24 % Al. The remaining mass was not quantified by ICP-OES and is presumed to correspond to oxygen or trace iron.

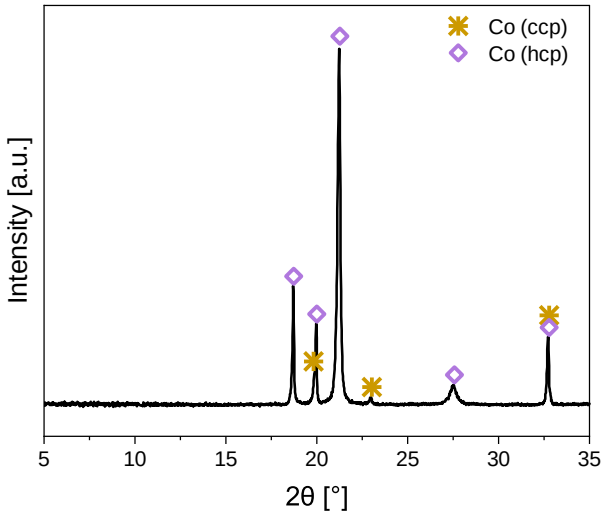


Figure 5.7: XRD pattern of an isolated metallic piece, collected after 3.2 min of milling LCO and Al at 650 rpm using 60 balls (6.35 mm), 2.0 g of powder, LCO/Al =1.0 and a BSR of 30.[175]

The results above clearly demonstrate that all observed transformations proceed according to the MSR mechanism.[136,141,152] During the milling stage before the pressure rise, the starting materials are thoroughly mixed and the crystals are fractured by repeated collisions. According to the diffraction pattern (Fig 5.6), the crystallites decreased in size and experienced strain, while the SEM images and SLS suggest that the primary particles merge into large agglomerates. At this stage, the mixture of starting materials becomes mechanically activated, but no reaction is detected yet (Sample II).

This activation gradually lowers the energy required to initiate the reaction. Eventually, a certain threshold is reached, and a collision with powder trapped between a ball and the wall provides sufficient energy to initiate the highly exothermic reaction. The heat released by the initial reaction provides the thermal energy needed to trigger further reactions in the surrounding powder, creating a self-heating reaction front that propagates throughout the entire volume (Sample III). As a consequence, the temperature in the powder experience a steep rise and reaches high values.

During this brief high-temperature stage, well-crystallized γ-$LiAlO_2$ and metallic cobalt form. However, the reaction front might not reach all the starting material, requiring further milling to complete the reaction. Continued milling breaks down the metallic particles and coarse agglomerates, forming a finely mixed powder. The particle sizes are refined, and crystallites become distorted again. Consequently, hexagonal cobalt transforms into the cubic polymorph, and the overall product mixture appears increasingly amorphous. The amorphization proceeds more rapidly for the brittle γ-$LiAlO_2$ than for the more ductile cobalt (Sample IV and V).

Furthermore, metallic cobalt may also exist as a nanocomposite with a γ-$LiAlO_2$ or Al_2O_3 phase as indicated by the pronounced peak broadening in the XRD (Fig. 5.6) and a homogeneous distribution of Co, Al, and O in the elemental maps (Fig. 5.3v-y).

In thermite-like reactions, the local temperature typically exceeds the melting points of the products, which are 1495 °C and 1625 °C for Co and γ-$LiAlO_2$, respectively,[183,184] and is limited by the lowest boiling point of the product.[135] In a mechanically induced reaction, however, the high thermal conductivity of the stainless-steel milling media promotes a rapid heat dissipation, preventing the bulk temperature from reaching such elevated values. Locally, on the particle scale, the reaction mixture can melt, allowing a phase separation that yields an almost pure metallic cobalt fraction, together with γ-$LiAlO_2$.

Considering that high temperatures are at least locally reached during the reaction, it is also important to rationalize the pressure curves shown in Fig. 5.2. The rapid propagation of the reaction front causes a fast rise in the local temperature and therefore the gas phase to expand. As the milling jar is tightly sealed, the result is a sudden increase in internal pressure. Heat dissipates quickly from the reaction zone into the stainless steel milling media, allowing the powder mixture to return to moderate temperature and pressure. As illustrated in Fig. 4.1, the temperature and pressure sensors in the setup are located in the lid and well protected by a punctured steel plate. Although pressure changes are detected instantaneously with this setup, the heat must be conducted through the milling media to reach the sensor, which dampens and delays the observed temperature rise. It is also worth noting that the pressure sensor transmits data in 1-2 s intervals. This is much longer than the duration of reaction propagation[137] and therefore, the maximum pressure may not be detected and exceeds the detected values. Nevertheless, the onset of the self-propagating behavior, and therefore the length of the activation stage, can be accurately measured by the detection of the pressure spike.

The MSR process involves rapid changes in temperature and pressure, which can pose a risk of failure of the milling vessel or even explosion. For small reaction volumes, the risk may be low, but when a reaction should be scaled up, the setup design could be challenging for proper risk mitigation. The milling vessel has to be highly stable, and at the same time the balls have to be sufficiently accelerated while being energy efficient. In a Simoloyer mill from ZOZ GmbH, Yang performed the synthesis of TiC *via* MSR on a 100 g scale, indicating that this type of mill might be suitable for this purpose.[149]

Furthermore, ceramics such as ZrO_2, which are often used to minimize contamination, are typically sensitive to rapid temperature fluctuations and temperature gradients.[185] This could lead to fracturing or even breaking of the milling media, resulting in higher contamination and operation costs for frequent replacement.

Despite the challenges posed by the MSR mechanism, it is an interesting reaction process that promises a fast and efficient treatment. The detection of the pressure spike provides a direct method

for evaluating how the experimental parameters affect the reaction time and overall mechanism. One of these parameters is the reducing agent itself.

5.2.2 Other reducing agents

The reducing agent obviously should have an effect on the reaction products, but it might be of interest how the choice of the reducing agent affects the MSR process, especially the ignition time, which products are formed and the suitability of the approach for recycling. To explore this question, the mechanochemical reactions of LCO with the elements in the second row of the periodic table between magnesium and sulfur were examined. Although some of these elements may have limited practical relevance, they were included to gain further scientific insight.

In this extra set of milling experiments, 2.17 g of a stoichiometric mixture of the starting materials were placed in a milling vial with 65 g of stainless steel balls (d=6.35 mm) and milled at 650 rpm in the *Pulverisette 7*. The stoichiometry of the respective reaction was planned based on the most stable oxidation states of the corresponding oxides, and on the assumption that LCO is always reduced to the metallic cobalt, which requires three electrons per formula unit. The most stable oxide forms of Mg, Al, Si, and P are assigned oxidation states +II, +III, +IV, and +V, respectively. Sulfur presents a more complex situation because many stable oxides such as SO_2, S_2O_3, and SO_3 exist. Moreover, produced metallic cobalt could react with elemental sulfur to form sulfides. As a compromise, a 1:1 molar ratio of LCO to S was adopted. The proposed reactions are expressed in Eqs. 5.1-5.5. These products might not reflect the real situation and are not based on experimental evidence, but are formulated solely to balance the equation.

$$2\,LiCoO_2 + 3\,Mg \longrightarrow Li_2O + 3\,MgO + 2\,Co \tag{5.1}$$

$$LiCoO_2 + Al \longrightarrow LiAlO_2 + Co \tag{5.2}$$

$$4\,LiCoO_2 + 3\,Si \longrightarrow 2\,Li_2SiO_3 + SiO_2 + Co \tag{5.3}$$

$$5\,LiCoO_2 + 3\,P \longrightarrow Li_5P_3O_{10} + 5\,Co \tag{5.4}$$

$$2\,LiCoO_2 + 2\,S \longrightarrow Li_2SO_4 + Co + CoS \tag{5.5}$$

The previous section of the thesis discusses that the spike in pressure marks the onset of the fast self-propagating reaction stage of the MSR process. This spike has been observed for all reducing agents except sulfur. The ignition times varied between 131 and 488 s (Fig. 5.8), but surprisingly, no obvious trend emerged with respect to the nature of the reducing agent or the reaction enthalpy ΔH_R. The values of ΔH_R were calculated from standard formation enthalpies in the literature ΔH_f^0 (Tab. S15) corresponding to Eqs. 5.1-5.5 and normalized for one mol of LCO.[186–189] However, the ignition times show a slight correlation with the particle sizes of commercial reducing agents (Fig. 5.8).

This implies that the activation is based significantly on particle size refinement and intense mixing to ensure a high contact area between the reactants.

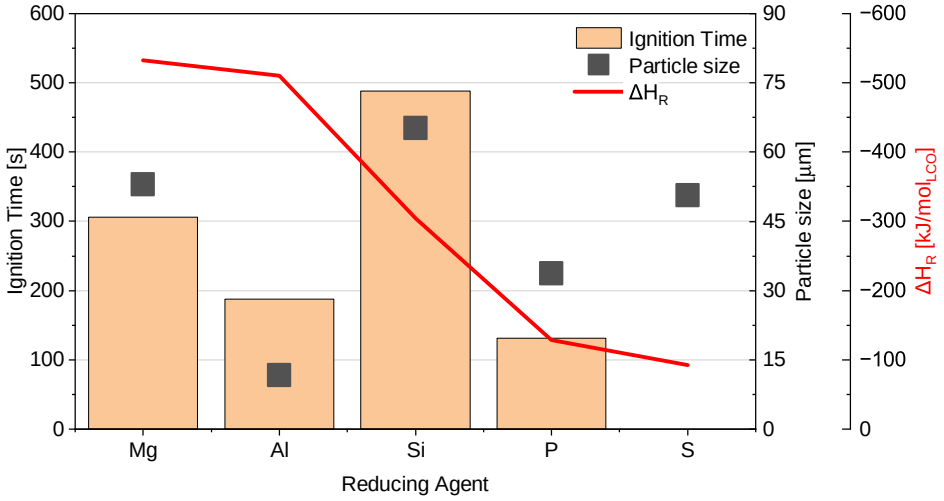


Figure 5.8: Ignition times of the MSR reaction of $LiCoO_2$ with different reducing agents. About 2.17 g of powder mixture was milled with 65 g balls (6.35 mm) at 650 rpm.

Phase identification using X-ray diffraction is performed to identify which products were formed during the mechanochemical reaction. During the self-propagating reaction stage, most of the starting materials are consumed, and crystalline products are formed. Because phases show the highest crystallinity immediately after the self-propagating stage, milling was stopped as soon as the pressure spike was detected, and a sample was collected. The corresponding XRD patterns are displayed in Fig. 5.9 and were used for phase identification.

The XRD patterns of the reaction employing Mg shows the formation of metallic cobalt in the hexagonal and cubic structures, as well as MgO. Reflections of $Li_xCo_{1-x}O$ overlap with the MgO reflection, and therefore, no conclusion can be drawn about its presence. Even reflections of Li_2O are visible, which is in accordance with Eq. 5.1. The Al-mediated reaction was already discussed in the previous section, and yields metallic cobalt in both polymorphs, alongside the formation of γ-$LiAlO_2$ instead of MgO and Li_2O. Weak reflections corresponding to $Li_xCo_{1-x}O$ indicate its presence in a small fraction.

When Si is used as the reducing agent, LCO is reduced to metallic cobalt in the cubic and hexagonal structure. In contrast to the former elements, intense peaks corresponding to $Li_xCo_{1-x}O$ are visible. Furthermore, Li, Si, and O form a mixture of Li_2SiO_3 and Li_4SiO_4, resulting in a complex diffraction pattern. Cobalt silicide (COD: 1008148) could also be formed as a minor fraction, but its distinct identification was not possible, as the reflections overlap with others.

The reaction of LCO with P also results in a complex diffraction pattern after the MSR. In addition to residual LCO and formed metallic Co in the cubic structure, CoO and Co_2P can be identified, while no reflections of hexagonal metallic Co are visible. Unassigned reflections could be associated with

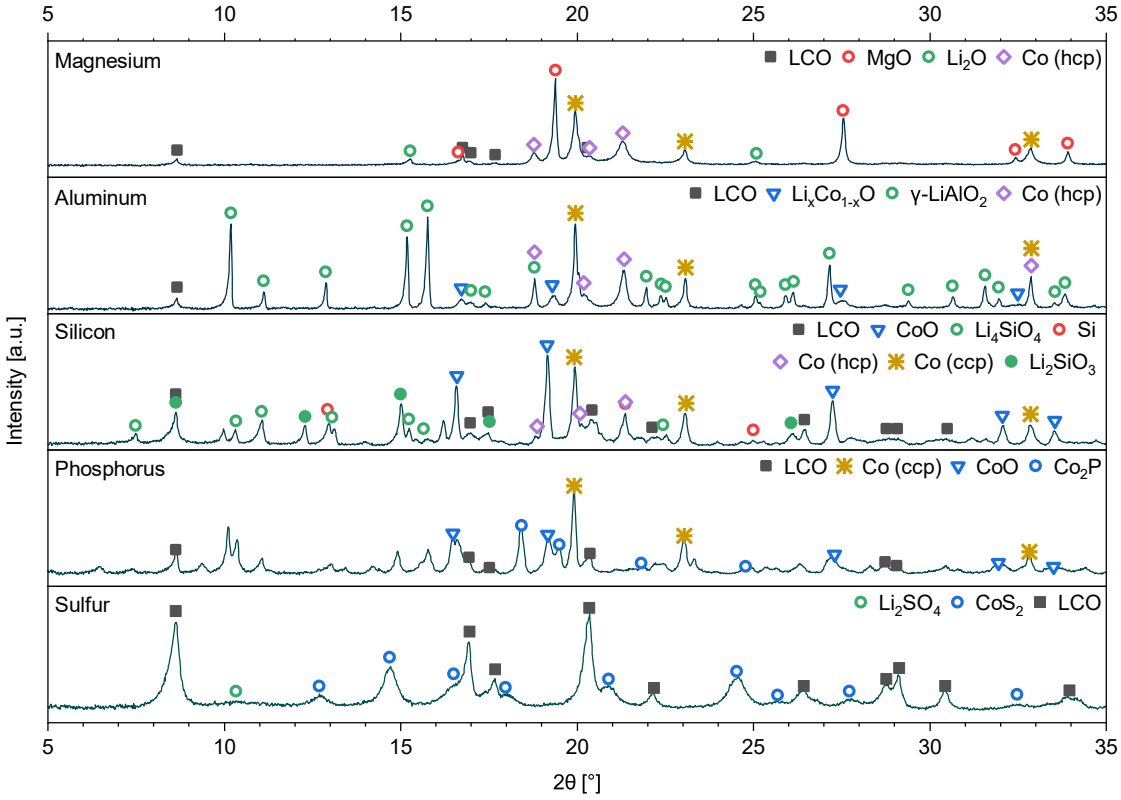


Figure 5.9: XRD pattern of powder after the mechanochemical reactions of LCO with different reducing agents. Samples of reactions employing Mg, Al, Si and P were collected after a pressure spike was detected and the reaction with S was sampled after 2 h of milling. About 2.17 g of mixture was milled with 65 g steel balls at 650 rpm.

lithium phosphates, but the peak positions do not match well. The reason could be the deformation of the lattice by mechanical impact or the condensation of phosphate groups into polymeric chains. For these compounds, no reference data have been found.

When LCO was milled with sulfur, the XRD pattern of a sample collected after 1 h of milling shows no evolution of new phases. After milling the mixture for one more hour, the recorded diffraction pattern still shows intense LCO reflections (Fig. 5.8), but it also clearly displays the formation of CoS_2. Additionally, the formation of Li_2SO_4 can be suggested, but the corresponding reflections are too weak and broad for a reliable identification. It seems that a reaction between S and LCO can be induced by mechanical force, but the reaction does not proceed *via* a MSR mechanism and exhibits slow reaction kinetics.

One of the main advantages of the mechanochemical recycling approach is the selective lithium extraction prior to any further potential hydrometallurgical treatment. Accordingly, aqueous leaching was tested with the powders obtained after the mechanochemical reaction of LCO with the elements of the second period (Mg - S). Directly after the initiation of the self-propagating reaction, residual LCO is still detectable by XRD (Fig. 5.8). Therefore, the reactions were milled for 1 h, except for the sulfur-based reaction, which was milled for 2 h before leaching.

After milling, DI water (≈50 mL) was added directly to the reaction mixture (2.17 g) in the milling vial. None of the experiments showed a vigorous reaction with water, and no gas formation or rise in temperature was observed. The suspension was then gently milled at 350 rpm for 5 min and filtered once. The collected filtrates were tested for Li concentration using a Li-selective electrode and Y_{Li} was calculated (Eqs. 4.1-4.3). The filtrates were subsequently evaporated to dryness, and the solid residues were analyzed by XRD. The extraction yields and XRD patterns are presented in Fig. 5.10.

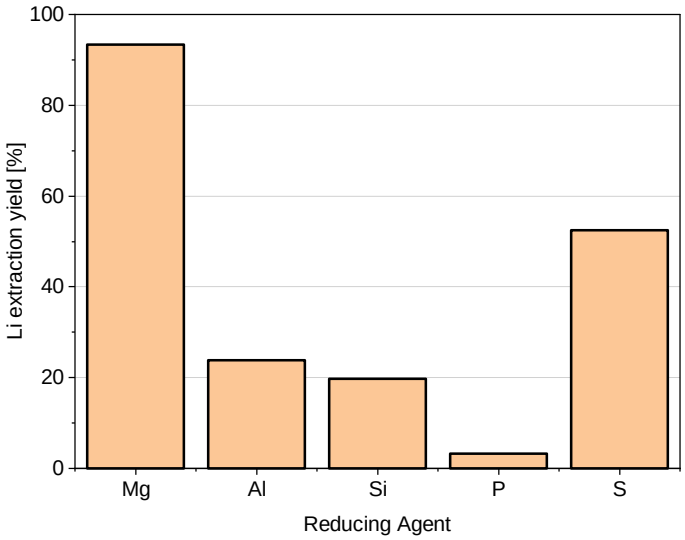


Figure 5.10: Lithium extraction yields of LCO milled with various reductants.

When LCO is reduced with Mg, very high Li extraction yields of 93 % are achieved. This high recovery is attributed to the formation of highly soluble Li_2O, which is the only Li-containing phase generated during the reaction. The XRD of the dried soluble fraction reveals the presence of phase pure Li_2CO_3 (Fig. 5.11). This confirms the presence of Li_2O as the only formed soluble Li salt, since it reacts with water during leaching to form LiOH, which in turn reacts with CO_2 from the air during drying, producing Li_2CO_3.

The Al-mediated reaction has been reported in detail in previous literature.[131] The γ-$LiAlO_2$ formed during the MSR becomes amorphous or decomposes with further milling, allowing part of the Li salt to dissolve and reaching a Y_{Li} of 24 %. The XRD of the dried soluble fraction suggests a mixture of Li_2CO_3 and LACHH.

When Si is used as the reducing agent, only 20 % of Li is extracted under the tested conditions. The XRD identifies the recovered salt after drying as barely crystalline Li_2CO_3. The XRD pattern of the insoluble residue is virtually identical to the pattern after milling (Fig. S1.1). Combined with the presence of Li_2CO_3 in the soluble fraction, it can be suggested that during milling some Li_2O is formed and subsequently extracted, but the major fraction is bound as insoluble silicates.

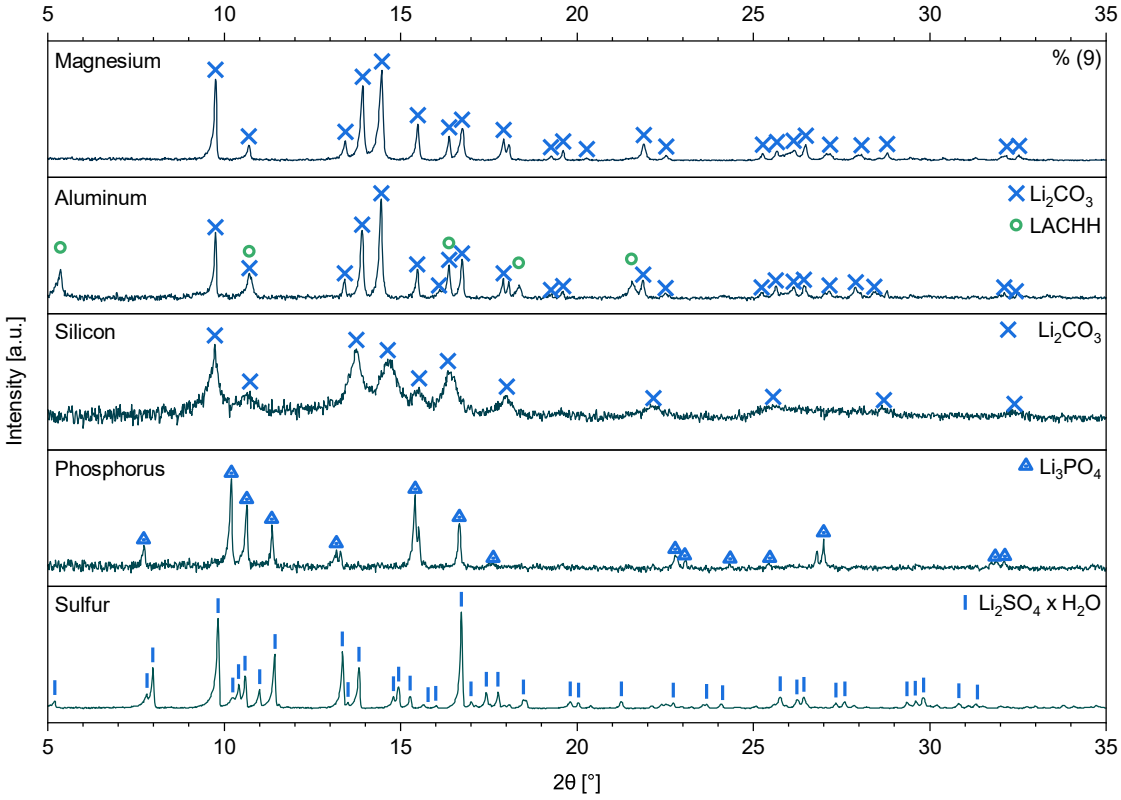


Figure 5.11: XRD patterns of the dried soluble fraction obtained from leaching the milled mixture of LCO with the respective reducing agent.

The Li extraction yield when P is employed as the reducing agent drops to 3 %. Similarly to the Si-based reaction, the XRD pattern of the as-milled powder and of the solid residue after leaching are almost identical (Fig. S1.1, showing, among others, the presence of Li_3PO_4. This phosphate has only a limited solubility of 350 mg/L,[190] which is roughly consistent with the measured Li concentration in the filter liquor (380 mg/L).

The extraction after the reaction with elemental sulfur shows an extraction yield of 52 %, although not all LCO was decomposed during the mechanochemical reaction. The XRD of the dried soluble fraction shows the formation of $Li_2SO_4 \cdot 2\,H_2O$ (Fig. 5.11), indicating that elemental sulfur is oxidized to sulfate during mechanochemical processing. If the decomposition of LCO would be completed, higher extraction yields are expected. Sulfur is also very cheap as it is produced in large quantities, for instance, in the desulfurization of crude oil and natural gas. Accordingly, the combination of high Li recovery and the low-cost and abundance of sulfur can make this approach an attractive process for LIB recycling. Despite the incomplete reaction, the extraction of Li_2SO_4 seemed promising for further investigations. The reaction mechanism and products of the sulfur-based reaction differ much from the MSR process of the other reducing agents. Therefore, more detailed results and discussions are provided in section 5.2.5.

Based on the XRD results and low Y_{Li}, Si and P are unsuitable reducing agents for the process because the formation of lithium silicates and lithium phosphates prevents efficient aqueous Li extraction. The reduction with Mg offers excellent Li extraction yields and high purity of recovered Li_2CO_3, but the metal is relatively expensive. In the Al-based system, the formation of γ-$LiAlO_2$ and LACHH results in a low Y_{Li}. However, Li extraction yields of more than 70 % have been reported with an adapted leaching procedure,[131] proving the high potential of aluminum for this process. Moreover, Al is already present in batteries as the current collector, offering good cost effectiveness. In consequence, Al is further considered to be a suitable candidate for the mechanochemical reduction of CAMs with the perspective for selective lithium extraction.

5.2.3 The effect of process parameters

This section contains results that have been published in *"Mechanistic Investigation of the Mechanochemical Reduction of $LiCoO_2$ with Al in the Context of Lithium-Ion Battery Recycling"*,[175] and expanded with additional findings.

The investigation of milling parameters is essential for mechanochemical reactions, as it provides valuable information about the kinetics and the energy efficiency. Moreover, the results could allow for tuning the reaction products or predicting the outcome for other reaction conditions.[108,147] The reactions of LCO with Al and Mg both proceed *via* the MSR mechanism. The characteristic pressure spike observed during milling marks the end of the activation stage and the initiation of the fast, self-propagating reaction. The elapsed time until the onset of the pressure spike is observed is defined as the ignition time (t_{ig}), which is highly sensitive to the exact milling conditions.[153] Consequently, t_{ig} is used to systematically investigate the influence of four milling parameters: rotation speed (ν_R), ball size (d_b), ball-to-sample mass ratio (BSR), and the total filling of the milling vial. The results of the individual experiments, together with the values derived from them, are summarized in the tables provided in the Appendix.

Rotation speed ν_R and ball size d_b:
During high-energy ball-milling, kinetic energy is transferred from the balls to the powder by numerous collisions. Because the balls do not always follow the same trajectory, the collision velocities and transferred energies follow a distribution. Therefore, multiple experiments were performed for each rotation speed, to achieve some statistical validation. In this study, balls with diameters of 3 mm, 6.35 mm and 12.7 mm were investigated, and are referred to as small (S), medium (M) and large (L) balls, respectively. The milling vial was loaded with 2.17 g of reaction mixture, 65 g of the respective balls and milling was performed at rotation speeds between 200 and 1000 rpm.

The dependency of t_{ig} on ν_R in the Al-mediated reduction of LCO is displayed in Fig. S2.1a-c. Identical experiments show only a minor spread of t_{ig} and often appear as a single entry, reflecting

good reproducibility. For all three ball sizes an exponential correlation is observed, which can be described by the following equation:

$$t_{ig} = a \cdot \nu_R^b \tag{5.6}$$

For a better comparison, these exponential fits are shown in Fig. 5.12a without the individual t_{ig} values. The fits suggest a faster reaction for larger balls, especially at lower rotation speeds. It is worth noting that for the small balls no MSR was observed at 350 rpm and below, which will be discussed in more detail below.

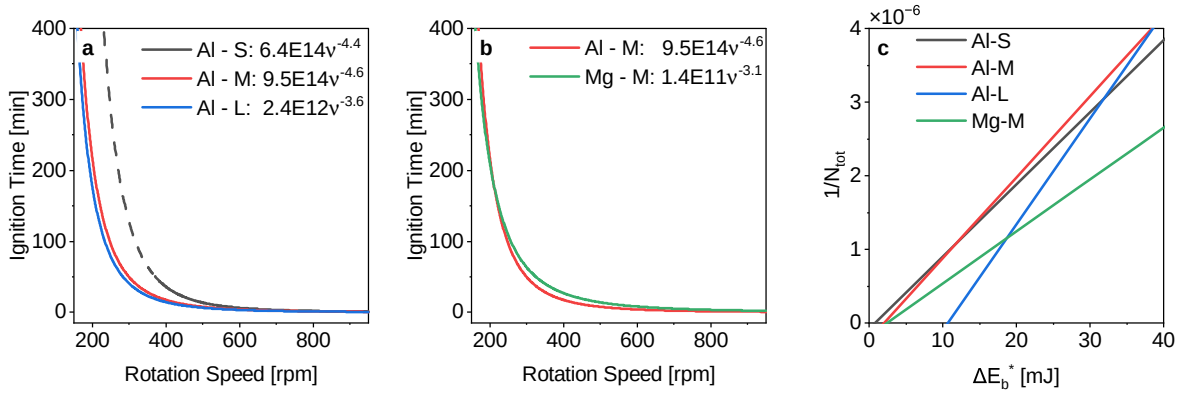


Figure 5.12: Influence of the rotation speed and the ball size on the mechanochemical reduction of LCO mixed with stoichiometric amounts of Al or Mg using 65 g steel balls , 2.17 g of powder and a BSR of 30. a) Comparison of various ball sizes (S = 3.0 mm, M = 6.35 mm, L = 12.7 mm) regarding ignition time in the LCO-Al mixture, b) Comparison between Al and Mg as the reductant using 6.35 mm balls. c) Representation of the reciprocal collision number $1/N_{tot}$ vs. the impact energy ΔE_b^* to determine the energy threshold E_0.

In MSR reactions, the kinetic energy that is transferred to the powder (milling dose, D) during the activation stage can be assumed to be constant under optimal conditions.[114] The collision model which was derived by Burgio et al.[106] and introduced in section 1.5.4 can help to estimate the transferred energy during milling in the *Pulverisette 7*. A closer look at the model shows the correlation $D_{ig} \propto \nu_R^3 \cdot t_{ig}$ (Eq. 1.8, 1.9 and 1.11). Therefore, the correlation $t_{ig} \propto \nu_R^{-3}$ can be assumed for purely inelastic collisions, where ΔE_b^* is completely transferred to the powder. The subscript "ig" indicates that only the time of the activation stage is considered, and ΔE_b^* is the energy released from one milling ball in a collision. However, not all of this energy is typically transferred to the powder, and some of it is released as heat. Therefore, the calculated values can be used as an estimate of the maximum energy transferred to the powder in a single collision.[112]

The best fits in 5.12a yield exponents ranging from -3.6 to -4.6 $\pm$ 1.0. The trend suggests that smaller balls exhibit more negative exponents, indicating that a larger total energy input is required to initiate a reaction when individual impact energies are low. Moreover, the deviation of t_{ig} between identical experiments increases for smaller ball sizes at low rotation speeds. Both observations could

be attributed to either an increase in the elastic component of a collision, the adoption of less efficient motion patterns by the balls,[147] or a higher contribution of friction at low rotation speeds.[191]

In Fig. 5.12, the dependence of ν_R on t_{ig} is compared between the mechanochemical reduction of LCO by Al and by Mg. Between 350 and 950 rpm, the activation stage of the Mg-based reduction is longer than that of the Al-based reduction, while at 200 rpm, the Mg system initiates the MSR reaction much faster. Moreover, the best t_{ig}-fit for the LCO - Mg reaction shows an exponent of -3.1, which is close to the theoretical value of -3.

The kinematic model provides a separate estimation of the number of collisions (N_{tot}, Eq. 1.10) and of ΔE_b^* (Eq. 1.8). Assuming that the milling dose D_{ig} during the activation stage is independent of the milling parameters and therefore constant, rearrangement of Eq. 1.11 yields an expected linear relationship:[153]

$$\frac{1}{N_{tot}} = \frac{\Delta E_b^*}{D_{ig} m_p} \tag{5.7}$$

Such a linear relationship is confirmed with the data obtained by the variation of ν_R in Fig. S2.2. The linear fits are plotted together in Fig 5.12c for better comparison. The intercept of the fits with the abscissa provides an estimate of the energy threshold E_0 that an impact must supply to induce the mechanical activation in the powder and consequently trigger the self-propagating reaction.[146] This energy threshold increases with ball size, ranging from 0.8 mJ for 3 mm to 2 mJ for 6.35 mm and 11 mJ for 12.7 mm balls.

At the beginning of the section it is mentioned that, for the 3 mm balls and $\nu_R = 350$ rpm, no spike in pressure or rise in temperature were observed during milling of LCO with Al (Fig. S2.3). Therefore, the self-propagating stage is not initiated. Nevertheless, reflections of metallic cobalt are visible in the XRD pattern after 32 h of milling (Fig. S1.2), which proves the conversion of LCO in a slow solid-state reaction.

For the small balls ΔE_b^* is about 0.8 mJ at 350 rpm, which matches the determined E_0. When experimental errors and limitations of the model are considered, ΔE_b^* might be even slightly lower than E_0. This implies that the milling energy is insufficient to promote the structural changes that are required to initiate the self-propagating stage of the MSR mechanism.

The onset of the self-propagating reaction requires sufficient reaction heat to be released to ignite the surrounding powder. At low impact energies, one could argue that Al particles experience only limited deformation. Consequently, the mixing between LCO and Al is less efficient on the micro-scale. Moreover, Al particles are covered with a surficial Al_2O_3 layer. At high impact energies, Al deformation results in cracking of this layer and the exposition of fresh metal surfaces, whereas at low impact energies, fresh metal surfaces may be generated only by superficial scratching. Therefore, a reaction

can occur only on the small fraction of the scratched particle surface, producing insufficient heat in the volume to induce a reaction in the surrounding material.

The dependency of E_0 on the ball size most probably reflects the amount of powder affected within a single collision. This fraction of the powder has to be located on the surface of the ball and the wall. The surface of a ball scales with the square of the balls radius. Consequently, E_0 should be divided by r_B^2 for comparison, which results in comparable values for all three ball sizes with an average of $\frac{E_0}{r_B^2} = 0.27 \pm 0.06$ mJ/mm^2 (Table 5.2).

Table 5.2: Summery of calculated parameters, obtained by variation of the rotation speed in the mechanochemical reduction of LCO

	b	E_0 [mJ]	$\frac{E_0}{r_B^2}$ [mJ/mm^2]	D_{ig}^* [kJ/g]
Al - S	-4.4	0.8	0.36	4.8
Al - M	-4.6	2.0	0.20	4.1
Al - L	-3.7	10.7	0.27	3.3
Mg - M	-3.1	2.4	0.23	7.0

b: exponential parameter of Eq. 5.6

The efficiency of the milling process can be estimated by calculating the milling dose that the powder receives during the activation stage according to Eq. 1.11. For the three ball sizes in the LCO-Al reaction and in the LCO-Mg reaction D_{ig} is not constant, but decreases exponentially with increasing impact energy, suggesting a lower efficiency at low ΔE_b^* (Fig. 5.13). Instead of the specific milling dose D_{ig} the specific activation dose D_{ig}^* can be calculated after Eq. 1.12, which considers the energy threshold E_0.[109,146,153]

In contrast to D_{ig}, D_{ig}^* is nearly constant in the experimental range for all four reactions. This behavior is consistent with observations of other MSR systems in literature.[109,146,153] Moreover, D_{ig}^* decreases with the ball size, from 4.8 kJ/g for 3 mm to 3.3 kJ/g for 12.7 mm balls, respectively (Fig. 5.13). Remarkably, D_{ig}^* is significantly larger when Mg is employed as the reducing agent.

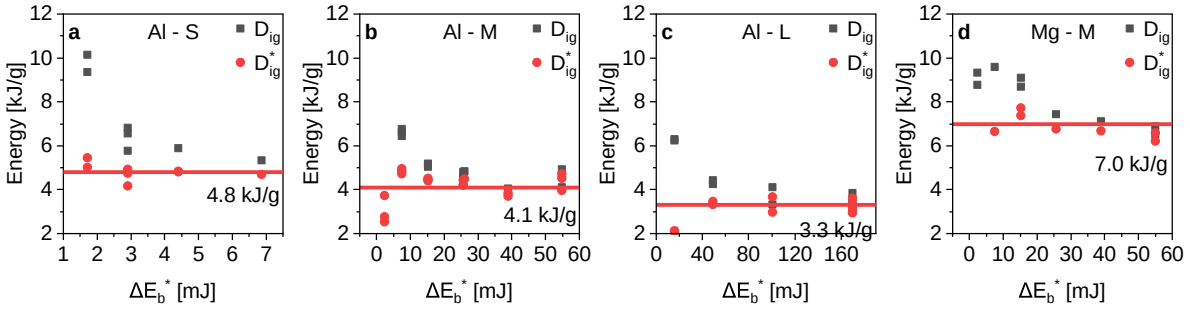


Figure 5.13: Comparison of the specific milling dose D_{ig} and the specific activation dose D_{ig}^* for the ball sizes a) 3 mm, b) 6.35 mm, and c) 12.7 mm in the mechanochemical reaction between LCO and Al, and d) for LCO-Mg using the 6.35 mm balls.

This suggests that more mechanical energy has to be transferred to the powder for a sufficient activation, although Mg is considered the more reactive metal. The larger particle size of the Mg powder (≈53 µm) compared to Al (≈11 µm) is most likely the major reason, as additional energy is consumed for particle size refinement. However, other properties of the metal powders, such as hardness or bulk modulus, could also have an influence.

In the literature, E_0 is considered as the activation energy threshold, which must be exceeded by a single impact to generate structural or chemical changes in the powder. However, if E_0 should be an activation energy, it is unclear why D_{ig} increases as the impact energy decreases. It would be more intuitive to expect that no reaction is induced when $\Delta E_b^* < E_0$ and that D_{ig} remains constant when $\Delta E_b^* > E_0$. Instead, the specific activation energy dose D_{ig}^* was introduced to achieve a constant milling dose.[109,146] However, a satisfying mechanistic explanation for this subtraction was not found.

Gotor et al. hinted at an apparent elasticity of the impact that changes with the collision energy. However, the dependency of D_{ig} on the rotation speed was explained by a transition of the ball trajectories from impact to friction mode.[108] Friction is explicitly neglected in the collision model, leading to strong deviation.

Another hypothesis focuses on the (in-)elasticity of impacts.[97,98] In each collision, the powder trapped between the ball and the wall is compressed, and if the impact energy exceeds E_0, structural or chemical changes occur. The powder may also undergo reversible elastic compression during each impact, which absorbs a fraction of the impact energy but does not accumulate energy over successive collisions. Instead, relaxation proceeds through thermal pathways, leading to thermal energy dissipation that resembles friction. In this context, the portion of energy consumed by elastic compression can be represented by E_0. Therefore, it is reasonable to subtract E_0 from ΔE_b^* of each collision, as the difference represents the mechanical energy that can be stored and accumulated in the powder. Accordingly, the MSR requires a constant amount of accumulated energy to be induced, which is D_{ig}^*.

Under the assumptions of Burgios collision model, which neglects friction and ball-to-ball interactions, the calculated values for E_0 and D_{ig} are properties of the reaction mixture but independent of the mill. Consequently, they can be used to compare the efficiency of various mills for a given reaction, to estimate the time of the activation stage under different conditions, or even between other milling types.[107]

For instance, the MSR reaction of LCO and Al using 6.35 mm steel balls can be induced, if the impact energy exceeds $E_0 = 2$ mJ, and such a steel ball reaches this kinetic energy at a velocity of 2 m/s. In drum mills, the motion can be approximated as a series of free-fall events under gravitational acceleration (g) and a free fall height of 55 % of the drum diameter.[192] With these assumptions, the minimum drum diameter (d_{drum}) necessary to achieve the same velocity (v_b) as in the planetary mill can be calculated from Eq. 5.8.

$$d_{drum} = \frac{v_b^2}{2g} \cdot \frac{1}{0.55} \tag{5.8}$$

Accordingly, a ball velocity of 2 m/s can be reached with a drum diameter of about 0.3 m. However, a comparison with a rotation speed of 200 rpm may be more appropriate, since the reaction was actually initiated under this condition. At this rotation speed, the ball velocity at impact is 2.4 m/s, which corresponds to a drum diameter of 0.5 m.

Ball-to-sample mass ratio (BSR):
The effect of the BSR on the t_{ig} and D_{ig} was examined for three different ball sizes (S, M, L) ranging from 3 mm to 12.7 mm in diameter. Because the kinetic energy of the balls is evenly distributed among the total powder, the BSR is directly related to the milling intensity. The ratio can be adjusted either by using different numbers of balls, by varying the milling media with different densities or by changing the amount of powder.[147]

In this subsection, the powder mass was adjusted while all other parameters were kept constant, as it provides the greatest flexibility. The milling vial was loaded with 65 g of balls and 1.3 - 8.13 g of the reaction mixture to set the BSR between 50 and 8 (1/BSR = 0.02 - 0.12). The ignition time is known to be highly sensitive towards the exact reaction condition, and therefore each experiment was conducted at least three times to obtain means and standard deviations (Tables S6 - S8). The results are plotted in Fig. 5.14a and show only minor deviations of t_{ig} between identical experiments using 6.35 and 12.7 mm balls, while the small balls exhibit a greater spread of t_{ig}.

For large and medium balls, t_{ig} increases linearly with 1/BSR. This is expected as the milling power must be shared among a larger powder mass. Consequently, a longer milling time is required to deliver the same specific milling dose. With small balls, the linear increasing trend is observed only up to 1/BSR $\approx$ 0.07 (BSR=15) and then t_{ig} reaches a plateau. This deviation could suggest changes in the ball dynamics, or a shift in the ratio of collisional and frictional forces.

Same as before, D_{ig} can be calculated from the measured ignition times with Eq. 1.11 and used to compare the milling efficiency. In summary, under constant impact energy conditions, the milling dose the powder receives prior to the ignition (D_{ig}), should remain constant. According to Fig. 5.14b, this holds true for the 6.35 mm balls with a $D_{ig} \approx$ 4.8 kJ/g.

For large balls, D_{ig} initially decreases as 1/BSR increases, but soon stabilizes around 2.7 kJ/g. At low 1/BSR, only a fraction of E_b^* delivered by the balls can be absorbed by the powder, while a large portion dissipates as heat and does not contribute to the mechanical activation. As the 1/BSR rises, more powder becomes trapped in each collision, allowing a larger fraction of the kinetic energy to accumulate in the powder instead of being lost as heat. Accordingly, less energy is required in total, and the milling becomes more efficient.

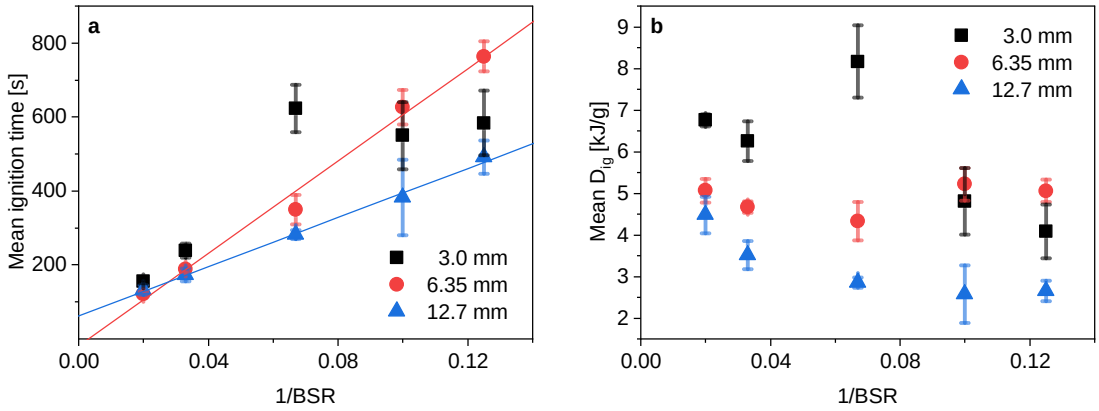


Figure 5.14: Impact of the 1/BSR and ball size on a) the ignition time and b) the specific energy dose of the mechanochemical reaction between LCO and Al using 65 g of balls, LCO/Al = 1.0 and a rotation speed of 650 with repeating cycles of 5 min milling and 5 min resting.[175]

For small balls, D_{ig} exhibits a pronounced maximum at a 1/BSR = 0.067 (Fig. 5.14), indicating a particular inefficient milling condition. Despite this maximum, D_{ig} generally decreases with increasing 1/BSR and at high 1/BSR, the small balls show a D_{ig} similar to the medium-sized balls. The impact energy of a single collision between a small ball and the wall (2.9 mJ) is only slightly higher than E_0 (0.8 mJ). Similarly to the low rotation speed for medium-sized balls, the activation may not be efficient. With an increase in 1/BSR, the already low impact energy is distributed over an increasing amount of powder, and t_{ig} increases disproportionately, leading to a decreasing efficiency.

Nevertheless, this does not provide a satisfactory explanation for the observed plateau in Fig. 5.14a. A plausible factor is the high surface-to-volume ratio of small balls. During milling, the powder attaches to the milling media (balls and wall) and covers them. At low 1/BSR, most of the powder is attached to the balls and because the impact energy is low, the exchange between attached and unattached powder is limited. This could result in inhomogeneous activation and less predictable values of t_{ig}. Moreover, small balls in large numbers generate more friction than a small number of large balls.[85] Since the Burgios kinetic collision model neglects any frictional contribution, the calculated energy input might not be accurate.

Aside from the calculations, the BSR strongly influences the morphology of the reaction products directly after the MSR. At high BSR, metallic Co appears as small needle-shaped structures, whereas at low BSR, it forms large metallic sheets (Fig. 5.15). The higher internal temperature rise associated with a lower BSR causes a larger fraction of cobalt to exceed its melting temperature. Because of centrifugal forces, the inner surface of the milling vial is covered with the LCO-Al mixture. Upon reaction, a layer of molten Co forms at the wall, where it solidifies into large pieces when the reaction cools down due to the rapid heat dissipation through the milling vial.

The large Co pieces result in a relatively easy separation of Co by sieving. However, these metallic pieces can be tightly attached to the walls of the vial or form a layer around the milling balls, especially

when small balls are used (Fig. 5.15c), which contradicts efficient Co recovery. Nevertheless, in an experiment using 65 g 6.35 mm balls and a BSR of 8, at $\nu_R = 650$ rpm allowed the recovery of 1.4 g metallic Co by sieving (500 µm mesh), which corresponds to roughly 50 % of the total Co. Residual Co was either attached to the milling media, or was too small and passed through the sieve.

Decreasing the BSR further could improve the Co recovery as even larger metallic pieces are formed. However, this would cause higher internal temperatures, which is expected to reflect in a stronger spike in the pressure profile. This can cause a safety risk and was therefore not further investigated, but could be explored with more specialized equipment.



Figure 5.15: Photographs of metallic pieces, obtained after the MSR between LCO and Al at BSR = 8.

Total filling of the vial:

The last process parameter that has been investigated is the total filling of the milling vial. Its effect on t_{ig} was tested by milling LCO with an equimolecular amount of Al at a constant BSR of 30 using 32, 64, and 128 stainless steel balls (d=6.35 mm). For comparison, the milling vial would be completely filled with 314 balls. Similarly to the investigation of rotation speeds at the beginning of the section, experiments were performed at rotation speeds between 350 and 950 rpm.

The measured ignition times are presented in Fig. 5.16 alongside the calculated values of N_{tot} and D_{ig} based on Burgios collision model (Tab S4, S9, and S10). At first glance, the ignition times appear similar for different fillings. However, a closer look at Fig. 5.16a shows that a high filling results in slower activation at low rotation speed but faster activation at high rotation speeds. For instance, at 950 rpm the increase in pressure, indicating the end of the activation stage, is observed already after 35 s when 128 balls are used, while roughly 60 s were necessary with fewer balls.

The effect of total filling becomes even more pronounced when the reciprocal of N_{tot} is plotted against ΔE_b^*. Expectedly, more balls result in more collisions, and therefore, $1/N_{tot}$ is normalized by multiplication with the number of balls. This would represent the number of collisions experienced by a single ball during the activation stage. For 32 and 64 of balls, an almost fully overlapping linear corelation emerges, while for 128 balls, the overlap is true only for $\Delta E_b^* < 28$ mJ (Fig. 5.16b). The linear extrapolations of all three datasets intercept the x-axis around 2 mJ, indicating that E_0 is not affected by the filling degree. At higher ΔE_b^*, there is a strong divergence from a linear correlation for experiments with a high filling degree. This is reflected in Fig. 5.16c in a low specific activation milling dose.

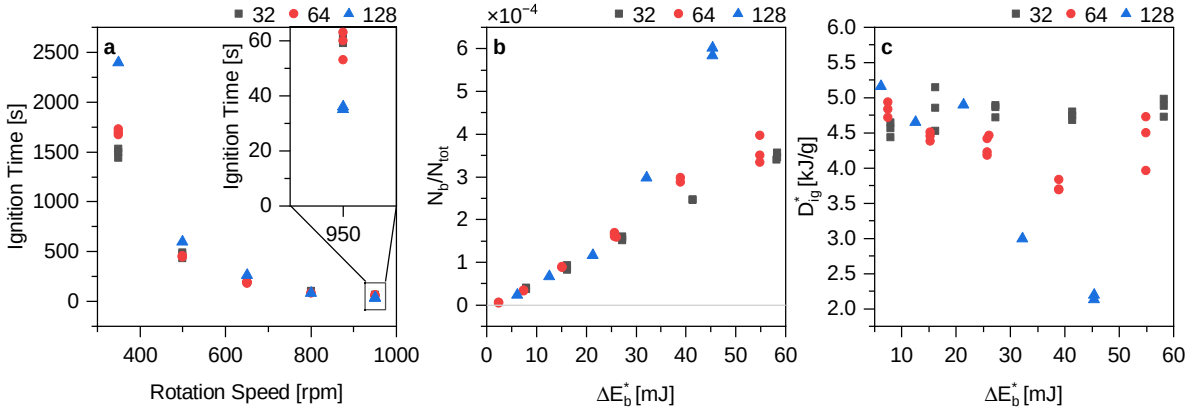


Figure 5.16: Influence of the total filling of the milling vial. LCO is milled with Al at a BSR of 30 using 6.35 mm steel balls. In total, 32 (black), 64 (red) and 128 (blue) balls were used. Panel a) shows the effect of the total filling on t_{ig}, b) on the number of collisions and c) on the specific activation dose.

The shorter activation stage, and therefore lower energy consumption, for the 128 balls is most probably based on enhanced ball-to-ball interactions. In the collision model, these interactions are respected by the introduction of φ_b (Eq. 1.5) in the calculation of the impact energy, which leads to a lower ΔE_b^*. However, it can be expected that a lower ΔE_0^* is not the only effect, as this would result in a longer activation stage and not in a shorter one. Moreover, the balls collide not only against the walls but also against each other with impact energies higher than E_0. These additional impacts are not represented in the collision model. While the additional impacts increase the efficiency of the milling for this system, the predictability t_{ig} based on the collision model is much lower.

Other parameters:

Other process parameters, such as the material of the milling media or the molar ratio between Al and LCO, were not studied here, as a similar study was published by Vauloup et al.[182] In that study the authors used ZrO_2-milling media and compared them with their stainless steel counterpart. At otherwise identical conditions, the observed milling times were at least 6 times longer for the ZrO_2 material, which is attributed to the lower density of the balls and therefore the lower impact energy.

Although the MSR mechanism was not mentioned by Vauloup et al., the formation of large metallic cobalt pieces and the kinetic profiles strongly suggest that a self-propagating reaction had occurred in their study. The authors also reported ZrO_2 contamination in the milled powder from damaged balls, which was attributed to extensive abrasion caused by the metallic pieces. Moreover, it is also likely that rapid temperature changes and internal temperature gradients play a role. These factors can cause stress in the milling media, which ultimately leads to their breaking.[185]

Furthermore, Vauloup et al. reported shorter durations of the activation stage for increasing Al molar ratios but also a promoted formation of Co-Al alloys. Unfortunately, the progress of the reaction was analyzed by sampling or measuring the external temperature, which results in less precise data for t_{ig}. However, the calculation of D_{ig}^* based on the reported data shows values higher but comparable to those in the present thesis (Table S11).

5.2.4 Influence of Graphite

Although the effect of several milling parameters on t_{ig} in the mechanochemical reduction of LCO with Al has been thoroughly examined, including calculations based on the collision model, this idealized system is representative only for well-sorted production scrap with minimal impurities. In modern recycling facilities, EoL LIBs are typically processed mechanically to produce black mass, which serves as the starting material for subsequent recycling processes. Such black mass consists of the active material from both the anode and the cathode alongside some impurities.[193] Accordingly, anodic graphite is typically the second largest fraction in a real black mass. Although chemically relatively inert, graphite can influence the mechanochemical process and therefore should be examined. To assess this effect, the graphite mass fraction was varied in an equimolecular LCO-Al mixture from 0 to 60 wt%. About 2 g of each powder mixture was milled with 60 g of stainless steel balls (d=6.35 mm) at 950 rpm in 5 minute milling and resting cycles.

In the graphite-free experiment, a pressure spike was detected after 58 s of milling. Increasing the graphite fraction to 10 wt%, increased t_{ig} to 167 s. However, when the graphite content was increased further, no spike in pressure was detected anymore within 1 h of milling, and only the zig-zag profile in temperature and pressure produced by the alternating milling and resting cycles are measured (Fig. S2.4).

The reaction progress was monitored by sampling the reaction after 10 min and 60 min of milling to record the XRD patterns of the powders. After 10 min of milling, the pattern of the 0 and 10 wt% graphite samples display broad reflections corresponding to the cubic cobalt phase, whereas no LCO reflections are detectable, indicating its complete consumption. (Fig. 5.17a). No pressure spike was detected for the reaction containing 20 wt% graphite, suggesting the absence of the self-propagating reaction. Nevertheless, the XRD pattern shows only weak LCO reflections, whereas Co peaks are intense and a $Li_xCo_{1-x}O$-phase emerges, as it was already discussed in section 5.2.1. Further increase in graphite content leads to a decrease in product related intensities and a corresponding increase of the LCO reflection intensity, indicting a lower reaction turnover.

After 60 min of milling, LCO reflections are absent in all samples (Fig. 5.17b) indicating its complete decomposition. For graphite loadings up to 40 wt% the pattern looks comparable, showing broad reflections of a cubic cobalt phase and a presumed Co-Fe alloy. At 60 wt% graphite, intense $Li_xCo_{1-x}O$ are visible alongside the metallic Co.

Notably, graphite reflections are absent in most patterns. Only the 60 wt% sample shows a broad baseline bump around $2\theta = 12°$, which could be associated with graphite. The initial graphite exhibits a sharp reflection around $2\theta = 12°$ (Fig. S1.3), caused by the stacking of the honeycomb-like carbon layers. Its absence or intense broadening indicate the exfoliation of graphite into a disordered structure.[194]

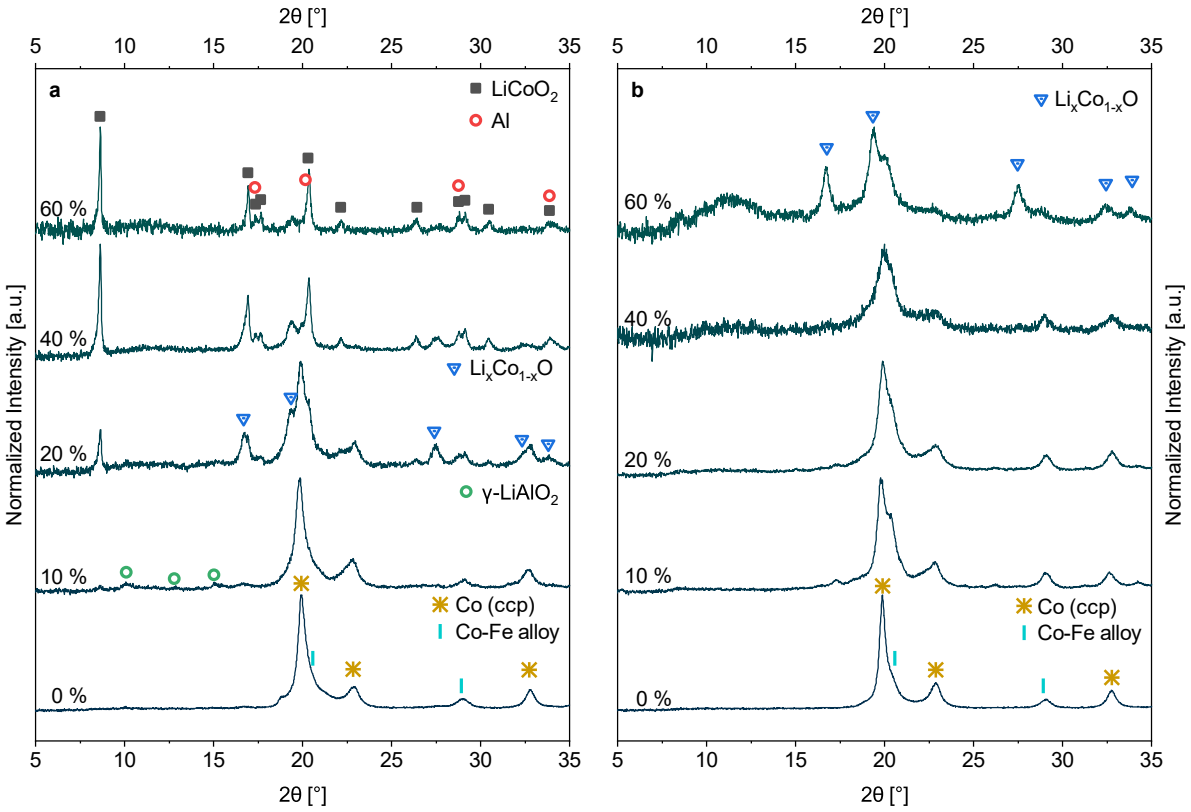


Figure 5.17: XRD patterns of the mechanochemical reduction of LCO with Al and in the presence of 0 - 60 wt% of graphite after a) 10 min and b) 60 min of milling. About 2 g of powder was milled with 60 balls of 6.35 mm diameter, a BSR of 30, LCO/Al = 1.0 at 950 rpm in repeating cycles of 5 min milling and 5 min resting.[175]

The loss of the pressure spike for the samples with 10 and 20 wt% graphite indicates the suppression of the self-propagating behavior (Fig. S2.4), which is supported by the XRD patterns. At graphite contents $\geq$ 20 wt% the LCO is not consumed in a fast reaction. Instead, it is reduced gradually by Al, forming first an intermediate Co(II) species, and is then reduced to the metal. Although graphite does not seem to directly participate in the reaction and therefore can be regarded as an inert additive, it can remarkably modify the reaction mechanism.

The suppression of the MSR by graphite may be caused by the interplay of several factors.

- Agglomeration: Graphite limits cold welding and lowers the adhesion of the powder, which diminishes its tendency to form agglomerates. Accordingly, secondary particles are smaller, less powder is affected by an impact, and less heat is released to initiate the self-propagating mechanism.[143]
- Dilution: As an inert material, graphite dilutes the system, which lowers the volumetric heat release. As a consequence, the thermal energy may not be sufficient to initiate a reaction in the surrounding powder, which is required for the reaction propagation.[141]

- Contact area: Graphite exfoliates and covers LCO and Al particles, reducing their contact area. Physical contact between reactants is crucial for a solid state reaction, and their spatial separation slows down the reaction rate.[195]
- Compression: Graphite is a soft material that could be reversibly compressed in an impact. Therefore, less energy is transferred to the reactants and the activation is less efficient.
- Friction: Graphite acts as a solid lubricant, reducing friction and thereby lowering the efficiency of energy transfer from the milling balls to the powder. This suppresses the formation of local hot spots and potentially leads to less favorable ball trajectories.[196,197]

The suppression of the MSR by graphite may be of great importance to scaling up the process to an industrial level. In the absence of the self-propagating reaction, the heat release is distributed over a longer time scale, thereby diminishing the increase in the internal temperature. Consequently, and even more important, no significant pressure builds up, and the reaction becomes safer and more controllable.[175]

5.2.5 Mechanochemical processing of CAMs with Sulfur

This subsection is based on the results obtained from a supervised Master's project carried out by Alexander Pöplow.[198]

In section 5.2.2, a promising reaction of LCO and sulfur was described. The mechanical treatment of LCO with chemically relatively inert S led to the formation of cobalt sulfides and water soluble Li_2SO_4. However, this reaction was not fully completed, and lithium yield was rather low.

The first question that arises is whether the reaction has been incomplete because of insufficient milling, because of an inadequate amount of sulfur, or a combination of both. To clarify this, LCO was milled with molar ratios of S: LCO (η) ranging from 1 to 3 at 950 rpm (BSR=20, 4 g powder), and sampled at regular intervals to analyze the reaction progress. The milling was stopped when the XRD pattern indicated no further progress.

The evolution of phases during the milling process is provided for the case for η=1. The recorded XRD patterns show the evolution of the crystalline phases during the milling process (Fig. 5.18a). Within the first 30 min all reflections of LCO and S broaden and decrease in intensity. This is associated with an overall reduced crystallite size and lattice distortions due to mechanical stress. Additionally, the first new reflections appear, which can be indexed to the CoS_2 phase (No. 205, COD:9008393). After 90 min of ball-milling, the formation of more phases is observed, including Li_2SO_4 (No. 14, COD:2106816), CoS (No. 186, COD:9008884) and CoO (No. 225, COD:1533087) and the intensities of CoS_2 reflections increased. The XRD pattern recorded after further milling suggests a continuous decrease of the LCO phase fraction. However, the reaction did not show further progress after 210 min and was stopped although some LCO still remained (Fig. 5.18a).

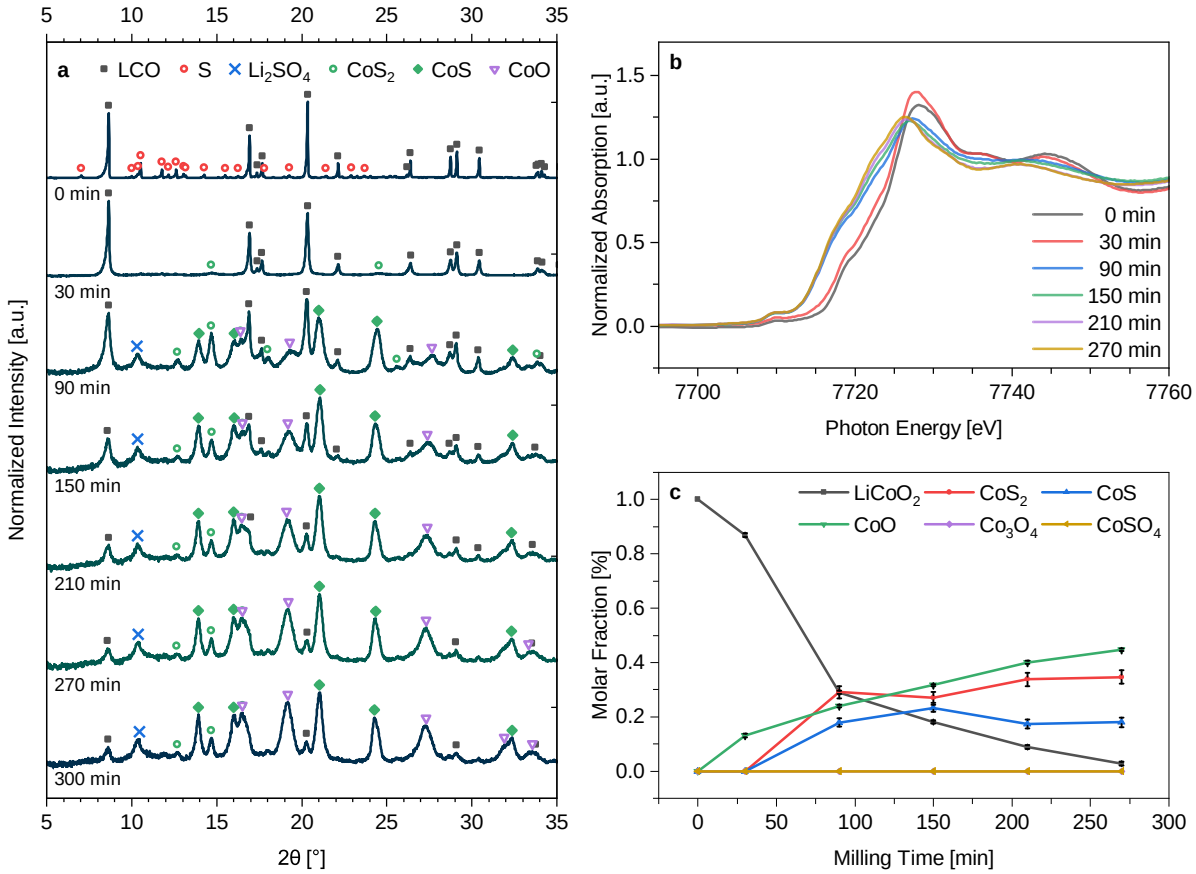


Figure 5.18: Mechanochemical reaction progress in equimolar LCO-S mixture. Evolution of a) XRD pattern, b) XANES spectra at the Co K-edge and c) phase fractions quantified by LCF.[198]

The phase identification by XRD requires sufficient crystallinity of the samples. However, prolonged high-energy ball-milling reduces crystallite sizes and overall crystallinity. The resulting broad, low-intensity peaks might hide amorphous phases or minor compounds. Therefore, XANES spectroscopy was employed to complement the XRD measurements.

The XANES spectra at the Co-K_α-edge in Fig. 5.18b exhibit a slight shift of the absorption edge to lower photon energies during the first 30 min of milling, indicating a minor reduction of Co(III), but the spectral shape remains essentially unchanged. After 90 min of milling, a pronounced shift of the absorption edge and a substantial change of the spectral shape are observed, suggesting a high degree of reaction turnover during this interval. Afterward, only minor changes between the spectra are visible.

Furthermore, the XANES spectra are fitted with linear combinations of XANES spectra from reference materials (Fig. S3.2), to quantify the evolution of phase fractions during the milling process. The set of reference materials was selected based on the XRD results and consists of LCO, CoS, CoS_2, and CoO, as well as Co_3O_4 and $CoSO_4 \cdot 7\,H_2O$ which are other stable combinations of Co, O, and S that could form. The results are presented in Figure 5.18c and suggest a sigmoidal decrease in the LCO

phase fraction with the highest reaction rate occurring between 30 and 90 min. This is accompanied by an increase of CoO (30 min), CoS (90 min), and CoS_2 (90 min) fractions, whereas Co_3O_4 and $CoSO_4 \cdot 7\,H_2O$ are not formed. These results are more or less consistent with the XRD observations (Figure 5.18a). Deviations, such as CoO formation before CoS_2, are within the error of the linear combination fit (LCF).

Interestingly, the XANES spectra and the respective linear combination fits (LCF) indicate further reaction progress after 210 min, whereas the XRD pattern shows no changes. According to panel c) in Fig. 5.18, LCO seems to be almost completely consumed, while in panel a) LCO reflections remain detectable in the XRD. It is difficult to determine from the XRD patterns whether LCO is completely consumed or not because of low intensities and peak overlap with other fractions. The prominent LCO reflection at $2\,\theta = 8.6°$ which is often used to identify LCO overlaps with a reflection of possibly formed Co_3O_4, preventing unambiguous discrimination. Although the LCF analysis did not identify Co_3O_4, the presence of four other phases could mask trace amounts. Despite this uncertainty, it can be concluded that the residual fraction of LCO is low after 270 min of milling.

The same analysis was performed for reactions with a higher sulfur content (η=1-3) to investigate the effect of the molar ratio. The XRD patterns show an increasingly long activation time before any new reflections appear (Fig. S1.4). While at $\eta = 1$ new reflections can be observed already after 30 min of milling, at $\eta = 3$ no indication for new phases can be seen before 300 min of milling. Moreover, the final phase composition after the mechanical treatment depends on η. At $\eta = 1$ and 1.5, main reflections are attributed to LCO and CoS, whereas these are not observed at higher η. Instead, the reflections of CoS_2 dominate the final pattern.

Both, XANES and LCF, confirm that the kinetics slow down as the sulfur content increases (Fig S3.3). This trend is further illustrated in Fig. 5.19a, which shows the evolution of the LCO atomic fraction during milling for different η, based on the LCF results. For visual representation, the data points were fitted with a logistic function (Eq. 5.9). The LCF results further suggest that at η=2, LCO is completely consumed after 210 min of milling, while at $\eta = 2.5$ and 3, full conversion is achieved after 270 and 480 min, respectively. At lower η values, the LCF results suggest that full conversion was not observed within the experimental time frame. However, the residual atomic fractions are small and fall within the uncertainty of the fitting procedure.

$$\chi(t) = \frac{1}{1 + e^{-k(t-t_0)}} \tag{5.9}$$

The relative phase compositions at the end of the milling process, based on LCF analysis, are presented in Figure 5.19b for $\eta = 1$-3. The data clearly show an increase of the CoS_2 fraction with increasing S content. Note that the LCF at η=2.5 and especially η=3, suggests substantial amounts of $CoSO_4 \cdot 7\,H_2O$.

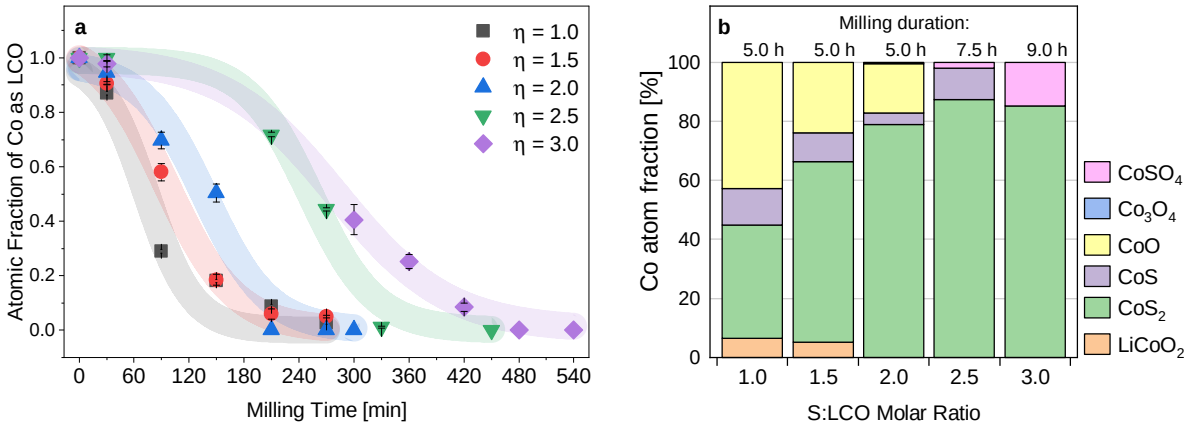


Figure 5.19: a) Evolution of atomic Co fraction as LCO during the mechanochemical reaction between LCO and S at different η quantified by LCF analysis. b) Final phase fractions derived from LCF analysis after the reaction of LCO with S.[198]

Combining the results from XRD and XANES, the following hypothesis for the milling process can be developed. High-energy ball-milling of LCO with S proceeds through an activation phase, in which the reactants are thoroughly mixed and crystallite sizes are reduced, resulting in an increased contact surface area between LCO and S. Mechanical fracture of CoO_6 octahedra in LCO and of the S_8 rings enable a quasi solid-state reaction with sigmoidal kinetics. LCO is reduced and forms CoO, CoS, and CoS_2, while Li might be released as Li_2O. Elemental sulfur is oxidized to S(VI) and can potentially form SO_3, while concurrently it is reduced to sulfide and disulfide. As the pressure did not increase during the reaction, it can be concluded that SO_3 reacts with lithium salts (Li_2O) to form Li_2SO_4.

Under the present reaction conditions, CoS_2 proved to be the favored Co-containing reaction product, and therefore an excess of sulfur is required to drive the reaction to completion. However, increasing the sulfur content slows down the reaction rate (Fig. 5.19), since sulfur is a soft material with a low melting point of about 115 °C).[132] When subjected to high-energy impacts, sulfur readily deforms and dissipates a fraction of the kinetic energy without leading to a chemical reaction. Moreover, milling can generate short living local hot spots, which may cause partial melting and strong agglomeration. Consequently, the milling becomes less efficient. This effect was especially observed at η=3, where the early samples had an almost viscous and slightly sticky appearance. Later, the samples were more powdery because the sulfur was partially consumed, which may have a self-accelerating effect on the mechanochemical reaction.

After the milling process, the separation of Li and Co was investigated. The Li_2SO_4 formed during milling is soluble in water, whereas cobalt sulfides and oxides are poorly soluble. Therefore, aqueous leaching should be suitable for separating Li from cobalt. This was tested with the milled samples of all five η. The powders were leached in three successive cycles, using a solid-to-liquid weight ratio of 1:40. The combined aqueous leachates were analyzed by ICP-OES to determine the concentration of dissolved Li, Co, and Fe ions (Table S13). Iron is a typical contamination due to abrasion during

milling in stainless steel vials. The Li extraction yields were calculated based on the measured Li concentration in the solution in relation to the theoretical Li content in the milled powder (Eq. 4.1).

Figure 5.20 shows that Y_{Li} increases slightly from 84 % to 91 % with increasing η. While η shows a minor effect on Y_{Li}, a strong effect is observed on the pH and co-extracted Co. With an increasing η the pH of the leaching liquor drops from 9 at η=1 over 7.5 at η=2 and down to 2.5 at η=3. Thereby, the co-extracted Co yield increases from 0 % to 5.8 %. Note that Fe is detected on the same order of magnitude as Co for η=3, while it remains below the detection limit for η between 1 and 2.

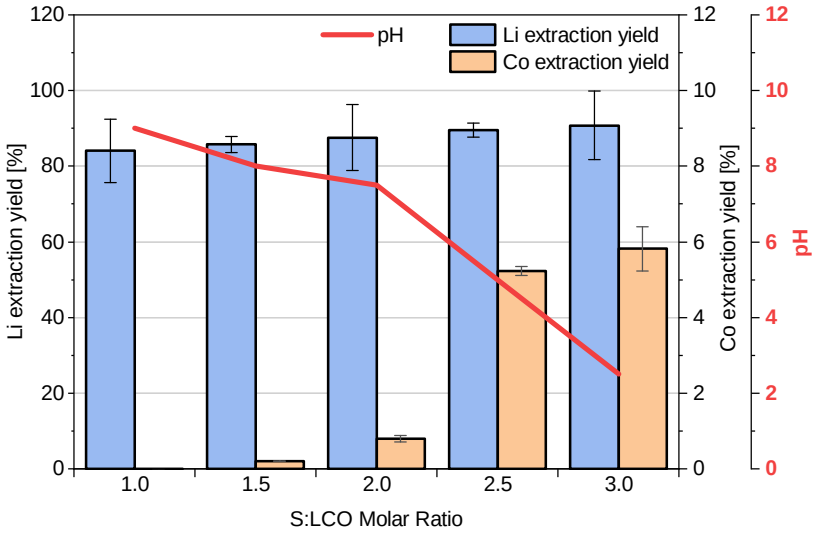


Figure 5.20: Li and Co extraction yields obtained from aqueous leaching of LCO milled with S at η in the range of 1 to 3, together with the pH of the respective leachates.[198]

In general, co-extraction of other ions should be avoided, because it lowers the purity of the recovered Li salt and it results in a loss in the transition metal recovery yield. The co-extraction is directly related to the pH level, since the solubility of TM ions is pH-dependent. At η=1, the leachate has a relatively high pH of 9, which can be explained with the coordination of protons to the surface of $LiCoO_2$ and CoO, generating a high concentration of OH^- in the solution. In addition, the possible formation of some Li_2O or Li_2S can not be excluded, which would result in alkaline solutions.

Higher sulfur content leads to a lower pH of the leachate, but none of the identified reaction products reacts acidic with water, so another explanation is required. During the reaction, sulfoxides such as SO_2 or SO_3 could have formed. At low η, these are compensated by Li_2O or CoO, but at high molar ratios, these react with humidity to form acids. Moreover, mechanically activated sulfur could show higher reactivity towards water or oxygen.[199] During the leaching process, activated sulfur might oxidize and form H_2SO_4 or H_2SO_3 in small quantities, lowering the pH.

The leachate was dried and XRD analysis of the obtained solid confirms the formation of Li_2SO_4 and the presence of $CoSO_4$ in the sample of η=3 (Fig. S1.5). Comparing the XRD pattern of the as-milled powder with the insoluble fraction shows the disappearance of the Li_2SO_4 reflections, while

the reflections of CoS and CoS_2 remain largely unchanged. Moreover, $Co(OH)_2$ is detected for η=1 and 1.5, while $CoSO_4$ is detected at η=2.5 and 3. In the pattern for η=2 no new reflections appear after aqueous leaching.

The reaction at η=2.0 delivers the most favorable outcome among the tested molar ratios. The complete conversion of LCO predominantly to Li_2SO_4 and CoS_2 results in a high lithium extraction yield and the almost neutral pH of the leachate minimizes the co-extraction of transition metals. Consequently, this molar ratio is selected as the optimal condition for a sulfur based mechanochemical LCO recycling process and used in subsequent investigations.

After the aqueous extraction, the XRD analysis suggests that the insoluble fraction consists mostly of CoS_2. Moreover, at η=3 the formation of $CoSO_4$ and a decrease in the pH of the leaching liquor have been observed. Although not favored during the Li extraction, the formation of sulfates and low pH are beneficial in the subsequent dissolution of TMs. This led to the idea that after lithium was extracted, cobalt could be dissolved without the addition of any acid by promoting the oxidation of mechanically activated sulfur or sulfides to SO_4^{2-}. Hydrogen peroxide is selected as a suitable oxidation reagent because it does not introduce any secondary pollution and it is already a widely used reactant in battery recycling. A possible reaction equation is proposed in Eq. 5.10, which suggests the simultaneous formation of water soluble $CoSO_4$ and of sulfuric acid to lower the pH.

$$CoS_2 + 7\,H_2O_2 \longrightarrow CoSO_4 + H_2SO_4 + 6\,H_2O \tag{5.10}$$

To evaluate cobalt dissolution, the solid residue from the aqueous Li extraction ($\eta = 2$) was added to a H_2O_2 solution at room temperature. The H_2O_2 content for this purpose was adjusted according to Eq. 5.10 to reach an excess between 0 and 8 molar equivalents of peroxide. After filtration, the Co^{2+} concentrations were determined by UV-Vis spectroscopy using a freshly prepared calibration curve. Additionally, the pH was monitored in each experiment. The Co extraction yield (Y_{Co}) was calculated similarly to Eq. 4.1. The initial Co content was calculated based on the assumption that the powder consists exclusively of CoS_2.

The extraction yields are presented in Figure 5.21 and show a steady increase in Y_{Co} from 8 % to 93 % with rising H_2O_2 dose and a simultaneous decrease in pH from 5 to 2. Notably, the transition from 1 to 2 equivalents of H_2O_2 produces a sharp increase in Y_{Co}, which could indicate a change in the dissolution mechanism. Although cobalt dissolution is an interesting topic, it is not the focus of this work and was therefore not investigated further.

When more than 8 equivalents of H_2O_2 were used, the solid was completely dissolved. However, Y_{Co} which were calculated based on UV-Vis spectroscopy data, did not reach 100 %. The discrepancy is most likely due to the fact that the starting powder does not entirely consist of CoS_2, as was assumed for the yield calculation. Therefore, the true Y_{Co} is probably slightly higher than the reported values.

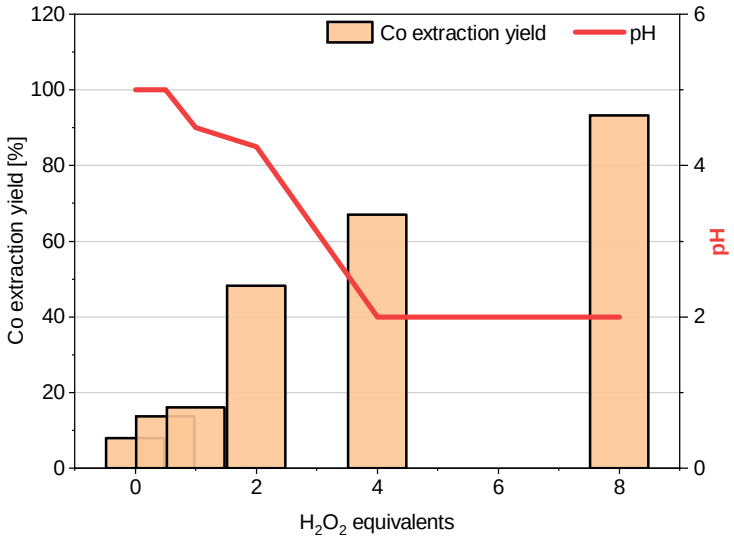


Figure 5.21: Dependency of Cobalt dissolution on addition of H_2O_2[198]

During the addition of the solid sample to the H_2O_2 solution, a temperature increase and a gas evolution were observed. The formed gas is most likely O_2, produced by the exothermic decomposition of H_2O_2 (Eq. 5.11). Although this reaction is usually very slow at room temperature, it can be catalyzed by transition metal salts.[132] The formation of another potential gas SO_2 was experimentally excluded. The formed gas was bubbled through an alkaline scrubbing solution, which was afterwards acidified and titrated with a $KMnO_4$-solution. The SO_2 gas would dissolve as SO_3^- in the alkaline solution. During subsequent titration, it would be oxidized, thereby reducing the intense colored permanganate to an almost colorless Mn^{2+} solution.

$$2\,H_2O_2 \longrightarrow 2\,H_2O + O_2 + 196.2\,kJ \tag{5.11}$$

Furthermore, iron was detected by ICP-OES in the solution, which was introduced by abrasion from the milling media. Iron has to be removed to ensure high purity of recovered cobalt salts for the production of new CAMs. Because H_2O_2 acts as an oxidant, all dissolved iron is present as Fe^{3+} and can be selectively precipitated as hydroxide by increasing the pH to 4.[200] ICP-OES measurements confirm that the Fe:Co mass ratio decreases from 2.6 % to 0.7 % after the selective precipitation allowing the recovery of a cobalt solution with good purity.

The experimental results demonstrate that mechanical stress can induce a quasi solid-state reaction between elemental sulfur and LCO. Subsequent aqueous leaching efficiently separates soluble Li salts from insoluble transition metal phases with Y_{Li} over 84 %. A S:LCO molar ratio of 2 provides the best compromise, allowing for a high Y_{Li} of 87 % and a relatively short milling time of 3 h. The sulfide phases formed during milling can be dissolved after the aqueous Li extraction by adding H_2O_2, which oxidizes sulfur and sulfides to their corresponding sulfates. This process therefore allows for

acid-free aqueous selective lithium extraction with high yields as well as an acid-free dissolution of transition metals.

It should be noted that this study was performed on pristine LCO, whereas modern electric vehicle batteries are typically based on NMC or LFP. Moreover, the typical feedstock for chemical recycling is black mass, which contains the cathode active material, the anode active material, the binder, and typically many impurities. Therefore, in order to resemble the black mass while keeping the material system simple, a mixture of LCO and graphite in equal weights was prepared, and the influence of graphite on the process without the contribution from other components was tested. The LCO-C mixture was milled with 2 equivalents of sulfur with respect to LCO at 950 rpm using 6.35 mm steal balls. In contrast to the LCO-S case, almost no conversion can be detected in the XRD pattern after 8 h of milling, and even after 20 h of milling, the LCO reflections remain visible (Fig. 5.22). As LCO is not completely decomposed, Y_{Li} would be low, and the separation of Li and Co would be poor. In an attempt to accelerate the reaction speed, alternative milling parameters such as small 3 mm balls, large 12.7 mm balls, as well as liquid assisted milling with ethanol were tested, but none yielded significant improvement. The incomplete and slow reaction indicates that the proposed sulfur based mechanochemical treatment cannot be directly transferred to a graphite containing black mass. Similar to the LCO-graphite-Al case, the reason is most likely based on the the smaller contact area between the starting materials and possibly less efficient ball trajectories.

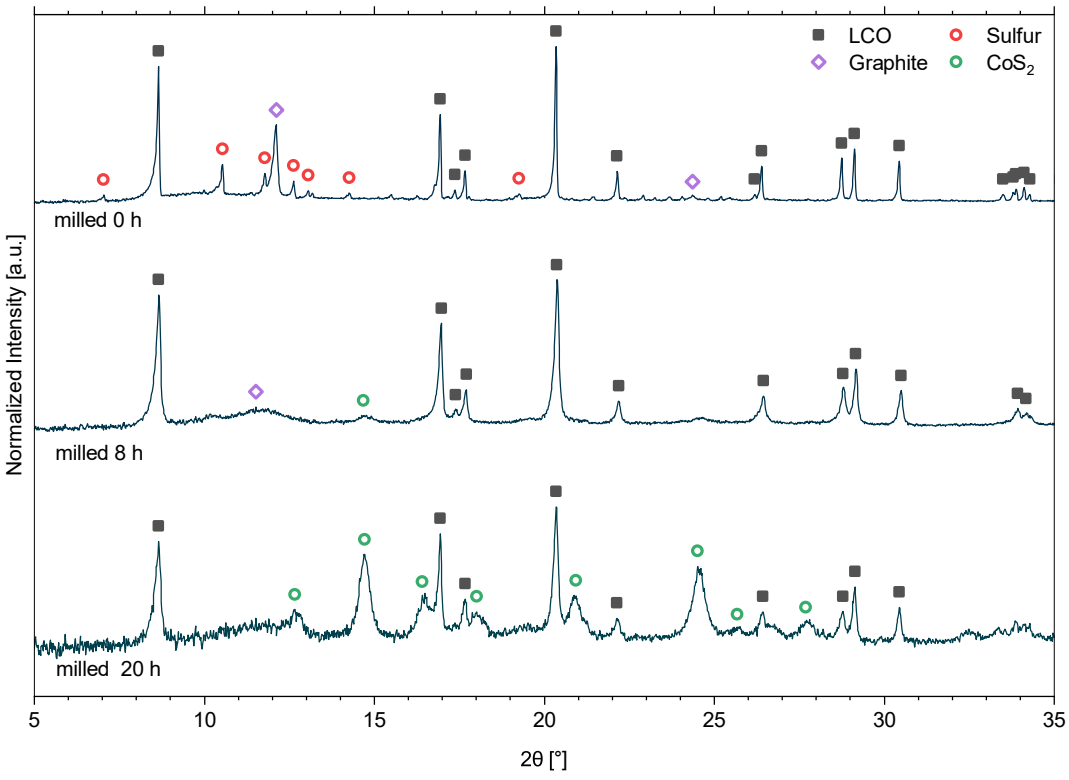


Figure 5.22: Evolution of XRD pattern during the mechanochemical processing of the LCO-graphite-S system.[198]

In order to overcome the limitations of the purely mechanical process, a combined approach involving mechanical activation followed by thermal treatment was investigated. High-temperature XRD measurements revealed that the decomposition of LCO in the LCO-graphite-S mixture starts around 650 °C, forming CoO. A mechanical treatment of this mixture for 30 min and 900 min prior to heating reduced the decomposition temperature of LCO to 550 °C and 350 °C, respectively, and produced cobalt sulfides and Li_2SO_4. Remarkably, if only the LCO-graphite mixture was mechanically activated and sulfur was introduced between mechanical and thermal treatment, the milling time was reduced to 60 min, while still achieving the thermal decomposition of LCO at 350 °C. Subsequent aqueous leaching of the thermally treated mixture has facilitated selective lithium extraction with a yield of up to 81 % and Co co-extraction below 5 %. A more detailed description can be found in the master's thesis.[198]

In summary, the mechanically induced reaction between CAMs and elemental sulfur, as well as the mechanical activation to facilitate a more efficient thermally driven reaction in a subsequent process, represent promising approaches towards sustainable and cost efficient LIB recycling. Nevertheless, the process as in the current state faces some challenges. The aqueous extraction in this study used a solid-to-liquid ratio (s/l-ratio) of 25 g/L, which is far above the solubility limit of Li_2SO_4 (≈340 g/L).[201] Increasing the s/l-ratio saves water, reduces energy costs and time required for evaporation, and is expected to reduce Co co-extraction. Moreover, the subsequent dissolution of Co by insitu acid formation consumed excess H_2O_2. Although it is a relatively inexpensive chemical, its consumption should be improved.

Furthermore, the process should be validated on a broader range of cathode materials such as NMC or LFP, and the sensitivity towards impurities that are typically in a BM should be evaluated. Finally, The influence of graphite should be studied further. In this study, 50 wt% graphite has been shown to impede the mechanochemical reaction, but it remains an open question as to which graphite content the reaction is still feasible.

5.3 Black Mass

Most of the content in this section has been submitted as a journal article *"Improved Mechanochemical Reduction of Industrial NMC-based Black Mass with Subsequent Selective Lithium Extraction"*.[176]

Up to this point, this study has primarily examined model systems of varying complexity. These simplifications are necessary in order to investigate the key mechanisms and to establish a robust understanding of the overall process. However, on the industrial scale, the situation is much more complicated. In modern recycling facilities, spent batteries are typically first processed in a pretreatment, which yields an intermediate product, the black mass. The BM serves as a feedstock for subsequent processing steps to recover various battery materials.

The intermediate BM is not a specified product and its composition varies both with the incoming stream of battery waste and with the condition and implementation of the pretreatment. Accordingly, BM may contain different cathode materials or their decomposition products together with the anode materials, as well as additional impurity phases originating from other cell components. Consequently, to evaluate the applicability and the transferability of the findings obtained from the model system, it is essential to first characterize the black mass

5.3.1 Analysis of the Black Mass

The black mass used in this study was produced by an industrial company. EoL batteries from electric vehicles were sorted, discharged, dismantled to the module level, and shredded in an inert atmosphere. The crushed mixture was classified by sieving, and the fine fraction collected as the black mass. Multiple analytical methods were applied to characterize this fraction and to determine its composition.

For this purpose, the crystalline phases in the black mass were identified by XRD. The pattern in Fig. 5.23 displays an intense and sharp set of reflections that can be best assigned to the layered-oxide material NMC-111 (COD: 4002443, space group No. 166). A second less intense set of reflections, slightly shifted to higher diffraction angles, indicate the presence of a second layered-oxide phase with marginally smaller lattice parameters that mach closely to LCO (COD: 1533825).

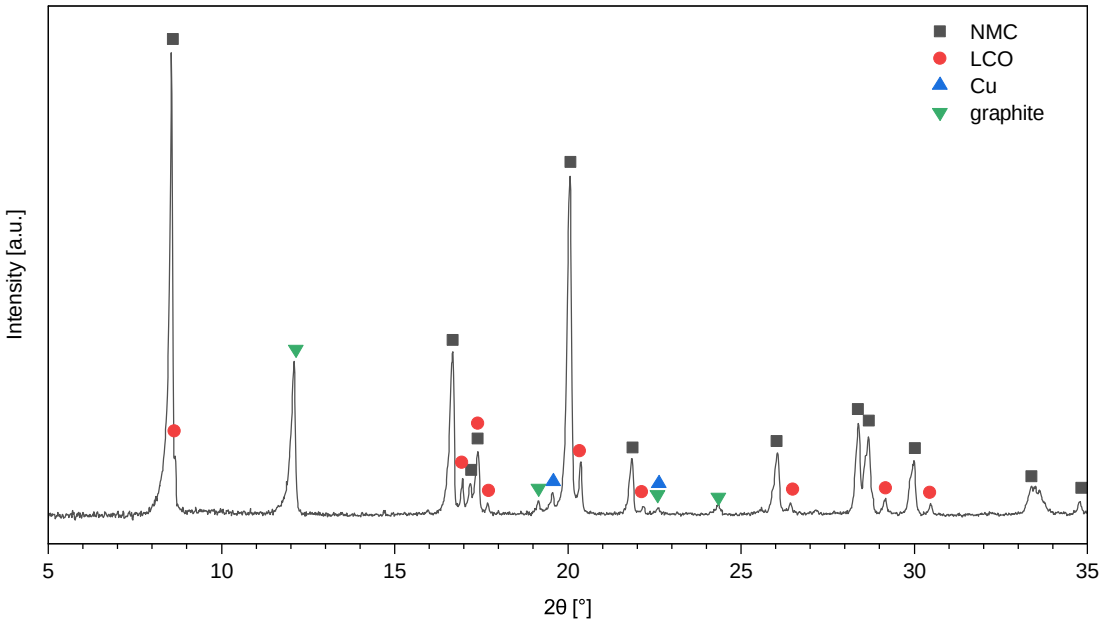


Figure 5.23: XRD pattern of the received black mas.[176]

The also relatively intense reflection at 2θ≈12° can be attributed to graphite, and additional graphite reflections are weakly visible. Besides the main components (CAMs and graphite), Cu can be identified,

which is used as anode current collector. Signals from Al, which is used as the cathode current collector, are not detectable, nor are there any reflections of transition metal oxides that would suggest decomposition of the cathode material. The oxidation state and electronic environment of Co, Ni and Mn were studied using XANES and confirm the presence of NMC (Fig. S3.4).

As it is displayed in the photograph in Fig. 5.24a, the BM appears as a relatively homogeneous black powder. The SEM images in the panels b-f provide insight into the powder's morphology. In contrast to the optical photograph, the low magnification overview SEM image (Fig. 5.24b) reveals a highly inhomogeneous mixture. The secondary particles vary widely in size and have irregular shapes.

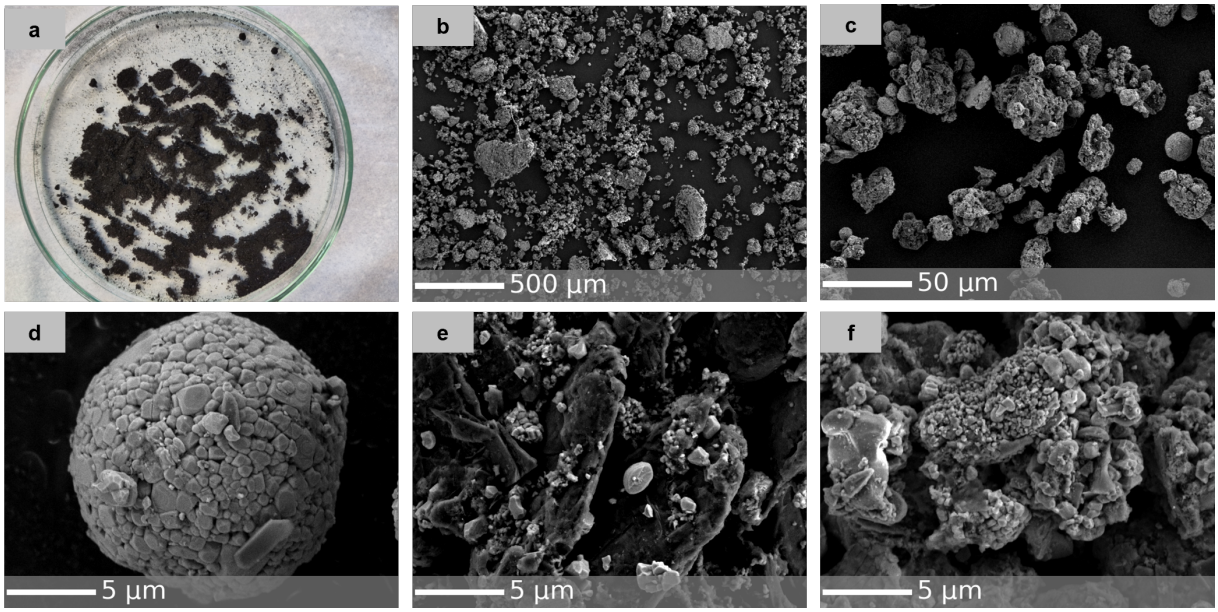


Figure 5.24: a) Photograph and b-f) SEM images of the received black mas.[176]

At higher magnification (Fig. 5.24c), the particles can be grouped into three categories: spherical particles, flake-like particles, and poorly defined agglomerates. The spherical particles as in Fig. 5.24d, measuring roughly 5 - 15 µm in diameter, exhibit a fairly crystalline structure that is typical for modern cathode materials such as NMC. The flake-like particles appear relatively dark in Fig. 5.24e, indicating a low atomic number that would be consistent with graphite. On the flakes, many small particles are attached. Their bright appearance indicates a high atomic number and, in combination with their sharp edges, they are most likely fractured CAMs or contamination introduced during pretreatment such as parts of the casing. Fig. 5.24f shows the magnification of an agglomerate. It appears to consist of many small crystallites of various sizes and shapes that are embedded in a less-crystalline matrix.

Furthermore, the SEM images were complemented with EDX measurements at two independent spots to gain insights into the elemental distribution of the particles (Fig. 5.25). Spot A shows one of the spherical particles, which primarily consist of Co, Ni, and O, while Mn is detected only in minor

amounts. This indicates that at least this particle consists of a Ni-rich NMC material. No copper is detected in this spot, but some small aluminum particles are present. In the background a flake-like carbon material can be seen, which is most likely graphite.

Spot B also contains particles made of Ni, Co, Mn, and O, whose elemental ratio varies significantly in some cases. In contrast to the first spot, a relatively large piece with almost exclusively Cu intensities is visible. At both locations, fluorine intensities are distributed throughout the entire sample.

As follows from the elemental mapping, the BM is made of NMC materials with varying stoichiometry, and residues of the Al- and Cu-current collector are clearly visible. The uniform distribution of F in both spots suggests the presence of a fluoride based binder such as PVDF or residues and decomposition products of the conductive salt $LiPF_6$.

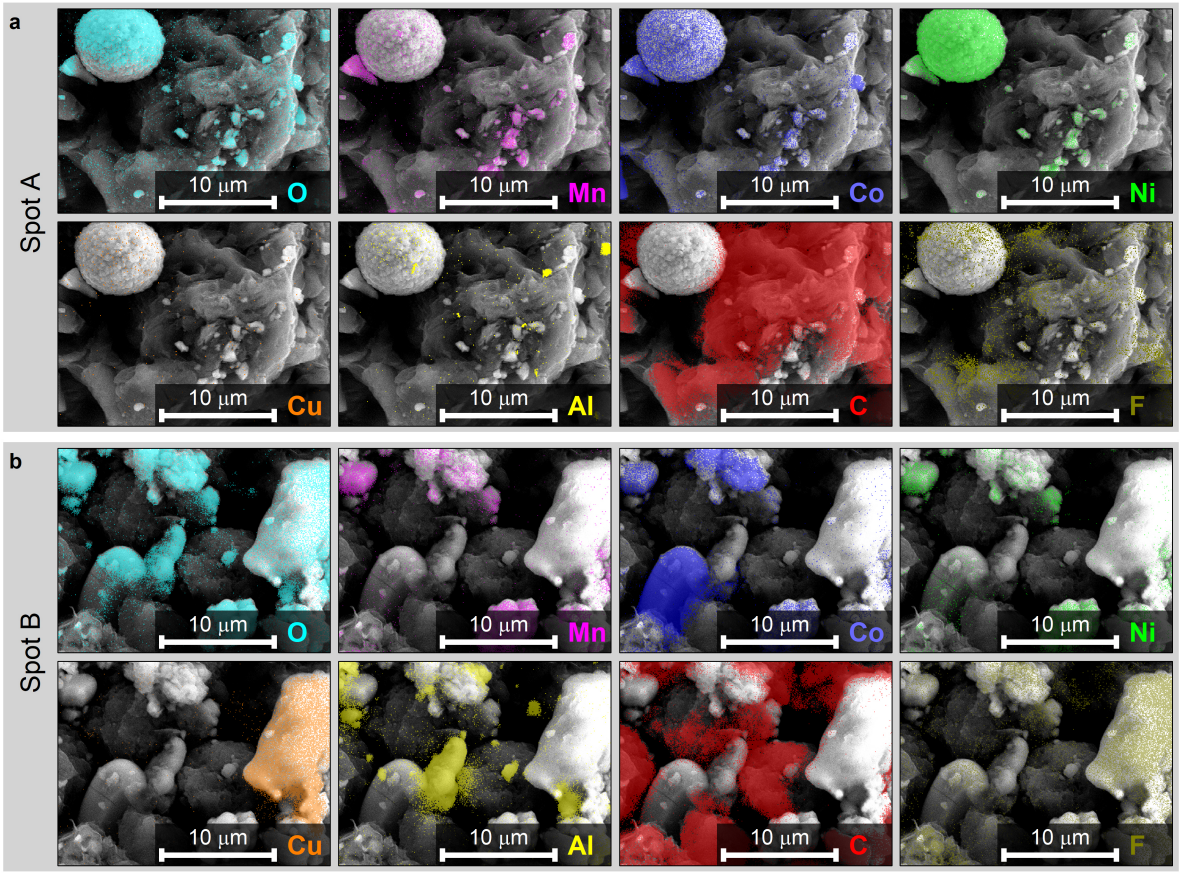


Figure 5.25: SEM images of the black mass at two locations with EDX based elemental overlay.[176]

The cation concentrations in the BM were quantified by ICP-OES (Table S14). The elemental ratio of Mn, Co, Ni, and Li closely resembles that of NMC-111 cathode material, corroborating the XRD and XANES results. Although the EDX indicates variations in the stoichiometry of individual particles, the overall ratio levels out in the bulk (Fig. 5.25). Copper and aluminum inclusions most likely originate from the current-collector foils. The higher Cu content compared with Al can be explained by two

considerations. (i) The liberation of the graphite from its Cu current collector during mechanical pretreatment may be less effective than the removal of the CAM from the Al foil. (ii) Cu is more dense than Al and in subsequent classification Cu may behave similarly to the layered-oxide materials. Trace iron most likely arises from cross-contamination with battery casings.

The black mass was further analyzed by TGA and dTG in an oxidizing atmosphere to quantify the mass fraction of volatile and carbonaceous compounds (Fig. 5.26a). The dTG curve exhibits several distinct stages of mass loss. The first stage up to 330 °C accounts for a loss of 9 wt% and is attributed to volatile compounds. Below 200 °C the mass loss is presumably caused by evaporation of linear organic carbonates and water, whereas the range between 200 and 330 °C is related to the evaporation of cyclic carbonates and electrolyte decomposition products such as ethers.[202,203] The next stage between 330 °C and 470 °C is associated with the decomposition of PVDF,[204] contributing roughly 3 wt% to the loss. The largest mass loss is caused by the oxidation of graphite and carbon black in the range between 470 and 950 °C, contributing to 36 wt%.

The characterization of the black mass can be summarized as follows. Although the cathode material in the BM is a mixture of multiple NMC phases alongside a minor LCO fraction, the total metal content resembles the case of NMC-111. The secondary particles may be partially crushed during pretreatment, but their crystalline phase remained intact. Consequently, the content of CAM can be calculated based on the transition metal mass fractions with Eq. 5.12, revealing a mass fraction χ_{CAM} of 47 %. Additionally to graphite, other carbonaceous compounds including fluorine based binder and volatile compounds, as well as some Cu and Al from current collectors are detected. In summary, the phase fractions were successfully determined and are presented in Fig. 5.26b.

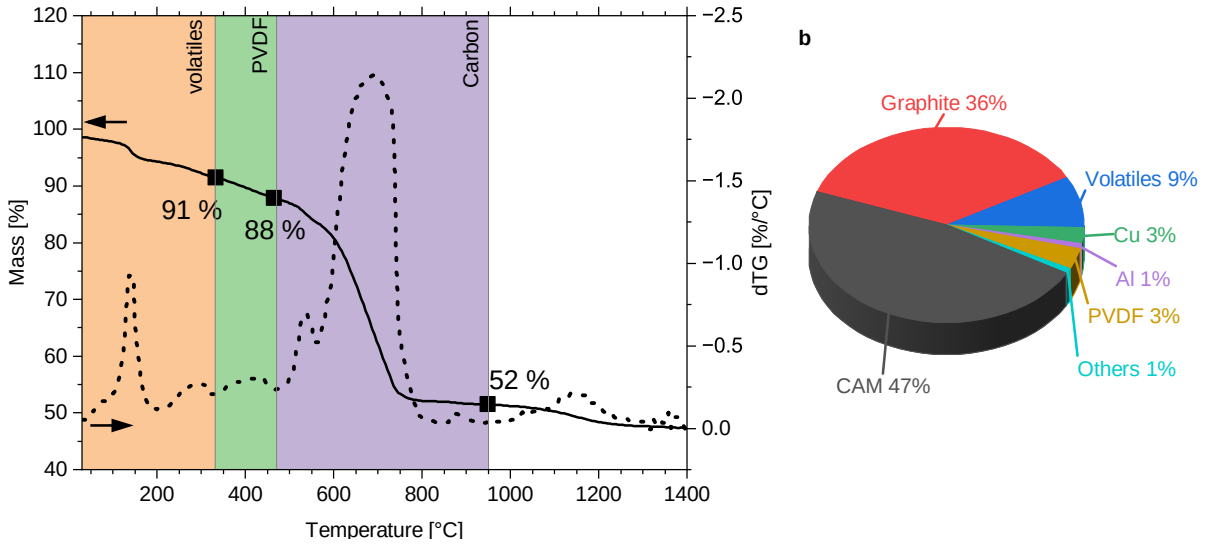


Figure 5.26: a) Thermo gravimetric analysis (solid line) and its derivative (dashed line) of the black mass in oxygen atmosphere. b) Phase composition of the black mass.[176]

$$\chi_{NMC} = \left(\frac{\chi_{Ni}}{M_{Ni}} + \frac{\chi_{Mn}}{M_{Mn}} + \frac{\chi_{Co}}{M_{Co}} \right) \cdot M_{NMC} \tag{5.12}$$

5.3.2 Reactive Milling of the black mass

Once the characterization of black mass was completed, it was subjected to reduction during mechanochemical treatment. As it is described in section 5.2.4, graphite slows down the reaction rate of the mechanochemical reduction of LCO with Al and even shifts the underlying mechanism from a mechanically induced self-propagating reaction pathway towards less instantaneous reaction kinetics. Since the black mass contains around 36 wt% graphite, a slow gradual reaction is expected to proceed according to Eq. 5.13. Minor components in the BM, such as PVDF or volatiles, should not participate chemically in the reaction, but nevertheless may influence the reaction.

In order to compensate for the slow kinetics and ensure a complete reaction, the molar ratio of Al:CAM was increased from 1 to 1.7. For this BM with 47 wt% CAM, this calculates to an Al content of 17 wt% in the reaction mixture.

$$\mathrm{LiNi}_x\mathrm{Mn}_y\mathrm{Co}_z\mathrm{O}_2 + \mathrm{Al} \longrightarrow \mathrm{LiAlO}_2 + (\mathrm{Ni}_x\mathrm{Mn}_y\mathrm{Co}_z) \tag{5.13}$$

During the milling process, the internal temperature and pressure are monitored and reveal a zig-zag profile that is caused by the alternating milling and resting cycles (Fig. S2.5). A spike in pressure would indicate a mechanically induced self-propagating reaction (MSR), as it is the case for NMC-Al in the absence of graphite.[175,205] However, when black mass is milled instead of pristine NMC, no spike in pressure can be detected, indicating the suppression of the MSR mechanism by graphite. Therefore, the reaction products were sampled every hour and analyzed by XANES and XRD to obtain information about the reaction progress.

Fig. 5.27 shows the evolution of XRD patterns during the mechanochemical processing of BM with Al powder in 60 min intervals. Before milling, the pattern shows sharp reflections of CAM, graphite, and Al. However, after 1 hour of processing, the signal intensity is significantly reduced, and the peaks show intense broadening, demonstrating a reduction in the long-range order due to lattice strain and crystallite size reduction. Especially the 002 reflection of graphite at 12° of 2 θ, experienced intense broadening and a decrease in intensity. Since this reflection arises from the stacking of honeycomb-like carbon layers, its broadening hints to exfoliation.

After 120 min of milling, the pattern represents a highly amorphous mixture. The observable reflections do not match the starting material anymore, hinting at the evolution of new phases. Transition metal oxides, such as NiO and CoO, alongside with residual NMC could be suggested (Fig. S1.6), but low crystallinity inhibits explicit phase identification. Further changes are observed by XRD after 180 min of milling (Fig. 5.27). The prominent broad reflection at 20° of 2 θ splits into two, and new reflections become visible, which could fit to γ-Al_2O_3 (No. 227, COD:2015530) and a metallic composite of Co, Ni, and Mn in a cubic structure. Further milling does not result in observable alterations in the XRD pattern, even after 240 and 300 min of milling.

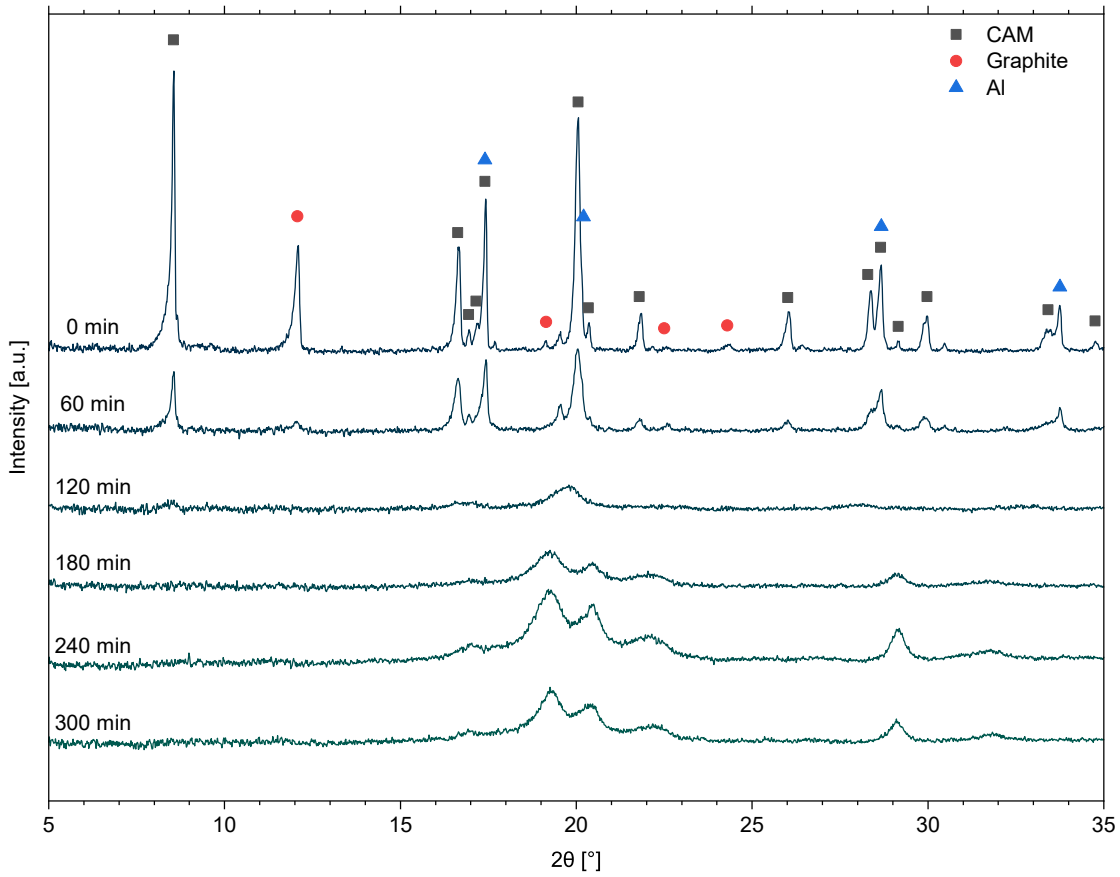


Figure 5.27: Evolution of XRD pattern during the mechanochemical processing of black mass with Al. About 4 g mixture of BM with 21.6 wt% Al was milled with 120 balls (d=6.35 mm) in alternating 5 min cycles of milling at 950 rpm and resting.[176]

The XRD phase identification was complemented with XANES measurements to analyze the reduction of transition metals. Fig. 5.28a-c displays recorded XANES spectra at the Mn-, Co- and Ni-K_α edge, respectively, for the BM milled with Al in 60-minute intervals. After the first 60 min of milling, the recorded spectra do not show any significant changes compared to the case of pristine BM. Upon further milling, all three transition metals show a gradual shift of the absorption edge towards lower photon energies, indicating their reduction. This is accompanied by a lowered white line intensity and increasing similarity in line shape to the respective metallic reference foils. The Mn-edge shows the largest shift of the absorption edge position, followed by Co and Ni showing the smallest shift. This order is reasonable considering that the oxidation states in pristine NMC are close to Mn^{4+}, Co^{3+}, and Ni^{2+} for Mn, Co, and Ni, respectively.[206] However, especially for Mn, the spectra after 300 min of milling differ from the spectra of the metallic foil, implying a partial reduction to the cubic oxide instead of straight to metals.

For further analysis of the XANES results, the obtained spectra were fitted by linear combination of the reference materials to determine the fraction of initial NMC, the transition metals and their oxides. According to Fig. 5.28d-f, the NMC fraction strongly decreases during the first 120 min

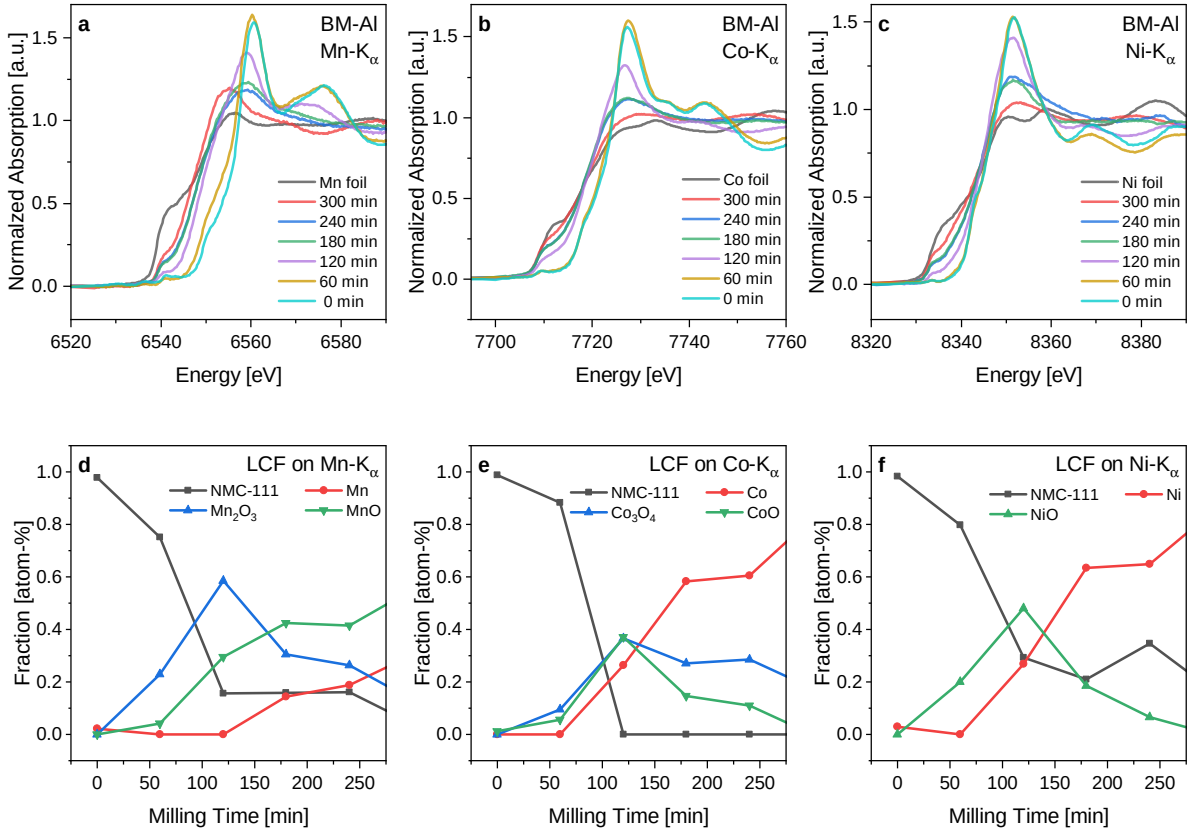


Figure 5.28: Evolution of XANES spectra during the milling process of BM with Al at the Mn- (a), Co- (b) and Ni-K_α edge (c) alongside with the spectra of respective reference metallic foils. Panels d – f) show the evolution of phase fractions in the milled powder obtained by linear combination fitting.[176]

of mechanochemical processing, in agreement with the XRD results, and then reaches a plateau (Fig. 5.27). In the same time range, the contributions from other oxides in lower oxidation states emerge, with most of them reaching the maxima after 120 minutes of milling. Although the XRD pattern showed no further changes (Fig. 5.27), the linear fits indicate a steady decrease of the respective oxide fractions except for MnO, whose atomic fraction further increases. The linear combination analysis suggests the presence of intermediate transition metal oxides, which are then further reduced by the aluminum, increasing the metallic fraction of Ni, Co, and Mn.

The obtained linear fits suggest a complete decomposition of NMC after 300 min of milling only for the absorption spectra at the Co-K_α edge (Fig. S3.5). According to the spectra at the Mn (Fig. S3.6) and Ni-K_α edge (Fig. S3.7), 5 and 15 atom% of Mn and Ni, respectively, remain as NMC in the mixture. However, these fits do not always precisely represent the recorded data due to various reasons. For instance, the powder might not consist of the reference materials as separate phases but as mixed oxides. The lithium and aluminum atoms could be incorporated into the structure, changing the local chemical environment. Moreover, the presence of other elements in the black mass could lead to the formation of non-oxide compounds as minor impurity phases. In some cases, high-energy ball-milling of graphite in the presence of Ni can even lead to the formation of carbides.[207] Although

the exact values of the fractions may not be highly accurate due to mentioned uncertainties, the overall trend of changing oxidation states can be confidently monitored through the reaction.

Combining the results of XRD and XANES, the reduction in crystallite size, the lattice strain, and intense mixing are dominant in the beginning of the process. Then, a gradual decomposition of CAM occurs, which is completed after roughly 180 min of high-energy ball-milling, and further processing results in the reduction of intermediate oxide phases. Noteworthy, no lithium containing phase besides the CAM itself could be identified in the XRD. As described in section 5.2.1 and reported in the literature, the formation of γ-$LiAlO_2$ is expected during the mechanochemical processing of CAMs with Al.[131,175,182]

However, due to suppression of the MSR, γ-$LiAlO_2$ is likely to form gradually, but persistent milling prevents the formation of a long ranged ordered crystallite lattice. Furthermore, lithium could be present as amorphous Li_2O or a Li-containing manganese oxide. To decrease the milling time for CAM decomposition in the BM, a more reactive metal than aluminum could be used instead. Therefore, Mg powder was selected as an alternative due to a low normal potential (ε_0 = -2.687 V vs. SHE for Mg/Mg^{2+})[132] in an alkaline environment. Moreover, in contrast to Al, it does not form mixed oxides with lithium, which could be beneficial for the subsequent Li extraction. The reaction between NMC and Mg is depicted in Eq. 5.14:

$$2\,LiNi_xMn_yCo_z + 3\,Mg \longrightarrow Li_2O + 3\,MgO + 2\,(Ni_xMn_yCo_z) \tag{5.14}$$

During milling of BM with Mg, an intense spike in the pressure curve was noticed after 206 min (Fig. S2.5b), followed by a remarkable rise in temperature, suggesting the MSR mechanism. This contrasts sharply with the reaction using Al as the reducing agent, where a pressure spike was not observed.

The XRD patterns for the Mg containing mixture show only minor changes during the first 180 min of milling (Fig. 5.29), such as broadening and decreasing intensity, but no new reflections. The graphite becomes XRD amorphous as indicated by the disappearing peak at 12° of 2θ. The XRD pattern of the sample collected after 240 min of milling is entirely different from those before, showing relatively sharp reflections that can be assigned to MgO and a metallic composite in a cubic structure. The peak positions of the metallic composite are shifted towards smaller angles to fit for pure Ni or Co and would match with those of Cu at room temperature. The reason could be a defect-rich structure with other atoms incorporated, which would increase the lattice parameters.

The corresponding XANES spectra in Fig. 5.30a-c show little change during the first 180 min of milling, which is consistent with the XRD analysis. Only a minor shift toward lower photon energies is evident, most notably at the Mn-edge, while the pattern's shape remains consistent. However, after 240 minutes of milling, the absorption spectra for all three K_α-edges exhibit a substantial shift in edge energy and shape, making them much more similar to the respective reference metallic foils.

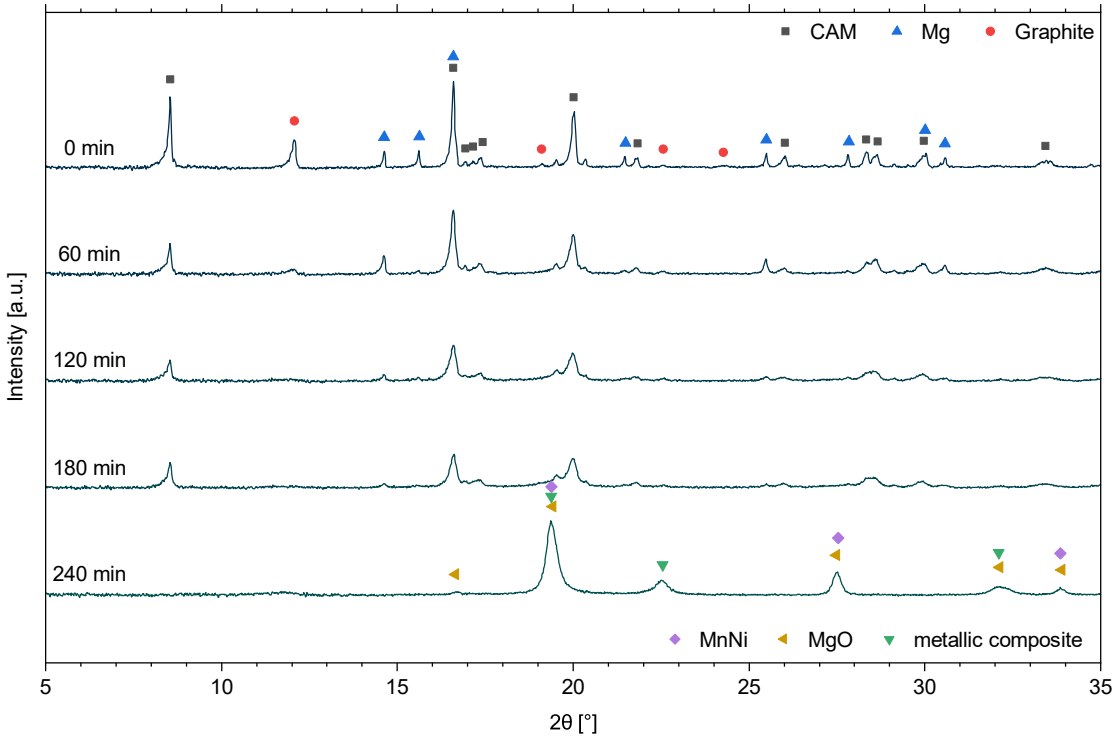


Figure 5.29: Evolution of XRD patterns during milling of the received BM with Mg.[176]

The linear combination fitting in Fig. 5.30d-f (and Figs. S3.8-S3.10) reveals a slight but continuous decrease in the NMC fraction combined with an increase in the Mn_2O_3, Co_3O_4, and NiO fractions during the initial 180 min. After 240 min of milling, the metallic fractions rise as the other compounds are further reduced.

The suppression of the MSR by graphite in Al-containing reactions versus its appearance in Mg-containing reactions is a surprising observation that needs further evaluation. The MSR process includes an activation stage at the beginning, during which the starting materials are subjected to mechanical forces applied by shear, friction, and compression. This leads to crystallite size reduction, intense mixing, and agglomeration of primary particles, while reactive surfaces form and crystalline structures degrade, as reflected in the reduced signal intensity and increased broadening of the XRD pattern of Fig. 5.27 and 5.29.

In the activation stage, the internal energy of the reactants increases, ultimately lowering the activation barrier. While shear and friction require the milling balls to slide a distance along the inner wall and so distribute mechanical energy to a relatively large amount of powder. Any collision causes the energy to be rapidly transferred to the powder that is trapped between the ball and the wall. This impact can further activate the powder or provide enough energy to overcome the reaction barrier, leading to the formation of products or intermediates while reaction heat is released. If the released heat is sufficient to overcome the activation barrier in the surrounding powder, the reduction reaction is thermally induced, and the reaction front propagates through the milling jar. However, if the reaction

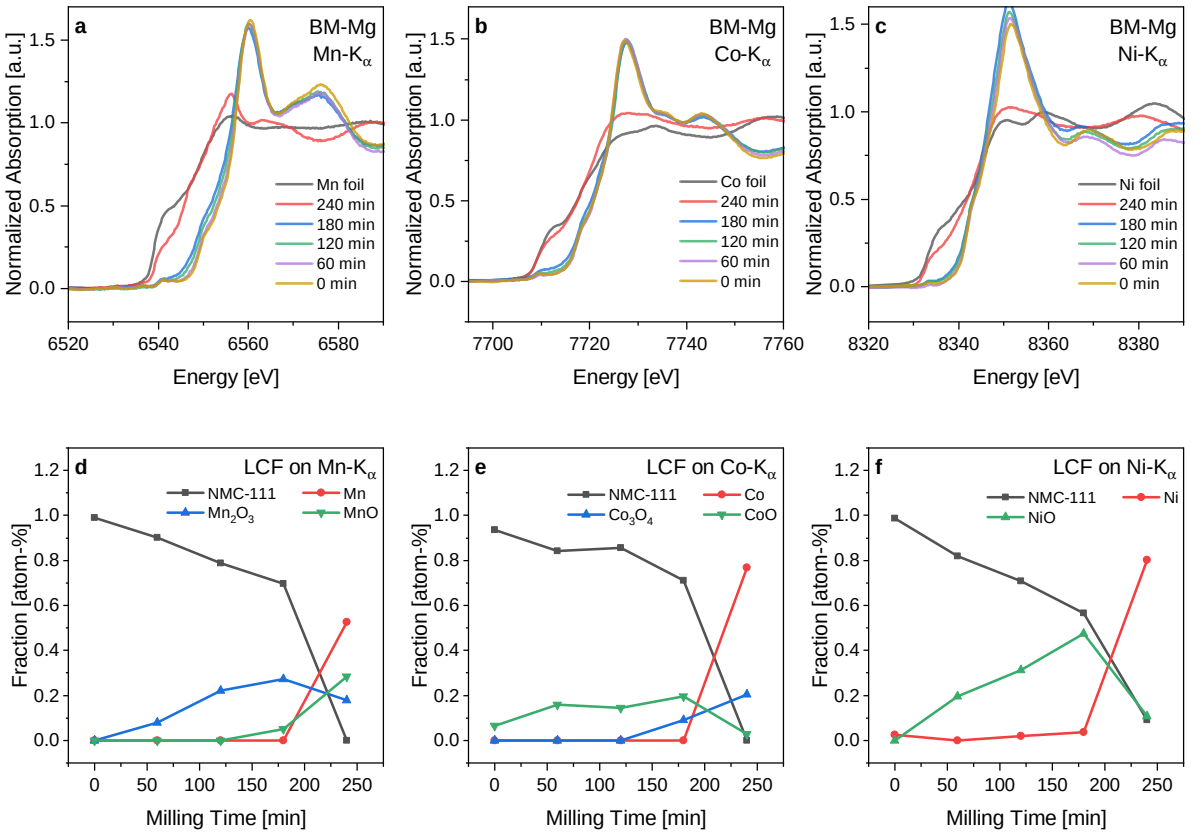


Figure 5.30: Evolution of XANES spectra during the milling process of BM with Mg at the a) Mn-, b) Co-, and c) Ni-K_α edge, alongside with the spectra of respective reference metallic foils. Panels d) – f) show the evolution of phase fractions in the milled powder obtained by linear combination fitting.[176]

heat is insufficient, the reaction cannot spread through the powder volume. The product formed during the collision acts as an inert material, causing a dilution of the system and lowering the chance of subsequent exothermic interaction. In this case, the MSR is suppressed, and the reaction proceeds continuously. This implies that the occurrence of the MSR depends on the interplay of mechanical activation and released reaction heat.[143,208]

The activation energy E_A for the oxidation of a clean Al or Mg surface is relatively low.[209–211] Therefore, it can be assumed that the activation barrier for the mechanochemical reduction of NMC primarily depends on the activation of NMC. The reaction enthalpy ΔH_R could provide an estimate of the released heat during the reaction. Assuming a complete reduction of NMC into the transition metals, this enthalpy can be calculated based on the standard enthalpy of formation provided in Table S15. The ΔH_R for the reduction of NMC with Al and with Mg are calculated to be -1.75 kJ/g and -1.69 kJ/g, respectively. As the activation energy and heat release are similar for both reducing agents, their distinct behavior is probably related to other factors. Furthermore, the Al-mediated reaction releases more heat per gram than the Mg-based reaction, which would favor the MSR for Al.

As the discrepancy between the Al and Mg system does not arise from E_A or ΔH_R, it probably arises from the different amount of powder trapped within each collision. The soft metals Mg and Al form nanocomposites with the CAMs[175] that tend to agglomerate,[88] while graphite acts as a lubricant due to exfoliation[212] and so impedes agglomeration.[213] The larger molar fraction of Mg in the milled powder compared to Al (Eqs. 5.13 and 5.14), allows for the formation of larger agglomerates, which increases the total amount of powder trapped in a collision. Consequently, the mechanical load on the powder trapped in a collision is higher in the Al system, which enhances the probability to induce a reaction. However, as the amount of powder is smaller, the released reaction heat is not sufficient to initiate the self-propagating behavior. Instead, product is formed only in the collision zone, which then dilutes the system, making a later MSR even less probable. In contrast in the Mg system, the lower mechanical load makes a reaction less probable, but when it is induced, the higher powder mass provides sufficient thermal energy to initiate the MSR.

5.3.3 The effect of milling parameters on black mass

In section 5.2.3, the effect of several milling parameters on the mechanochemical reduction of the LCO model system is demonstrated. Now, it will be tested how the ball size, the BSR, and the total filling affect the mechanochemical reduction of the black mass. Although the milling time in the Mg-mediated reaction is slightly longer than in the Al-mediated one, the sharp onset of the MSR allows for a better identification of the reaction end point. Therefore, the BM-Mg system was selected for this part of the study, using a reaction mixture of BM with 20 wt% Mg. The mechanochemical reaction was sampled in 1 h time intervals and analyzed by XRD to determine the respective milling times for complete conversion.

The rotation speed was set to 950 rpm for the balls with d = 6.35 mm and to 750 rpm for the 12.7 mm balls. The total weight of the balls was tested in the 33 - 123 g range, with a BSR ranging between 10 and 50. When using the 6.35 mm balls, the required milling time increases approximately linearly with the reciprocal of the BSR and is almost independent of the total ball mass (Fig. 5.31a). A lower 1/BSR corresponds to a higher energy transfer per unit mass of powder, leading to a faster reaction but limits the throughput. Because the milling time does not depend on the total ball mass, it can be concluded that the trajectory of an individual milling ball is only minimally influenced by the presence of other balls, and a comparable amount of powder is trapped in each collision. The collisions between a ball and the wall have the highest impact energy and typically drive the reaction. Since the number of collisions scales linearly with the number of balls (Eq. 1.10), a similar milling time can be expected for a given BSR.

In contrast, the experiments using 12.7 mm balls at 750 rpm show a strong dependency on the total ball mass (Fig. 5.31b). Full conversion was achieved significantly faster for a high loading (123 g) compared to 65 g or 33 g, which contradicts the predictions of the collision model. This behavior may be explained by high-energy ball-to-ball collisions, which are not accounted for in the model.

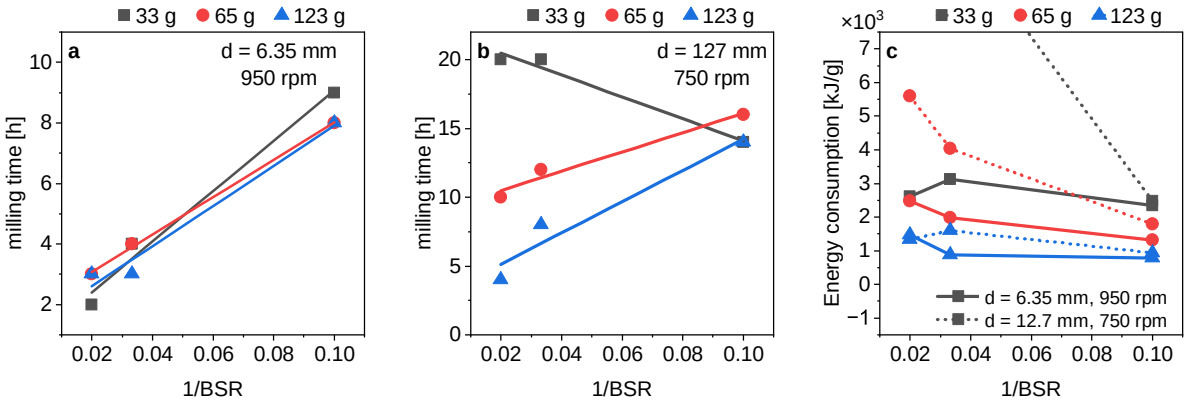


Figure 5.31: Influence of the total ball mass and the BSR on the milling time for of the mechanochemical reduction of BM with Mg using a) 6.35 mm and b) 12.7 mm balls. c) Total energy consumption of the planetary ball-mill scaled to the powder mass.[176]

Typically, these collisions are infrequent and low in energy, and therefore are neglected. However, larger spheres occupy more space in the milling vial, which could lead to more frequent ball-to-ball collisions. With the high kinetic energy of the 12.7 mm balls, even the ball-to-ball collisions could provide sufficient energy to drive the mechanochemical reaction. Interestingly, the milling time for the low loading experiments (33 g) even decreases with increasing 1/BSR. When a small number of balls and a low amount of powder is used, a substantial fraction of the powder was observed to remain at the bottom of the vial, experiencing only a few collisions and making milling inefficient.

A direct comparison of the two ball sizes shows that the reaction proceeds significantly faster when 6.35 mm balls are used. In addition to the ball size, the rotational speed plays a major role, which is set to 950 rpm for the 6.35 mm balls but limited to 750 rpm for the 12.7 mm balls to ensure safe operation. To better compare the efficiency, the energy consumption of the mill was measured, which scales linearly with the milling time. As shown in Fig. 5.31c, the specific energy consumption decreases significantly as the total mass load increases. Furthermore, while the specific energy consumption for the 6.35 mm balls is almost independent of the BSR, for the larger balls it declines strongly with increasing 1/BSR.

At a ball load of 123 g, the specific energy consumption for 6.35 mm balls operating at 950 rpm and 12.7 mm balls operating at 750 rpm is approximately the same. The difference for the two ball sizes at this condition (123 g of total ball load and BSR=10) was further analyzed using Burgios collision model.[106] The impact energy is calculated to be 203 mJ/hit and 47 mJ/hit for the 12.7 mm and 6.35 mm balls, respectively. Although the rotation speed is lower when the 12.7 mm balls are used, their larger mass results in a higher impact energy (Fig. 5.32). However, the lower impact energy of the 6.35 mm balls is overcompensated for by their much higher collision frequency of approximately 5600 hits/s versus 525 hits/s for the larger balls. Consequently, despite the shorter milling time of the 6.35 mm balls, the calculated specific milling dose is higher, indicating a less efficient energy transfer from the balls to the powder. However, when the actual energy consumption of the machine was measured instead, the 6.35 mm balls proved slightly more efficient (Fig. 5.31c).

In summary, the 6.35 mm balls are less affected by the total ball load, enabling a reliable comparison of milling times between experiments with different ball loads. Furthermore, the energy consumption is lower and the overall process for this mill is more efficient. Consequently, the 6.35 mm balls are the preferred size for experiments in this mill.

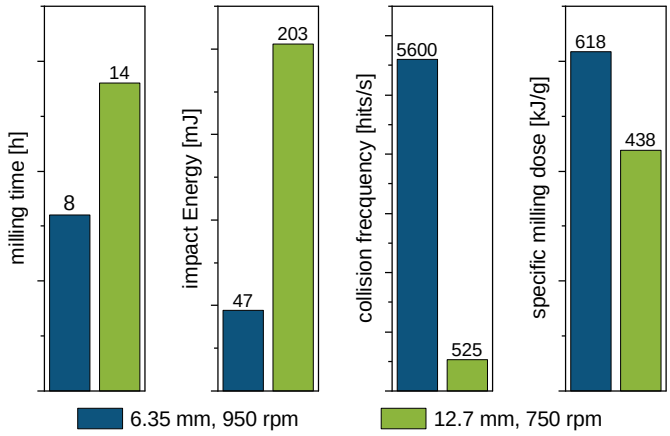


Figure 5.32: Comparison between 12.7 mm and 6.35 mm balls in the mechanochemical reduction of black mass using 20.2 wt% Mg powder, 123 g balls, and a BSR of 10.

5.3.4 The influence of volatiles and organics

The mechanochemical reduction of CAMs in the received BM with Al and with Mg requires approximately 180 min and 240 min, respectively, which is relatively long. In a model experiment for comparison, pristine NMC, mixed with 50 wt% graphite was milled with Al powder under otherwise identical milling conditions. According to XRD analysis, complete decomposition of NMC was achieved within 30 minutes (Fig. S1.7). Compared to experiments using the initial BM, the reaction rate is considerably faster, indicating that other compounds in the BM have a significant influence on the reaction kinetics. While Cu and Al are unlikely to have a major effect, residual organic compounds, including volatile electrolyte and binder, might affect the process and are relatively easy to remove. Therefore, two different pretreatments were performed before milling.

The initial BM was vacuum-dried at 180 °C to remove volatiles and the obtained solid is labeled as dried black mass (BM_{dried}). In another pretreatment, the initial BM was washed with NMP and ethyl acetate, followed by vacuum drying to eliminate volatile compounds and other organics, such as decomposition products or binder. This resulting BM is labeled as washed black mass (BM_{washed}). The TGA and dTG curves for differently treated samples of BM in Fig. 5.33 clearly show the efficiency of selected routes. The mass loss below 375 °C, which accounts for volatile compounds, is lowered from 7.9 wt% to 0.6 wt% after drying and to ≈0 wt% in the BM_{washed}. In the temperature range of 375 – 510 °C, the observed mass loss is primarily attributed to the decomposition of PVDF binder and its associated degradation products.[214] In this region, the mass loss is lowered from 2.6 wt% to

2.2 and 0.8 wt% after drying and washing, respectively. The TGA results suggest that the binder can be partially removed by washing but is almost unaffected by vacuum drying. At temperatures above 700 °C, carbothermal reduction of metal oxides occurs, resulting in further mass loss.

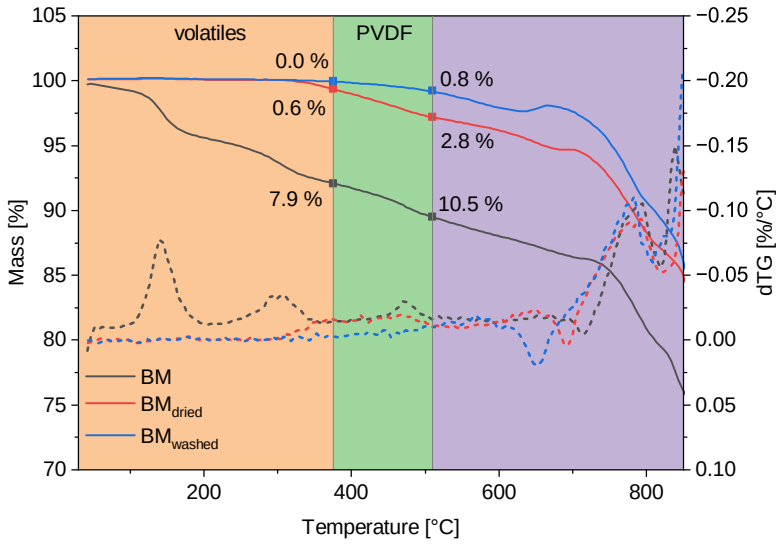


Figure 5.33: TGA (solid lines) and dTG (dotted lines) of the black mass in argon atmosphere.[176]

To test the influence of volatile compounds and binder on the kinetics of the mechanochemical reaction, powders of BM_{dried} and BM_{washed} were employed as the starting material in the high-energy milling process, using Al and Mg powders as reducing agents. In all Mg-based experiments, a spike in pressure was observed, indicating the occurrence of the MSR, whereas in the Al-based reactions the spike was never observed. Based on the linear combination fits of the sampled reactions (Figs. 5.28, 5.30, and Figs. S3.11-S3.14), a mean oxidation state has been calculated by summing the oxidation states of the reference materials, weighted by their respective atomic fractions. The evolution of mean oxidation states during the mechanochemical reduction of BM, BM_{dried} and BM_{washed} is shown in Fig. 5.34, with the enlarged data points marking the disappearance of NMC reflections in the respective XRD patterns (Figs. 5.27, 5.29, and Fig. S1.8).

When Mg is used as the reducing agent, the mean oxidation states remain essentially constant at the initial values of Mn^{4+}, Co^{3+}, and Ni^{2+}, respectively, until the transition metals begin to reduce after 140 min of milling. The corresponding spike in pressure occurs at 206, 148 and 146 minutes for the initial BM, BM_{dried} and BM_{washed}, respectively. This evolution is accompanied by a significant change in the XRD patterns (Fig. S1.8b, d), showing a transition from a slightly amorphized NMC and magnesium to a mixture of MgO and metallic composite, similar to the evolution of XRD patterns in Fig. 5.29. The removal of volatiles during the pretreatment clearly has a positive impact on the reaction kinetics, as the activation phase is reduced from 206 minutes to 148 minutes. However, the mean oxidation states (Fig. 5.34) and the XRD pattern (Fig. S1.8b, d) are essentially the same for

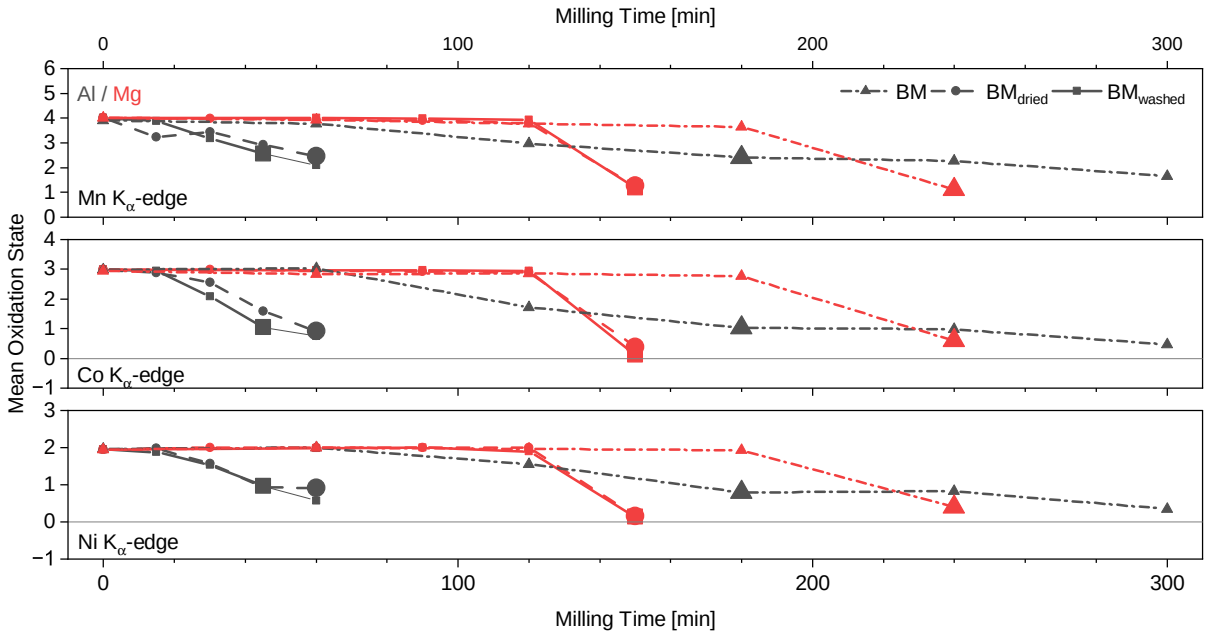


Figure 5.34: Evolution of mean oxidation state provided by XANES analysis during the mechanochemical processing of different treated BM with Al (black) and Mg (red) as the reducing agent. Enlarged data points represent the dis-appearance of NMC reflections in the XRD.[176]

BM_{dried} and BM_{washed} when milled with Mg. Therefore, washing plus vacuum drying the black mass has no benefit over just vacuum drying in the Mg system.

When Al is used as the reducing agent, the mean oxidation states decrease continuously as function of milling duration (Fig. 5.34). Both types of pretreatments significantly accelerate the reaction kinetics, reducing the milling time from 180 min to 60 min for BM_{dried} and to 45 min for BM_{washed}, respectively. The reaction for BM_{dried} is only slightly faster than for BM_{washed}, indicating a considerable impact of volatiles on the Al based mechanochemical reduction of CAMs, while residual nonvolatile organics have a minor effect.

Although the presence of volatile compounds can significantly influence the milling duration for the reduction of CAMs with Mg or Al, it does not seem to change the reaction mechanism. Such outcome can be explained based on the following considerations. Firstly, volatiles can evaporate in the hot collision zone and subsequently condense in a cooler area of the milling jar, thereby enhancing the heat dissipation from the collision zone. As a consequence, it would take more time to reach the temperature required to ignite the surrounding powder. Secondly, volatile organic compounds could react with or stabilize freshly formed, reactive metallic surfaces. Thereby, the potential energy is lowered and a more intense activation would be necessary to initiate a reaction.[215]

After washing the BM with NMP, a significant fraction of the binder is expected to be removed, but only minor differences are observed compared to reactions using the dried black mass. The binder might act as a lubricant in the mechanochemical reaction, potentially reducing shear and friction, or absorbing some of the impact energy. However, its contribution is negligible in the presence of the

large graphite fraction, which might have a similar influence. Removing volatiles from the BM by vacuum drying clearly improves reaction kinetics and is a simple treatment, whereas washing the BM provides little additional benefit but increases complexity of the pretreatment. Therefore, BM_{dried}, milled with Al and Mg, was selected for subsequent lithium extraction.

5.3.5 Selective Lithium extraction from milled black mass

One of the major potential advantages of the mechanochemical recycling process could be the selective lithium extraction from the milled BM *via* acid-free aqueous leaching to recover high purity lithium salts, that can be used for the production of new battery materials. Aqueous leaching has already been demonstrated for pristine cathode materials,[130,131] and therefore it is of practical interest to test its applicability for the industrial black mass. The vacuum-dried black mass (BM_{dried}), which was reduced with Al or with Mg, served as the starting material for the leaching experiments described in detail in section 4.3.2.

In the mechanochemical reaction of dried BM with Al, the lithium containing salts Li_2O , γ-$LiAlO_2$, or a mixture of both are formed.[131,175] In the reactions involving Mg, Li_2O is expected to be the only Li-containing compound. Although Li_2O is highly soluble in water as LiOH, the presence of Al is known to complicate aqueous extraction.[130,131] The produced transition metal composite or oxides as well as MgO and Al_2O_3 are expected to be insoluble in water. This should allow for the selective dissolution of lithium salts, their separation by filtration, and crystallization as Li_2CO_3, utilizing CO_2 from the air. The four pathways presented in Fig. 5.35 were explored for this purpose.

The phase composition of the dried and milled black mass in the course of different pathways for lithium recovery was monitored by XRD (Fig. 5.36a-d). Furthermore, the Li concentrations in the filtered liquors were measured with an ion-selective electrode after each extraction cycle. The Li extraction yields (Y_{Li}) for the four processes shown in Fig. 5.36e were calculated according to Eq. 4.1.

Aluminum mediated direct Li-extraction:
In the first extraction route, the Al-milled BM_{dried} was directly immersed in water, with subsequent filtering and drying. The recorded XRD pattern of the solid residue indicates the presence of a low-crystalline mixture (Fig. 5.36a). The largest reflections in the pattern of the milled powder are still detected after extraction and can be attributed to a metallic composite. However, additional reflections emerge, which can be assigned to lithium aluminum carbonate hydroxy hydrate (LACHH, $Li_2Al_4(CO_3)(OH)_{12} \cdot 3\,H_2O$). The XRD pattern of the recovered lithium salt shows the presence of crystalline Li_2CO_3, LiF, and LACHH. With the direct extraction, a Y_{Li} of 48 % was achieved (Fig. 5.36e). In accordance with the XRD pattern (Fig. 5.36a), elemental analysis identified Al and F-ions as the main impurities in the Li bearing solution, with 0.76 and 0.73 mg/mg_{Li}, respectively (Fig. 5.36f). The transition metals were detected in relative concentrations below 1 $\mu g/mg_{Li}$ (Fig. S4.2).

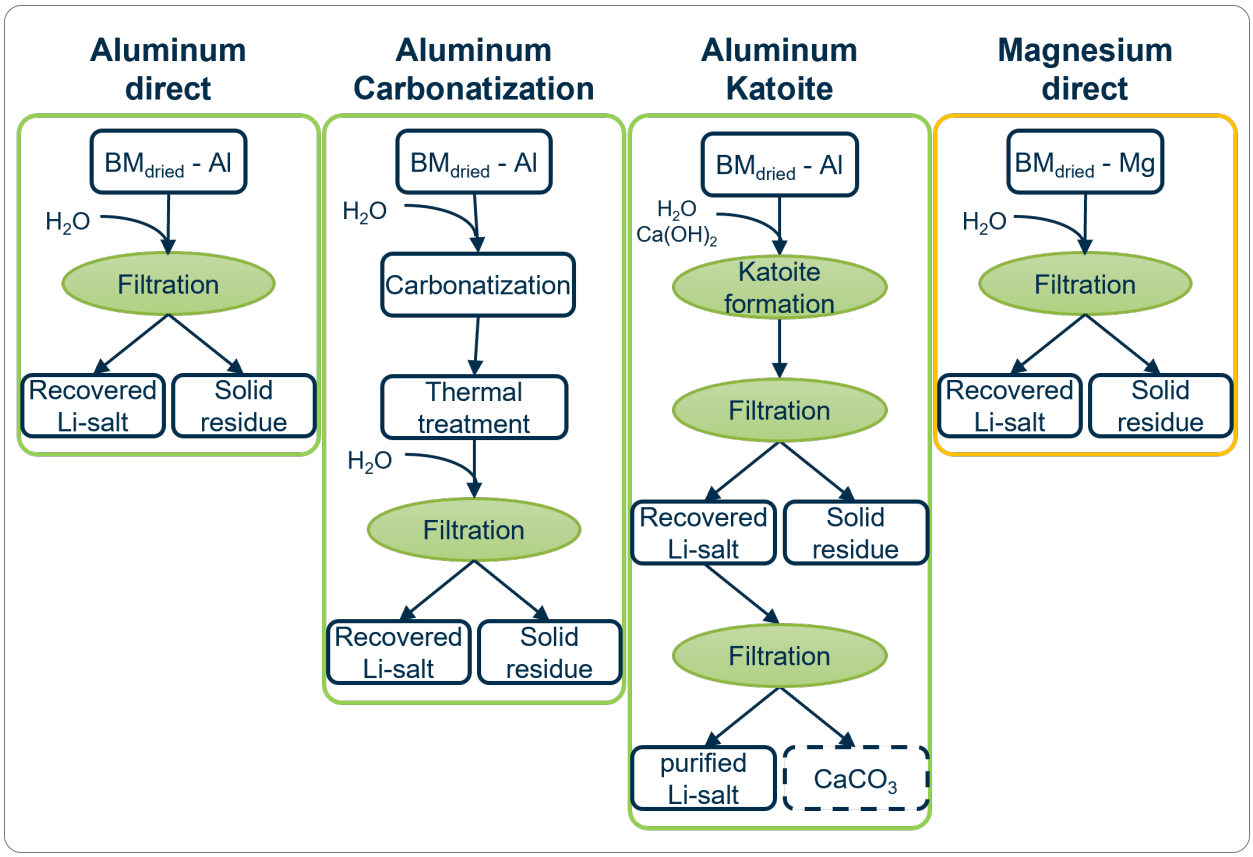


Figure 5.35: Flow sheet of the aqueous lithium extraction from milled black mass.[176]

The immersion of as-milled powder in water rises the pH of the solution due to the reaction of Li_2O and residual metallic Al with water. Due to the amphoteric character of aluminum salts, a fraction of Al^{3+} is dissolved at such alkaline conditions and react with atmospheric CO_2 to form LACHH according to the Eq. 1.14-1.16. The presence of LACHH in the insoluble fraction results in a loss in lithium extraction yield, while its presence in the soluble fraction causes Al contamination. The presence of LiF during aqueous leaching can be challenging, as its low water solubility hinders the extraction of lithium and leads to fluorine contamination in the final product. Nonetheless, Y_{Li} is still slightly higher compared to the extraction yield of pristine NMC, milled with Al ($Y_{Li} = 35$ %).[131] The presence of graphite and suppression of MSR are supposed to lead to smaller particle sizes, which might increase leaching efficiency. The fluoride ions likely originate from the decomposition of electrolyte salt $LiPF_6$ during BM production and from PVDF decomposition during ball-milling.

Aluminum - *Carbonatization* Process:

The *Carbonatization* route in Fig. 5.35 was adapted from Dolotko et al.,[131] to address the Li loss and Al contamination caused by LACHH formation. This route is based on facilitating the LACHH formation (Eq. 1.14-1.16) during the carbonatization step and its subsequent thermal decomposition according to Eq. 1.17.

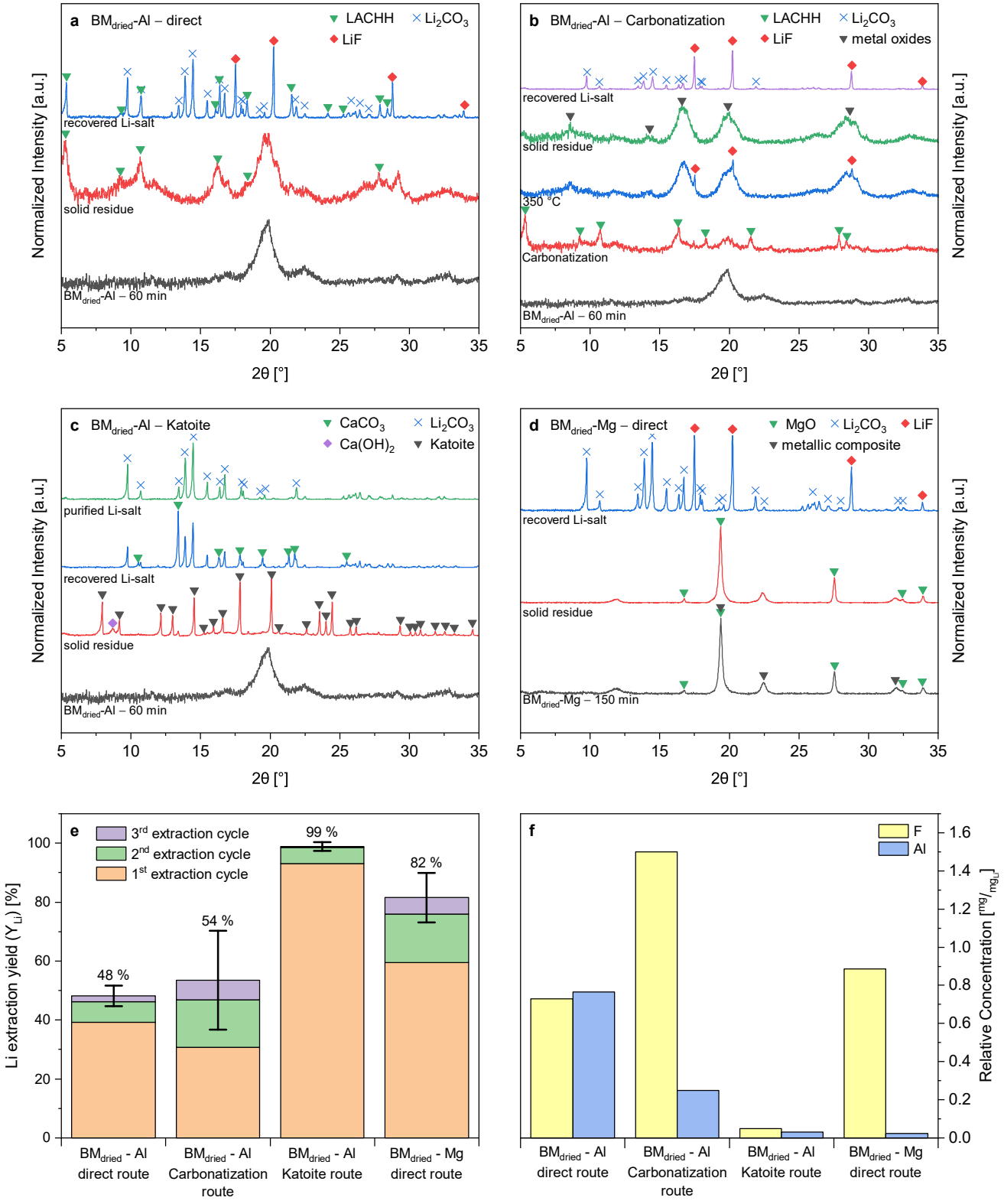


Figure 5.36: Evolution of XRD during the aqueous lithium extraction of dried BM milled with Al a)-c) and Mg d). Separation was per-formed by direct filtration a) and d), after *Carbonatization* b) and after *Katoite* process c). Panel e shows the Li extraction yield. The error bars indicate the spread of two independent extraction experiments. Panel f) shows the relative concentrations of Al and F-ions in the recovered Li salt solution.[176]

Fig. 5.36b shows the evolution of the XRD pattern during the *Carbonatization* route. The formation of LACHH is clearly visible during the carbonatization step, followed by its decomposition during heating. However, in addition to LACHH transformations, new reflections appear after heating to 350 °C, indicating the formation of transition metal oxides and the crystallization of LiF. Subsequent aqueous extraction helps to separate the mixture of LiF and Li_2CO_3 from the insoluble fraction, containing graphite, transition metals and their oxides. Fig. 5.36e illustrates that Y_{Li} is slightly higher in the *Carbonatization* process (55 %) compared to the direct extraction (48 %). However, the extraction yield falls short of the expectations outlined in a previous study (74 %).[131]

The relative content of Al in the recovered lithium saline solution is much lower in the *Carbonatization* process than in the direct extraction, but the relative concentration of F-ions is twice as high (Fig. 5.36f), which is consistent with the XRD results in Fig. 5.36b. Moreover, the concentrations of all transition metal ions are also the highest of all four processes (Fig. S4.2). The XRD pattern after the thermal treatment of the *Carbonatization* process (Fig. 5.36b) indicates the formation of transition metal oxides. The oxides of manganese are known to react with lithium salts and form a lithium manganese oxide at high temperatures or in hydrothermal reactions.[49,216,217] Although the crystallinity of the material is low, the presence of $LiMn_2O_4$ in the solid residue is very likely (Fig. S1.9). Beside the incomplete decomposition of LACHH, the formation of lithium manganese oxides during thermal treatment or subsequent aqueous leaching can explain the low Y_{Li}. Furthermore, the high temperature facilitates the leaching of transition metals (Fig. S4.2) and leads to a higher fluoride concentration in the recovered lithium salt (Fig. 5.36f), probably due to thermal decomposition of PVDF. As a consequence, the *Carbonatization* process can effectively reduce Al contamination of recovered Li salts but suffers from low Y_{Li} and fluoride contamination, when applied to a BM. Therefore, a third process was developed.

Aluminum - *Katoite* Process:

As various modifications to the first and second processes were also tested to increase both the yield and the purity of the Li-containing solution, with particular attention paid to the removal of fluoride salts. A common method for precipitating F^- ions from the solution involves the addition of calcium salts. In this case, the use of calcium hydroxide is attractive, as it does not introduce any additional contamination from the anion. However, the Li-containing solution is very alkaline (pH=13–14) and consequently $Ca(OH)_2$ precipitates, whereas CaF_2 does not form, preventing simple fluoride removal.

In contrast, a combination of the high-temperature leaching step and an excess of $Ca(OH)_2$ proved promising. At elevated temperatures, $Ca(OH)_2$ reacts with the Al-salts to form $Ca_3Al_2(OH)_{12}$, and LiF becomes thereby undetectable by XRD. This observation served as the basis for the development of the *Katoite* process, named after the mineral with the chemical formula $Ca_3Al_2(OH)_{12}$. Furthermore, experiments showed a slight sensitivity of the Katoite formation towards CO_2, which is consistent with the literature.[218]

In the final version of the process, as it is described in 4.3.2, DI water was boiled to remove CO_2 and according to Eq. 5.15, $Ca(OH)_2$ was added in a 3:2 molar ratio regarding to the Al used to reduce the BM. To this hot suspension, the milled BM_{dried}-Al mixture was added to transform γ-$LiAlO_2$ into Katoite.

$$2\,LiAlO_2 + 3\,Ca(OH)_2 + 4\,H_2O \longrightarrow Ca_3Al_2(OH)_{12} + 2\,LiOH \tag{5.15}$$

With the formation of insoluble Katoite, highly soluble LiOH is formed, which can be separated by filtration, as the XRD pattern in Fig. 5.36c confirms. This results in a high Y_{Li} of 99 %, with 93 % already in the first extraction cycle (Fig. 5.36e). Simultaneously, dissolved Al^{3+} ions are consumed to form the Katoite. Thereby, the fluoride ions can either be adsorbed on the surface, forming a CaF_2-layer or the ions can participate in the Katoite formation reaction by substituting OH^- in the lattice to yield $Ca_3Al_2(OH)_{12-x}F_x$.[219,220] In the XRD of the solid residue, only reflections of Katoite and $Ca(OH)_2$ are detectable (Fig. 5.36c), whereas no peaks are visible at the expected positions for CaF_2. Accordingly, the formation of $Ca_3Al_2(OH)_{12-x}F_x$ seems more likely.

The fluoride content in the reaction can be estimated from the amount of binder present. The milled powder consists of 83 wt% BM, which contains 3 wt% PVDF binder. Since PVDF contains 59 wt% fluorine and, therefore, each gram of milled powder contains roughly 15 mg of F (0.77 mmol) and 170 mg of Al (6.3 mmol). Katoite incorporates six OH^- ions per Al atom, so at most about 2 % of the OH^- sites could be substituted by F^-.

Consequently, the content of Al and F-ion impurities in the recovered lithium salt is relatively low (Fig. 5.36f). Furthermore, the XRD pattern of the recovered lithium salt (Fig. 5.36c) reveals the presence of $CaCO_3$. It forms from unreacted $CaOH_2$ at contact with atmospheric CO_2, implying that not all Al is available for the formation of Katoite phase. However, a second filtration is sufficient to remove $CaCO_3$ impurities resulting in the pure Li_2CO_3 phase. Elemental analysis by ICP-OES and ISE validated a purity for the recovered Li_2CO_3 of 98.2 % (Table S18).

Although the *Katoite* Process allows remarkable Y_{Li} and high purity, the process can benefit from further improvements. Most Li (93 %) is extracted within the first leaching cycle, which meets typical recovery benchmarks, and the other two leaching steps are not strictly necessary. Also the water volume could be minimized to reduce costs for heating and evaporation. Moreover, an optimized Al content will reduce the demand for $Ca(OH)_2$ and therefore reduce costs and waste generation.

Furthermore, the subsequent processing has to be considered. After the aqueous extraction, the formed Katoite is mixed with the transition metal compounds in the insoluble fraction. This would lead to excessive acid consumption in a subsequent hydrometallurgical process to recover transition metal oxides. Therefore, additional techniques, such as froth flotation, should be tested before any acid treatment to separate katoite from the transition metal compounds, which could reduce chemical consumption.

Magnesium mediated direct Li-extraction:
The BM_{dried} reduced with Mg was directly extracted with water in the fourth process. The XRD patterns of the dried residual solid and recovered Li salt are presented in Fig. 5.36d. The pattern of the insoluble part closely resembles that of the as-milled powder, displaying reflections from MgO and the metallic composite. Although this extraction pathway is very similar to the first process, about 82 % of Li was extracted (Fig. 5.36e), which can be attributed to the absence of Al compounds. As shown in Fig. 5.36d, the recovered Li salts consist of Li_2CO_3 and LiF. The lithium extraction yield is lower than expected according to Eq. 5.14, most likely because LiF is poorly soluble and Mg promotes the MSR mechanism, potentially leading to coarse agglomerates.[175] This results in low co-extraction of transition metals (Fig. S4.2), but the agglomerates could contain Li-salt inclusions, which are inaccessible to water and therefore the extraction yield might be lowered.

According to the XRD pattern and ICP-OES results (Fig. 5.36d,f), the major impurity of the recovered Li-containing phase from the $BM_{dried}-Mg$ system is LiF. A purification route is proposed to eliminate fluoride salts, and the corresponding XRD patterns of the solids collected during this process are presented in Fig. 5.37. As discussed above, the high pH of the solution prevents effective F^- removal by CaF_2 precipitation. Consequently, the pH was lowered for the purification using HCl. At $pH = 5$, a $CaCl_2$-solution was added, resulting in a colorless precipitate, identified as CaF_2 and some $CaCO_3$. The excess of Ca^{2+} ions was subsequently precipitated as carbonate using Na_2CO_3. Afterwards, the solution was concentrated, which resulted in the precipitation of Li_2CO_3, while most Na^+ ions remain in solution. A final recrystallization yielded Li_2CO_3 of 99.9 % purity, theoretically fulfilling the specification for battery production. Although the purity is very high, approximately 30 wt% Li is lost during the process. Most of the lost Li remains in solution during the recrystallization step and could be, in principle, added to a new batch.

5.4 Further optimization and process implementation

During the doctoral project, the milling time, the lithium extraction yield, and the Li_2CO_3 purity were successfully optimized. Nevertheless, several parameters require further investigation in order to minimize both chemical and energy consumption.

One major parameter is the optimization of the Al consumption. On the one hand, Al as the current collector is one fraction of the battery waste stream and is therefore considered to be cheap, and it is expected to lower the required milling time. On the other hand, the $Ca(OH)_2$ amount required in the *Katoite* process scales with the aluminum content. Consequently, in downstream processes more Katoite has to be separated or worse, dissolved if more Al is used. Moreover, Al contamination in final transition metal sulfates was found to be critical in the production of NMC materials and should be eliminated.[221] Therefore, the Al consumption should be as low as possible.

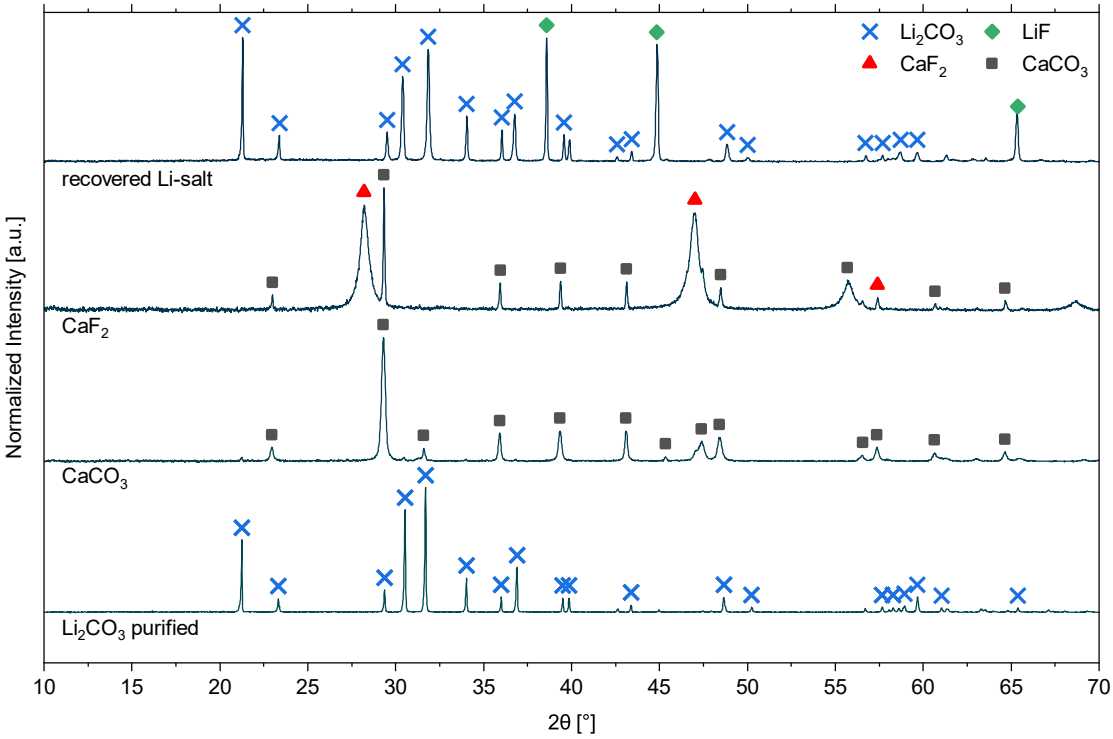


Figure 5.37: Evolution of XRD pattern during the purification process of the Li salt solution. The pattern were collected using Cu-$K_{\alpha 1}$ radiation.

For aqueous leaching, large volumes of DI water are currently used. DI water is expensive and evaporation is energy intensive. Therefore, the water use requires further optimization. This is particularly feasible in the *Katoite* process, where 93 % of Li is already extracted in the first leaching cycle.

Furthermore, the developed process should not be evaluated as a stand alone methodology but should be thought of as an integrated step in a full recycling process. From an upstream perspective, the process is well suitable for integration because the processing of black mass was successfully demonstrated. In future work, the downstream integration has to be addressed with particular emphasis on the efficient recovery of the TMs.

After the Katoite-based Li extraction, the insoluble residue contains graphite, transition metals, and Katoite. Although it is possible to dissolve Katoite together with the TMs in acid, such an approach would require substantial acid consumption and would generate large volumes of liquid waste. Preserving Katoite by avoiding its dissolution is therefore desirable. Alternative strategies such as selective dissolution of the TMs or physical separation techniques, such as froth flotation, should be tested.

Flotation can also be beneficial for graphite recycling, which is becoming an increasingly important topic.[194,222,223] After the mechanochemical treatment, the graphite becomes exfoliated and distorted,

so it is unclear whether it can be reused as an anode material. A first study in this direction was published by Schiavi et al. in collaboration, who compared graphite waste from different LIB pretreatment processes for the production of reduced graphene oxide using Hummers' method.[194]. The graphite recovered from the mechanochemical treatment yielded the highest amount of reduced graphene oxide (96 %), exceeding the yield from pristine graphite, and from graphite recovered from a purely mechanical or thermal pretreatment. However, its application as an anode material in an actual battery has not yet been tested.

5.5 Safety Considerations

The presented mechanochemical processing of NMC based black mass with a strong reductant such as metallic Mg or Al can provide an attractive alternative route to traditional recycling methods. However, this comes along with some risks that should be taken into account.

The fundamental reduction is a highly exothermic reaction that can proceed *via* an MSR mechanism. Through parameterization, ranges were identified in which the undesirable MSR is suppressed. Nevertheless, it must be noted that different compositions in the BM can shift this range and that significant amounts of heat must be dissipated when processing large quantities of material.

Furthermore, if a MSR takes place during BM processing, pressure spikes of up to 10 bar were detected, which can be significantly lowered by prior drying or washing of the BM. This suggests that some components of the BM vaporize or decompose into gaseous products at the high temperatures of the milling process or during the MSR. Such pressure spikes always carry the risk of an explosion if they are not taken into account. Therefore, a pre-dried BM with at least 20 wt% graphite should be processed with Al as the option with the lowest risk.

After ball-milling, a very fine powder consisting of oxides, metallic composites, and mechanically stressed graphite is produced. This mixture proved to be highly sensitive to atmospheric oxygen and moisture. Upon exposure to the air, the powder becomes very hot and may even self-ignite.

A similar phenomenon has been observed observed by Zhu et al. when milling graphite with steel balls in the presence of dry ice. When the milling vials were opened to the air, it resulted in intense sparking that was attributed to the hydration of reactive carbon species.[224,225] During high-energy ball-milling of graphite containing BM, the graphite is subjected to severe mechanical stress, as it is indicated by the peak broadening in the XRD pattern. The mechanical stress can lead to bond breaks as well as the formation of radicals, which can be highly reactive. When exposed to air, exothermic reactions occur that can ignite the powder. Very fine metallic particles in the milled BM could further intensify this effect once it is ignited.

On a laboratory scale, the risk can be easily mitigated by carefully introducing air into the milling vial, so that the powder reacts slowly and in a controlled manner without igniting. An alternative

option is to work under an inert condition while transferring the powder from the milling vial to the water for leaching.

In the leaching step, gas formation was observed when the freshly milled powder was added to water, particularly when working under an inert atmosphere. The resulting gas is most likely hydrogen, produced by the reaction of reactive metal surfaces with water. In combination with air, hydrogen forms an explosive mixture in the range of 4 vol% to 77 vol%.[226] However, this risk can be effectively resolved through appropriate gas venting.

Another hazard comes from the powder itself. The very fine powder produced after ball-milling can easily be stirred up and forms toxic aerosols. Transition metals and their related compounds, in particular, are harmful to health. Exposure through the skin, mucous membranes, or lungs must be avoided at all costs, which requires careful and safe handling of the powder, for insance in a dedicated cabinet.

6 Summary

This work expands the understanding of the mechanochemical reduction of layered-oxide cathode active materials and demonstrates the transfer of the process to an industrial battery black mass, with subsequent aqueous based selective lithium extraction with high yields and purity.

First, it was shown that the mechanochemical reaction in the lithium cobalt oxide (LCO) - aluminum model system proceeds *via* the mechanically-induced self-propagating reaction (MSR) mechanism, producing metallic cobalt and $LiAlO_2$. The abrupt rise in temperature, characteristic of this mechanism, temporally exceeds the melting point of the reaction products. In the molten state, cobalt separates from the other phases, allowing the recovery of large metallic pieces after cooling. As the milling vial is tightly sealed, the abrupt temperature rise causes a remarkable spike of the internal pressure, which proved valuable for systematic investigations of process parameters.

Subsequent experiments revealed that other elements, such as magnesium, silicon, and phosphorus, also react via the mechanically-induced self-propagating reaction mechanism with LCO, whereas sulfur proceeds in a more gradual reaction. The collision model based calculations provided additional insights into the energetic situation and enabled quantitative assessment of process parameters. Larger milling balls exhibit higher theoretical efficiency, based on the maximal energy transfer from the balls to the powder, but their performance is strongly influenced by variations in the ball-to-sample mass ratio and the total material load, making cross-experiment comparison difficult. Consequently, the 6.35 mm balls were preferred in most experiments.

A key finding is that graphite suppresses the mechanically-induced self-propagating reaction. When the graphite mass fraction exceeds 20 wt%, the reaction between LCO and aluminum shifts from the abrupt MSR to less instantaneous kinetics. Although the overall reaction rate declines, this moderation is advantageous for practical applications. The lower temperatures and pressures, as well as their slower changes and smaller temperature gradients, result in less stress in the milling media and improve process control and safety.

Before applying the process to the industrial black mass, it was thoroughly characterized by various techniques. In addition to 47 wt% cathode active material, the black mass contains 36 wt% graphite, which was sufficient to suppress the MSR in the aluminum mediated system. The cathode active material appeared to be a mixture of different lithium nickel manganese cobalt oxide (NMC) materials with an overall elemental composition close to NMC-111. Furthermore, approximately 9 wt% of volatile compounds, such as water, organic carbonates, and ether, as well as around 3 wt% fluoride based binder, have been quantified.

In the mechanochemical reduction of black mass with aluminum powder, laboratory scale X-ray absorption spectroscopy proved to be a powerful tool to track the reaction progress complementing

X-ray diffraction. The data demonstrate a gradual reduction of the transition metals in the NMC material, which intermediately form oxides and subsequently approach the metallic state.

In contrast to the aluminum mediated reaction, a MSR is observed in the black mass - magnesium system. The reason why the MSR is suppressed for aluminum but not for magnesium remains unclear. A plausible explanation is the higher volume fraction of magnesium, which promoted agglomeration and increased physical contact with NMC particles. Surprisingly, despite the presence of MSR, the total milling time in the magnesium system exceeds that of the aluminum system.

Furthermore, volatile components, which contribute approximately 9 wt% to the black mass, drastically slow down the reaction kinetics. Most likely, these components evaporate in the hot collision zone, thereby contributing to a fast energy dissipation and reducing the stress imparted to the NMC, magnesium, and aluminum particles. The elimination of volatiles, for instance by vacuum drying, markedly shortens the milling time from 3 h to 1 h in the aluminum system and from 4 h to 2.5 h in the magnesium system. By contrast, the binder shows a negligible effect under the tested reaction conditions.

The dried and mechanochemically reduced black mass was then subjected to several extraction pathways for the lithium extraction. Evaluation of the lithium extraction yields and the purity of the obtained filtrates reveals that the presence of aluminum and fluoride poses significant challenges to the mechanochemical induced lithium extraction process from black mass. The direct extraction of the Al-reduced black mass yields a lithium extraction efficiency of 48 %, but suffers from high aluminum and fluoride contamination. Unexpectedly, the *Carbonatization* process does not significantly improve lithium recovery. The heating step, involved in this process, promotes the formation of lithium manganese oxides and enhances fluoride dissolution, which lowered purity and yield of the recovered lithium salts.

The newly developed Katoite process addresses these issues by adding $Ca(OH)_2$, which reacts with $LiAlO_2$ to form $Ca_3Al_2(OH)_{12}$ and LiOH. This rises the lithium extraction yield to approximately 99 %, while greatly reducing the contamination of other ions. The direct extraction of black mass milled with magnesium also shows a high extraction yield (82 %) and a low aluminum content, but at the expense of fluoride impurities. A subsequent purification process, that includes pH adjustment for efficient CaF_2 precipitation yielded Li_2CO_3 in 99.9 % purity.

7 Conclusions

As summarized in the previous section, it can be concluded that an industrial lithium-ion battery black mass can be reduced using a reactive metal, such as aluminum, in a high-energy ball-milling process, allowing for selective lithium extraction. Within the work, the key performance parameters, such as the milling time, the lithium extraction yield, and product purity, were optimized.

While a mixture of layered oxide cathode active material and aluminum proceeds *via* the mechanically induced self-propagating reaction mechanism, the graphite naturally present in the black mass suppresses such an abrupt reaction, shifting the process to gradual kinetics. Consequently, the milling time is longer, but the process operation is safer and better scalable, as intense and instantaneous temperature and pressure changes no longer occur. Volatile compounds in the black mass, such as water or carbonates, should be removed from the input material prior to the mechanochemical process, for instance by vacuum drying, as they drastically reduce the reaction kinetics.

During aqueous leaching, the formation of lithium aluminum carbonate hydroxy hydrate and lithium fluoride poses significant challenges for the selective lithium extraction. Because both compounds are poorly soluble in water, they significantly reduce the lithium recovery rate and the purity of the final product. The newly developed Katoite process simultaneously eliminates aluminum and fluoride impurities by the formation of $Ca_3Al_2(OH)_{12}$, and allows for an almost quantitative lithium extraction with high purity. A current limitation of this process is that the transition metals in the insoluble residue are mixed with the Katoite afterwards, and their separation has not been investigated yet.

With further process optimization, the combination of solvent-free, high-energy ball-milling of black mass with aluminum from the current collector and the *Katoite* process for lithium extraction offers great potential for a sustainable, cost-effective recycling route for lithium-ion battery black mass.

8 Outlook

Future work should focus on minimizing the aluminum and water consumption, the implementation of downstream processes for transition metal recovery, and scaling of the process. In particular, the efficient separation of Katoite from the transition metal compounds will improve the overall viability. Thereafter, the complete process should be evaluated by life cycle assessment or similar tools. Moreover, the process may be adapted to treat other valuable waste streams that are currently difficult to recycle, such as rare earth based magnets.

Beyond the application-oriented objectives, some fundamental scientific questions remain that are worth to investigate in the future. Although the reaction between LCO and aluminum has been demonstrated to proceed *via* the MSR mechanism, the microstructural changes that ultimately trigger the reaction have not been identified yet. Moreover, it is unclear whether mechanical activation is primarily localized at the cathode active material, at the aluminum, or whether particle fragmentation and thorough mixing dominate. Likewise, the relative contributions of compressive forces in collisions and shear stress during ball sliding to reaction initiation are not understood. Targeted tribological experiments with various loading conditions and setups could provide valuable insights.

References

(1) *Lithium-Ion Batteries: Basics and Applications*; Korthauer, R., Ed.; Springer Berlin Heidelberg: Berlin, Heidelberg, 2018.

(2) Wulandari, T.; Fawcett, D.; Majumder, S. B.; Poinern, G. E. J. Lithium-Based Batteries, History, Current Status, Challenges, and Future Perspectives. *Battery Energy* **2023**, *2*, 20230030.

(3) Krishnan, R.; Packirisamy, V.; Palani, D.; Ariyamuthu, R. Historical Perspective in Technological Advances in Lithium-Ion Battery Development. *JCIS Open* **2026**, *21*, 100163.

(4) Moeller, K.-C. In *Lithium-Ion Batteries: Basics and Applications*, Korthauer, R., Ed.; Springer Berlin Heidelberg: Berlin, Heidelberg, 2018, pp 3–10.

(5) European Council; European Parliament Regulation (EU) 2024/1252 of the European Parliament and of the Council of 11 April 2024 Establishing a Framework for Ensuring a Secure and Sustainable Supply of Critical Raw Materials and Amending Regulations (EU) No 168/2013, (EU) 2018/858, (EU) 2018/1724 and (EU) 2019/1020Text with EEA Relevance. *Off. J. Eur. Communities: Legis.* **2024**, 1–67.

(6) Garlapati, K. K.; Dutta, J.; Panigrahi, B. B.; Martha, S. K. Correlative Insights into the Degradation Pathways and Direct Regeneration Healing Mechanisms of Spent Lithium-Ion Battery Active Materials. *J. Power Sources* **2025**, *650*, 237528.

(7) Frith, J. T.; Lacey, M. J.; Ulissi, U. A Non-Academic Perspective on the Future of Lithium-Based Batteries. *Nat. Commun.* **2023**, *14*, 420.

(8) Ma, X.; Meng, Z.; Bellonia, M. V., et al. The Evolution of Lithium-Ion Battery Recycling. *Nat. Rev. Clean Technol.* **2025**, *1*, 75–94.

(9) Chacana-Olivares, J.; Peceño, B.; Grageda, M., et al. Lithium-Ion Battery Recycling: A Perspective on Key Challenges and Opportunities. *npj Mater. Sustain.* **2025**, *3*, 38.

(10) European Parliament; European Council Regulation (EU) 2023/ of the European Parliament and of the Council of 12 July 2023 Concerning Batteries and Waste Batteries, Amending Direc Tive 2008/98/EC and Regulation (EU) 2019/1020 and Repealing Directive 2006/66/EC. *Off. J. Eur. Communities: Legis.* **2023**, *191*, 1–117.

(11) Directorate-General for Research and Innovation (European Commission), *Horizon Europe Strategic Plan 2021-2024*; Publications Office of the European Union: 2021.

(12) Leuthner, S. In *Lithium-Ion Batteries: Basics and Applications*, Korthauer, R., Ed.; Springer: Berlin, Heidelberg, 2018, pp 13–19.

(13) Mizushima, K.; Jones, P. C.; Wiseman, P. J.; Goodenough, J. B. Li_xCoO_2 ($0 < X \leq 1$): A New Cathode Material for Batteries of High Energy Density. *Mater. Res. Bull.* **1980**, *15*, 783–789.

(14) Manthiram, A. A Reflection on Lithium-Ion Battery Cathode Chemistry. *Nat. Commun.* **2020**, *11*, 1550.

(15) Mikami, M.; Saito, J.; Ochiai, T., et al. Controlling Lithium Cobalt Oxide Phase Transition Using Molten Fluoride Salt for Improved Lithium-Ion Batteries. *Commun. Mater.* **2024**, *5*, 108.

(16) Akhilash, M.; Salini, P. S.; John, B.; Mercy, T. D. A Journey through Layered Cathode Materials for Lithium Ion Cells – From Lithium Cobalt Oxide to Lithium-Rich Transition Metal Oxides. *Journal of Alloys and Compounds* **2021**, *869*, 159239.

(17) Myung, S.-T.; Maglia, F.; Park, K.-J., et al. Nickel-Rich Layered Cathode Materials for Automotive Lithium-Ion Batteries: Achievements and Perspectives. *ACS Energy Lett.* **2017**, *2*, 196–223.

(18) Yuan, L.-X.; Wang, Z.-H.; Zhang, W.-X., et al. Development and Challenges of LiFePO4 Cathode Material for Lithium-Ion Batteries. *Energy Environ. Sci.* **2011**, *4*, 269–284.

(19) Graf, C. In *Lithium-Ion Batteries: Basics and Applications*, Korthauer, R., Ed.; Springer Berlin Heidelberg: Berlin, Heidelberg, 2018, pp 29–41.

(20) IEA *Global Critical Minerals Outlook 2025*; Paris: IEA, 2025.

(21) Koech, A. K.; Mwandila, G.; Mulolani, F.; Mwaanga, P. Lithium-Ion Battery Fundamentals and Exploration of Cathode Materials: A Review. *S. Afr. J. Chem. Eng.* **2024**, *50*, 321–339.

(22) Rani, B.; Yadav, J. K.; Saini, P.; Dixit, A. $LiMn_2O_4$ as a Cathode Material: Challenges and Opportunities for Lithium-Ion Batteries. *Sustainable Energy Fuels* **2025**, *9*, 4262–4285.

(23) Zou, F.; Manthiram, A. A Review of the Design of Advanced Binders for High-Performance Batteries. *Adv. Energy Mater.* **2020**, *10*, 2002508.

(24) Yi, X.; Qi, G.; Liu, X., et al. Challenges and Strategies toward Anode Materials with Different Lithium Storage Mechanisms for Rechargeable Lithium Batteries. *J. Energy Storage* **2024**, *95*, 112480.

(25) Wurm, C.; Oettinger, O.; Wittkaemper, S., et al. In *Lithium-Ion Batteries: Basics and Applications*, Korthauer, R., Ed.; Springer Berlin Heidelberg: Berlin, Heidelberg, 2018, pp 43–58.

(26) Wang, X.-T.; Gu, Z.-Y.; Ang, E. H., et al. Prospects for Managing End-of-Life Lithium-Ion Batteries: Present and Future. *Interdiscip. Mater.* **2022**, *1*, 417–433.

(27) Hartnig, C.; Schmidt, M. In *Lithium-Ion Batteries: Basics and Applications*, Korthauer, R., Ed.; Springer: Berlin, Heidelberg, 2018, pp 59–74.

(28) Liu, Y.-K.; Zhao, C.-Z.; Du, J., et al. Research Progresses of Liquid Electrolytes in Lithium-Ion Batteries. *Small* **2023**, *19*, 2205315.

(29) Manthiram, A.; Yu, X.; Wang, S. Lithium Battery Chemistries Enabled by Solid-State Electrolytes. *Nat. Rev. Mat.* **2017**, *2*, 16103.

(30) Deimede, V.; Elmasides, C. Separators for Lithium-Ion Batteries: A Review on the Production Processes and Recent Developments. *Energy Technol.* **2015**, *3*, 453–468.

(31) Weber, C. J.; Roth, M. In *Lithium-Ion Batteries: Basics and Applications*, Korthauer, R., Ed.; Springer: Berlin, Heidelberg, 2018, pp 75–88.

(32) Tembo, P. M.; Dyer, C.; Subramanian, V. Lithium-Ion Battery Recycling—a Review of the Material Supply and Policy Infrastructure. *NPG Asia Mater.* **2024**, *16*, 43.

(33) Örüm Aydin, A.; Zajonz, F.; Günther, T., et al. Lithium-Ion Battery Manufacturing: Industrial View on Processing Challenges, Possible Solutions and Recent Advances. *Batteries* **2023**, *9*, 555.

(34) Nekahi, A.; Feyzi, E.; Srivastava, M., et al. Advanced Lithium-Ion Battery Process Manufacturing Equipment for Gigafactories: Past, Present, and Future Perspectives. *iScience* **2025**, *28*, 112691.

(35) Pettinger, K.-H.; Kampker, A.; Hohenthanner, C.-R., et al. In *Lithium-Ion Batteries: Basics and Applications*, Korthauer, R., Ed.; Springer: Berlin, Heidelberg, 2018, pp 211–226.

(36) Chen, W.; Han, X.; Pan, Y., et al. Defects in Lithium-Ion Batteries: From Origins to Safety Risks. *Green Energy and Intelligent Transportation* **2025**, *4*, 100235.

(37) IEA *EV Battery Supply Chain Sustainability*; IEA, 2024.

(38) IEA *Global EV Outlook 2024*; Paris: IEA, 2024.

(39) Forecasting the Ramp-up of Battery Cell Production in Europe: A Risk Assessment Model Fraunhofer Institute for Systems and Innovation Research ISI, https://www.isi.fraunhofer.de/en/blog/themen/batterie-update/batterie-zell-produktion-europa-hochlauf-risiko-bewertung-gescheiterte-projekte.html (accessed 01/04/2026).

(40) Tian-ming, G.; MNR Key Laboratory of Metallogeny and Mineral Assessment, Institute of Mineral Resources Chinese Academy of Geological Sciences, Beijing 100037, China; Na, F., et al. Lithium Extraction from Hard Rock Lithium Ores (Spodumene, Lepidolite, Zinnwaldite, Petalite): Technology, Resources, Environment and Cost. *China Geol.* **2023**, *6*, 137–153.

(41) Eom, Y.; Dyer, L.; Nikoloski, A. N.; Alorro, R. D. Mechanochemical Treatment for the Extraction of Lithium from Hard Rock Minerals: A Comprehensive Review. *Metals* **2024**, *14*, 1260.

(42) Meng, F.; McNeice, J.; Zadeh, S. S.; Ghahreman, A. Review of Lithium Production and Recovery from Minerals, Brines, and Lithium-Ion Batteries. *Miner. Process. Extr. Metall. Rev.* **2021**, *42*, 123–141.

(43) Kalungi, P.; Yao, Z.; Huang, H. Aspects of Nickel, Cobalt and Lithium, the Three Key Elements for Li-Ion Batteries: An Overview on Resources, Demands, and Production. *Materials* **2024**, *17*, 4389.

(44) Flexer, V.; Baspineiro, C. F.; Galli, C. I. Lithium Recovery from Brines: A Vital Raw Material for Green Energies with a Potential Environmental Impact in Its Mining and Processing. *Sci. Total Environ.* **2018**, *639*, 1188–1204.

(45) Yang, X.; Wen, H.; Lin, Y., et al. Emerging Research Needs for Characterizing the Risks of Global Lithium Pollution under Carbon Neutrality Strategies. *Environ. Sci. Technol.* **2023**, *57*, 5103–5106.

(46) Gibb, B. C. The Rise and Rise of Lithium. *Nat. Chem.* **2021**, *13*, 107–109.

(47) Gerardo, S.; Song, W. Lithium Recovery from U.S. Oil and Gas Produced Waters: Resource Quality and Siting Considerations. *Environ. Sci. Water Res. Technol.* **2025**, *11*, 536–541.

(48) Farahbakhsh, J.; Arshadi, F.; Mofidi, Z., et al. Direct Lithium Extraction: A New Paradigm for Lithium Production and Resource Utilization. *Desalination* **2024**, *575*, 117249.

(49) Herrmann, L.; Bohn, N.; Pfau, A., et al. Synthesis of Lithium Manganese Oxide and Ti-Substituted LMO Sorbents for Lithium Extraction in a Spray-Drying Process. *ChemSusChem* **2025**, *18*, e202500530.

(50) Tian, G.; Yuan, G.; Aleksandrov, A., et al. Recycling of Spent Lithium-ion Batteries: A Comprehensive Review for Identification of Main Challenges and Future Research Trends. *Sustain. Energy Technol. Assessments* **2022**, *53*, 102447.

(51) Guo, R.; Wang, F.; Akbar Rhamdhani, M., et al. Managing the Surge: A Comprehensive Review of the Entire Disposal Framework for Retired Lithium-Ion Batteries from Electric Vehicles. *J. Energy Chem.* **2024**, *92*, 648–680.

(52) Kim, S.; Bang, J.; Yoo, J., et al. A Comprehensive Review on the Pretreatment Process in Lithium-Ion Battery Recycling. *J. Cleaner Prod.* **2021**, *294*, 126329.

(53) Pinegar, H.; Smith, Y. R. End-of-Life Lithium-Ion Battery Component Mechanical Liberation and Separation. *JOM* **2019**, *71*, 4447–4456.

(54) Zhang, L.; Xu, Z. A Review of Current Progress of Recycling Technologies for Metals from Waste Electrical and Electronic Equipment. *J. Cleaner Prod.* **2016**, *127*, 19–36.

(55) Harper, G. D. J.; Kendrick, E.; Anderson, P. A., et al. Roadmap for a Sustainable Circular Economy in Lithium-Ion and Future Battery Technologies. *J. Phys. Energy* **2023**, *5*, 021501.

(56) Sommerville, R.; Shaw-Stewart, J.; Goodship, V., et al. A Review of Physical Processes Used in the Safe Recycling of Lithium Ion Batteries. *Sustainable Mater. Technol.* **2020**, *25*, e00197.

(57) Brückner, L.; Frank, J.; Elwert, T. Industrial Recycling of Lithium-Ion Batteries—A Critical Review of Metallurgical Process Routes. *Metals* **2020**, *10*, 1107.

(58) Makuza, B.; Tian, Q.; Guo, X., et al. Pyrometallurgical Options for Recycling Spent Lithium-Ion Batteries: A Comprehensive Review. *J. Power Sources* **2021**, *491*, 229622.

(59) Wang, M.; Liu, K.; Yu, J., et al. Recycling Spent Lithium-Ion Batteries Using a Mechanochemical Approach. *Circular Economy* **2022**, *1*, 100012.

(60) Dolotko, O.; Knapp, M.; Ehrenberg, H. Batterierecycling–Technologien im Überblick. *CITplus* **2023**, *26*, 16–19.

(61) Liu, Z.; Guo, X.; Xu, Z.; Tian, Q. Recent Advancements in Aqueous Electrowinning for Metal Recovery: A Comprehensive Review. *Miner. Eng.* **2024**, *216*, 108897.

(62) Marcinov, V.; Klimko, J.; Takáčová, Z., et al. Lithium Production and Recovery Methods: Overview of Lithium Losses. *Metals* **2023**, *13*, 1213.

(63) Liu, S.; Liu, H.; Bokov, A., et al. Insights into the Mechanisms Behind Structural Repair of Spent Layered Cathode Materials for Lithium-Ion Batteries. *Angew. Chem., Int. Ed.* **2025**, *64*, e202504382.

(64) Ahuis, M.; Aluzoun, A.; Keppeler, M., et al. Direct Recycling of Lithium-Ion Battery Production Scrap – Solvent-based Recovery and Reuse of Anode and Cathode Coating Materials. *Journal of Power Sources* **2024**, *593*, 233995.

(65) Compagnoni, M.; Grazzi, M.; Pieri, F.; Tomasi, C. Extended Producer Responsibility and Trade Flows in Waste: The Case of Batteries. *Environ. Resour. Econ.* **2025**, *88*, 43–76.

(66) Homepage Materials for Batteries Hub, https://www.materialsforbatterieshub.eu/ (accessed 05/11/2026).

(67) Battery Recycling in Europe Continues to Pick up Speed: Recycling Capacities of Lithium-Ion Batteries in Europe - Fraunhofer ISI https://www.isi.fraunhofer.de/en/blog/themen/batterie-update/lithium-ionen-batterie-recycling-europa-kapazitaeten-update-2024.html (accessed 05/11/2026).

(68) Brunn, M. Begehrte Schwarzmasse – wie Europas Rohstoffe nach China wandern RECYCLING magazin, https://www.recyclingmagazin.de/2025/10/23/begehrte-schwarzmasse-wie-europas-rohstoffe-nach-china-wandern/ (accessed 05/26/2026).

(69) Homepage Rhinoceros project, https://www.rhinoceros-project.eu/ (accessed 05/11/2026).

(70) Colacino, E. Terminology and Symbolism for Mechanochemistry. *Chem. Int.* **2024**, *46*, 34–34.

(71) Michalchuk, A. A. L.; Boldyreva, E. V.; Belenguer, A. M., et al. Tribochemistry, Mechanical Alloying, Mechanochemistry: What Is in a Name? *Front. Chem.* **2021**, *9*, 685789.

(72) Baláž, P.; Achimovičová, M.; Baláž, M., et al. Hallmarks of Mechanochemistry: From Nanoparticles to Technology. *Chem. Soc. Rev.* **2013**, *42*, 7571.

(73) Howard, J. L.; Cao, Q.; Browne, D. L. Mechanochemistry as an Emerging Tool for Molecular Synthesis: What Can It Offer? *Chem. Sci.* **2018**, *9*, 3080–3094.

(74) Auvray, T.; Friščić, T. Shaking Things from the Ground-Up: A Systematic Overview of the Mechanochemistry of Hard and High-Melting Inorganic Materials. *Molecules* **2023**, *28*, 897.

(75) Batteas, J.; Blank, K. G.; Colacino, E., et al. Moving Mechanochemistry Forward. *RSC Mechanochem.* **2025**, *2*, 10–19.

(76) Wang, G.-W. Mechanochemical Organic Synthesis. *Chem. Soc. Rev.* **2013**, *42*, 7668–7700.

(77) Baláž, P., *Mechanochemistry in Nanoscience and Minerals Engineering*; Springer Berlin Heidelberg: Berlin, Heidelberg, 2008.

(78) Baláž, M., *Environmental Mechanochemistry: Recycling Waste into Materials Using High-Energy Ball Milling*; Springer International Publishing: Cham, 2021.

(79) Wang, M.; Tan, Q.; Chiang, J. F.; Li, J. Recovery of Rare and Precious Metals from Urban Mines—A Review. *Front. Environ. Sci. Eng.* **2017**, *11*, 1.

(80) Lv, K.; Wei, C.; Tu, R., et al. Mechanocatalysis: Driving Sustainable Chemical Reactions Under Mild Conditions. *ChemSusChem* **2026**, *19*, e202501610.

(81) Haneef, J.; Ali, S. Medicinal Mechanochemistry: Sustainable and Efficient Route towards Synthesis of Active Pharmaceutical Ingredients. *Sustainable Chem. Pharm.* **2025**, *45*, 102044.

(82) Ozer, D. In Advances in Science, Technology & Innovation; Springer International Publishing: 2021, pp 23–39.

(83) Concas, A.; Lai, N.; Pisu, M.; Cao, G. Modelling of Comminution Processes in Spex Mixer/Mill. *Chem. Eng. Sci.* **2006**, *61*, 3746–3760.

(84) Rappen, M. F.; Mäder, J.; Grätz, S.; Borchardt, L. Motion Matters: The Role of Milling Ball Trajectories in Mechanochemical Reactions. *RSC Mechanochem.* **2025**, DOI: 10.1039/D5MR00112A.

(85) Suryanarayana, C. Mechanical Alloying and Milling. *Prog. Mater. Sci.* **2001**, *46*, 1–184.

(86) Burmeister, C. F.; Kwade, A. Process Engineering with Planetary Ball Mills. *Chem. Soc. Rev.* **2013**, *42*, 7660–7.

(87) Zoz, H.; Ren, H.; Reichardt, R.; Benz, H. U. High Energy Milling / Mechanical Alloying / Reactive Milling https://group.zoz.de/zoz.main/pdf_content/publications/v14.pdf (accessed 10/24/2024).

(88) Pradeep, N. B.; Parameshwara, S.; Chethan, S. G., et al. In *Mechanically Alloyed Novel Materials*, Rajendrachari, S., Ed.; Springer Nature Singapore: Singapore, 2024; Vol. 220, pp 1–10.

(89) Carta, M. Mechanochemical Transformations: Bridging the Gap between Global and Local Kinetics, en, University of Cagliari, 2024.

(90) Ji, S.; Liu, L. In *Computational Granular Mechanics and Its Engineering Applications*; Springer Singapore: Singapore, 2020, pp 51–96.

(91) Danylenko, V. A.; Mykulyak, S. V.; Polyakovskyi, V. O., et al. Force Distribution in a Granular Medium under Dynamic Loading. *Phys. Rev. E* **2017**, *96*, 012906.

(92) Carta, M.; Colacino, E.; Delogu, F.; Porcheddu, A. Kinetics of Mechanochemical Transformations. *Phys. Chem. Chem. Phys.* **2020**, *22*, 14489–14502.

(93) Vugrin, L.; Carta, M.; Lukin, S., et al. Mechanochemical Reaction Kinetics Scales Linearly with Impact Energy. *Faraday Discuss.* **2023**, *241*, 217–229.

(94) Thiessen, P. A.; Heinicke, G.; Meyer, K., *Grundlagen der Tribochemie*, Reprint 2022; Abhandlungen der Deutschen Akademie der Wissenschaften zu Berlin / Klasse für Chemie, Geologie und Biologie 1966, 1; De Gruyter: Berlin Boston, 2022; 1 p.

(95) Takacs, L. The Historical Development of Mechanochemistry. *Chem. Soc. Rev.* **2013**, *42*, 7649–7659.

(96) Dong, L.; Li, L.; Chen, H., et al. Mechanochemistry: Fundamental Principles and Applications. *Adv. Sci.* **2025**, *12*, 2403949.

(97) Tromans, D.; Meech, J. A. Enhanced Dissolution of Minerals: Stored Energy, Amorphism and Mechanical Activation. *Minerals Engineering* **2001**, *14*, 1359–1377.

(98) Massalimov, I. A.; Massalimov, B. I.; Shayakhmetov, A. U., et al. Absorption of Impact and Shear Energy by Crystal Lattices of Mechanically Activated Inorganic Substances: A Review. *Phys. Mesomech.* **2024**, *27*, 592–617.

(99) Li, W.; Deng, X.; Rosakis, A. J. Determination of Temperature Field around a Rapidly Moving Crack-Tip in an Elastic-Plastic Solid. *Int. J. Heat Mass Transfer* **1996**, *39*, 677–690.

(100) Greer, A. L.; Cheng, Y. Q.; Ma, E. Shear Bands in Metallic Glasses. *Mater. Sci. Eng.: R: Rep.* **2013**, *74*, 71–132.

(101) Oghenevweta, J.; Wexler, D.; Calka, A. Early Stages of Phase Formation before the Ignition Peak during Mechanically Induced Self-Propagating Reactions (MSRs) of Titanium and Graphite. *Scr. Mater.* **2016**, *122*, 93–97.

(102) Tonejc, A.; Tonejc, A. M.; Bagović, D.; Kosanović, C. Comparison of the Transformation Sequence from γ-AlOOH (Boehmite) to α-Al_2O_3 (Corundum) Induced by Heating and by Ball Milling. *Mater. Sci. Eng. A* **1994**, *181–182*, 1227–1231.

(103) Weichert, R.; Schönert, K. On the Temperature Rise at the Tip of a Fast Running Crack. *J. Mech. Phys. Solids* **1974**, *22*, 127–133.

(104) Urakaev, F. K.; Boldyrev, V. V. Mechanism and Kinetics of Mechanochemical Processes in Comminuting Devices: 1. Theory. *Powder Technol.* **2000**, *107*, 93–107.

(105) *Mechanically Alloyed Novel Materials: Processing, Applications, and Properties*; Rajendrachari, S., Ed.; Advanced Structured Materials, Vol. 220; Springer Nature Singapore: Singapore, 2024.

(106) Burgio, N.; Iasonna, A.; Magini, M., et al. Mechanical Alloying of the Fe-Zr System. Correlation between Input Energy and End Products. *Il Nuovo Cimento D* **1991**, *13*, 459–476.

(107) Kessler, M.; Rinaldi, R. Kinetic Energy Dose as a Unified Metric for Comparing Ball Mills in the Mechanocatalytic Depolymerization of Lignocellulose. *Front. Chem.* **2022**, *9*, 816553.

(108) Gotor, F. J.; Achimovicova, M.; Real, C.; Balaz, P. Influence of the Milling Parameters on the Mechanical Work Intensity in Planetary Mills. *Powder Technol.* **2013**, *233*, 1–7.

(109) Delogu, F.; Mulas, G.; Schiffini, L.; Cocco, G. Mechanical Work and Conversion Degree in Mechanically Induced Processes. *Materials Sci. Eng. A* **2004**, *382*, 280–287.

(110) Xie, C.; Zhao, Y. Investigation of the Ball Wear in a Planetary Mill by DEM Simulation. *Powder Technol.* **2022**, *398*, 117057.

(111) Santhanam, P. R.; Dreizin, E. L. Predicting Conditions for Scaled-up Manufacturing of Materials Prepared by Ball Milling. *Powder Technol.* **2012**, *221*, 403–411.

(112) Peterson, G. I. Responsible Use of Kinematic Models: Correspondence on "Navigating Ball Mill Specifications for Theory-to-Practice Reproducibility in Mechanochemistry". *Angew. Chem. Int. Ed.* **2025**, *64*, e202512324.

(113) Magini, M.; Iasonna, A.; Padella, F. Ball Milling: An Experimental Support to the Energy Transfer Evaluated by the Collision Model. *Scripta Materialia* **1996**, *34*, 13–19.

(114) Gil-González, E.; Rodríguez-Laguna, M. D. R.; Sánchez-Jiménez, P. E., et al. Unveiling Mechanochemistry: Kinematic-kinetic Approach for the Prediction of Mechanically Induced Reactions. *J. Alloys Compd.* **2021**, *866*, 158925.

(115) Iwasaki, T.; Yabuuchi, T.; Nakagawa, H.; Watano, S. Scale-up Methodology for Tumbling Ball Mill Based on Impact Energy of Grinding Balls Using Discrete Element Analysis. *Advanced Powder Technology* **2010**, *21*, 623–629.

(116) Mhadhbi, M. Modelling of the High-Energy Ball Milling Process. *Adv. Mater. Phys. Chem.* **2021**, *11*, 31–44.

(117) Shi, H.; Teng, L.; Liu, W., et al. Mechanical Activation-Assisted Technology for Recovering Valuable Metal Elements from Spent Lithium-Ion Batteries: A Review. *Applied Energy* **2026**, *406*, 127285.

(118) Seo, J.; Jeon, H.; Nam, H.-i., et al. Lithium Recycling from Spent NCM523 Cathode and Resynthesis of High-Nickel Lithium-Ion Battery Using Recovered Material. *ChemSusChem* **2025**, e202501510.

(119) Wang, M.-M.; Zhang, C.-C.; Zhang, F.-S. An Environmental Benign Process for Cobalt and Lithium Recovery from Spent Lithium-Ion Batteries by Mechanochemical Approach. *Waste Manage.* **2016**, *51*, 239–244.

(120) Cai, L.; Lin, J.; Fan, E., et al. Eco-Friendly Organic Acid-Assisted Mechanochemical Process for Metal Extraction from Spent Lithium-Ion Batteries. *ACS Sustainable Chem. Eng.* **2022**, *10*, 10649–10657.

(121) Gao, G.; Luo, X.; Liu, N., et al. Exploration of Sequential Mechanochemical Activation and Complexation Leaching for Enhanced Recovery of Valuable Metals from Spent Lithium-Ion Batteries. *Ionics* **2023**, *29*, 3585–3596.

(122) Yu, Y.; Jiang, S.; Yao, Y., et al. Mechanochemical Ball Milling Achieves Green and Ultrahighly Efficient Recycling of Lithium-Ion Batteries. *Environ. Sci. Technol.* **2025**, *59*, 12352–12363.

(123) Zhang, S.; Zhang, C.; Zhang, X.; Ma, E. A Mechanochemical Method for One-Step Leaching of Metals from Spent LIBs. *Waste Manage.* **2023**, *161*, 245–253.

(124) Liu, K.; Liu, L.; Tan, Q.; Li, J. Selective Extraction of Lithium from a Spent Lithium Iron Phosphate Battery by Mechanochemical Solid-Phase Oxidation. *Green Chem.* **2021**, *23*, 1344–1352.

(125) Liu, Z.; Liu, G.; Cheng, L., et al. Ultra-Fast Mechanochemistry Reaction Process: An Environmentally Friendly Instant Recycling Method for Spent $LiFePO_4$ Batteries. *Sep. Purif. Technol.* **2024**, *335*, 126174.

(126) Jiang, Y.; Chen, X.; Yan, S., et al. Mechanochemistry-Induced Recycling of Spent Lithium-Ion Batteries for Synergistic Treatment of Mixed Cathode Powders. *Green Chem.* **2022**, *24*, 5987–5997.

(127) Wang, S.; Yan, S.; Chen, Z., et al. Boosting the Sustainable Recycling of Spent Lithium-Ion Batteries through Mechanochemistry. *Green Chem.* **2025**, *27*, 9917–9926.

(128) Wang, M.; Tan, Q.; Huang, Q., et al. Converting Spent Lithium Cobalt Oxide Battery Cathode Materials into High-Value Products via a Mechanochemical Extraction and Thermal Reduction Route. *J. Hazard. Mater.* **2021**, *413*, 125222.

(129) Rao, F.; Sun, Z.; Lv, W., et al. A Sustainable Approach for Selective Recovery of Lithium from Cathode Materials of Spent Lithium-Ion Batteries by Induced Phase Transition. *Waste Manage.* **2023**, *156*, 247–254.

(130) Dolotko, O.; Hlova, I. Z.; Mudryk, Y., et al. Mechanochemical Recovery of Co and Li from LCO Cathode of Lithium-Ion Battery. *J. Alloys Compd.* **2020**, *824*, 153876.

(131) Dolotko, O.; Gehrke, N.; Malliaridou, T., et al. Universal and Efficient Extraction of Lithium for Lithium-Ion Battery Recycling Using Mechanochemistry. *Commun. Chem.* **2023**, *6*, 49.

(132) Holleman, A. F.; Wiberg, E.; Wiberg, N., *Lehrbuch der anorganischen Chemie*, 102.; de Gruyter: Berlin, 2008.

(133) Geiß, D.; Dolotko, O.; Indris, S., et al. Revealing the Mechanism of Reductive, Mechanochemical Li Recycling from $LiFePO_4$. *RSC Mechanochem.* **2024**, *1*, 349–360.

(134) Dolotko, O.; Gehrke, N.; Knapp, M.; Ehrenberg, H. Mechanochemically Induced Hydrometallurgical Method for Recycling D-Elements from Li-Ion Battery Cathodes. *J. Alloys Compd.* **2024**, *976*, 172884.

(135) Jia, X.; Tong, L.; Hu, X.; Mao, J. General Mechanism Review of Aluminum-Based Thermite Reaction. *Adv. Eng. Mater.* **2025**, *27*, e202501172.

(136) Takacs, L. Self-Sustaining Reactions Induced by Ball Milling. *Prog. Mater. Sci.* **2002**, *47*, 355–414.

(137) Nièpce, J. .-.; GFA members Main Recent Contributions to SHS from France. *Int. J Self-Propag. High-Temp. Synth.* **2007**, *16*, 235–255.

(138) Grigoreva, T. F.; Kiseleva, T. Y.; Petrova, S. A., et al. Mechanochemically Stimulated Reactions of the Reduction of Iron Oxide with Aluminum. *Phys. Metals Metallogr.* **2021**, *122*, 572–578.

(139) Oghenevweta, J. E.; Wexler, D.; Calka, A. Study of Reaction Sequences during MSR Synthesis of TiC by Controlled Ball Milling of Titanium and Graphite. *Mater. Charact.* **2018**, *140*, 299–311.

(140) Monagheddu, M.; Doppiu, S.; Deidda, C.; Cocco, G. The Self-Combustion of Structurally Co-Deformed Powder Mixtures: A Direct View of the Process. *J. Phys. D: Appl. Phys.* **2003**, *36*, 1917–1922.

(141) Takacs, L. Self-Sustaining Reactions as a Tool to Study Mechanochemical Activation. *Faraday Discuss.* **2014**, *170*, 251–65.

(142) A. Bakhshai; R. Pragani; L. Takacs Self-Propagating Reaction Induced by Ball Milling in a Mixture of Cu2O and Al Powders. *Metall. Mater. Trans. A* **2002**, *33A*, 3521.

(143) Chakurov, C.; Rusanov, V.; Koichev, J. The Effect of Inert Additives on the Explosive Mechanochemical Synthesis of Some Metal Chalcogenides. *J. Solid State Chem.* **1987**, *71*, 522–529.

(144) Schaffer, G. B.; McCormick, P. G. Anomalous Combustion Effects during Mechanical Alloying. *Metall. Trans. A* **1991**, *22*, 3019–3024.

(145) Schaffer, G. B.; Forrester, J. S. The Influence of Collision Energy and Strain Accumulation on the Kinetics of Mechanical Alloying. *J. Mater. Sci.* **1997**, *32*, 3157–3162.

(146) Deidda, C.; Delogu, F.; Maglia, F., et al. Mechanical Processing and Self-Sustaining High-Temperature Synthesis of TiC Powders. *Materials Sci. Eng. A* **2004**, *375–377*, 800–803.

(147) Chicardi, E.; Gotor, F.; Alcalá, M.; Córdoba, J. Influence of Milling Parameters on the Solid-Gas Synthesis of TiC_xN_{1-x} by Mechanically Induced Self-Sustaining Reaction. *Powder Technol.* **2017**, *319*, 12–18.

(148) Delogu, F.; Takacs, L. Information on the Mechanism of Mechanochemical Reaction from Detailed Studies of the Reaction Kinetics. *J. Mater. Sci.* **2018**, *53*, 13331–13342.

(149) Yang, C.-J. Fast and Efficient Approach to Synthesis of Ultra-Fine TiC Powder. *Mater. Res. Express* **2020**, *7*, 016508.

(150) Takacs, L. Reduction of Magnetite by Aluminum: A Displacement Reaction Induced by Mechanical Alloying. *Mater. Lett.* **1992**, *13*, 119–124.

(151) Takacs, L.; Susol, M. A. Combustive Mechanochemical Reactions in Off-Stoichiometric Powder Mixtures. *Mater. Sci. Forum* **1996**, *225–227*, 559–562.

(152) Carta, M.; Delogu, F. Mechanochemical Ignition of Self-Propagating Reactions in Equimolar Al–Ni Powder Mixtures and Multilayers. *Phys. Chem. Chem. Phys.* **2024**, *26*, 12316–12323.

(153) Caggiu, L.; Enzo, S.; Stievano, L., et al. Solvent-Free Mechanochemical Approach towards Thiospinel $MgCr_2S_4$ as a Potential Electrode for Post-Lithium Ion Batteries. *Batteries* **2020**, *6*, 43.

(154) Benediktovitch, A.; Feranchuk, I.; Ulyanenkov, A. In *Theoretical Concepts of X-Ray Nanoscale Analysis: Theory and Applications*, Benediktovich, A., Feranchuk, I., Ulyanenkov, A., Eds.; Springer: Berlin, Heidelberg, 2014, pp 1–51.

(155) Cockcroft, J. K.; Fitch, A. N. In *Powder Diffraction*, Dinnebier, R. E., Billinge, S. J. L., Eds.; Royal Society of Chemistry: Cambridge, 2008, pp 20–57.

(156) Schnohr, C. S.; Ridgway, M. C. In *X-Ray Absorption Spectroscopy of Semiconductors*, Schnohr, C. S., Ridgway, M. C., Eds.; Springer: Berlin, Heidelberg, 2015, pp 1–26.

(157) Spieß, L.; Teichert, G.; Schwarzer, R., et al. In *Moderne Röntgenbeugung: Röntgendiffraktometrie für Materialwissenschaftler, Physiker und Chemiker*, Spieß, L., Teichert, G., Schwarzer, R., et al., Eds.; Springer Fachmedien: Wiesbaden, 2019, pp 41–94.

(158) Dinnebier, R. E.; Billinge, S. J. L. In *Powder Diffraction*, Dinnebier, R. E., Billinge, S. J. L., Eds.; Royal Society of Chemistry: Cambridge, 2008, pp 1–19.

(159) Chantler, C. T.; Bunker, G.; D'Angelo, P.; Diaz-Moreno, S. X-Ray Absorption Spectroscopy. *Nat. Rev. Methods Primers* **2024**, *4*, 89.

(160) Yano, J.; Yachandra, V. K. X-Ray Absorption Spectroscopy. *Photosynth. Res.* **2009**, *102*, 241–254.

(161) Ul-Hamid, A. In *A Beginners' Guide to Scanning Electron Microscopy*; Springer International Publishing: Cham, 2018, pp 1–14.

(162) Goldstein, J. I.; Newbury, D. E.; Michael, J. R., et al. In *Scanning Electron Microscopy and X-Ray Microanalysis*; Springer New York: New York, NY, 2018, pp 15–28.

(163) Goldstein, J. I.; Newbury, D. E.; Michael, J. R., et al. In *Scanning Electron Microscopy and X-Ray Microanalysis*; Springer New York: New York, NY, 2018, pp 29–37.

(164) Goldstein, J. I.; Newbury, D. E.; Michael, J. R., et al. In *Scanning Electron Microscopy and X-Ray Microanalysis*; Springer New York: New York, NY, 2018, pp 39–63.

(165) Ul-Hamid, A. In *A Beginners' Guide to Scanning Electron Microscopy*; Springer International Publishing: Cham, 2018, pp 265–307.

(166) Goldstein, J. I.; Newbury, D. E.; Michael, J. R., et al. In *Scanning Electron Microscopy and X-Ray Microanalysis*; Springer New York: New York, NY, 2018, pp 209–234.

(167) Haraguchi, H.; Hasegawa, T.; Abdullah, M. Inductively Coupled Plasmas in Analytical Atomic Spectrometry: Excitation Mechanisms and Analytical Feasibilities. *Pure Appl. Chem.* **1988**, *60*, 685–696.

(168) Khan, S. R.; Sharma, B.; Chawla, P. A.; Bhatia, R. Inductively Coupled Plasma Optical Emission Spectrometry (ICP-OES): A Powerful Analytical Technique for Elemental Analysis. *Food Anal. Methods* **2022**, *15*, 666–688.

(169) Lerner, N.; Avraham, H.; Leffler, N., et al. Argentometric Chloride Determination by Inductively Coupled Plasma-Optical Emission Spectroscopy in a Wide Range of Sample Matrices. *Anal. Methods* **2023**, *15*, 1594–1600.

(170) Atkins, P. W.; de Paula, J., *Atkins' Physical Chemistry*, 8. ed; Oxford University Press: Oxford, 2006; 1064 pp.

(171) Hauser, P. C. In *The Alkali Metal Ions: Their Role for Life*, Sigel, A., Sigel, H., Sigel, R. K. O., Eds.; Springer International Publishing: Cham, 2016, pp 11–25.

(172) Mettler-Toledo International Inc all rights Ionenselektive Elektroden Ionenselektive Elektroden, https://www.mt.com/de/de/home/library/guides/lab-analytical-instruments/Ion-selective-electrode-guide.html (accessed 04/21/2026).

(173) Newville, M. Larch: An Analysis Package for XAFS and Related Spectroscopies. *J. Phys.: Conf. Ser.* **2013**, *430*, 012007.

(174) De la Peña, F.; Prestat, E.; Fauske, V. T., et al. Hyperspy/Hyperspy: V2.1.1, version v2.1.1, Zenodo, 2024.

(175) Sieweck, R.; Bokov, A.; Dolotko, O., et al. Mechanistic Investigation of the Mechanochemical Reduction of $LiCoO_2$ with Al in the Context of Lithium-Ion Battery Recycling. *RSC Mechanochem.* **2026**, *3*, 243–253.

(176) Sieweck, R. Improved Mechanochemical Reduction of Industrial NMC-based Black Mass with Subsequent Selective Lithium Extraction, unpublished manuscript in submission, 2026.

(177) Owen, E. A.; Jones, D. M. Effect of Grain Size on the Crystal Structure of Cobalt. *Proc. Phys. Soc. B* **1954**, *67*, 456–466.

(178) Xie, Z.; Ni, S.; Song, M. Effect of Y_2O_3 Doping on FCC to HCP Phase Transformation in Cobalt Produced by Ball Milling and Spark Plasma Sintering. *Powder Technol.* **2018**, *324*, 1–4.

(179) Amirkhanyan, N. H.; Zakaryan, M. K.; Kharatyan, S. L., et al. Stabilization of Metastable γ-Co: Combustion Synthesis and Rapid Processing. *Mater. Chem. Phys.* **2024**, *319*, 129368.

(180) Okayasu, M.; Tomida, S. Phase Transformation System of Austenitic Stainless Steels Obtained by Permanent Compressive Strain. *Mater. Sci. Eng. A* **2017**, *684*, 712–725.

(181) Johnston, W. D.; Heikes, R. R.; Sestrich, D. The Preparation, Crystallography, and Magnetic Properties of the $Li_xCo_{(1-x)}O$ System. *J. Phys. Chem. Solids* **1958**, *7*, 1–13.

(182) Vauloup, J.; Bouilhac, C.; Coppey, N., et al. Advancing Sustainable Practices in Li-ion Battery Cathode Material Recycling: Mechanochemical Optimisation for Magnetic Cobalt Recovery. *RSC Mechanochem.* **2024**, *1*, 393–401.

(183) Ortman, M. S.; Larsen, E. M. Preparation and Melting Point of Octalithium Zirconate. *J. Am. Ceram. Soc.* **1983**, *66*, 142–144.

(184) Sembira, A.; Dunn, J. High Temperature Calibration of DTA and DSC Apparatus Using Encapsulated Samples. *Thermochim. Acta* **1996**, *274*, 113–124.

(185) Meng, Q.; Zhang, K.; He, R.; Qu, Z. A Review of Thermal Shock Behavior of Ceramics: Fundamental Theory, Experimental Methods, and Outlooks. *Int. J. Applied Ceramic Tech.* **2024**, *21*, 3789–3811.

(186) Masoumi, M.; Cupid, D. M.; Reichmann, T. L., et al. Enthalpies of Formation of Layered $LiNi_xMn_xCo_{1-2x}O_2$ ($0 \leq x \leq 0.5$) Compounds as Lithium Ion Battery Cathode Materials. *Int. J. Mater. Res.* **2017**, *108*, 869–878.

(187) Jin, L.; Wang, J.; Rousselot, S., et al. Experimental and Thermodynamic Study of Li-O and Li_2O-P_2O_5 Systems. *Can. J. Chem. Eng.* **2019**, *97*, 2234–2241.

(188) De Abreu, D. A.; Löffler, M.; Kriegel, M. J.; Fabrichnaya, O. Experimental Investigation and Thermodynamic Modeling of the Li_2O–Al_2O_3 System. *J. Phase Equilib. Diffus.* **2024**, *45*, 36–55.

(189) Chase, M., *NIST-JANAF Thermochemical Tables, 4th Edition*; American Institute of Physics, -1: 1998.

(190) Song, Y.-J. Recovery of Lithium as Li_3PO_4 from Waste Water in a LIB Recycling Process. *Korean J. Met. Mater.* **2018**, *56*, 755–762.

(191) Real, C.; Gotor, F. Effects of the Speed Ratio on the Efficiency of Planetary Mills. *Heliyon* **2019**, *5*, e01227.

(192) Zoz, H.; Ren, H.; Reichardt, R.; Benz, H. U. In Thermec2000, International Conference on Processing & Manufacturing of Advanced Materials, Las Vegas, 2000.

(193) Vanderbruggen, A.; Gugala, E.; Blannin, R., et al. Automated Mineralogy as a Novel Approach for the Compositional and Textural Characterization of Spent Lithium-Ion Batteries. *Miner. Eng.* **2021**, *169*, 106924.

(194) Schiavi, P. G.; D'Annibale, L.; Marrani, A. G., et al. Graphite Recovery and Synthesis of Graphene Oxide from End-of-Life Li-ion Batteries: Impact of Thermal, Mechanical, and Mechanochemical Pretreatments. *Carbon* **2025**, *238*, 120295.

(195) Zhu, S. G.; Wu, C. X.; Luo, Y. L. Effects of Stearic Acid on Synthesis of Nanocomposite WC–MgO Powders by Mechanical Alloying. *J. Mater. Sci.* **2010**, *45*, 1817–1822.

(196) Chen, Y.; Renner, P.; Liang, H. A Review of Current Understanding in Tribochemical Reactions Involving Lubricant Additives. *Friction* **2023**, *11*, 489–512.

(197) Aborkin, A. V.; Elkin, A. I.; Ryabkova, V. V., et al. Numerical Analysis of the Effect of Friction on the Motion and Collision Forces of Grinding Bodies in a Planetary Mill. *Metallurgist* **2025**, *69*, 147–157.

(198) Pöplow, A. M. Mechanochemical Transformation of $LiCoO_2$ Cathode Material Using Al_2O_3 or Sulphur to Extract Lithium and 3d Metals, Master's Thesis, Karlruhe Institutes for Technology, 2025.

(199) Hasan, H.; Arshad, F.; Sk, M. P. Mechanochemical Conversion of Elemental Sulfur into Functional Sulfur Nanomaterials for Promising Applications. *RSC Mechanochem.* **2025**, *2*, 786–801.

(200) Chernyaev, A.; Zhang, J.; Seisko, S., et al. Fe^{3+} and Al^{3+} Removal by Phosphate and Hydroxide Precipitation from Synthetic NMC Li-ion Battery Leach Solution. *Sci. Rep.* **2023**, *13*, 21445.

(201) Ma, Y.; Svärd, M.; Xiao, X., et al. Precipitation and Crystallization Used in the Production of Metal Salts for Li-Ion Battery Materials: A Review. *Metals* **2020**, *10*, 1609.

(202) Ohneseit, S.; Finster, P.; Floras, C., et al. Thermal and Mechanical Safety Assessment of Type 21700 Lithium-Ion Batteries with NMC, NCA and LFP Cathodes–Investigation of Cell Abuse by Means of Accelerating Rate Calorimetry (ARC). *Batteries* **2023**, *9*, 237.

(203) Parimalam, B. S.; MacIntosh, A. D.; Kadam, R.; Lucht, B. L. Decomposition Reactions of Anode Solid Electrolyte Interphase (SEI) Components with $LiPF_6$. *J. Phys. Chem. C* **2017**, *121*, 22733–22738.

(204) Qu, X.; Zhang, B.; Zhao, J., et al. Salt-Thermal Methods for Recycling and Regenerating Spent Lithium-Ion Batteries: A Review. *Green Chem.* **2023**, *25*, 2992–3015.

(205) Baláž, M.; Džunda, R.; Bureš, R., et al. Mechanically Induced Self-Propagating Reactions (MSRs) to Instantly Prepare Binary Metal Chalcogenides: Assessing the Influence of Particle Size, Bulk Modulus, Reagents Melting Temperature Difference and Thermodynamic Constants on the Ignition Time. *RSC Mechanochem.* **2024**, *1*, 94–105.

(206) Xu, J.; Lin, F.; Doeff, M. M.; Tong, W. A Review of Ni-based Layered Oxides for Rechargeable Li-ion Batteries. *J. Mater. Chem. A* **2017**, *5*, 874–901.

(207) Ghosh, B.; Dutta, H.; Pradhan, S. Microstructure Characterization of Nanocrystalline Ni_3C Synthesized by High-Energy Ball Milling. *J. Alloys Compd.* **2009**, *479*, 193–200.

(208) Bakhshai, A.; Soika, V.; Susol, M.; Takacs, L. Mechanochemical Reactions in the Sn–Zn–S System: Further Studies. *J. Solid State Chem.* **2000**, *153*, 371–380.

(209) Nie, H.; Schoenitz, M.; Dreizin, E. L. Oxidation of Magnesium: Implication for Aging and Ignition. *J. Phys. Chem. C* **2016**, *120*, 974–983.

(210) Vijh, A. K. Correlation between the Thermodynamic Driving Force and the Kinetic Activation Energy for the Thermal Oxidation of Metals. *J. Mater. Sci. Lett.* **1988**, *7*, 139–140.

(211) Pivkina, A.; Streletskii, A.; Kolbanev, I., et al. Mechanochemically Activated Nano-Aluminium: Oxidation Behaviour. *J. Mater. Sci.* **2004**, *39*, 5451–5453.

(212) Pragatheeswaran, A.; Ravi, R.; Bakshi, S. R. Microstructural and Morphological Changes during Ball Milling of Copper-Silver-Graphite Flake Mixtures. *Adv. Powder Technol.* **2019**, *30*, 2759–2767.

(213) Chipakwe, V.; Semsari, P.; Karlkvist, T., et al. A Critical Review on the Mechanisms of Chemical Additives Used in Grinding and Their Effects on the Downstream Processes. *J. Mater. Res. Technol.* **2020**, *9*, 8148–8162.

(214) Akbaş, Y.; Petranikova, M.; Ebin, B. Co-Solvent Controlled PVDF Extraction from Spent Li-ion Batteries Using Supercritical CO_2. *Sep. Purif. Technol.* **2025**, *376*, 134056.

(215) Nouri, A.; Wen, C. Surfactants in Mechanical Alloying/Milling: A Catch-22 Situation. *Crit. Rev. Solid State Mater. Sci.* **2014**, *39*, 81–108.

(216) Straub, T. B.; Haberkorn, R.; Kickelbick, G. Mechanochemical Activation of Mn_3O_4 : Implications for Lithium Intercalation. *Inorg. Chem.* **2025**, *64*, 6420–6433.

(217) Weng, D.; Duan, H.; Hou, Y., et al. Introduction of Manganese Based Lithium-Ion Sieve-A Review. *Prog. Nat. Sci.: Mater. Int.* **2020**, *30*, 139–152.

(218) Romero-Hermida, I.; Santos, A.; Pérez-López, R., et al. New Method for Carbon Dioxide Mineralization Based on Phosphogypsum and Aluminium-Rich Industrial Wastes Resulting in Valuable Carbonated by-Products. *J. CO_2 Util.* **2017**, *18*, 15–22.

(219) Ni, J.; Ma, D.; Zhang, Y.-X.; Jia, Y. Efficient Removal of Fluoride from Water by CaO / $Ca_{12}Al_{14}O_{33}$ / $Ca_5Al_6O_{14}$ Composites: Performance and Mechanism. *J. Mol. Struct.* **2025**, *1320*, 139771.

(220) He, H.; Suito, H. Immobilization Mechanism of Fluorine in Aqueous Solution with Calcium Aluminates. *ISIJ Int.* **2001**, *41*, 506–512.

(221) Chable, J.; Bohn, N.; Raab, M., et al. Deciphering the Impacts of Al, Fe, Li Sulfate Impurities on the Synthesis and Performances of $LiNi_{0.6}Mn_{0.2}Co_{0.2}O_2$ Cathode Materials. *J. Electrochem. Soc.* **2025**, *172*, 020532.

(222) Bhattacharyya, S.; Roy, S.; Lin, X., et al. Graphite: The New Critical Mineral. *Nat. Rev. Mater.* **2025**, 1–14.

(223) Olutogun, M.; Vanderbruggen, A.; Frey, C., et al. Recycled Graphite for More Sustainable Lithium-Ion Batteries. *Carbon Energy* **2024**, *6*, e483.

(224) Zhu, H.; Cao, Y.; Zhang, J., et al. One-Step Preparation of Graphene Nanosheets via Ball Milling of Graphite and the Application in Lithium-Ion Batteries. *J. Mater. Sci.* **2016**, *51*, 3675–3683.

(225) Jeon, I.-Y.; Shin, Y.-R.; Sohn, G.-J., et al. Edge-Carboxylated Graphene Nanosheets via Ball Milling. *Proc. Natl. Acad. Sci. U.S.A.* **2012**, *109*, 5588–5593.

(226) Gefährdungsbeurteilung beim Einsatz von Wasserstoff etem - Das Magazin Ihrer Berufsgenossenschaft, https://etem.bgetem.de/6.2025/etem/gefaehrdungsbeurteilung-beim-einsatz-von-wasserstoff (accessed 05/06/2026).

(227) Wang, M.; Navrotsky, A. Enthalpy of Formation of LiNiO2, LiCoO2 and Their Solid Solution, LiNi1-xCoxO2. *Solid State Ionics* **2004**, *166*, 167–173.

(228) Chase, M. W. NIST-JANAF Thermochemical Tables, 4th Edition. *NIST*.

(229) Benington, K. O.; Ferrante, M. J.; Stuve, J. M. Thermodynamic Properties of Two Lithium Silicates (Li2sio3 and Li2si2o5) https://stacks.cdc.gov (accessed 05/31/2026).

SI: Supporting Information

1 Supporting Tables

Table S1: Elemental composition, determined by ICP-OES, of Products obtained after mechanochemical reaction between LCO and Al at 650 rpm using 65 g balls (6.35 mm), 2.17 g of powder, LCO/Al =1.0 and a BSR of 30. A large metallic piece was obtained milling was stopped after 3.2 min, directly after the spike in pressure was observed. A homogeneous powder was analyzed after 60 min of total milling.[175]

Element	metallic piece [wt.%]	LCO milled with Al for 1h [wt.%]
Li	0.01	4.56
Al	0.24	17.12
Co	97.00	39.44
Cr	N.A.	0.44
Fe	N.A.	2.72
Sum	97.25	64.28

Table S2: Experimental and calculated data presented in Fig. 5.12. Milling of LCO with Al at different ν_R using small balls.[175]

ν_R [rpm]	d_b [mm]	m_b^{tot} [g]	m_p [g]	$1/BSR$	t_{ig} [s]	N_b	$\frac{10^{-8}}{N_{tot}}$	ΔE_b^* [mJ]	D_{ig} [kJ/g]	D_{ig}^* [kJ/g]
500	3.0	65.46	2.18	0.033	856	601	7.8	1.7	10.1	5.4
500	3.0	65.50	2.18	0.033	787	602	8.4	1.7	9.3	5.0
650	3.0	65.45	2.18	0.033	251	601	20.4	2.9	6.5	4.7
650	3.0	65.45	2.18	0.033	261	601	19.6	2.9	6.8	4.9
650	3.0	65.45	2.18	0.033	221	601	23.2	2.9	5.8	4.2
800	3.0	65.42	2.18	0.033	121	601	34.4	4.4	5.9	4.8
800	3.0	65.48	2.18	0.033	121	602	34.3	4.4	5.9	4.8
1000	3.0	65.44	2.18	0.033	56	601	59.4	6.9	5.3	4.7
1000	3.0	65.52	2.18	0.033	56	602	59.3	6.9	5.3	4.7

Table S3: Experimental and calculated data presented in Fig. 5.12. Milling of LCO with Al at different ν_R using large balls.

ν_R [rpm]	d_b [mm]	m_b^{tot} [g]	m_p [g]	$1/BSR$	t_{ig} [s]	N_b	$\frac{10^{-6}}{N_{tot}}$	ΔE_b^* [mJ]	D_{ig} [kJ/g]	D_{ig}^* [kJ/g]
200	12.7	65.55	2.19	0.033	10574	8	1	16	6.2	2.1
200	12.7	65.46	2.18	0.033	10634	8	1	16	6.3	2.1
350	12.7	65.43	2.18	0.033	1340	8	5	49	4.2	3.3
350	12.7	65.49	2.18	0.033	1397	8	5	49	4.4	3.5
500	12.7	65.38	2.18	0.033	444	8	11	101	4.1	3.7
500	12.7	65.41	2.18	0.033	360	8	14	101	3.3	3.0
650	12.7	65.72	2.19	0.033	175	8	22	170	3.5	3.3
650	12.7	65.62	2.19	0.033	190	8	20	170	3.8	3.6
650	12.7	65.46	2.18	0.033	156	8	25	170	3.2	3.0
650	12.7	65.65	2.19	0.033	167	8	23	170	3.4	3.2
650	12.7	65.53	2.18	0.033	154	8	25	170	3.1	2.9

Table S4: Experimental and calculated data presented in Fig. 5.12. Milling of LCO with Al at different ν_R using medium balls.[175]

ν_R [rpm]	d_b [mm]	m_b^{tot} [g]	m_p [g]	$1/BSR$	t_{ig} [s]	N_b	$\frac{10^{-8}}{N_{tot}}$	ΔE_b^* [mJ]	D_{ig} [kJ/g]	D_{ig}^* [kJ/g]
200	6.35	65.69	2.19	0.033	28841	65	5	2.4	20.8	3.7
200	6.35	65.33	2.18	0.033	19505	65	8	2.4	14.2	2.5
200	6.35	65.28	2.17	0.033	21148	65	7	2.4	15.4	2.7
350	6.35	65.89	2.20	0.033	1669	65	53	7.5	6.4	4.7
350	6.35	65.28	2.18	0.033	1731	65	51	7.5	6.7	4.9
350	6.35	65.29	2.18	0.033	1695	65	52	7.5	6.6	4.8
500	6.35	65.77	2.19	0.033	447	65	138	15.2	5.0	4.4
500	6.35	65.34	2.18	0.033	452	65	136	15.2	5.1	4.5
500	6.35	65.37	2.18	0.033	457	65	135	15.2	5.2	4.5
650	6.35	60.12	2.00	0.033	194	59	269	26.0	4.8	4.5
650	6.35	65.47	2.18	0.033	182	65	260	25.7	4.5	4.2
650	6.35	65.60	2.19	0.033	193	65	245	25.7	4.8	4.4
800	6.35	65.59	2.19	0.033	84	65	458	38.9	3.9	3.7
800	6.35	65.41	2.18	0.033	84	65	458	38.9	3.9	3.7
800	6.35	65.34	2.18	0.033	87	65	442	38.9	4.0	3.8
950	6.35	65.58	2.19	0.033	53	65	611	54.9	4.1	4.0
950	6.35	65.37	2.18	0.033	63	65	514	54.9	4.9	4.7
950	6.35	65.58	2.18	0.033	60	65	540	54.9	4.7	4.5

Table S5: Experimental and calculated data presented in Fig. 5.12. Milling of LCO with Mg at different ν_R using medium balls.[175]

ν_R [rpm]	d_b [mm]	m_b^{tot} [g]	m_p [g]	$1/BSR$	t_{ig} [s]	N_b	$\frac{10^{-8}}{N_{tot}}$	ΔE_b^* [mJ]	D_{ig} [kJ/g]	D_{ig}^* [kJ/g]
200	6.35	65.15	2.17	0.033	12195	64	13	2	8.8	0.5
200	6.35	65.15	2.17	0.033	12931	64	12	2	9.3	0.5
350	6.35	65.15	2.17	0.033	2481	64	36	7	9.6	6.6
350	6.35	65.15	2.17	0.033	2481	64	36	7	9.6	6.6
500	6.35	65.15	2.17	0.033	772	64	81	15	8.7	7.4
500	6.35	65.15	2.17	0.033	807	64	77	15	9.1	7.7
650	6.35	65.15	2.17	0.033	300	64	160	26	7.4	6.7
650	6.35	65.15	2.17	0.033	300	64	160	26	7.4	6.7
800	6.35	65.15	2.17	0.033	154	64	254	39	7.1	6.7
800	6.35	65.15	2.17	0.033	154	64	254	39	7.1	6.7
950	6.35	65.15	2.17	0.033	89	64	370	55	6.9	6.6
950	6.35	65.15	2.17	0.033	84	64	392	55	6.5	6.2

Table S6: Experimental and calculated data presented in Fig. 5.14: Milling of LCO with Al at different $1/BSR$ using small balls.[175]

ν_R [rpm]	d_b [mm]	m_b^{tot} [g]	m_p [g]	$1/BSR$	t_{ig} [s]	N_b	$\frac{10^{-8}}{N_{tot}}$	ΔE_b^* [mJ]	D_{ig} [kJ/g]	D_{ig}^* [kJ/g]
650	3	65.40	1.31	0.020	153	601	33.5	2.9	6.6	2.1
650	3	65.41	1.31	0.020	158	601	32.4	2.9	6.9	2.1
650	3	60.16	1.20	0.020	150	553	37.1	3.0	6.6	2.1
650	3	65.49	1.32	0.020	160	602	31.9	2.9	6.9	2.2
650	3	60.82	2.00	0.033	241	559	22.8	2.9	6.4	2.1
650	3	65.45	2.18	0.033	251	601	20.4	2.9	6.5	2.0
650	3	65.45	2.18	0.033	261	601	19.6	2.9	6.8	2.1
650	3	65.45	2.18	0.033	221	601	23.2	2.9	5.8	1.8
650	3	60.12	2.00	0.033	217	552	25.7	3.0	5.7	1.9
650	3	60.09	4.00	0.067	673	552	8.3	3.0	8.9	2.9
650	3	65.38	4.36	0.067	564	601	9.1	2.9	7.4	2.3
650	3	65.38	4.36	0.067	699	601	7.3	2.9	9.1	2.8
650	3	65.37	4.36	0.067	554	600	9.3	2.9	7.2	2.3
650	3	60.07	4.00	0.067	623	552	8.9	3.0	8.2	2.7
650	3	60.18	6.02	0.100	636	553	8.7	3.0	5.6	1.8
650	3	65.42	6.54	0.100	456	601	11.2	2.9	4.0	1.2
650	3	65.42	6.54	0.100	462	601	11.1	2.9	4.0	1.3
650	3	65.40	6.54	0.100	643	601	8.0	2.9	5.6	1.7
650	3	60.11	6.01	0.100	552	552	10.1	3.0	4.9	1.6
650	3	65.44	8.17	0.125	546	601	9.4	2.9	3.8	1.2

Table S7: Experimental and calculated data presented in Fig. 5.14: Milling of LCO with Al at different $1/BSR$ using medium balls.[175]

ν_R [rpm]	d_b [mm]	m_b^{tot} [g]	m_p [g]	$1/BSR$	t_{ig} [s]	N_b	$\frac{10^{-8}}{N_{tot}}$	ΔE_b^* [mJ]	D_{ig} [kJ/g]	D_{ig}^* [kJ/g]
650	6.35	65.74	1.31	0.020	123	65	385	25.7	5.1	4.7
650	6.35	65.78	1.32	0.020	127	65	373	25.7	5.2	4.8
650	6.35	60.51	1.21	0.020	126	60	407	26.0	5.3	4.9
650	6.35	65.34	1.31	0.020	112	65	423	25.7	4.7	4.3
650	6.35	60.12	2.00	0.033	194	59	269	26.0	4.8	4.5
650	6.35	60.90	2.03	0.033	185	60	277	26.0	4.6	4.3
650	6.35	65.78	2.19	0.033	185	65	256	25.7	4.6	4.2
650	6.35	65.60	2.19	0.033	193	65	245	25.7	4.8	4.4
650	6.35	65.47	2.18	0.033	182	65	260	25.7	4.5	4.2
650	6.35	65.90	4.39	0.067	354	65	134	25.7	4.4	4.0
650	6.35	60.73	4.05	0.067	307	60	167	26.0	3.8	3.5
650	6.35	65.17	4.34	0.067	386	64	125	25.8	4.8	4.4
650	6.35	60.78	6.08	0.100	681	60	75	26.0	5.7	5.2
650	6.35	65.28	6.53	0.100	567	65	83	25.7	4.7	4.4
650	6.35	65.24	6.52	0.100	635	65	75	25.7	5.3	4.9
650	6.35	60.13	7.52	0.125	706	59	74	26.0	4.7	4.3
650	6.35	65.81	8.23	0.125	765	65	62	25.7	5.1	4.7
650	6.35	65.29	8.16	0.125	800	65	59	25.7	5.3	4.9

Table S8: Experimental and calculated data presented in Fig. 5.14: Milling of LCO with Al at different $1/BSR$ using large balls.[175]

ν_R [rpm]	d_b [mm]	m_b^{tot} [g]	m_p [g]	$1/BSR$	t_{ig} [s]	N_b	$\frac{10^{-8}}{N_{tot}}$	ΔE_b^* [mJ]	D_{ig} [kJ/g]	D_{ig}^* [kJ/g]
650	12.7	65.73	1.30	0.020	144	8	2671	170.1	4.9	4.8
650	12.7	65.48	1.31	0.020	134	8	2870	170.1	4.5	4.5
650	12.7	65.49	1.31	0.020	119	8	3232	170.1	4.0	4.0
650	12.7	65.46	2.18	0.033	156	8	2465	170.1	3.2	3.1
650	12.7	65.62	2.19	0.033	190	8	2024	170.1	3.8	3.8
650	12.7	65.72	2.19	0.033	175	8	2198	170.1	3.5	3.5
650	12.7	65.73	4.38	0.067	295	8	1304	170.1	3.0	2.9
650	12.7	65.48	4.37	0.067	281	8	1369	170.1	2.8	2.8
650	12.7	65.44	4.36	0.067	270	8	1425	170.1	2.7	2.7
650	12.7	65.66	6.57	0.100	274	8	1404	170.1	1.8	1.8
650	12.7	65.49	6.55	0.100	327	8	1176	170.1	2.2	2.2
650	12.7	65.54	6.55	0.100	505	8	762	170.1	3.4	3.4
650	12.7	65.41	6.54	0.100	424	8	907	170.1	2.9	2.8
650	12.7	65.50	8.19	0.125	508	8	757	170.1	2.7	2.7
650	12.7	65.51	8.19	0.125	440	8	874	170.1	2.4	2.3
650	12.7	65.53	8.19	0.125	526	8	731	170.1	2.8	2.8

Table S9: Experimental and calculated data presented in Fig. 5.16. Milling of LCO with Al at different ν_R using 32 medium balls.

ν_R [rpm]	d_b [mm]	m_b^{tot} [g]	m_p [g]	$1/BSR$	t_{ig} [s]	N_b	$\frac{10^{-8}}{N_{tot}}$	ΔE_b^* [mJ]	D_{ig} [kJ/g]	D_{ig}^* [kJ/g]
350	6.35	32.56	1.09	0.033	1495	32	119	8	6.1	4.6
350	6.35	32.23	1.07	0.033	1438	32	124	8	5.9	4.4
350	6.35	32.77	1.09	0.033	1532	32	117	8	6.2	4.6
500	6.35	32.43	1.08	0.033	464	32	269	16	5.5	4.9
500	6.35	32.40	1.08	0.033	432	32	289	16	5.2	4.5
500	6.35	32.08	1.07	0.033	486	32	257	16	5.9	5.1
650	6.35	32.80	1.10	0.033	204	32	471	27	5.3	4.9
650	6.35	32.09	1.07	0.033	192	32	501	27	5.1	4.7
650	6.35	32.28	1.08	0.033	199	32	483	27	5.2	4.9
800	6.35	32.14	1.07	0.033	101	32	774	41	5.0	4.7
800	6.35	32.29	1.10	0.034	102	32	766	41	4.9	4.7
800	6.35	32.12	1.07	0.033	102	32	766	41	5.0	4.8
950	6.35	32.93	1.10	0.033	62	33	1029	58	5.2	5.0
950	6.35	32.07	1.07	0.033	61	32	1079	58	5.1	4.9

Table S10: Experimental and calculated data presented in Fig. 5.16. Milling of LCO with Al at different ν_R using 128 medium balls.

ν_R [rpm]	d_b [mm]	m_b^{tot} [g]	m_p [g]	$1/BSR$	t_{ig} [s]	N_b	$\frac{10^{-8}}{N_{tot}}$	ΔE_b^* [mJ]	D_{ig} [kJ/g]	D_{ig}^* [kJ/g]
350	6.35	130.04	4.33	0.033	2399	129	18	6	7.7	5.2
500	6.35	129.79	4.33	0.033	595	128	53	13	5.5	4.7
650	6.35	128.85	4.33	0.034	266	127	91	21	5.4	4.9
800	6.35	129.84	4.33	0.033	84	128	233	32	3.2	3.0
950	6.35	129.88	4.33	0.033	36	128	457	45	2.3	2.2
950	6.35	129.72	4.32	0.033	35	128	470	45	2.2	2.1

Table S11: Kinematic calculations based on Burgios model. Data obtained from a study by Vauloup et. al.[182]

ν_R [rpm]	d_b [mm]	m_b^{tot} [g]	m_p [g]	t_{ig} [s]	N_b	$\frac{10^{-6}}{N_{tot}}$	ΔE_b^* [mJ]	D_{ig} [J]	D_{ig}^* [J]
500	10	20	3	2700	7	2.12	41	6496	6196
400	10	30	3	2160	10	2.31	26	3790	3516
400	10	20	3	4320	7	1.65	26	5321	4938
500	10	12.5	1	2160	4	4.63	41	8914	8503
450	10	20	1	1800	7	3.53	33	9471	8932
450	10	20	2	3000	7	2.12	33	7892	7443
450	10	20	3	5400	7	1.18	33	9471	8932
450	10	20	5	9600	7	0.66	33	10102	9527

Table S12: Normal potentials of redox pairs in aqueous solutions (pH=1 and 14) according to Ref. [132]

Cathodic materials			Reducing Agents		
Redox Pair	ε_0^{acidic}	ε_0^{basic}	Redox Pair	ε_0^{acidic}	ε_0^{basic}
Co/Co^{2+}	−0.277	−0.733	Al/Al^{3+}	-1.676	-2.31
Co/Co^{3+}	0.414	−0.432	Mg/Mg^{2+}	-2.356	-2.687
Co^{2+}/Co^{3+}	1.808	0.17	Si/SiO_2	-0.909	-1.69
Mn/Mn^{2+}	−1.18	−1.55	P_4/H_3PO_2	-0.508	-2.05
Mn/Mn^{3+}	−0.28	−1.12	P_4/H_3PO_3	-0.932	-1.73
Mn/Mn^{4+}	0.025	−0.8	P_4/H_3PO_4	-0.412	-1.49
Mn^{2+}/Mn^{3+}	1.34	0.25	$S_8/S_2O_3^{2-}$	0.6	-0.742
Mn^{2+}/Mn^{4+}	1.23	−0.25	S_8/SO_2	0.5	-0.659
Ni/Ni^{2+}	−0.257	−0.72	S_8/SO_3	0.386	-0.751

Table S13: Ion concentrations determined by ICP-OES in filtrates obtained from mechanochemical reaction between sulfur and LCO at different molar ratios η.[198]

Element	η=1.0 [g/mol]	η=1.5 [g/mol]	η=2.0 [g/mol]	η=2.5 [g/mol]	η=3.0 [g/mol]
Li	181 ± 18	165 ± 4	151± 15	141 ± 3	131 ± 13
Co	0.061 ± 0.006	3.29± 0.07	11.6 ± 1.2	69.7 ± 1.5	71.1 ± 7.1
Fe	<0.003	<0.005	<0.003	0.188 ± 0.004	32.2 ± 3.2

Table S14: Elemental analysis of the Black Mass done by ICP-OES measurements of three independent samples.

Element	MW [g/mol]	Mass fraction [wt%]	Molar fraction [mmol/g]
Co	58.93	10.11 ± 1.16	1.72 ± 0.20
Ni	58.69	10.24 ± 0.55	1.75 ± 0.09
Mn	54.94	8.03 ± 0.38	1.46 ± 0.07
Li	6.94	3.50 ± 0.29	5.04 ± 0.41
Al	26.98	0.88 ± 0.13	0.33 ± 0.05
Cu	63.55	2.70 ± 1.97	0.42 ± 0.31
Fe	55.85	0.07 ± 0.00	0.01 ± 0.00
Ca	40.08	0.14 ± 0.10	0.03 ± 0.02
Na	22.99	0.59 ± 0.37	0.25 ± 0.16
P	30.97	0.34 ± 0.24	0.11 ± 0.08

Table S15: Standard enthalpy of formation of selected compounds.

Starting material	H_f^0 [kJ/mol]	Products	H_f^0 [kJ/mol]
$LiNi_{1/3}Mn_{1/3}Co_{1/3}O_2$[186]	-717	γ-$LiAlO_2$[188]	-1189
$LiCoO_2$[227]	-678	MgO[228]	-601
		Li_2O[228]	-598
		Li_2SiO_3[229]	-1647
		SiO_2[228]	-911
		$Li_5P_3O_{10}$[187]	-4674
		Li_2SO_4[228]	-1436

Table S16: Elemental analysis in mg/L of the combined filtrated obtained from different leaching routes of dried black mass. Leaching experiments were performed as doublets and the difference is presented as the uncertainty.[176]

Element	$BM_{dried} - Al$ direct	BM_{dried} – Al Carbonatization	BM_{dried} – Al Katoite	BM_{dried} – Mg direct
Li	105.5 ± 3.5	116 ± 1	202.5 ± 1.5	168 ± 18
F	76.95 ± 16.05	174 ± 3	9.8 ± 2.8	149 ± 12
Mg	0.094 ± 0	0.054 ± 0.001	0.006± 0.006	0.0625± 0.0625
Al	80.7 ± 45.3	28.8 ± 0.4	6.245 ± 2.985	4 ± 4
Ca	0 ± 0	0 ± 0	115.7 ± 101.3	0 ± 0
Mn	0.0985± 0.0635	0.248 ± 0.001	0.04 ± 0.04	0.003 ± 0.003
Fe	0.002 ± 0.002	0.022 ± 0.001	0.008 ± 0.008	0 ± 0
Co	0.104 ± 0.07	0.325± 0.002	0.0425± 0.0425	0 ± 0
Ni	0.105 ± 0.067	0.416 ± 0.002	0.036± 0.036	0.004± 0.004

Table S17: Elemental analysis in wt% of the insoluble residue obtained from different leaching routes of dried black mass.[176]

Element	$BM_{dried} - Al$ direct	BM_{dried} – Al Carbonatization	BM_{dried} – Al Katoite	BM_{dried} – Mg direct
Li	1.18 ± 0.03	1.41 ± 0.03	0.07 ± 0.00	0.45± 0.01
Na	<0.05	<0.05	<0.05	<0.05
Mg	<0.2	<0.2	<0.2	19.90 ± 0.64
Al	13.00± 0.43	16.90 ± 0.56	8.14± 0.27	0.89 ± 0.13
Ca	<0.1	<0.1	16.60± 3.32	<0.1
Mn	5.76 ± 1.44	7.47± 1.87	3.48 ± 0.87	5.25 ± 1.31
Fe	0.98 ± 0.02	0.52 ± 0.01	0.25 ± 0.01	0.20 ±0.00
Co	6.80 ± 0.14	8.78 ± 0.18	4.10± 0.09	6.02± 0.13
Ni	7.33 ± 0.14	9.57 ± 0.18	4.47 ± 0.08	6.59 ± 0.13
Cu	2.52 ± 0.04	3.08 ± 0.05	1.56 ± 0.03	2.44 ±0.04

Table S18: Elemental analysis in wt% of the recovered and purified Li_2CO_3 salt obtained from different leaching routes of dried black mass.

Element	BM_{dried} – Al Katoite	BM_{dried} – Mg direct
Li	17.60 ± 0.46	18.90 ± 0.43
O	63.80 ± 3.83	63.90 ± 3.64
F	0.30 ± 0.02	< 0.10
Na	1.22± 0.04	0.01± 0.00
Al	0.21 ± 0.01	0.00 ± 0.00
Ca	0.02 ± 0.00	0.02 ± 0.00
Mn	< 0.0002	< 0.0004
Fe	0.00 ± 0.00	< 0.0008
Co	< 0.0003	< 0.0003
Ni	< 0.0004	0.00 ± 0.00
Cu	< 0.0002	0.00 ± 0.00
Purity [%]	98.17	99.97

2 Supporting Figures

S1 XRD-Pattern

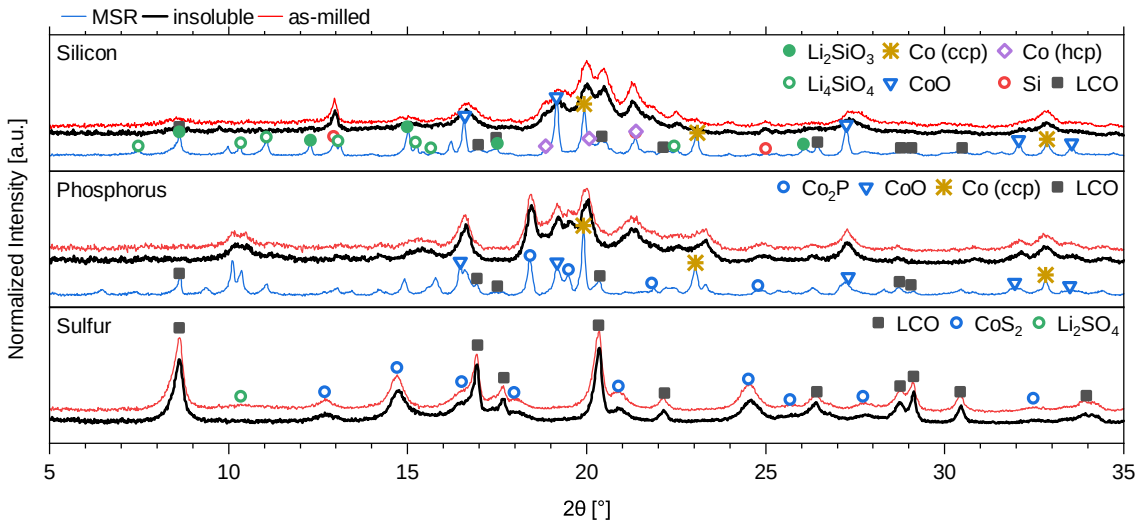


Figure S1.1: XRD pattern of the insoluble residue obtained after aqueous leaching of LCO milled with Si, P, and S. XRD pattern of the as-milled sample and of the MSR sample are included for comparison.

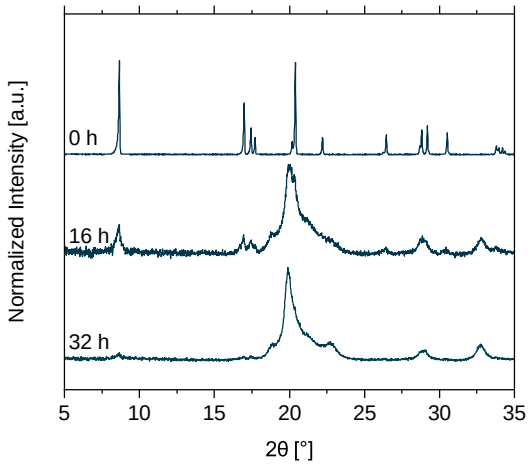


Figure S1.2: Evolution of XRD pattern during the milling of LCO with Al at 350 rpm with 3.0 mm balls.

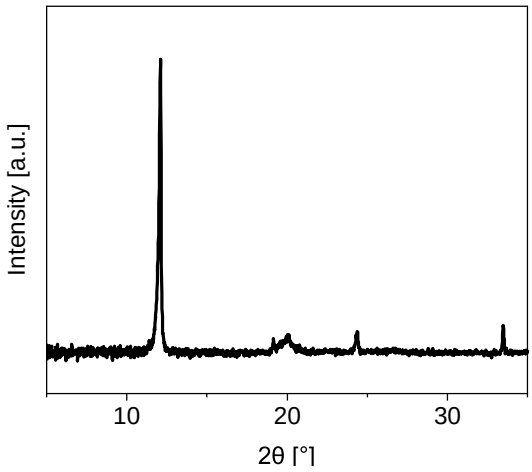


Figure S1.3: XRD pattern of pristine graphite.

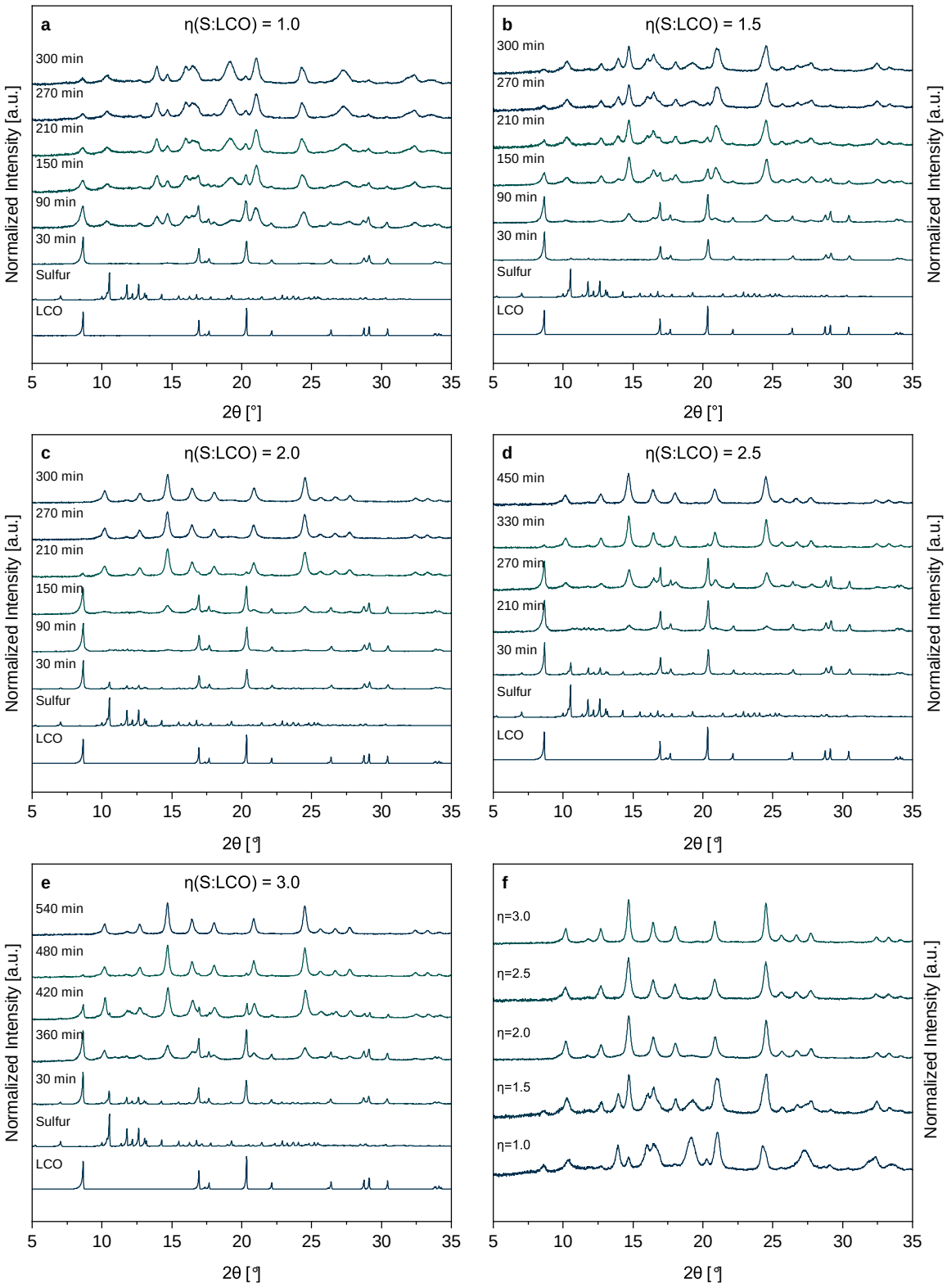


Figure S1.4: Evolution of XRD pattern during the mechanochemical processing of LCO with different amounts of elemental Sulfur, and a comparison of the final XRD pattern.[198]

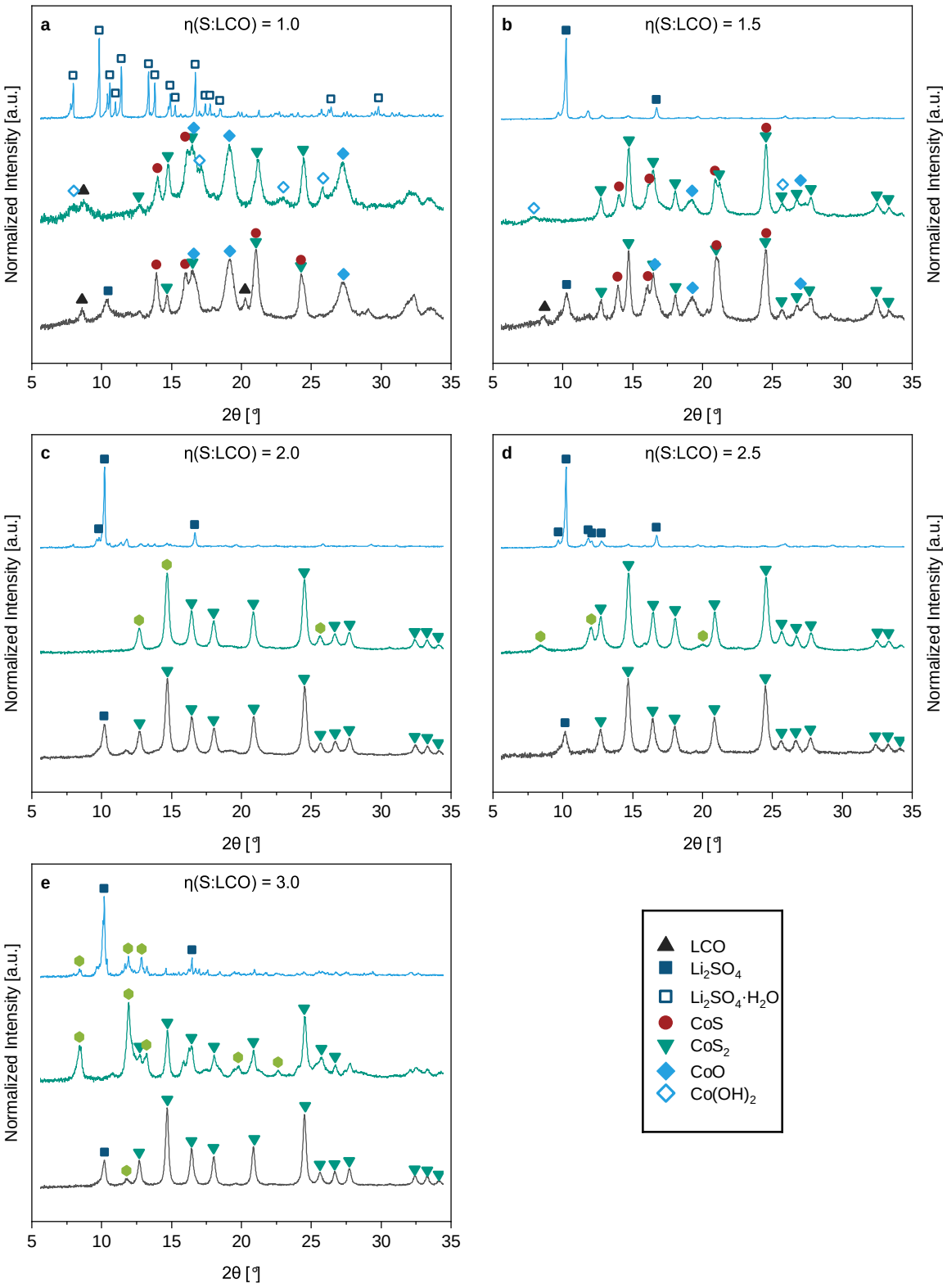


Figure S1.5: Evolution of XRD pattern during the selective Li-extraction of a milled S:LCO mixture in various molar ratios η.[198]

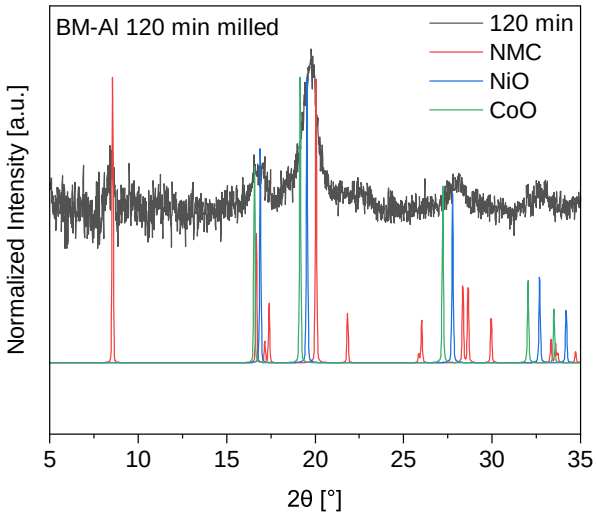


Figure S1.6: XRD pattern of black mass milled with Al for 120 min. As reference materials, NMC, NiO and CoO are presented with the COD ID 4002443, 1010095 and 1533087, respectively.

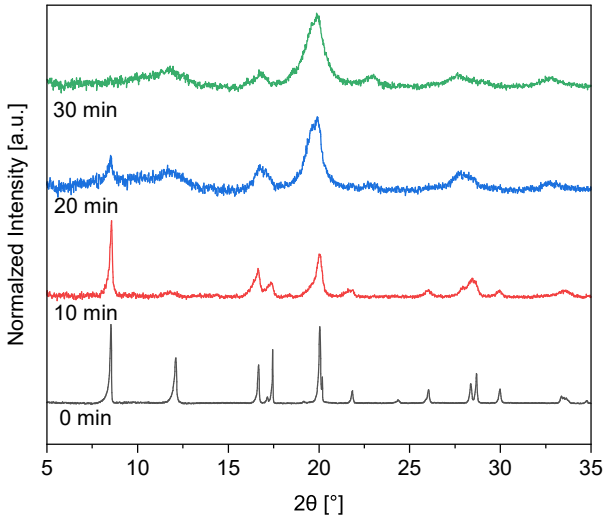


Figure S1.7: Evolution of XRD pattern during the milling of commercial NMC powder mixed with graphite and Al.[175]

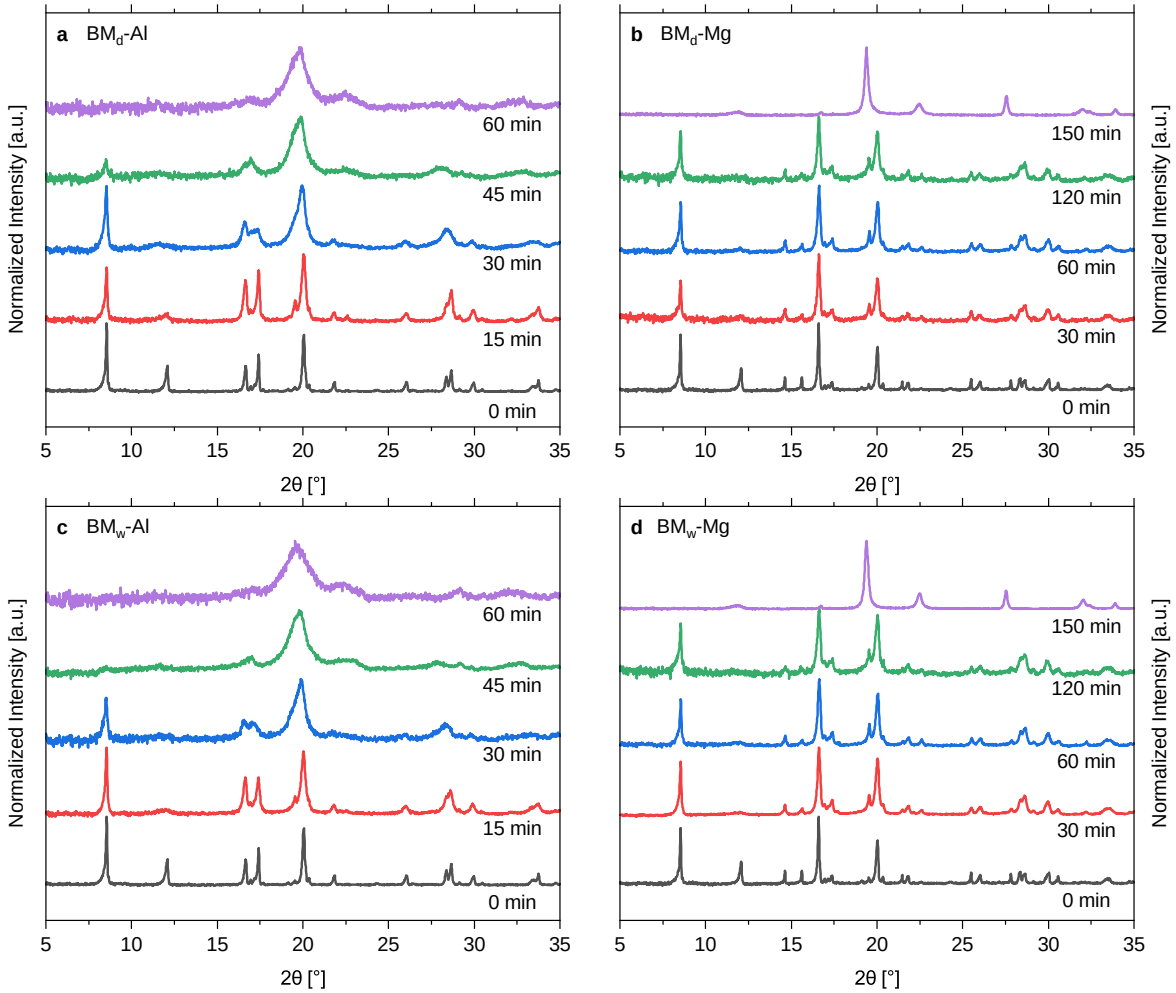


Figure S1.8: Evolution of XRD patterns during the reaction of BM_{dried} with a) Al, b) Mg and of BM_{washed} with c) Al and d) Mg.[176]

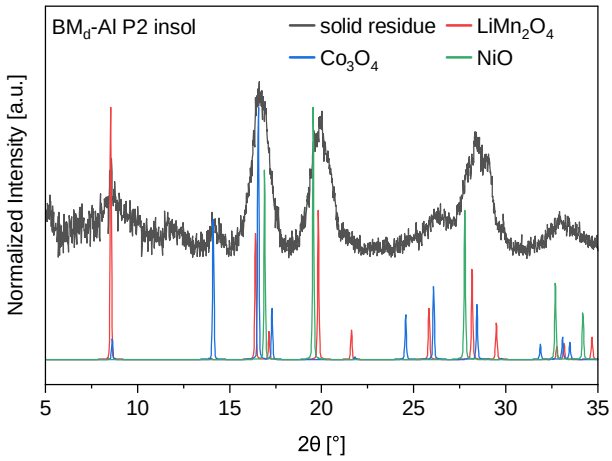


Figure S1.9: XRD pattern of the insoluble fraction, obtained from the carbonatization process. As reference materials, $LiMn_2O_4$, Co_3O_4 and NiO are presented with the COD ID 1513962, 5910031 and 1010095, respectively.

S2 Milling plots

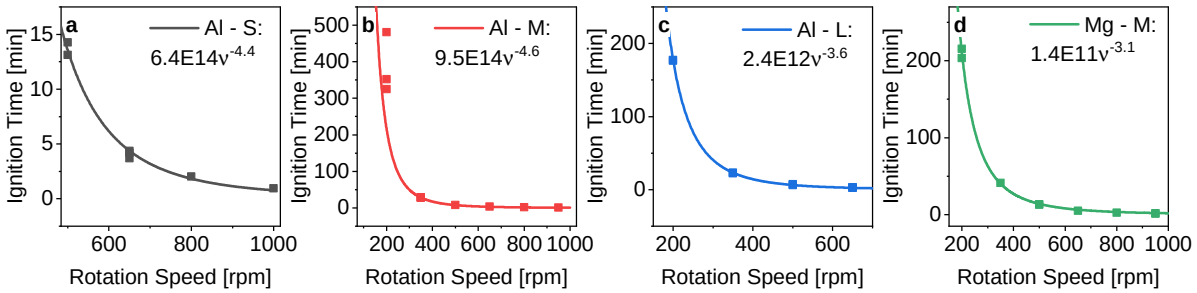


Figure S2.1: Measured t_{ig} during mechanochemical reaction of LCO with Al (a-c) and LCO with Mg (d). The lines represent the best fit of the formula $t_{ig} = A \cdot \nu^b$

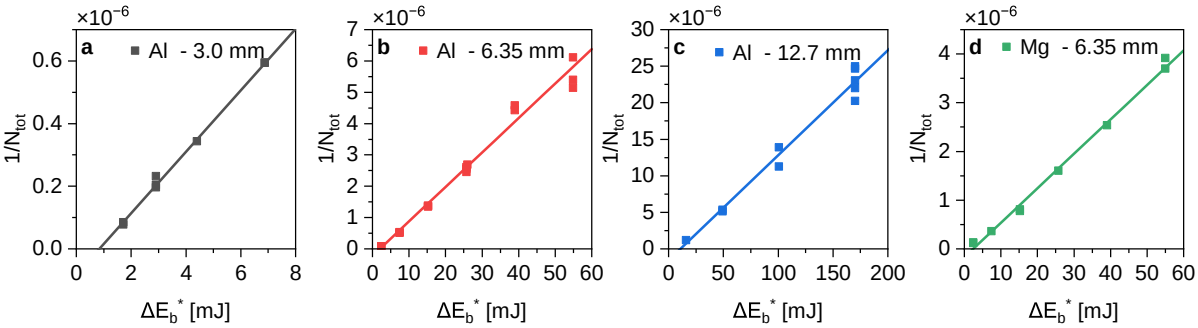


Figure S2.2: Measured t_{ig} during mechanochemical reaction of LCO with Al (a-c) and LCO with Mg (d). The lines represent the best fit of the formula $t_{ig} = A \cdot \nu^b$

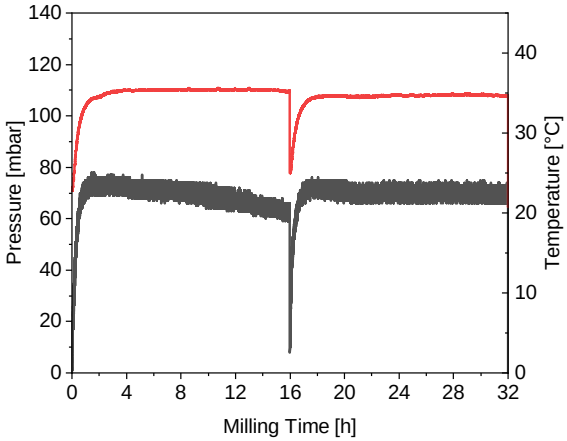


Figure S2.3: Temperature and pressure profile during the milling of LCO with Al using 65 g of 3 mm balls and 2.17 g of powder at 350 rpm.

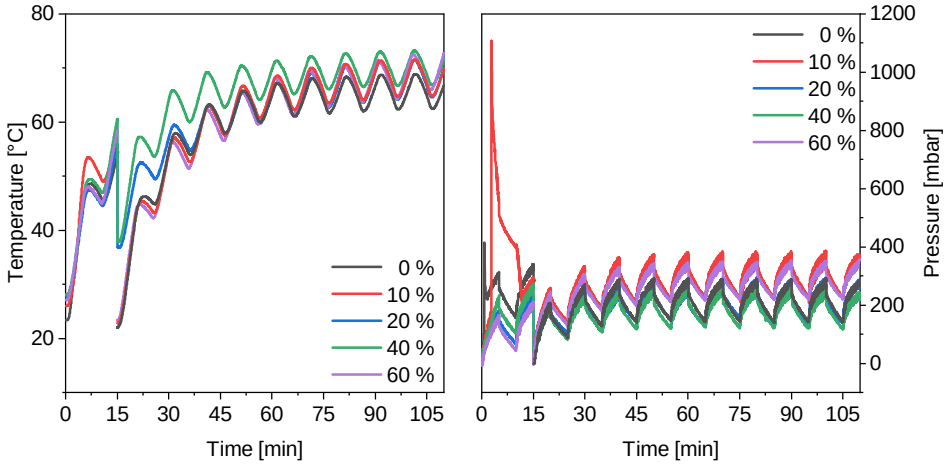


Figure S2.4: Temperature and pressure profiles recorded during the milling of LCO with Al and 0 - 60 wt% graphite.[175]

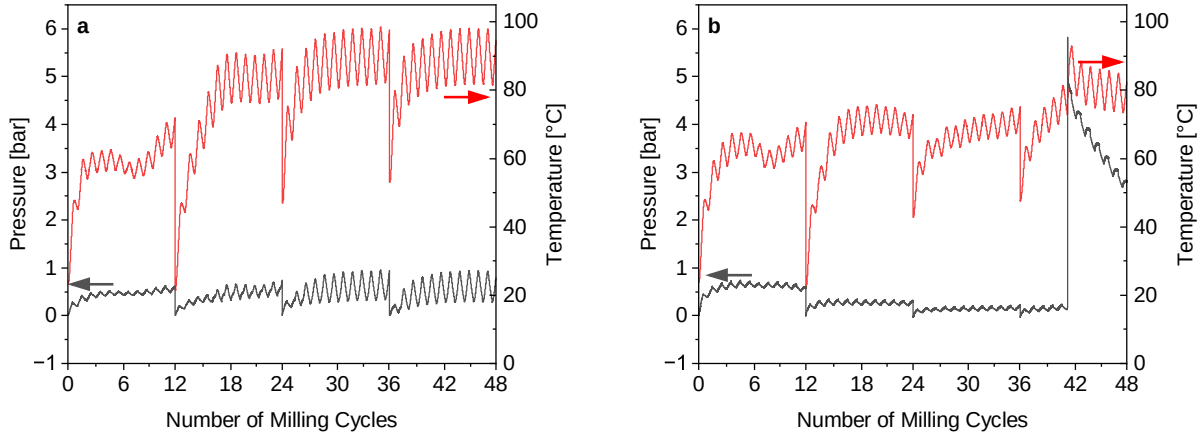


Figure S2.5: Pressure and temperature profiles, recorded during the milling of received black mass with a) Al and b) Mg. The zig-zag profiles show alternating cycles of 5 min milling and 5 min resting. The strong drops in T and p show the sampling points, where the milling vial was opened. When referred to the milling time, the resting time is not included. Therefore the spike in the pressure curve in panel b is after 206 min (41 x 5 min + 1 min) of milling.[176]

S3 X-ray Spectroscopy

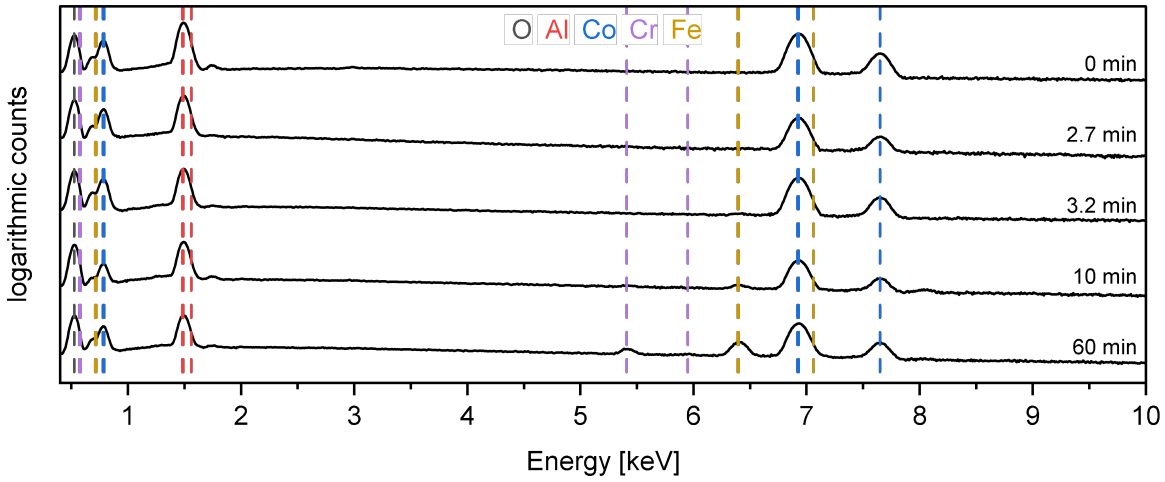


Figure S3.1: Evolution of EDX-spectra during the mechanochemical reduction of LCO with Al. 2.17 g of a stoichiometric mixture was milled at 650 rpm using 65 g of stainless steel balls (d=6.35 mm).[175]

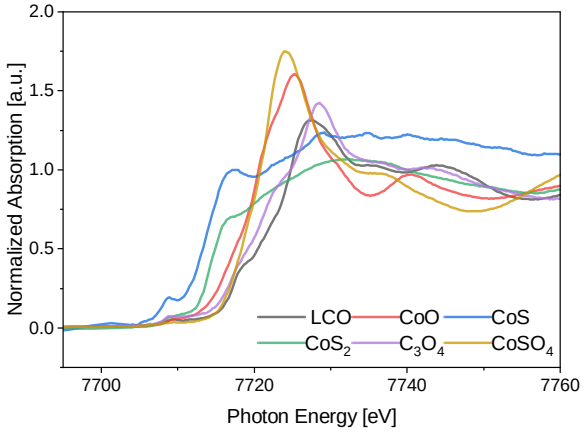


Figure S3.2: XANES spectra of Reference materials at the Co K_α-edge. The spectra have been used to fit the XANES spectra of obtained from samples collected during mechanochemical processing of LCO with S.

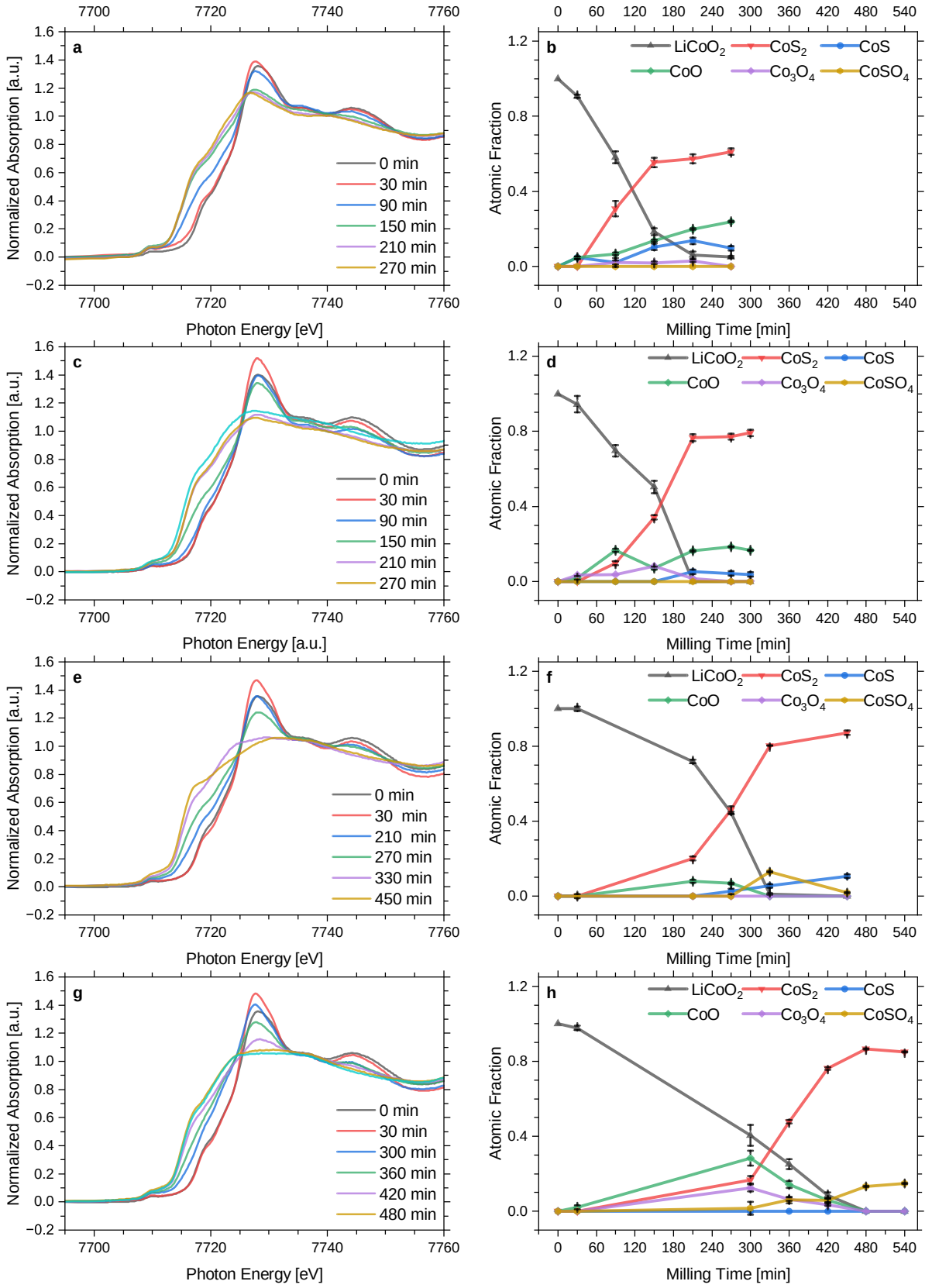


Figure S3.3: Evolution of XANES Spectra and atomic fractions determined by LCF during the mechanochemical reaction between LCO and S at molecular ratios η of a,b) 1.5, c,d) 2.0, e,f) 2.5 and g,h) 3.0.[198]

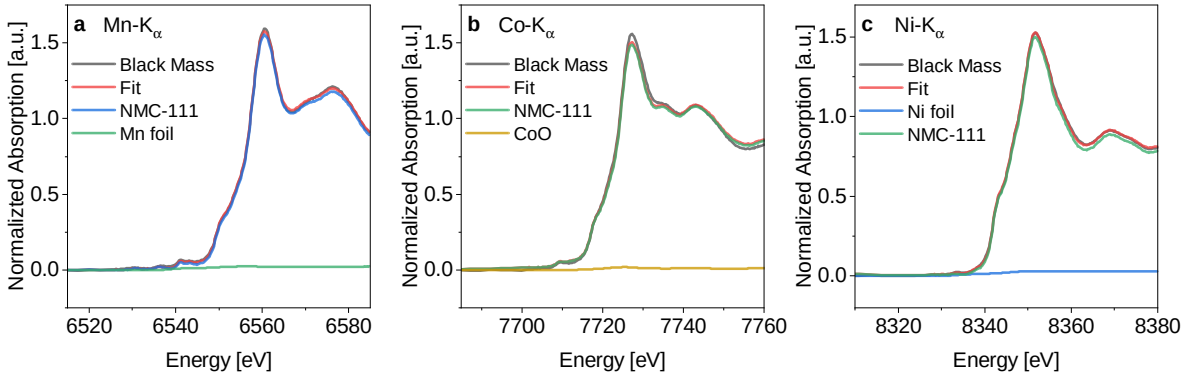


Figure S3.4: XANES spectra of on the K_α-edges of a) Mn, b) Co, and c) Ni of the BM and the LCF showing the presence of NMC-111.[176]

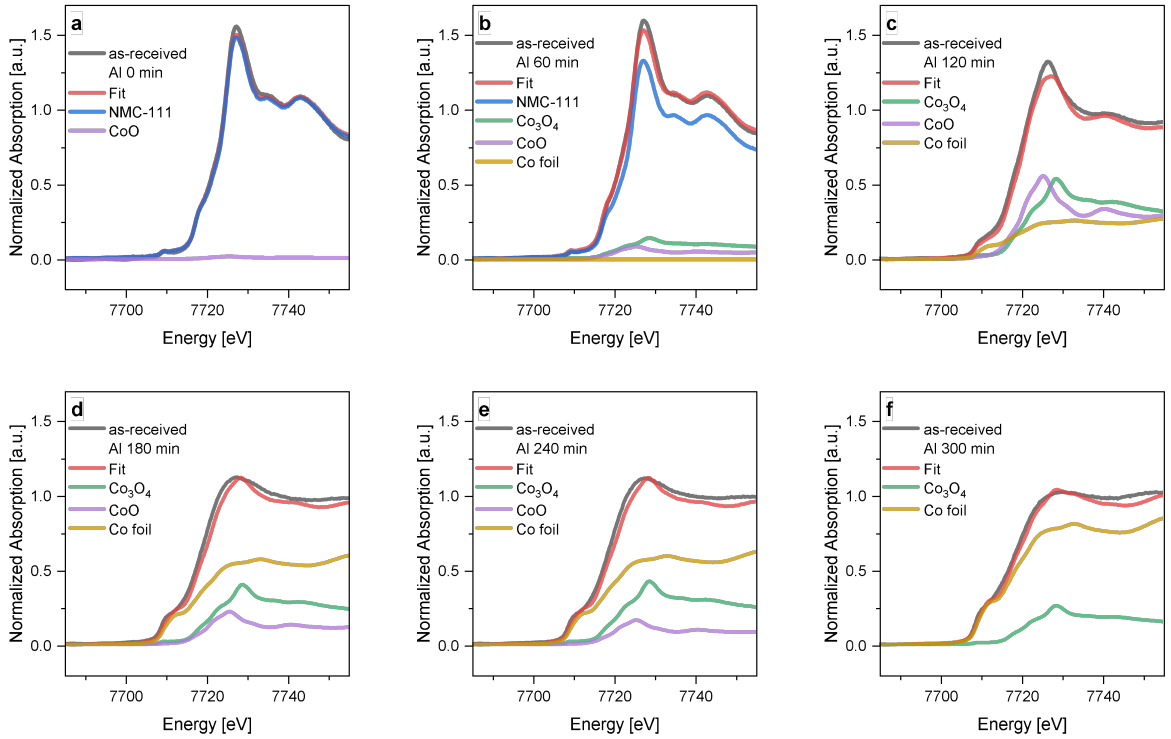


Figure S3.5: Linear combination fitting of XANES Co-K_α edge obtained from initial black mass milled with Al.[176]

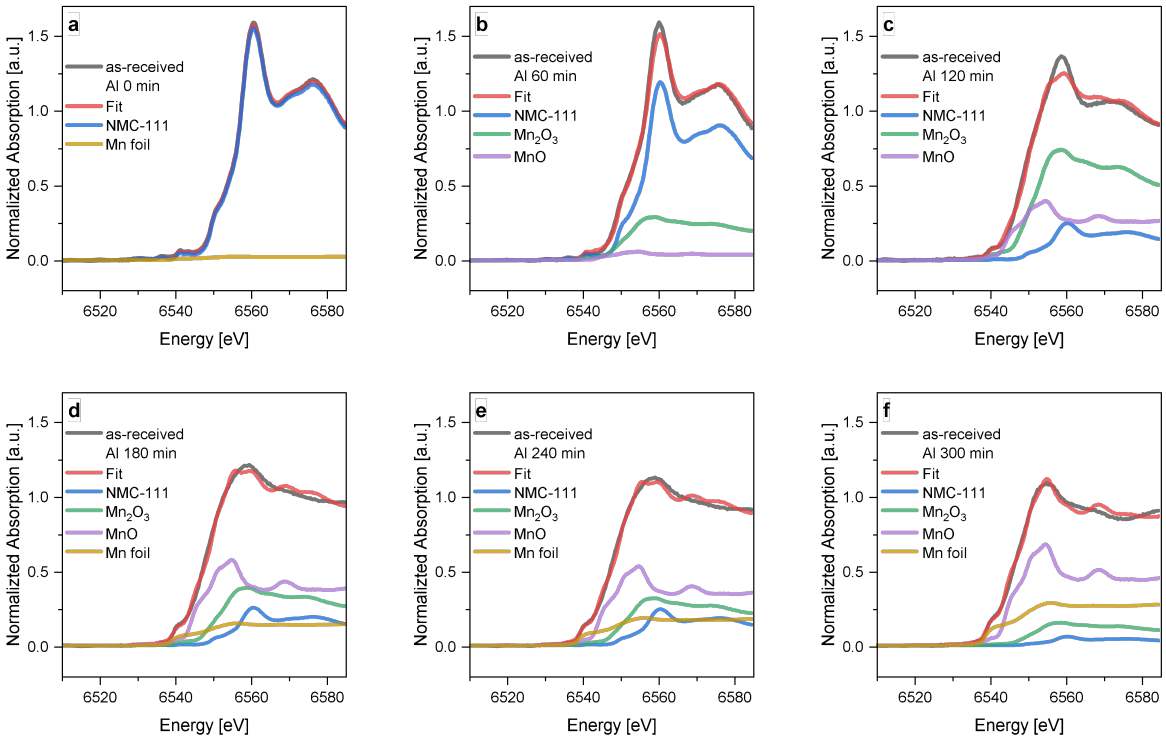


Figure S3.6: Linear combination fitting of XANES Mn-K_α edge obtained from initial black mass milled with Al.[176]

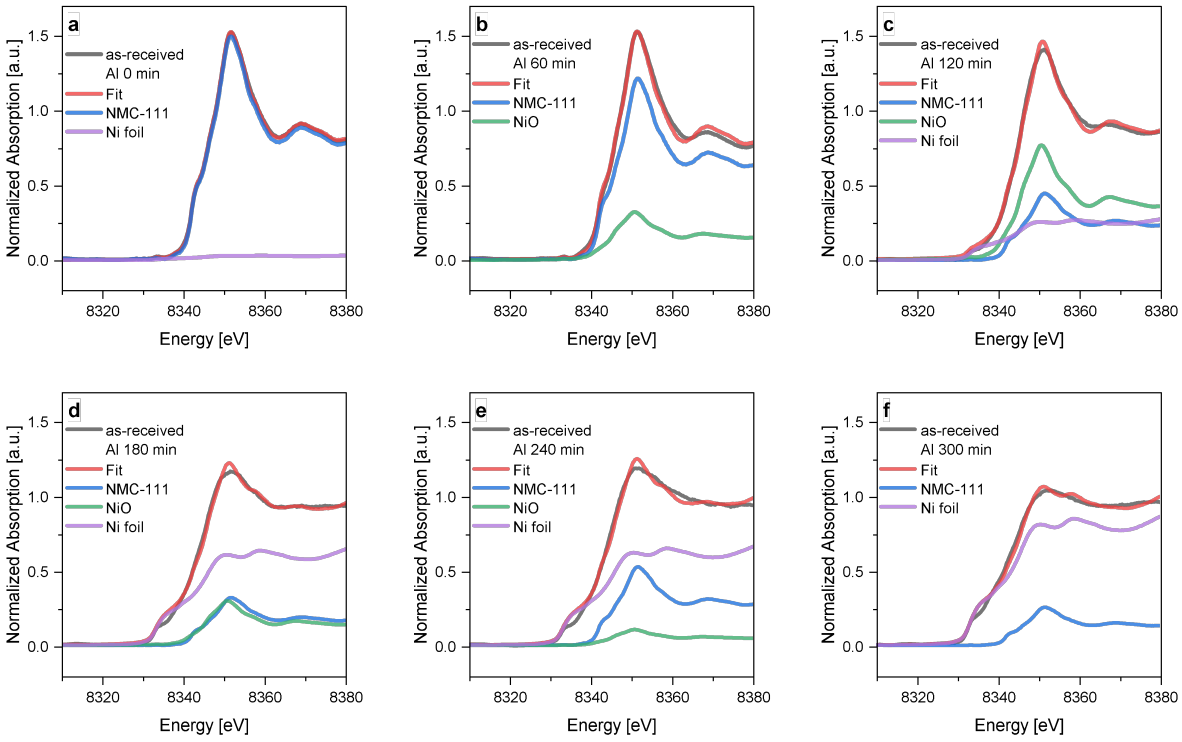


Figure S3.7: Linear combination fitting of XANES Ni-K_α edge obtained from initial black mass milled with Al.[176]

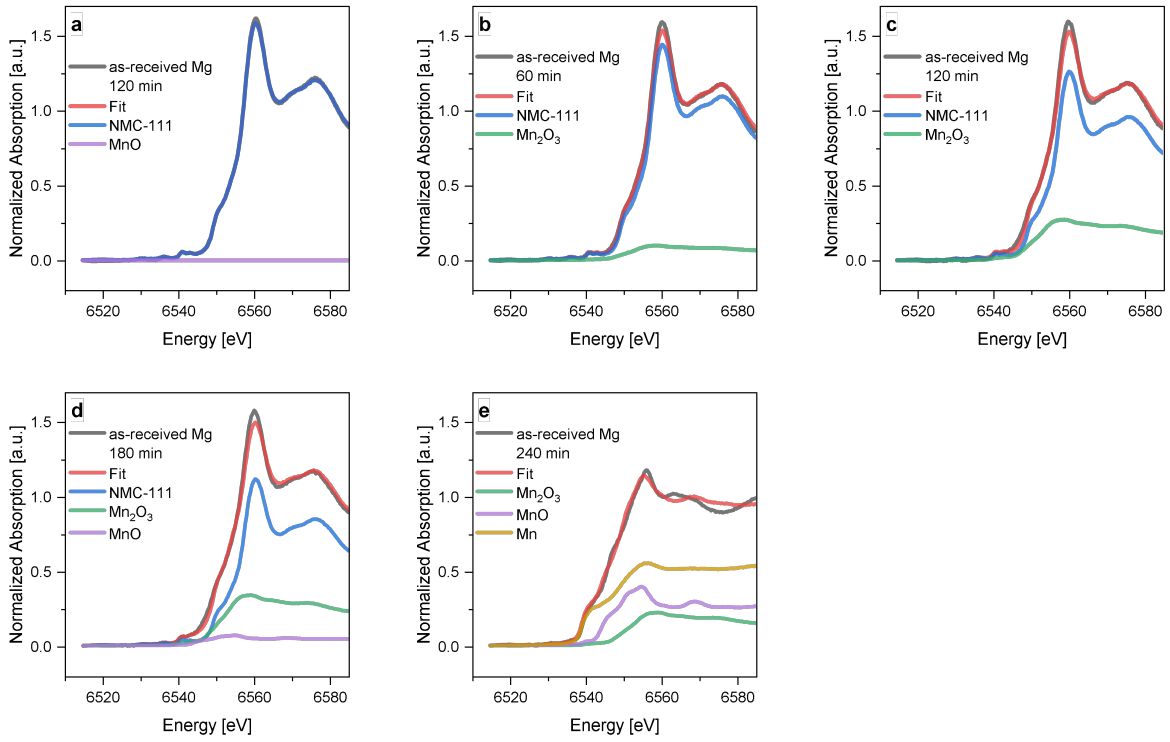


Figure S3.8: Linear combination fitting of XANES Mn-K edge obtained from black mass milled with Mg.[176]

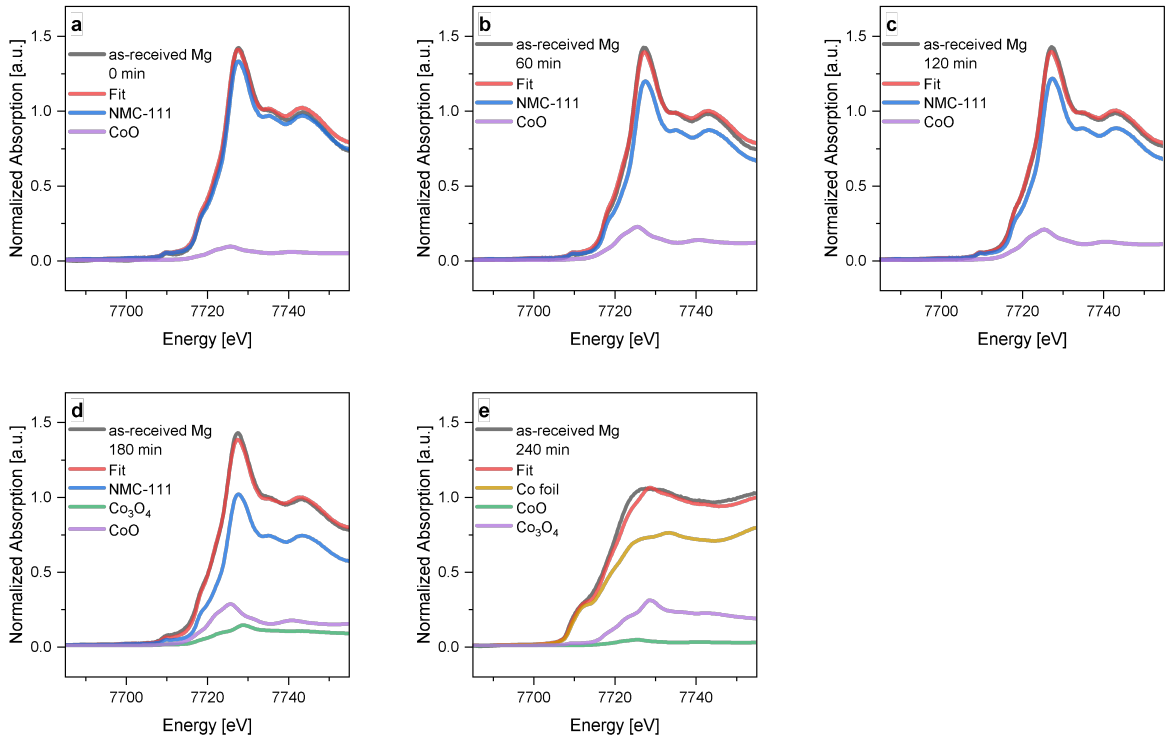


Figure S3.9: Linear combination fitting of XANES Co-K edge obtained from black mass milled with Mg.[176]

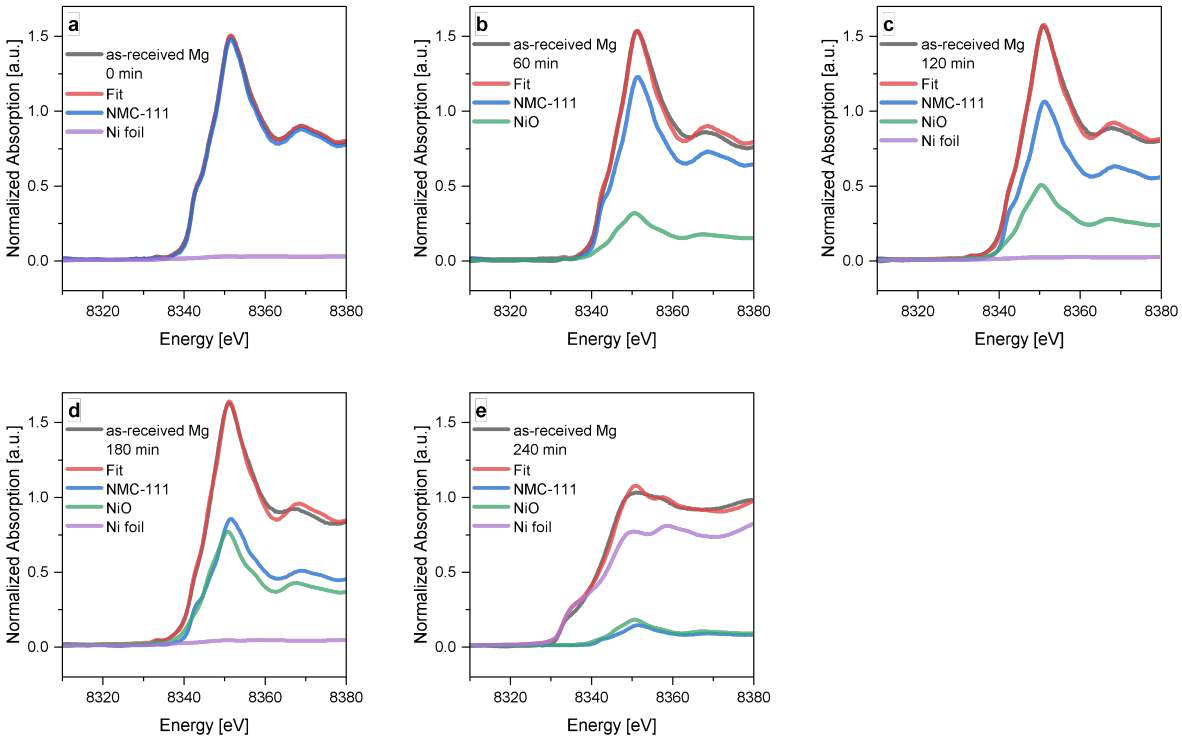


Figure S3.10: Linear combination fitting of XANES Ni-K edge obtained from black mass milled with Mg.[176]

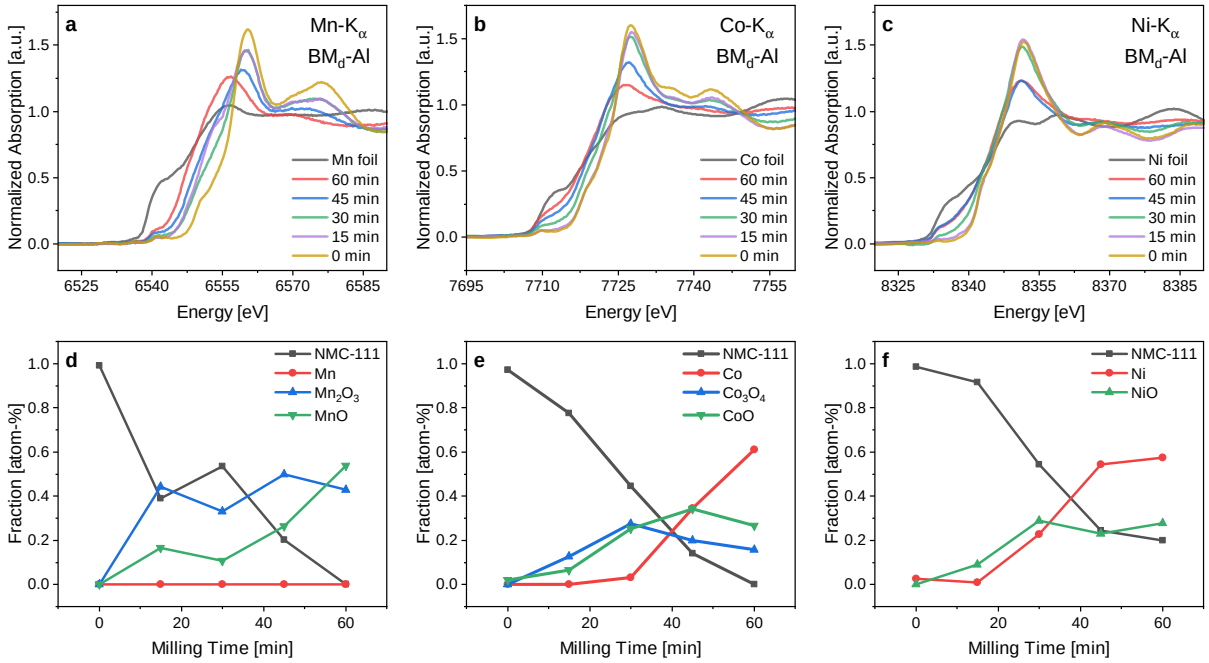


Figure S3.11: Evolution of XANES spectra during the milling process of BM_{dried} with Al at the Mn- (a), Co- (b) and Ni-K_α edge (c), alongside with the spectra of respective reference metallic foils. Panels d – f show the evolution of phase fractions in the milled powder obtained by linear combination fitting.[176]

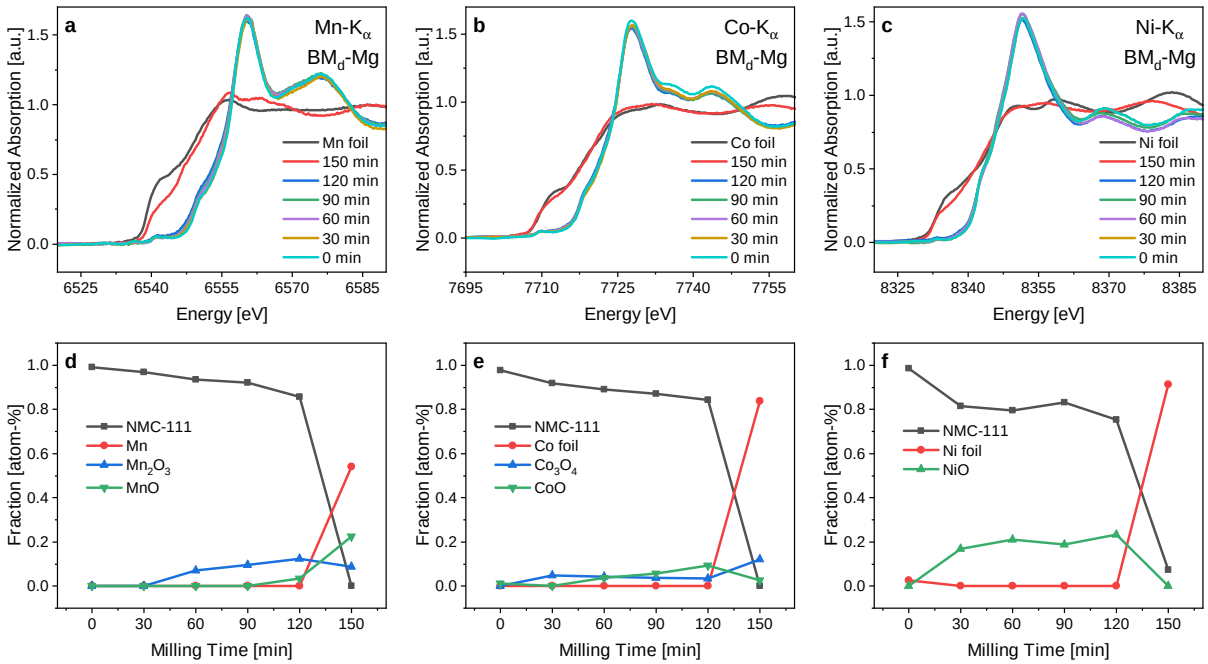


Figure S3.12: Evolution of XANES spectra during the milling process of BM_{dried} with Mg at the Mn- (a), Co- (b) and Ni-K_α edge (c), alongside with the spectra of respective reference metallic foils. Panels d – f show the evolution of phase fractions in the milled powder obtained by linear combination fitting.[176]

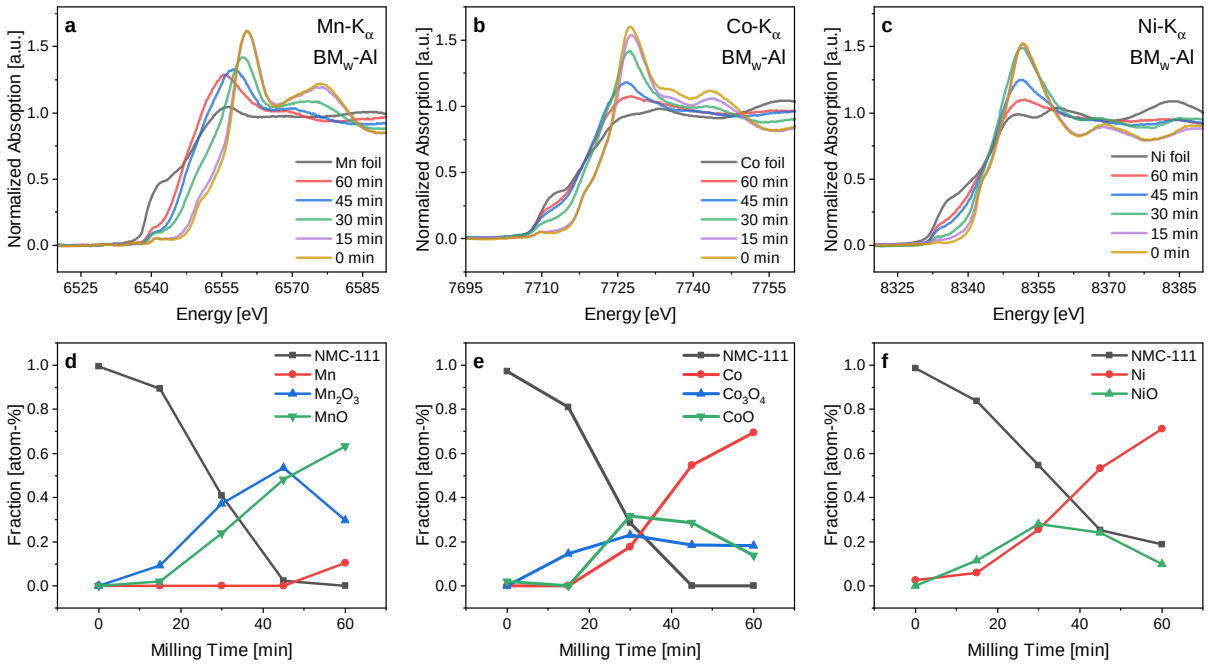


Figure S3.13: Evolution of XANES spectra during the milling process of BM_{washed} with Al at the Mn- (a), Co- (b) and Ni-K_α edge (c), alongside with the spectra of respective reference metallic foils. Panels d – f show the evolution of phase fractions in the milled powder obtained by linear combination fitting.[176]

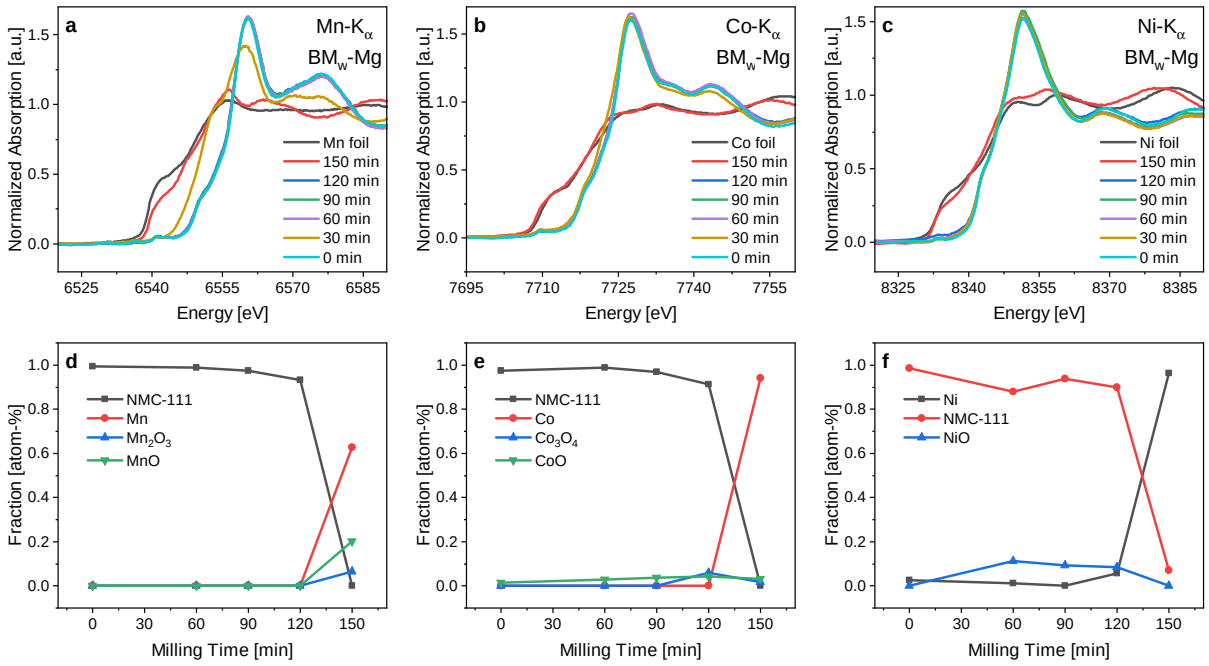


Figure S3.14: Evolution of XANES spectra during the milling process of BM_{washed} with Mg at the Mn- (a), Co- (b) and Ni-K_α edge (c), alongside with the spectra of respective reference metallic foils. Panels d – f show the evolution of phase fractions in the milled powder obtained by linear combination fitting.[176]

S4 Supporting Pictures

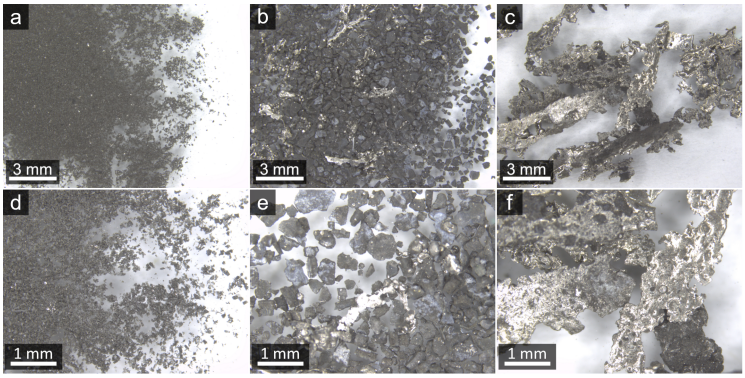


Figure S4.1: Light microscopy images of Sample III, after sieving. The fractions belong to 90 µm and less (a,d), 90-500 µm (b,e), and larger than 500 µm (c,f). The sample was collected after 3.2 min, when the spike in pressure was observed in the mechanochemical reaction between LCO and Al at 650 rpm with 60 balls (6.35 mm), 2.0 g of powder, LCO/Al =1.0 and a 1/BSR of 0.033.[175]

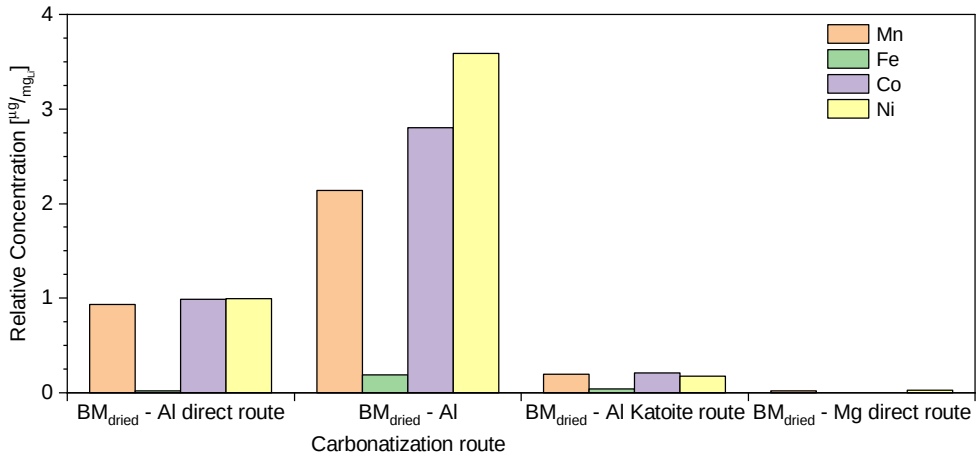


Figure S4.2: Relative concentrations of transition metals in the recovered lithium salt solution from different extraction processes.[176]